Electron Diffraction and Microscopy Study of Nanotubes and Nanowires

Hakan Deniz

A dissertation submitted to the faculty of the University of North Carolina at Chapel Hill in partial fulfillment of the requirements for the degree of Doctor of Philosophy in the Department of Physics and Astronomy.

Chapel Hill
2007

Approved by:

Advisor: Professor Lu-Chang Qin

Reader: Professor Hugon Karwowski

Reader: Professor Rene Lopez

Reader: Professor Laurie McNeil

Reader: Professor Sean Washburn

ABSTRACT

HAKAN DENIZ: Electron Diffraction and Microscopy Study of Nanotubes and Nanowires

(Under the direction of Dr. Lu-Chang Qin)

Carbon nanotubes have many excellent properties that are strongly influenced by their atomic structure. The realization of the ultimate potential of carbon nanotubes in technological applications necessitates a precise control of the structure of as-grown nanotubes as well as the identification of their atomic structures. Transmission electron microscopy (TEM) is a technique that can deliver this by combining the high resolution imaging and electron diffraction simultaneously. In this study, a new catalyst system (the Co/Si) was investigated in the production of single-walled carbon nanotubes (SWNTs) by laser ablation. It was discovered that the Co/Si mixture as a catalyst was as successful as the Ni/Co in the synthesis of SWNTs. The isolated individual SWNTs were examined by using nanobeam electron diffraction for the structure identification and it was found that carbon nanotubes grown by this catalyst mixture tend to be slightly more metallic.

The electron diffraction technique has been refined to establish a new methodology to determine the chirality of each shell in a carbon nanotube and it has been applied to determine the atomic structure of double-walled carbon nanotubes (DWNT), few-walled carbon nanotubes (FWNT) and multi-walled carbon nanotubes (MWNT). We observed that there is no strong correlation in the structure of two adjacent shells in DWNTs.

Several FWNTs and MWNTs have been examined by our new electron diffraction method to determine their atomic structures and to test the efficiency and the reliability of this method for structure identification. We now suggest that a carbon nanotube of up to 25 shells can be studied and the chirality of each shell can be identified by this new technique. The guidelines for the automation of such procedure have been laid down and explained in this work.

The atomic structure of tungsten disulfide (WS_2) nanotubes was studied by using the methods developed for the structure determination of carbon nanotubes. The WS_2 nanotubes are another example of the tube forming ability of the layered structures and a member of the family of inorganic fullerene-like structures. These nanotubes are much larger in diameter than carbon nanotubes. The tubes studied here have helicities less than 18^o and usually have near zigzag structure.

The short-range order (SRO) in the atomic structure of carbon soot produced by laser ablation was investigated using electron diffraction and radial distribution function (RDF) analysis. The effects of the furnace temperature and the metal catalyst on the SRO in the carbon soot were also studied. It was discovered that the SRO structure is the same for all carbon soot samples studied and is very similar to that of amorphous carbon. These techniques were also applied to determine the atomic structure of amorphous boron nanowires. We found out that the atomic structure of these boron nanowires agree well with the previously reported structure of bulk amorphous boron.

ACKNOWLEDGEMENTS

I would like to extend my sincere gratitude and thanks to my advisor Lu-Chang Qin who has supported me, guided me and encouraged me in my research and in my struggles over last three years here making it possible for me to finish this work. I would like to express my special thanks to Qi Zhang from whom I have learned a lot of information about operation and application of transmission electron microscopy. I also would like to thank my previous and current group members, Zejian Liu, Gongpu Zhao, Han Zhang, Letian Lin who were always kind and helpful to me in my research and my life in the group. I especially want to thank my friend Anna Derbakova by making my life easier in my research with computer scripts that she wrote.

I would like to give my thanks to Dr. Otto Zhou who was so nice in letting me use his laser ablation system and his laboratory extensively for my research. I also would like to thank my entire committee members, Dr. Hugon Karwowski, Dr. Laurie McNeil, Dr. Rene Lopez, and Dr. Sean Washburn for their guidance and encouragement. Finally, I would like to thank my best friends Shon Gilliam and Ted Uyeno for their friendship, for their encouragement, and for being there for me in my difficult times.

TABLE OF CONTENTS

Chapter

ABBREVIATIONS

CNT	Carbon nanotube
CRN	Continuous random network
DWNT	Double-walled carbon nanotube
FEM	Fluctuation electron microscopy
FWNT	Few-walled carbon nanotube
HRTEM	High-resolution transmission electron microscopy
MRO	Medium-range order
MWNT	Multi-walled carbon nanotube
NBED	Nano-beam electron diffraction
RDF	Radial distribution function
RRS	Resonant Raman spectroscopy
SRO	Short-range order
STM	Scanning tunneling microscopy
SWNT	Single-walled carbon nanotube
TEM	Transmission electron microscopy

Chapter 1

Introduction

Since its invention in 1932, transmission electron microscopy (TEM) has been a major tool for researchers to study the structure of materials from crystalline to amorphous. It has been in use for imaging, diffraction and chemical analysis of solids. Traditionally, x-ray or neutron diffraction has been the principal method for the study of crystals while TEM has been used to image individual atoms and to study defects in crystals. TEM has now become an indispensable technique for research in the field of nanotechnology in the last decade especially after the observation of carbon nanotubes was first carried out in a TEM [1].

1.1 Structural Order and Disorder

The atomic structure of materials can be grouped in three major categories: short-range order (SRO), medium-range order (MRO) and long-range order (LRO). The long range order refers to the crystalline form of matter. The structure of perfect crystals is relatively easy to describe because they follow translational periodicity and symmetry.

SRO and MRO

The atomic structure of amorphous materials lacks the periodicity and symmetry of its crystalline counterparts. Since there is no long-range order in amorphous materials, the

structure can only be defined in terms of a unit cell with an infinite number of atoms. Therefore, a statistical description of the structure is inevitable. Although there is no long range order in amorphous materials, there is a very well defined short-range order since two atoms can not approach each other closer than a typical bond length. So, the atomic structure can be described in terms of a pair density function that gives the probability of finding an atom at a distance r from an average atom excluding itself. The atomic structure can be obtained statistically through the radial distribution function (RDF) constructed from experimentally measured scattering intensities. The RDF curves show a very sharp first peak corresponding to the nearest inter-atomic distance in the sample and the successive peaks following it with broadened widths. It only gives the information about a single structural unit and its immediate connection to the next neighbors and fades away very quickly, making it difficult to obtain any kind of structural information beyond the length scale of ~0.8 nm [2-4]. Since the RDF analysis gives information about the average structure of the material, the three-dimensional atomic structure can never be determined unambiguously.

The continuous random network (CRN) model was introduced in early 1930s to explain the structure of covalently bonded glasses [5]. In the CRN model, the basic structural unit of the glass is similar to that of its crystalline counterpart. For example, the structural unit for vitreous SiO_2 is a SiO_4 tetrahedron. In the SiO_4 tetrahedron, each Si atom is bonded to four oxygen atoms and each oxygen atom to two Si atoms (Fig. 1.1.1). The connections of the tetrahedra lead to a network structure in three dimensions with no translational symmetry, in contrast to the structure of crystalline quartz. The complete characterization of the short-range order requires the knowledge of the bond lengths and

the coordination numbers of the structural unit and the distribution of the bond angles and lengths. The medium-range order is the next structural length scale in glasses and amorphous materials. It refers to the way that the basic units connect to each other to describe a structure on the length scale up to 2 nm [6]. For the SiO_2 case, the tetrahedra are connected to each other through the corners with a random distribution of torsion angles, and this leads to the structure (CRN) with almost non-existent medium range order. The deviations from the corner sharing basic units, such as edge or face sharing tetrahedra are an indication of an order higher than that of the short-range.

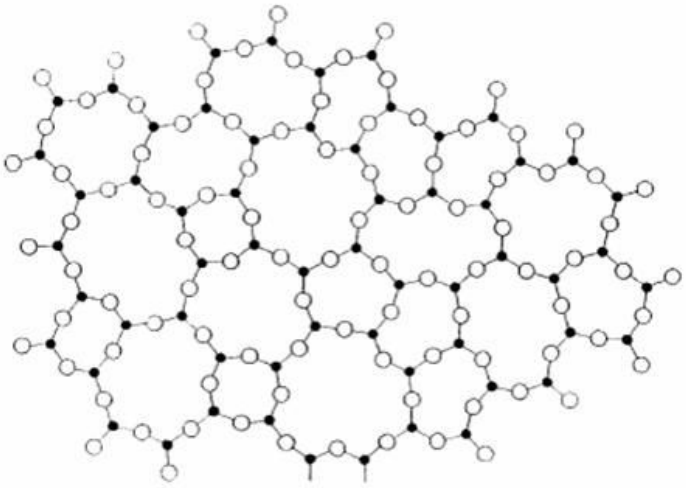

Fig. 1.1.1 Two dimensional schematic representation of the CRN model for SiO_2 (black dots for Si atoms and open circles for oxygen atoms). Adapted from reference [5].

Although the CRN model is successful in explaining the short range order and other basic features of the network glasses, it fails to elucidate other properties such as mass density, thermal vibrations, and the first sharp diffraction peak seen in the structure factor of these materials. The first sharp diffraction peak (FSDP) is believed to be the manifestation of medium range order in the disordered materials. It is located at low

scattering vector values, meaning that it corresponds to larger distances in real space beyond that of the short-range order. It is anomalous in the way that the real space correlation function remains almost unchanged whether or not the FSDP is included in the Fourier transform of the structure factor [7].

1.2 Carbon Nanotubes (CNT)

Carbon nanotubes have drawn an enormous amount of interest in the scientific community since their discovery by Iijima in 1991 [1]. This novel form of carbon has many extraordinary properties due to their nanometer-size diameter, large aspect ratio and hollow core [8-11]. They are envisaged to have promising applications in areas ranging from atomic probes, sensors, drug delivery systems, and transistors to flat panel displays and electron field emitters. The properties of carbon nanotubes are very sensitive to the geometry of their atomic structures [12-16] and the realization of the above mentioned technological applications of carbon nanotubes requires precise control and knowledge of their atomic structure.

1.2.1 Structure

A single-walled carbon nanotube (SWNT) can be obtained by rolling up a graphene about an axis perpendicular to the chiral vector (perimeter vector) $\vec{C}_h$ to make a seamless hollow cylinder. The chiral vector is defined in terms of the primitive vectors of the hexagonal graphene lattice by:

$$\vec{C}_h = u\vec{a}_1 + v\vec{a}_2 , \qquad (1.2.1)$$

where u and v are integers and are called the chiral indices of the nanotube (Fig. 1.2.1).

The angle between the basis vector $\vec{a}_1$ and the chiral vector is called the chiral angle (helical angle) or the helicity of the nanotube and is given by

$$\alpha = \arctan[\frac{\sqrt{3}v}{(v+2u)}]. \tag{1.2.2}$$

The diameter d of the tubule is given by C_h/π where C_h is the circumference of the tube and can be expressed as

$$d = C_h / \pi = \left|\vec{C}_h\right| / \pi = a_0 \sqrt{u^2 + v^2 + uv} / \pi, \tag{1.2.3}$$

in terms of the chiral indices and the lattice parameter a_0 of the two dimensional graphene (0.246 nm). Carbon nanotubes come in two different classes of symmetry: chiral (helical) and achiral (non-helical) nanotubes. For chiral nanotubes, the chiral angle lies in the range of [0^o, 30^o] if the handedness of the tubes is ignored (u ≥ v ≥ 0). For achiral nanotubes, there are two special cases. One is called the zigzag nanotube with chiral indices of (u, 0) having the chirality of 0^o. The other is called the armchair nanotube with chiral indices of (u, u) having the chiral angle 30^o.

The periodicity of the nanotube is given by the translational vector $\vec{T}$ which runs parallel to the tube axis and perpendicular to the chiral vector $\vec{C}_h$. Together they define the unit cell of the nanotube, also called the radial projection net. The translation vector $\vec{T}$ can be written using the basis vectors as

$$\vec{T} = u_t \vec{a}_1 + v_t \vec{a}_2 \tag{1.2.4}$$

where u_t and v_t are integers. Using the orthogonality relation between the chiral and translational vectors ($\vec{C}_h \cdot \vec{T} = 0$), the integers u_t and v_t can be calculated and given as

$$u_t = -\frac{u+2v}{M}, \tag{1.2.5}$$

and

$$v_t = \frac{2u+v}{M}, \tag{1.2.6}$$

where M is the greatest common divisor of $(2u+v)$ and $(u+2v)$. Then the periodicity of the tube takes the form of:

$$\left|\vec{T}\right| = \sqrt{3}a_0\sqrt{u^2+v^2+uv}/M = \sqrt{3}C_h/M\,. \tag{1.2.7}$$

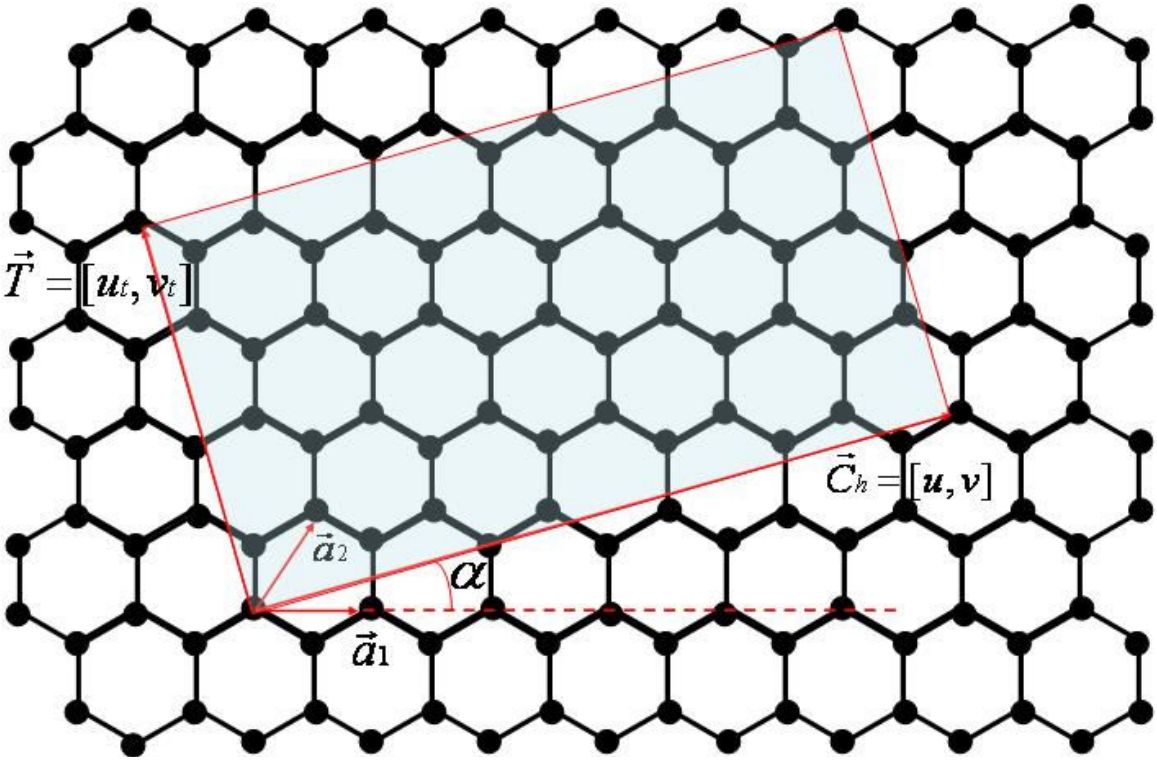

Fig. 1.2.1 The unrolled graphene lattice of a carbon nanotube, with chiral indices of (5, 2). The shaded rectangular region is the unit cell of the tube.

1.2.2 Electronic Properties

The electronic band structure of a single-walled carbon nanotube is closely related to that of the two-dimensional graphene sheet that is rolled up to form the tube. The monolayer thickness of the tube imposes a periodic boundary condition along the circumference or the $\vec{C}_h$ direction and the wave vector $\vec{k} = (k_x, k_y)$ is quantized circumferentially, whereas the wave vector along the tube axis is continuous for a tube with an infinite length. The energy dispersion relation of the tube can be obtained from the dispersion relation of a two-dimensional graphene sheet and is given by [12]

$$E_\mu(k) = E_{g2D}(\vec{k})(k\vec{K}_2 / K_2 + \mu\vec{K}_1), \tag{1.2.8}$$

where $E_{g2D}(\vec{k})$ is the dispersion relation of graphene expressed as

$$E_{g2D}(\vec{k}) = \pm\gamma_0\{1 + 4\cos(\frac{\sqrt{3}k_x a_0}{2})\cos(\frac{k_y a_0}{2}) + 4\cos^2(\frac{k_y a_0}{2})\}^{1/2} \tag{1.2.9}$$

and γ_0 is the nearest neighbor hopping parameter (2.9 eV for graphene) and a_0 is the lattice constant [12]. In equation (1.2.8), $\vec{K}_1$ is the discrete wave vector along the circumference of the tube, $\vec{K}_2$ is the reciprocal lattice vector along the axis of the tube, and μ is an integer. Using the quantization condition along the circumference, which is $\vec{k} \cdot \vec{C}_h = 2\pi q$ where q is an integer, leads to the following result at which metallic conductance for a tube occurs [13, 14]:

$$(u - v) = 3q. \tag{1.2.10}$$

All armchair tubes ($\alpha = 30^o$) satisfy this general rule and therefore are metallic. For zigzag nanotubes with the chiral indices of (u, 0), only the tubes where u is equal to $3q$ are metallic, otherwise they are semiconducting. The calculated energy dispersion

relations for metallic nanotubes of (5, 5) and (9, 0) and semiconducting nanotube (10, 0) support the conclusion that the electronic structure is dependent on the helicity and diameter of the nanotubes (see Fig. 1.2.2) [16]. Approximately, one third of all nanotube species will be metallic and the remaining two thirds semiconducting.

These interesting results can be understood better in terms of the band structure of 2D graphene which is a zero gap semiconductor. For an infinite graphene sheet, the allowed wave vectors $\vec{k}$ are infinite as well in two dimensions. For a nanotube with a small diameter, the periodic boundary conditions along the circumference only allow a few discrete sets of wave vectors $\vec{k}$. A few of the discrete $\vec{k}$ vectors are shown in Fig.1.2.3 in the direction of $\vec{K}_1$ with a separation K_1 between two adjacent vectors. For each $\vec{K}_1$ vector we can define the continuous $\vec{k}$ vectors along the $\vec{K}_2$ direction. So, the energy bands of the tube are composed of the lines in 1D which are the cross sections of the band structure of the graphene in 2D. The 2D graphene band structure is a hexagonal Brillouin zone with a degenerate density of states at the K-points (zone corners) where bonding and anti-bonding π bands meet. For a tubule having the condition $(u - v) = 3$ satisfied, the line (the wave vector $k\vec{K}_2 / K_2 + \mu\vec{K}_1$) will pass through one of the K-points in the Brillouin zone and the tube will be metallic with zero energy band gap. For the tubes where $(u - v) \neq 3$, none of the lines will pass through at the zone corners and the tube will be a semiconductor with a moderate energy gap [17]. As the diameter increases, the band structure of the tubule resembles more that of graphene and the energy gap will decrease proportional to the inverse tube diameter for semiconducting tubes.

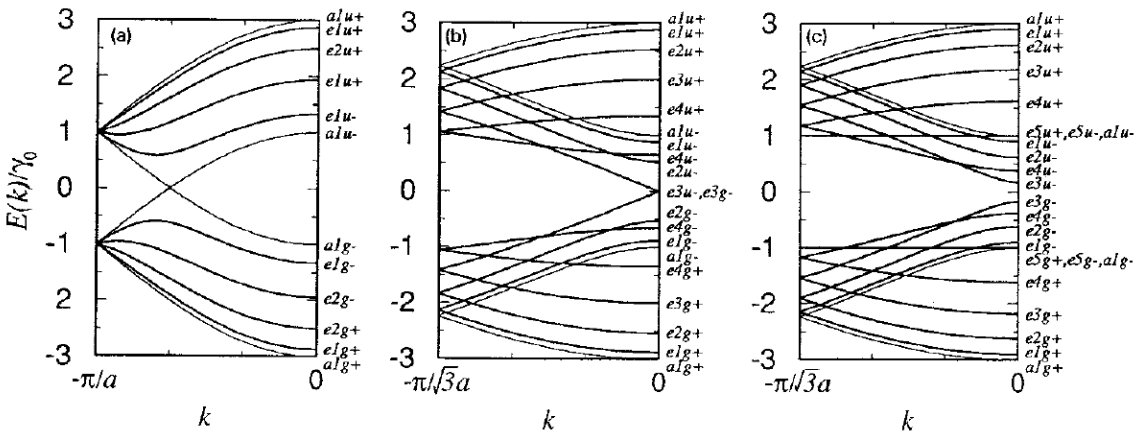

Fig. 1.2.2 One dimensional energy dispersion relations for (a) armchair nanotube of (5, 5), (b) zigzag nanotube of (9, 0) and (c) zigzag nanotube of (10, 0). Adapted from reference [16].

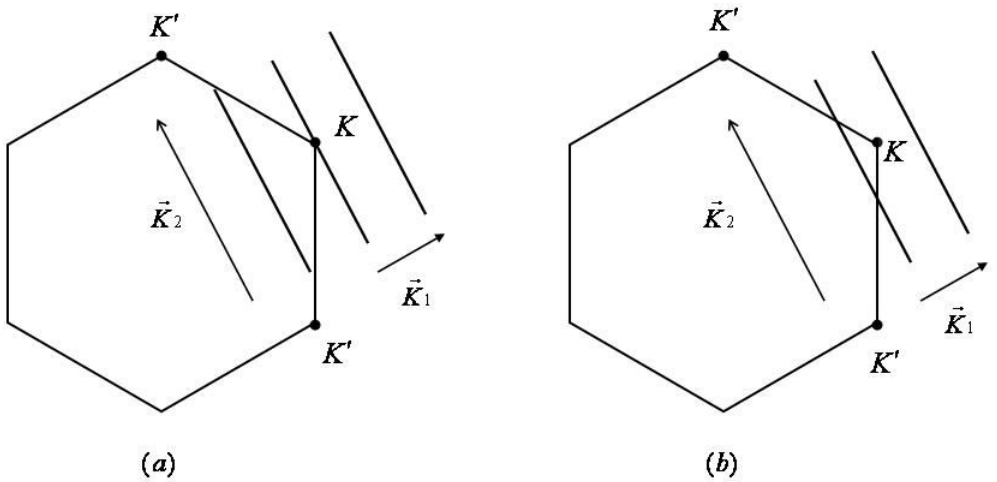

Fig. 1.2.3 The wave vector $\vec{k}$ for 1D carbon nanotube is shown as bold lines in the 2D Brillouin zone of graphene for (a) metallic tube and (b) for semiconducting tube. It has discrete values in the direction of $\vec{K}_1$ and continuous in the direction of $\vec{K}_2$. $\vec{K}_1$ and $\vec{K}_2$ are defined in the text.

The electronic band structure of carbon nanotubes shows sharp peaks or spikes known as van Hove singularities (vHS) at the onsets of energy sub-band edges due to one dimensional character of nanotubes (see Fig. 1.2.4). For metallic nanotubes, the 1D band structure has a small but non-vanishing constant density of states (DOS) at the Fermi level. For semiconducting nanotubes, the band structure shows an energy gap with zero DOS. These vHS are important for property measurements of nanotubes by scanning tunneling microscopy, resonant Raman spectroscopy, etc. The separation of symmetric vHS peaks in valance and conduction bands is known to depend on diameter [18]. The band gap of a semiconducting tube is given by $E_{gap} = 2\gamma_0 a_{c-c} / d$ where a_{c-c} is nearest-neighbor distance between carbon atoms (0.142 nm) and the separation of the first vHS on both sides of the constant DOS of a metallic tube is $E_{11}^{\ M} = 6\gamma_0 a_{c-c} / d$ [17].

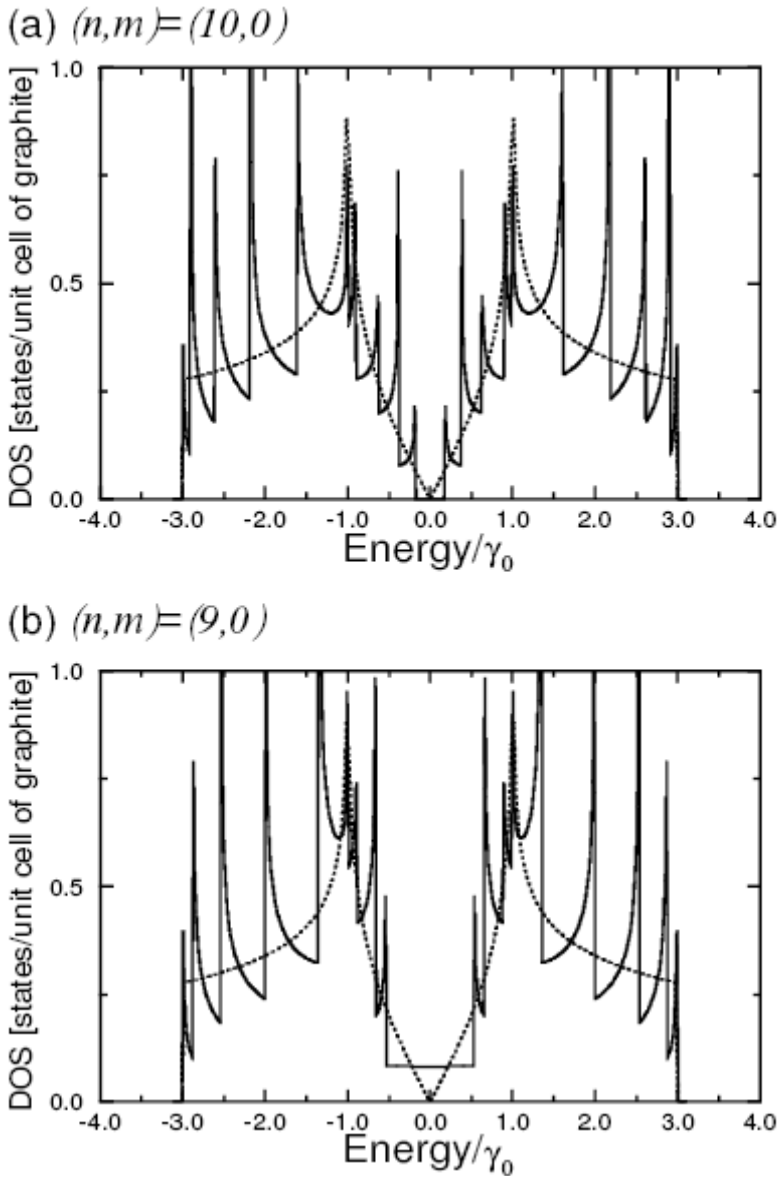

Fig. 1.2.4 Electronic density of states for two zigzag carbon nanotubes: (a) the (10, 0) nanotube which is semiconducting and (b) the (9, 0) nanotube which is metallic. The dotted line shows the DOS for the 2D graphene. Adapted from reference [16].

1.3 CNT Characterization Techniques

Many techniques have been used to characterize carbon nanotubes including X-ray diffraction, scanning electron microscopy (SEM), transmission electron microscopy (TEM), atomic force microscopy (AFM), Raman spectroscopy, scanning tunneling microscopy (STM), optical absorption spectroscopy, and nuclear magnetic resonance (NMR). Among these Raman spectroscopy, optical absorption spectroscopy, and STM are the most commonly applied ones to resolve and to determine the atomic structure (chiral indices) of carbon nanotubes in addition to electron diffraction and TEM.

1.3.1 Scanning Tunneling Microscopy (STM)

STM is a non-optical microscopy technique in which a sharp metal tip is scanned across a surface to reveal geometric and electronic structure by detecting a tunneling current flowing between the tip and the surface. The magnitude of tunneling current is dependent on distance between the tip and the surface, bias voltage between them, barrier height, etc. Topographic images are obtained by operating the STM in constant current mode where the tip to sample separation (a few atomic diameters) is controlled by a feedback loop. Atomic resolution is achieved when the tip is reduced to a single atom at the very end. In scanning tunneling spectroscopy (SPS), the variation of tunneling current versus bias voltage (I-V curve) is measured at a fixed sample position and fixed tip-to-sample distance. The differential conductance (dI/dV) calculated from I-V curve is proportional to the local DOS of the material under study.

STM and STS studies of purified SWNTs have shown that the electronic properties depend sensitively on the atomic structure (diameter and helicity) [19-21]. In a high

resolution STM image of SWNT, a triangular lattice of dark dots, which are attributed to the centers of the hexagons, is seen (see Fig. 1.3.1). The solid and dashed lines represent the tube axis and the zigzag direction respectively. The angle between them is the chiral angle that can be measured from the image. The diameter can be estimated using either tube heights with respect to the surface or line profiles obtained perpendicular to the tube axis. An accuracy of $\pm 1^{o}$ in chiral angle and ±0.1 nm in diameter measurements obtained allows for an identification of chiral indices unambiguously [22]. Spectroscopy measurements performed on nanotubes can further narrow down possible choices of indices to a unique assignment by distinguishing between metallic or semiconducting state.

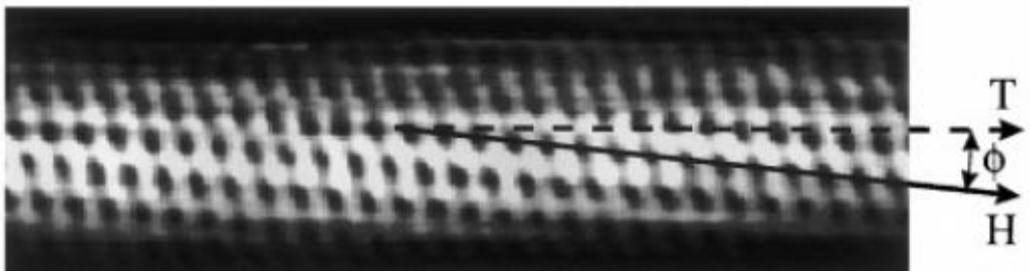

Fig. 1.3.1 Atomically resolved STM image of an individual single-walled carbon nanotube. **T, H** and ϕ represents the tube axis, chiral direction and chiral angle respectively. Adapted from reference [19].

STM is a powerful characterization tool in the sense that the atomic structure and electronic properties can be investigated simultaneously. Most of previous STM studies of carbon nanotubes focused on the determination of atomic and electronic structure of SWNTs. Existing studies on MWNTs showed that the STM resolves the chirality and the

properties of outer shell only. The effect of other shells on the electronic spectroscopy of MWNTs is weak [23]. A recent work demonstrated that the chirality of inner shell in DWNTs can be found from combined STM and SPS measurements [24].

1.3.2 Raman Spectroscopy

Raman spectroscopy is a powerful tool to study the diameter dependence of vibrational mode frequencies and electronic structure of carbon nanotubes. Raman scattering is a resonant process and occurs when the energy of the incident photons is matched by one of the inter-band electronic transitions in a nanotube. A typical Raman spectrum of a SWNT sample shows a sharp peak located between 120 and 350 cm^{-1} and another high intensity one located between 1490 and 1630 cm^{-1}. These are the radial breathing mode (RBM) and the graphitic mode (or G-band), respectively. The RBM mode is due to the equal radial displacement of all C atoms in the tube. It's a low frequency vibrational mode and dependent on the diameters of the tubes but not on their chiralities. The G-band results from the stretching of C-C bond in sp^2 bonded carbon. The frequency w_{RBM} of RBM mode is inversely proportional to the diameter and commonly used to determine the diameter of SWNTs. It is given by

$$w_{RBM} = \frac{A}{d} + B \,. \tag{1.3.1}$$

The constants A and B have been found to be 248 cm^{-1} nm and 0 cm^{-1} respectively for isolated SWNTs on Si/SiO_2 substrate [25]. The different values of A and B have been reported so far and the disagreement might be due to nanotube-nanotube interactions in bundles, nanotube-substrate interactions, and other environmental effects [26].

The diameter information from RBM mode alone is not enough for the assignment of chiral indices because the assignment is very sensitive to the precise values of A and B. The second information needed is the inter-band transition energies (E_{ii}) which can be obtained from Resonant Raman Scattering (RRS) experiments. In RRS, a laser light of several different energies is used to obtain complete chirality distribution on a mixture of nanotubes in the sample and their transition energies. A plot of E_{ii} versus d from experiment can be compared with a similar plot from tight-binding calculations. The identification of the families of nanotubes from geometrical patterns in both plots leads to the chiral index assignment [27]. The calculated energy separations $E_{ii}(d)$ for all nanotubes whose diameters lie between 0.7 nm to 3.0 nm is given in reference [17].

Raman spectroscopy is a technique sensitive to the nanotubes of small diameters (<2.0 nm). RBM signal gets very weak and broadened for MWNTs due to large outer shells. Since they are much larger in diameter and contain an ensemble of the tubes with diameters ranging from small to larger, their Raman spectra resemble to that of graphite. However, it has been shown that the innermost walls of MWNTs exhibit strong RBM modes in the spectra and these individual walls can be characterized by Raman spectroscopy due to their very small inner diameter (<2.0 nm) [28, 29].

1.3.3 Optical Absorption Spectroscopy

Most materials absorb ultraviolet (UV) or visible light. Absorption at particular wavelengths corresponds to an electronic transition to an excited state. Since the absorption of the light in visible and UV part of the spectrum is generally the result of interactions by electrons in atoms or molecules, studying absorption characteristics at a

broad range of wavelengths will produce information about electronic structure of the material in question. Luminescence is a process of emission of a photon with energy equal to the energy difference between the ground and excited states and again it will yield information about the structure of the electronic states. That's why optical absorption and photoluminescence is unique and common tool to characterize and obtain the inter-band transition energies and electronic structure of SWNTs. Photoluminescence can only identify semiconducting single-walled nanotubes whereas optical absorption can identify both metallic and semiconducting nanotubes. SWNTs well dispersed in solutions show high energy-resolution in their optical absorption spectra, which leads to the accurate determination of $E_{ii}(d)$ [30]. A large number of nanotubes can be studied easily. The chiral index assignment method here works similar to the one for RRS.

1.4 Inorganic Nanotubes

After the discovery of carbon nanotubes, the news of the synthesis of tungsten disulfide (WS_2) nanotubes by Tenne et al [31] in 1992 showed that forming a tubular structure of nanometer size is not unique to carbon. This was followed by reports of other new types of nanotubes, such as MoS_2 [32], WSe_2 [33], $MoSe_2$ [33], BN [34], and GaN [35], from inorganic compounds with layered structures. The different families of inorganic nanotubes synthesized so far include transition metal chalcogenides (WS_2, MoS_2, etc.), transition metal oxides (TiO_2, SiO_2, ZnO, GaO, etc.), transition metal halides ($NiCl_2$), boron and silicon based (BN, BCN, Si) and metal (Au, Cu, Ni, Bi, etc.) nanotubes. The full list of inorganic nanotubes synthesized so far up to the year 2004 can be found in reference [36].

The inorganic nanotubes have structures similar to those of carbon nanotubes (they are composed of coaxial cylindrical tubules) but the 2D sheet structure differs from that of the graphite. For example, in transition metal chalcogenides MX_2 where M is W or Mo and X is S or Se, the sheet structure contains three layers where a single layer of metal atoms is sandwiched between two layers of chalcogenide atoms [31]. This kind of structure leads to properties different from those of carbon nanotubes. The WS_2 and MoS_2 nanotubes do not possess tensile strength as high as that of carbon nanotubes but they are stronger under compression. They are predicted to be semiconducting and their electronic structure varies only slightly with their helicity and diameter [37]. The WS_2 and MoS_2 powders have long been known as good lubricants and are in use in lubrication industry. Their nanotubes have been shown to have good lubrication qualities as well [38]. Their use as a scanning probe tip was also demonstrated and it was shown that they could be much better AFM tips than carbon nanotubes due to their inert nature and durable structure [39]. The boron nitride tubes were first theoretically predicted [40] and then were successfully synthesized in the laboratory [34]. They are predicted to be insulating and their band gap approaches that of hexagonal BN (5.8 eV) as the tube diameter increases, in contrast to carbon nanotubes in this aspect. The electronic properties of BN nanotubes are not dependent on their chirality, diameter and the number of walls, unlike their carbon relatives [40]. It has been suggested that they could be used in molecular electronics because their electronic properties can be modified with doping. The first inorganic nanotubes WS_2 and MoS_2 were synthesized by the reduction of metal oxides in a forming gas followed by sulfurization in a flow of H_2S at elevated temperatures [31, 32]. They can also be produced by the methods similar to the

production of carbon fullerenes and nanotubes, for instance laser ablation or arc evaporation. The other methods used for synthesis are substitution reaction, template growth, hydrothermal pyrolysis, decomposition of precursor crystals, etc described in following reviews [41-43]. Although inorganic nanotubes is fast growing field, the reports and the studies on their properties do not match those on carbon nanotubes and still await to be conducted.

1.5 Objectives

In this work, our aim is to determine the atomic structure of each and every shell in MWNTs using TEM and electron diffraction. For future technological applications and scientific studies of MWNTs, it is of primary interest to know the structure of MWNT samples accurately. Other characterization techniques reviewed in section 1.3 are powerful in studying the atomic structure of SWNTs but have limitations for the characterization of the atomic structure of MWNTs. STM can measure the structure and electronic properties at the same time and enables us to correlate them with each other but it only allows studying the outer shell. Raman spectroscopy is a non-destructive and cheap technique and allows characterizing large number of nanotubes with a single measurement. However, it is only sensitive to characterize the nanotubes of diameter less than 2.0 nm.

Although electron diffraction has been applied successfully and extensively to determine the atomic structure of single-walled carbon nanotubes, it has not been widely used as a well-established technique for the atomic structure determination of MWNTs due to the difficulties in its application. As the number of the walls in a nanotube

increases, it becomes difficult to identify the structure of each wall since the number of possibilities for the chiral indices of the tube increases with increasing diameter. When this is coupled with the inter-shell interferences, it is a quite challenging task to identify the chirality and the structure of each and every shell in a MWNT. The MWNTs are the main focus of this work, and the objectives are listed under a few headings:

1. Characterize the diameter and the helicity of the SWNTs synthesized by laser ablation of a new catalyst system;
2. Determine the structure of DWNTs and few-walled carbon nanotubes (FWNTs) accurately and extend the applications to MWNTs;
3. Develop a systematic method to determine the atomic structure of every layer in a MWNT and test the accuracy and the limit of the method;
4. Apply the method developed for MWNT structure determination to identify the structure of WS_2 inorganic nanotubes;
5. Determine the structure of amorphous boron nanowires produced by CVD using electron diffraction and radial distribution function analysis;
6. Characterize the SRO and MRO structure of carbon soot produced by low temperature laser ablation using the methods mentioned in previous step and fluctuation electron microscopy.

1.6 References

1. Iijima, S. (1991). Helical microtubules of graphitic carbon. *Nature* **354**, 56-58.

2. Warren, B.E. (1990). *X-Ray Diffraction.* Dover Publishing Inc.: New York.

3. Wright, A.C. (1990). Diffraction studies of glass structure. *Journal of Non-crystalline Solids* **123**, 129-148.

4. Qin, L.C. (2001). *Progress in Transmission Electron Microscopy 1*, Edited by Zhang, X.F., Zhang, Z. Springer: New York.

5. Zachariasen, W.H. (1932). The atomic arrangement in glass. *J. Am. Chem. Soc*. **54**, 3481-3851.

6. Elliott, S.R. (1991). Medium-range structural order in covalent amorphous solids. *Nature* **354**, 445-452.

7. Elliott, S.R. (1991). Origin of the first sharp diffraction peak in the structure factor of covalent glasses. *Phys. Rev. Lett*. **67**, 711-714.

8. Yao, Z., Postma, H.W., Balents, L., Dekker, C. (1999). Carbon nanotube intramolecular junctions. *Nature* **402**, 273-276.

9. De Heer, W.A., Chatelain, A., Ugarte, D. (1995). A carbon nanotube field emission electron source. *Science* **270**, 1179-1180.

10. Dai, H., Hafner, J.H., Rinzler, A.G., Colbert, D.T., Smalley, R.E. (1996). Nanotubes as nano-probes in scanning probe microscopy. *Nature* **384**, 147-150.

11. Kong, J., Franklin, N.R., Zhou, C., Chapline, M.G., Peng, S., Cho, K., Dai, H. (2000). Nanotube molecular wires as chemical sensors. *Science* **287**, 622-625.

12. Saito, R., Dresselhaus, G., Dresselhaus, M.S. (1999). *Physical Properties of Carbon Nanotubes.* Imperial College Press: London.

13. Hamada, N., Sawada, S., Oshiyama, A. (1992). New one-dimensional conductors: Graphitic microtubules. *Phys. Rev. Lett*. **68**, 1579-1581.

14. Saito, R., Fujita, M., Dresselhaus, G., Dresselhaus, M.S. (1992). Electronic structure of chiral graphene tubules. *Appl. Phys. Lett*. **60**, 2204-2206.

15. Meyyappan, M. (2005). *Carbon Nanotubes Science and Applications* CRC Press: Boca Raton, Florida.

16. Dresselhaus, M.S., Eklund, P.C. (2000). Phonons in carbon nanotubes. *Advances in Physics* **49**, 705-814.

17. Saito, R., Dresselhaus, G., Dresselhaus, M.S. (2000). Trigonal warping effect of carbon nanotubes. *Phys. Rev. B* **61**, 2981-2990.

18. Mintmire, J.W., White, C.T. (1998). Universal density of states for carbon nanotubes. *Phys. Rev. Lett*. **81**, 2506-2509.

19. Wildoer, J.W.G., Venema, L.C., Rinzler, A.G., Smalley, R.E., Dekker, C. (1998). Electronic structure of atomically resolved carbon nanotubes. *Nature* **391**, 59-62.

20. Odom, T.W., Huang, J.L., Kim, P., Lieber, C.M. (1998). Atomic structure and electronic properties of single-walled carbon nanotubes. *Nature* **391**, 62-64.

21. Hassanien, A., Tokumoto, M., Kumazawa, Y., Kataura, H., Maniwa, Y., Suzuki, S., Achiba, Y. (1998). Atomic structure and electronic properties of single-walled carbon nanotubes probed by STM at room temperature. *Appl. Phys. Lett*. **73**, 3839-3841.

22. Venema, L.C., Meunier, V., Lambin, P., Dekker, C. (2000). Atomic structure of carbon nanotubes from scanning tunneling microscopy. *Phys. Rev. B* **61**, 2991-2996.

23. Rubio, A. (1999). Spectroscopic properties and STM images of carbon nanotubes. *Appl. Phys. A* **68**, 275-282.

24. Giusca, C.E., Tison, Y., Stolojan, V., Borowiak-Palen, E., Silva, S.R.P. (2007). Inner-tube chirality determination for double-walled carbon nanotubes by scanning tunneling microscopy. *Nano Letters* **7**, 1232-1239.

25. Jorio, A., Saito, R., Hafner, J.H., Lieber, C.M., Hunter, M., McClure, T., Dresselhaus, G., Dresselhaus, M.S. (2001). Structural (n, m) characterization of

isolated single-wall carbon nanotubes by resonant Raman scattering. *Phys. Rev. Lett.* **86**, 1118-1121.

26. Fantini, C., Jorio, A., Souza, M., Strano, M.S., Dresselhaus, M.S., Pimenta, M.A. (2004). Optical transition energies for carbon nanotubes from resonant Raman scattering: environment and temperature effects. *Phys. Rev. Lett*. **93**, 147406.

27. Telg, H., Maultzsch, J., Reich, S., Hennrich, F., Thomsen, C. (2004). Chirality distribution and transition energies of carbon nanotubes. *Phys. Rev. Lett*. **93**, 177401.

28. Benoit, J.M., Buisson, J.P., Chauvet, O., Godon, C., Lefrant, S. (2002). Low-frequency Raman studies of multiwalled carbon nanotubes: experiments and theory. *Phys. Rev. B* **66**, 073417.

29. Zhao, X., Ando, Y., Qin, L.C., Kataura, H., Maniwa, Y., Saito, R. (2002). Radial breathing modes of multiwalled carbon nanotubes. *Chem. Phys. Lett*. **361**, 169-174.

30. Lian, Y., Maeda, Y., Wakahara, T., Akasaka, T., Kazaoui, S., Minami, N., Choi, N., Tokumoto, H. (2003). Assignment of the fine structure in the optical absorption spectra of soluble single-walled carbon nanotubes. *J. Phys. Chem. B* **107**, 12082-12087.

31. Tenne, R., Margulis, L., Genut, M., Hodes, G. (1992). Polyhedral and cylindrical structures of tungsten disulfide. *Nature* **360**, 444-446.

32. Feldman, Y., Wasserman, E., Srolovitz, D.J., Tenne, R. (1995). High-rate, gas phase growth of MoS_2 inorganic nested fullerenes and nanotubes. *Science* **267**, 222-225.

33. Nath, M., and Rao, C.N.R. (2001). $MoSe_2$ and WSe_2 nanotubes and related structures. *Chem. Comm*. **2001**, 2236-2237.

34. Chopra, N.G., Luyken, R.J., Cherrey, K., Crespi, V.H., Cohen, M.L., Louie, S.G., Zettl, A. (1995). Boron nitride nanotubes. *Science* **269**, 966-967.

35. Li, J.Y., Chen, X.L., Qiao, Z.Y., Cao, Y.G., Li, H. (2001). Synthesis of GaN nanotubes. *J. of Mat. Science Lett*. **20**, 1987-1988.

36. Remskar, M. (2004). Inorganic nanotubes. *Advanced Materials* **16**, 1497-1504.
37. Seifert, G., Terrones, H., Terrones, M., Jungnickel, G., Fruenheim, T. (2000). Structure and electronic properties of MoS_2 nanotubes. *Phys. Rev. Lett*. **85**, 146-149.

38. Rapoport, L., Billik, Y., Feldman, Y., Homyonfer, M., Cohen, S.R., Tenne, R. (1997). Hollow particles of WS_2 as potential solid-state lubricants. *Nature* **387**, 791-793.

39. Rothschild, A., Cohen, S.R., Tenne, R. (1999). WS_2 nanotubes as tips in scanning probe microscopy. *Appl. Phys. Lett.* **75**, 4025-4027.
40. Rubio, A., Corkill, J.L., Cohen, M.L. (1994). Theory of graphitic boron nitride nanotubes. *Phys. Rev. B* **49**, 5081-5084.

41. Rao, C.N.R., Nath, M. (2003). Inorganic nanotubes. *Dalton Transactions* **1,** 1-24.

42. Tenne, R., Rao, C.N.R. (2004). Inorganic nanotubes. *Phil. Trans. R. Soc. London A* **362**, 2099-2125.

43. Ivanovskii, A.L. (2002). Non-carbon nanotubes: synthesis and simulation. Russ. Chem. Rev. **71**, 175-194.

Chapter 2

Theory of Electron Diffraction and Imaging for Carbon Nanotubes

2.1 Theory of Diffraction

The kinematical theory of electron diffraction can be applied to understand the electron diffraction patterns of carbon nanotubes, since carbon atoms have a low scattering intensity for fast electrons and the tubule is composed of only a few thin layers of graphite. The electron diffraction patterns of carbon nanotubes differ noticeably from those of graphite due to the finite size of the tube in the radial direction and its curvature. The scattering intensities from a carbon nanotube exhibit themselves as a set of equally-spaced layer lines perpendicular to the tube axis similar to the diffraction patterns of a DNA molecule. These layer lines result from the fact that the honeycomb lattice of graphite has a well-defined periodicity in the direction parallel to the tubule axis. As a result, the diffraction spots of a nanotube are sharply defined along the z-axis but elongated perpendicular to the tubule axis due to the curvature of the tube.

The (u,v) carbon nanotube can be considered as a composition of u helix pairs parallel to the $\vec{a}_2$ direction or v helix pairs parallel to the $\vec{a}_1$ direction (where each helix consists of a pair of atomic helices). The structure factor of a whole tubule will be the sum of the successive helix-pair structure factors. The theory of diffraction by helical structures was first developed in 1952 by Cochran, Crick and Vand (C. C. V. theory) and

applied to determine the structure of synthetic polypeptides [1]. Later, their theory was used and further developed by Qin [2] and Lucas et al [3, 4] to explain the electron diffraction patterns of carbon nanotubes.

The structure factor of a continuous helix can be written down following the C. C. V. theory and their notation:

$$F(R,\psi,Z) = J_n(2\pi Rr)\times\exp[in(\psi+\pi/2)], \tag{2.1.1}$$

where (r,ϕ,z) are the cylindrical coordinates in real space, (R,ψ,Z) are the corresponding cylindrical coordinates in reciprocal space, C is the pitch length of a continuous helix, and J_n denotes the Bessel function of order n where n is an integer (see Fig. 2.1.1). In the structure factor (2.1.1), Z is equal to n/C and the diffraction spots are on the layer lines along the z-axis equally spaced by 1/C. The square modulus of the structure factor, which is the intensity distribution in the reciprocal space, is independent of ψ. For a discontinuous helix, we can define the structure as a set of atoms lying on a helical line which has periodicity of c with a distance Δ between atoms along the vertical axis (see Fig. 2.1.2). In reciprocal space the layer lines result from the convolution of the structure factor of a continuous helix with the Fourier transform of a set of the atoms, which is a discrete set of points located at $Z = j/\Delta$ on the Z-axis [2]. The result is the transform of a discontinuous helix seen at the heights on the Z-axis given by the selection rule:

$$Z = l/c = n/C + m/\Delta, \tag{2.1.2}$$

where m is an integer. Then, the structure factor becomes

$$F(R,\psi,l/c) = \sum_n J_n(2\pi Rr)\times\exp[in(\psi+\pi/2)] \tag{2.1.3}$$

and l and n are related by the selection rule (2.1.2).

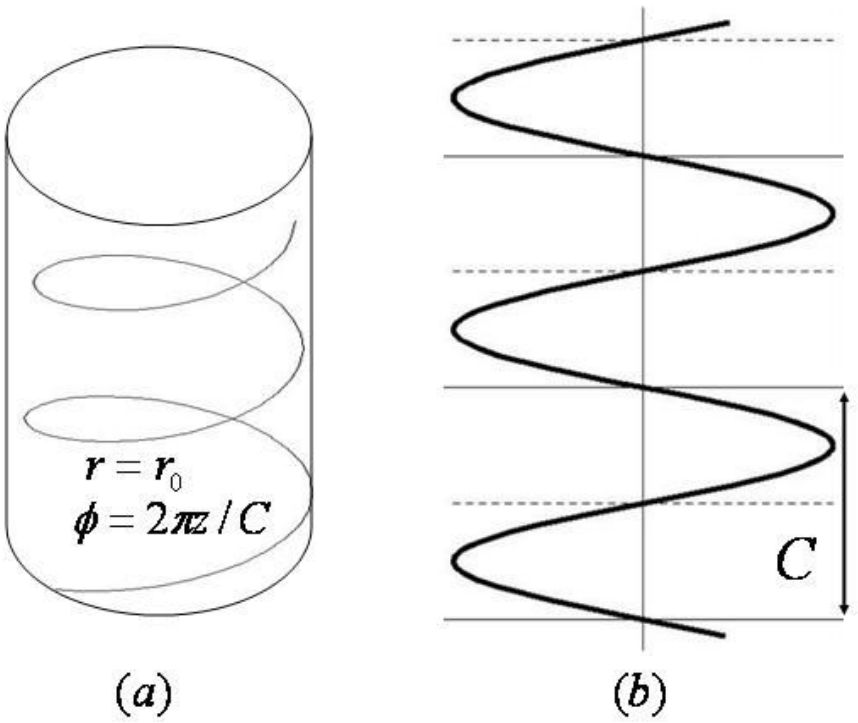

Fig. 2.1.1 (a) A continuous helix of radius r_0 with pitch length C and (b) its projected structure in two dimensions.

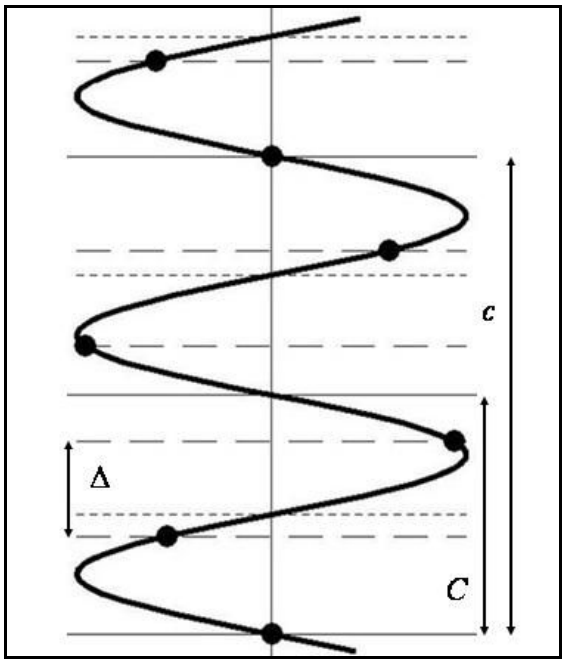

Fig. 2.1.2 Structure of a discontinuous helix in two dimensional projection. Atoms repeat themselves at a period of c and are equally spaced along the z-axis.

For a helix with more than one atom in the unit cell (asymmetric unit), the summation should be done over all the atoms within the unit cell:

$$F(R,\psi,l) = \sum_n J_n(2\pi Rr)\exp[in(\psi+\pi/2)]\sum_j f_j \exp[i(-n\phi_j + 2\pi l z_j / c)] \qquad (2.1.4)$$

where f_j is the atomic scattering amplitude for carbon atoms and (ϕ_j, z_j) is the relative atomic shifts of all composing helices. When all atoms are on the cylindrical surface of diameter *d*, the structure factor *F* becomes

$$F(R,\psi,l) = \sum_n J_n(\pi Rd)\exp[in(\psi+\pi/2)]\sum_j f_j \exp[i(-n\phi_j + 2\pi l z_j / c)]. \qquad (2.1.5)$$

For a SWNT of chiral indices (u,v) with perimeter C_h and helicity α, the pitch C is $C = C_h \tan(60^\circ - \alpha)$ and the distance between atoms is $\Delta = a_0 \sin(60^\circ - \alpha)$ [5]. The axial periodicity is given by $c = \sqrt{3}C_h / M$ where *M* is the maximum common divisor of $(2u+v)$ and $(u+2v)$. Then the selection rule (2.1.2) can be rewritten as

$$l = \frac{[n(u+2v) + 2m(u^2+v^2+uv)]}{uM}. \qquad (2.1.6)$$

Adding the structure factors of all the composing helices with the relative atomic shifts of $(d/2, \phi_j, z_j)$ leads to

$$F_{uv}(R,\psi,l) = \sum_{n,m} f[1+\exp\{2\pi i[n+(2u+v)m]/3u\}]\frac{1-\exp[-2\pi i(n+mv)]}{1-\exp[-2\pi i(n+mv)/u]} \qquad (2.1.7)$$
$$J_n(\pi dR)\exp[in(\psi+\pi/2)].$$

Unless $(n+mv)/u$ is an integer, the quotient in equation (2.1.7) is zero [6]. This restricts the layer lines of nonzero intensity to a discrete set which produces a hexagonal distribution of diffraction spots. The intensity distribution is obtained by

$$I_{uv}(R,\psi,l) = \left|F_{uv}(R,\psi,l)\right|^2. \qquad (2.1.8)$$

The intensity distribution on each layer line is governed by Bessel functions of different orders, which take the cylindrical curvature of the tube into account, and is dominated by a single Bessel function determined by the selection rule [7]. On the equatorial layer line where $l = 0$, the order of the dominant Bessel function is $n = 0$ and the intensity distribution is proportional to the square of Bessel function of zeroth order. Three principal layer lines in an electron diffraction pattern of a nanotube correspond to the {100} reflections of two hexagons twisted relative to each other and half of the twist angle is the helicity of the nanotube. Fig. 2.1.3 shows a simulated electron diffraction pattern of a carbon nanotube with chiral indices (18, 3). Three layer lines seen above and below the equatorial layer line in the simulation are labeled l_1, l_2 and l_3 in descending order and their values are $l_1 = (2u + v)/M$, $l_2 = (u + 2v)/M$ and $l_3 = (u - v)/M$, respectively [6, 8]. The order of the Bessel function that dominates the intensity distribution on each layer line can be found from equation (2.1.6) and the values of l given just above. They are $n_1 = -v$, $n_2 = u$, and $n_3 = -(u + v)$, respectively. Thus, the scattering intensities on the three principal layer lines l_1, l_2 and l_3 are

$$I(R, \psi, l_1) \propto \left| J_v(\pi d R) \right|^2, \tag{2.1.9}$$

$$I(R, \psi, l_2) \propto \left| J_u(\pi d R) \right|^2, \tag{2.1.10}$$

and

$$I(R, \psi, l_3) \propto \left| J_{u+v}(\pi d R) \right|^2. \tag{2.1.11}$$

Equations (2.1.9-2.1.11) enable us to determine the chiral indices (u, v) of a carbon nanotube from its electron diffraction pattern accurately and unambiguously. Since the intensity distribution on each layer line is governed by a single Bessel function and the

peak positions of each Bessel function are unique, the order of the Bessel function can be determined by measuring the ratio of its first two peak positions. The layer line spacings D_1 and D_2 shown in Fig. 2.1.3 can be used as supplementary information to determine the chiral indices (u,v). The ratio of v to u can be expressed as [9, 10]

$$\frac{v}{u} = \frac{(2D_2 - D_1)}{(2D_1 - D_2)}. \tag{2.1.12}$$

This equation together with the measured diameter of a nanotube from TEM images can be used as a complementary relation to determine the chiral indices (u,v) of a single-walled carbon nanotube.

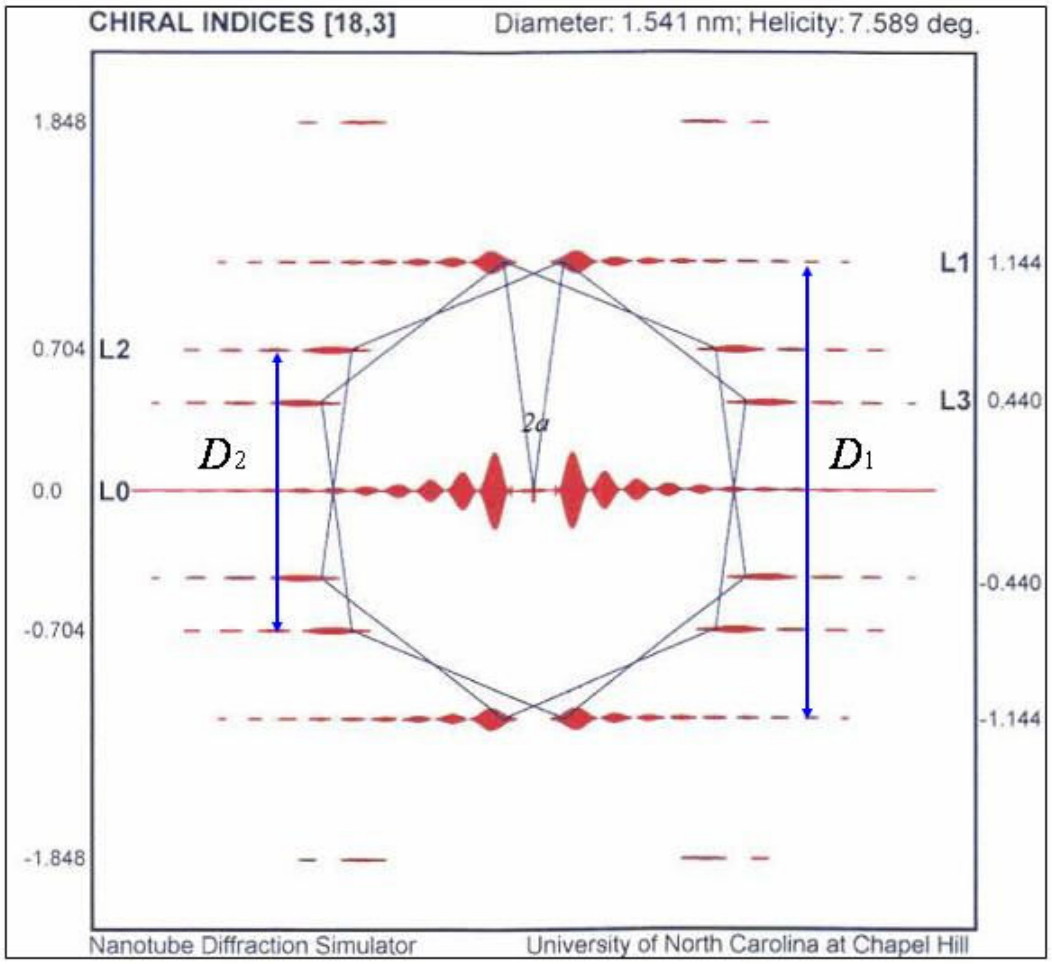

Fig. 2.1.3 Simulated electron diffraction pattern of (18, 3) chiral carbon nanotube. Uppercase letters are used for labeling the layer lines in the simulation. (simulation from http://www.physics.unc.edu/project/lcqin/www1/nds/hdsh/hdsh.html).

2.2 Imaging of CNT by TEM

The analytical techniques to characterize carbon nanotubes include (but are not limited to) transmission electron microscopy (TEM), Raman spectroscopy, and scanning probe microscopy. The simultaneous imaging and diffraction capabilities that a TEM provides have made it the primary instrument over the years to study such sub-nanometer materials. The high resolution TEM (HRTEM) has been frequently employed for the

study of the structure, the diameter and the crystallinity of carbon nanotubes. However, great caution must be taken when it comes to interpreting TEM images of carbon nanotubes for the determination of the structure and the diameter since they are not free of imperfections.

2.2.1 Theory

There are two major contrast mechanisms used in TEM to create an image of a specimen: amplitude contrast and phase contrast. The amplitude contrast is obtained in an image if a small objective aperture is used to exclude most scattered electron beams except the selected beam. The areas of the specimen with higher mass or stronger atomic potential will scatter more electrons toward larger angular regions (regions away from the optical axis and the central beam) and will appear dark in the images. Phase contrast results from the differences in the phases of the electron waves scattered through a thin specimen. In a phase contrast image, a larger objective aperture is usually used to allow more scattered beams to pass through the objective lens to form a final image. It offers higher resolution on the structure imaged and it is usually called HRTEM. The HRTEM images of carbon nanotubes in the literature mostly refer to phase contrast imaging conditions. It is very sensitive to the imaging conditions such as specimen thickness, orientation, scattering factor of the specimen, aberrations and variations in defocus value of the objective lens. These all make phase contrast images difficult to interpret but this high level of sensitivity is what makes the imaging of atomic structure in a specimen possible.

An electron microscope transforms each point in the specimen into a disk in the final image. If we represent the specimen by a specimen function $t(x,y)$ then a point (x,y) in the specimen is transformed to a region defined by $g(x,y)$ in the image. This can be written mathematically as [11]

$$g(\vec{r}) = t(\vec{r}) \otimes h(\vec{r}). \qquad (2.2.1)$$

$g(\vec{r})$ is called the convolution of $t(\vec{r})$ with $h(\vec{r})$ where $h(\vec{r})$ is called the point spread function of the microscope since it spreads a point into a disk. We see disks in the image because the imaging system is not perfect. Moreover, more than one point in the specimen might contribute to what we see in the final image since the disks could overlap. Therefore, what we need to do is to correlate what we see in the image with the structure of the specimen in a linear fashion [11].

The high resolution seen in an image means high spatial frequencies required to form an image. This means the beams diffracted far away from the optical axis should be included in the image-forming field of the objective lens to increase the fine details observed in a final image. The beams away from the optical axis will be bent at greater angles by the objective lens and these beams will be focused at a point different than those beams closer to the optical axis because of spherical aberration of the lens. This will cause a loss of fine detail in the final image. Thus, the resolution of an electron microscope is limited by the spherical aberration of the objective lens.

To be able to simulate or interpret phase contrast images of a thin specimen, first we need to formulate the specimen structure. In an electron microscope column, we can consider the electrons moving along the optical axis (z-direction) incident on the specimen as plane waves. For a plane wave along the z-direction, the wave function is

$$\Psi(\vec{z}) = \exp(2\pi i u_z z) = \exp(2\pi i z/\lambda), \tag{2.2.2}$$

where λ is the wavelength of the electron and u_z is the propagation wave vector along the z-axis. The relativistic expression for the electron wavelength in vacuum is

$$\lambda = \frac{hc}{\sqrt{eV(2m_0c^2 + eV)}}. \tag{2.2.3}$$

In the expression, m_0 is the rest mass of the electron and V is the accelerating voltage of the microscope (eV is the kinetic energy of the electron). For modern microscopes, the energy of the incident electrons is much higher than that of the electrons in the specimen. For a thin specimen, the electrons interact with the weak electrostatic potential of the specimen when they are transmitted through it and acquire a phase factor at the exit face. The wave function transmitted through the specimen at the exit face is the multiplication of the incident plane wave by the specimen transmission function:

$$\Psi_t = t(\vec{r})\Psi(\vec{z}) = t(\vec{r})\exp(2\pi i z/\lambda) \tag{2.2.4}$$

and

$$t(\vec{r}) = \exp[i\sigma V_z(\vec{r})]. \tag{2.2.5}$$

In the transmission function, σ is the interaction constant (not scattering cross-section) and $V_z(\vec{r})$ is the projected atomic potential of the specimen along the z-axis. $V_z(\vec{r})$ is the integral of the 3D specimen potential along the optical axis:

$$V_z(\vec{r}) = V_z(x,y) = \int V_s(x,y,z)dz. \tag{2.2.6}$$

The interaction constant is $\sigma = 2\pi me\lambda/h^2$ where m is the relativistic mass of the electron (assuming $V_s/V \ll 1$). The specimen here is represented as a phase object and what it does to the incident electrons is to modify their wave function by the transmission function. This is known as phase object approximation (POA) [12]. This holds true when the

specimen is thin so that the potential inside is small and the specimen structure can be projected on two dimensions by a simple integral along z-axis. In the weak phase object approximation (WPOA), $V_z(x, y)$ is much smaller than one so that the exponential term in the transmission function can be expanded as (neglecting higher order terms in expansion)

$$t(\vec{r}) = 1 + i\sigma V_z(x, y)\,. \tag{2.2.7}$$

The WPOA is telling us that the amplitude of the transmission function is linearly related to the projected structure of specimen [11].

At the back focal plane of the objective lens, the transmission function of the specimen will be received and propagated through to contribute to the final image contrast by the transfer function of the lens. Equation (2.2.1) can be rewritten in terms of Fourier transforms in the reciprocal space:

$$G(\vec{u}) = T(\vec{u})H(\vec{u}) \tag{2.2.8}$$

and

$$H(\vec{u}) = A(\vec{u})E(\vec{u})\exp[i\chi(\vec{u})]\,. \tag{2.2.9}$$

A convolution of two functions in real space is the multiplication of their Fourier transforms in reciprocal space. Here $T(\vec{u})$ is Fourier transform of the transmission function of the specimen which arrives at the back focal plane (we ignored the phase term due to plane waves because we are looking for the intensity in the final image). The transmitted electrons at the back focal plane are collected by the objective lens and modified by its contrast transform function $H(\vec{u})$ to form the final image in the imaging plane. In $H(\vec{u})$, $A(\vec{u})$ is the aperture function, $E(\vec{u})$ is the envelope function and $\chi(\vec{u})$ inside the exponential is a function of the spherical aberration constant C_s and defocus

value Δf of the objective lens, which is also known as the aberration function or phase-distortion function [11] :

$$\chi(\vec{u}) = \pi\Delta f\lambda u^2 + 0.5\pi C_s\lambda^3 u^4 . \tag{2.2.10}$$

The image wave function will be an inverse Fourier transform of equation (2.2.8) in the image plane:

$$\Psi_i = FT^{-1}[G(\vec{u})] . \tag{2.2.11}$$

Then the image intensity $g(x, y)$ will be the square modulus of the wave function in real space in the image plane of the objective lens:

$$g(\vec{r}) = \left|\Psi_i\right|^2 = \left|t(\vec{r}) \otimes h(\vec{r})\right|^2 . \tag{2.2.12}$$

In the WPOA theory, we know that only the imaginary part of $H(\vec{u})$ will contribute to the contrast in the final image [11, 12]. Thus we can rewrite the contrast transfer function in terms of the sine of the phase-distortion function:

$$B(\vec{u}) = A(\vec{u})E(\vec{u})\sin[\chi(\vec{u})]. \tag{2.2.13}$$

Even though $B(\vec{u})$ is not identical to $H(\vec{u})$, sometimes $B(\vec{u})$ is called the contrast transfer function. In the aperture term, the objective lens aperture will collect only the diffracted beams falling inside and cut off all others larger than the value defined by the radius of the aperture [11, 12].

If we ignore the envelope function and take the aperture function as unity for the beams falling inside the objective aperture and zero for all other beams, then $\sin[\chi(\vec{u})]$ will be solely responsible for the output of the transmission system and the image formation process in WPOA. Fig.2.2.1 shows the calculated contrast transfer functions for $C_s = 1.0$ mm and beam energy of 200 keV at defocus values of $\Delta f = -30$ nm and

$\Delta f = -50$ nm for a TEM (like JEOL JEM-2010F for example). In the calculated functions we see the band of constant transmission and an oscillatory band with zeros. In an ideal contrast transfer function one would like to see a constant horizontal line. The oscillatory behavior means that the CTF acts like a band-pass filter and the high frequency part of the spectrum is filtered out and makes no contribution in the final image. The optimum CTF is the one that has the fewest zeros and an almost constant spectrum in transmission. The effect of spherical aberration of the objective lens and the negative defocus value can be balanced against each other and such imaging condition is known as the "Scherzer defocus" [11,12]. At the Scherzer defocus, all diffracted beams have almost a constant phase until the first cross-over of the horizontal axis which defines the optical resolution of the imaging system. This is also known as the Scherzer resolution and it is the best that we can expect from the microscope [11, 12]. This is not the information limit but it's the limit to what we can interpret intuitively from the images:

$$\Delta f_{sch} = -1.2(C_s\lambda)^{1/2} \tag{2.2.14}$$

and

$$r_{sch} = 0.66 C_s^{1/4}\lambda^{3/4}. \tag{2.2.15}$$

The ultimate resolution or the information limit of the microscope will be determined by other factors like energy spread, chromatic aberration and electrical instabilities that are included in the envelope function. The final form of contrast transfer function will be obtained by multiplying the phase-distortion function with the envelope function. The effect of the envelope function will be a sharp cut-off of the spectrum at high spatial frequencies. If this limit is larger than the Scherzer resolution limit, it will define the

information limit and any information beyond this limit can only be retrieved by sophisticated image analysis processes. The Scherzer resolution will still be the directly interpretable limit read from the images.

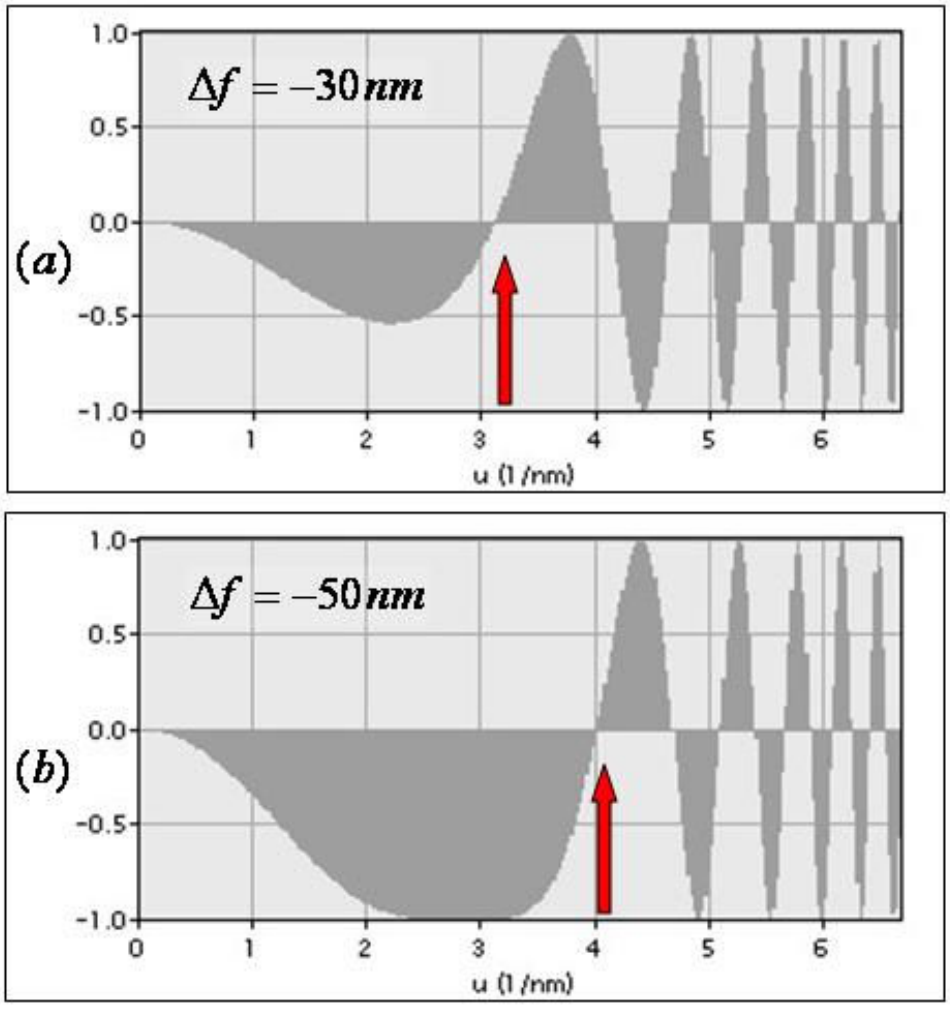

Fig. 2.2.1 The contrast transfer function calculated for JEOL JEM-2010F at the defocus values of (a) -30 nm and (b) -50 nm, respectively. The red arrows indicate the first cross-over of the spatial frequency axis and the Scherzer resolution of the microscope.

2.2.2 TEM Images of CNT

The images of carbon nanotubes can be interpreted in terms of the WPOA theory. A SWNT has only two atomic layers of carbon at the top and the bottom in the electron beam direction. The top and bottom atomic layers are parallel to one another and perpendicular to the electron beam except near the edges of the tube. Moreover, the carbon atoms are weak scatterers for energetic electrons due to the low atomic number (Z=6) of carbon. A high-resolution image of a SWNT can be easily obtained using a modern TEM equipped with a field emission gun. Ignoring image deteriorations due to thermal and mechanical vibrations and the stage drift, the final image will give the ultimate structure of the SWNT in terms of the projected potential of the tube. However, no electron microscope is perfect. The projected potential of the tube will be deteriorated because of vibrations, aberrations and electrical instabilities of the lenses.

Figure 2.2.2 shows high resolution TEM images of a SWNT, a double-walled (DWNT) and a few-walled carbon nanotube (FWNT) together with their cross sections. We see two hollow concentric cylinders in a cross section of the DWNT for example. What we see in its HRTEM image is two parallel dark lines that run along the tubule axis. The dark lines are the projected structure of the tube at the edges. The diameter of the inner and outer shells can be measured using the dark lines in the images. We need to be cautious of the fact that the structure seen in the images is very sensitive to the imaging conditions. The widths of the dark lines seen in images vary with the defocus of the objective lens and the contrast might not be uniform inside the dark lines [13]. This makes the determination of the diameter more obscure because the diameter values will vary depending upon where in the dark lines the measurements are made.

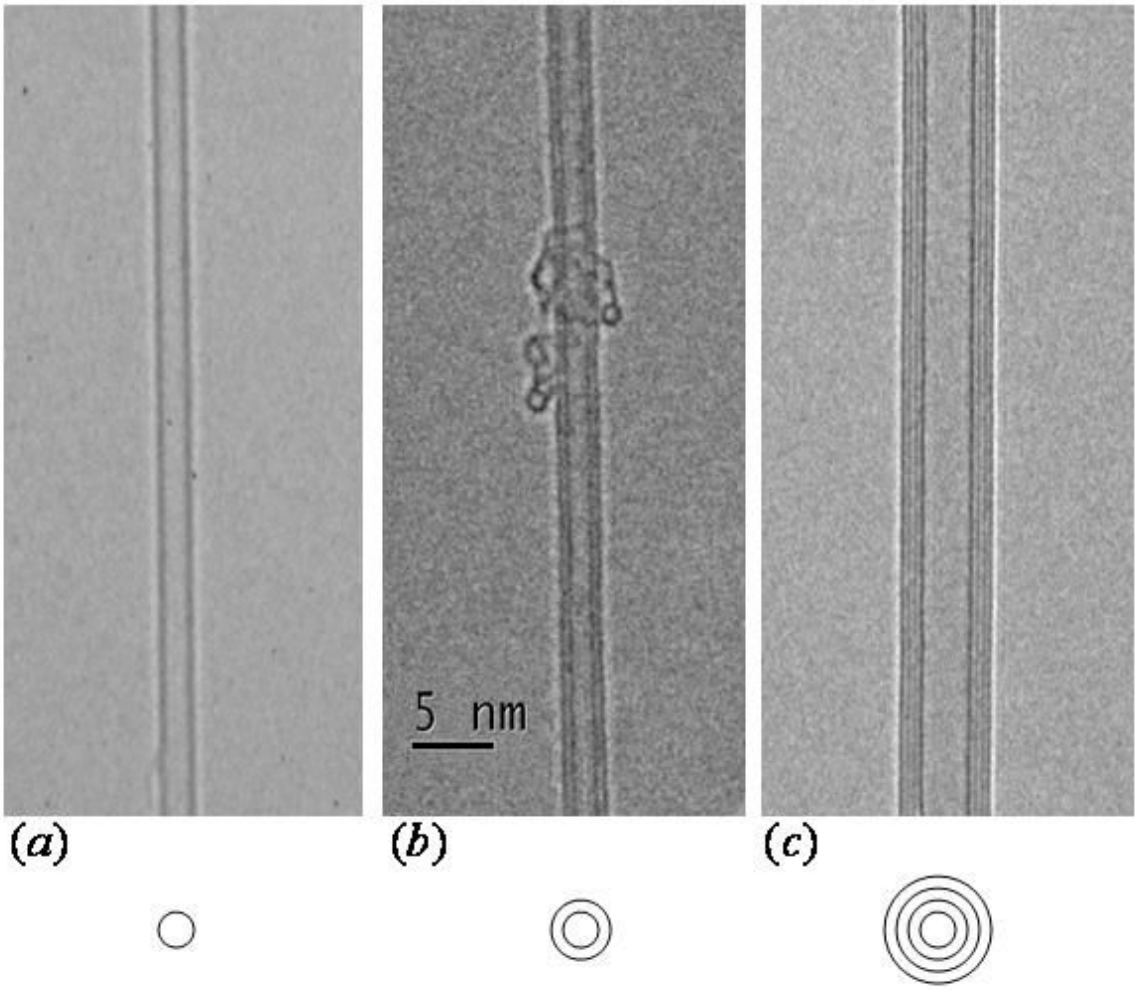

Fig. 2.2.2 Electron micrographs of a SWNT (a), a DWNT (b) and a FWNT (c) with four walls. The cross-sections of each nanotube are shown at bottom. The scale bar is same for all images.

The error in diameter measurements becomes more significant for the smaller tubes due to the pronounced curvature [13]. There are other important factors that need to be taken into account when the carbon nanotubes are imaged inside the TEM for structural measurements. The orientation of the nanotube with respect to the electron beam is one of them. In most imaging situations, it is assumed that the nanotube lies on a flat plane perpendicular to the incident beam direction. The tilt of the plane of the nanotube or the rotation of the nanotube about the tube axis is additional sources of error in diameter measurements [13, 14]. The other situation that needs to be avoided is imaging of nanotubes when they overlap with thin amorphous carbon films [15].

The smallest of the carbon nanotubes were discovered with HRTEM. The first discovery was the synthesis of a 0.4 nm diameter carbon nanotube inside a multi-walled carbon nanotube [16]. Later this was followed by the news of the smallest nanotube yet with a 0.3 nm diameter, inside a MWNT [17]. The formation of an individual SWNT as small as 0.3 nm in diameter was also observed using high resolution TEM [18]. When we use TEM to study such sub-nanometer scale materials, caution must be taken. Sometimes, a ghost image appears in TEM micrographs due to the coherently scattered electrons with the use of field emission gun and improper focusing conditions [14]. This also makes the imaging and interpretation of bundles of nanotubes difficult to figure out if they are composed out of the SWNTs or DWNTs only. Fig. 2.2.3 illustrates the observation of a small carbon nanotube inside a MWNT due to use of a field emission gun and improper defocus. The MWNT seems to be completely filled inside with the innermost tube being 0.4 nm in diameter. A focus series of images of the same tube needs to be taken to show that the innermost tube is seen due to image artifacts.

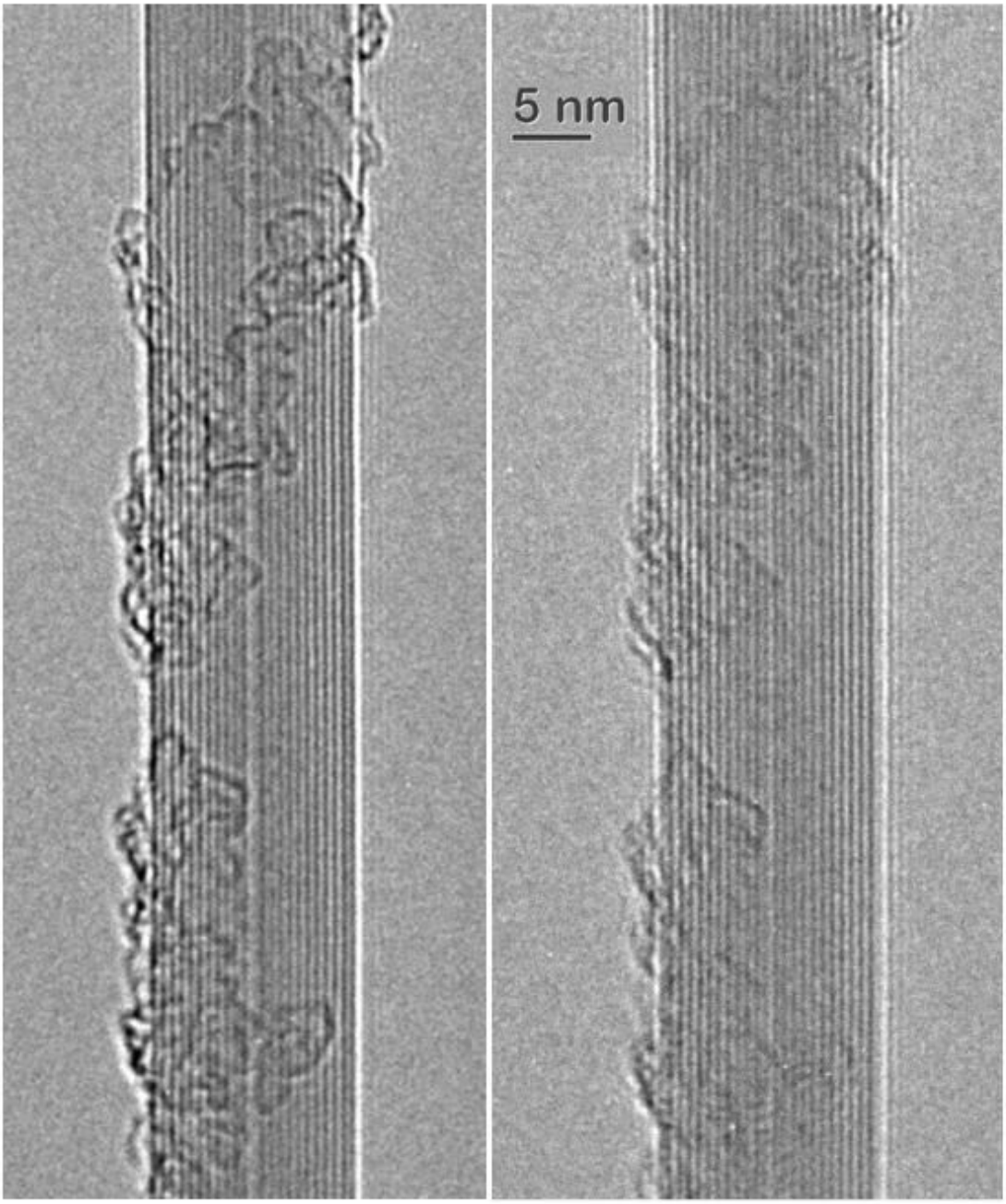

Fig. 2.2.3 Electron microscopy images of a MWNT taken at two different defocus values. The scale bar is same for both images. The image on the right shows the appearance of a ghost tube due to the artifacts.

2.3 References

1. Cochran, W., Crick, F. H. C., Vand, V. (1952). The structure of synthetic polypeptides. I. The transform of atoms on a helix. *Acta Cryst*. **5**, 581-586.

2. Qin, L. C. (1994). Electron diffraction from cylindrical nanotubes. *J. Mater. Res*. **9**, 2450-2456.

3. Lucas, A. A., Bruyninckx, V., Lambin, Ph. (1996). Calculating the diffraction of electrons or X-rays by carbon nanotubes. *Europhysics Lett*. **35**, 355-360.

4. Lambin, Ph., Lucas, A. A. (1997). Quantitative theory of diffraction by carbon nanotubes. *Phys. Rev. B* **56**, 3571-3574.

5. Liu, Z., Zhang, Q., Qin, L. C. (2000). Determination and mapping of diameter and helicity for single-walled carbon nanotubes using nano-beam electron diffraction. *Phys. Rev. B* **71**, 245413.

6. Qin, L. C. (2006). Electron diffraction from carbon nanotubes. *Rep. Prog. Phys*. **69**, 2761-2821.

7. Liu, Z., and Qin, L.C. (2004). Symmetry of electron diffraction from single-walled carbon nanotubes. *Chem. Phys. Lett.* **400**, 430-435.

8. Qin, L. C. (2007). Determination of the chiral indices of carbon nanotubes by electron diffraction. *Phys. Chem. Chem. Phys*. **9**, 31-48.

9. Gao, M., Zuo, J. M., Twesten, R. D., Petrov, I., Nagahara, L. A., Zhang, R. (2003). Structure determination of individual single-walled carbon nanotubes by nano-area electron diffraction. *Appl. Phys*. *Lett*. **82**, 2703-2705.

10. Liu, Z., Zhang, Q., Qin, L.C. (2005). Accurate determination of atomic structure of multiwalled carbon nanotubes by nondestructive nanobeam electron diffraction. *Appl. Phys. Lett*. **86**, 191003.

11. Williams, D. B. and Carter, C. B. (1996). *Transmission electron microscopy*. New York: Plenum Press.

12. Kirkland, E. J. (1998). *Advanced computing in electron microscopy*. New York: Plenum Press.

13. Qin, Q. and Peng, L. M. (2002). Measurement accuracy of the diameter of a carbon nanotube from TEM images. *Phys. Rev. B* **65**, 155431.

14. Hayashi, T., Muramatsu, H., Kim, Y. A., Kajitani, H., Imai, S., Kawakami, H., Kobayashi, M., Matoba, T., Endo, M., Dresselhaus, M. S. (2006). TEM image simulation study of small carbon nanotubes and carbon nanowires. *Carbon* **44**, 1130-1136.

15. Qin, L. C., Zhao, X., Hirahara, K., Ando, Y., Iijima, S. (2001). Electron microscopic imaging and contrast of smallest carbon nanotubes. *Chem. Phys. Lett*. **349**, 389-393.

16. Qin, L. C., Zhao, X., Hirahara, K., Miyamoto, Y., Ando, Y., Iijima, S. (2000). The smallest carbon nanotube. *Nature* **408**, 50.

17. Zhao, X., Liu, Y., Inoue, S., Suzuki, T., Jones, R. O., Ando, Y. (2004). Smallest carbon nanotube is 3 Å in diameter. *Phys. Rev. Lett*. **92**, 125502.

18. Peng, L. M., Zhang, Z. L., Xue, Z. Q., Wu, Q. D., Gu, Z. N., Pettifor, D. G. (2000). Stability of carbon nanotubes: How small can they be? *Phys. Rev. Lett*. **85**, 3249-3252.

Chapter 3

Characterization of SWNTs Produced by Laser Ablation of Si Containing Catalysts

3.1 Synthesis of CNTs

Carbon nanotubes can be synthesized using numerous techniques. The major growth methods include arc-discharge, laser ablation and chemical vapor deposition (CVD). Each growth method has been optimized and refined to get the best yield and quality of carbon nanotubes. Yet, there has been not a single growth method that offers control over the structure and properties of carbon nanotubes. The first carbon nanotubes were synthesized by arc-discharge evaporation of two graphite electrodes [1] in a method that is similar to the ones used to produce the fullerenes [2]. Later, single-walled carbon nanotubes were synthesized successfully by incorporating transition metals into one of the graphite electrodes in the arc-discharge production [3, 4].

In a regular arc-discharge synthesis, discharge plasma is created between two graphite electrodes with application of either AC or DC voltage. The two electrodes are separated by approximately 1 mm and the cathode is larger in diameter than the anode (about 8-12 mm and 6-8 mm, respectively). A discharge current of 60-100 A is obtained by applying a bias of 10-40 volts to the electrodes in an inert gas atmosphere (helium) at a pressure of about 500 Torr. The high temperature plasma evaporates the material on the anode, which is transported and condensed on the opposite electrode (cathode). To sustain the

plasma the anode is moved closer towards the cathode as it vaporizes away. The nanotubes are found in the deposits on the cathode. If no transition metal is used in the anode, the method always produces multi-walled carbon nanotubes [5]. The single-walled carbon nanotubes are produced when the anode is doped with transition metals. The best metal catalysts for the production of SWNTs in arc-discharge are found to be a mixture of Co/Y and Ni/Y [6-8].

In the CVD method, the nanotubes are grown by the catalytic decomposition of hydrocarbon-containing precursors in the presence of metal catalysts at elevated temperatures [9]. It involves the pyrolysis of carbon-rich gas molecules on the metal catalysts and subsequent conversion of carbon into nanotubes by precipitation on the surface of supersaturated catalyst particles at temperature of 500-1100 $^{\circ}$C. There are more variations of this method used to grow nanotubes than the other two (arc-discharge and laser ablation). Two main CVD routes can be mentioned: one is supported catalyst growth and the other is gas phase growth [10, 11]. In supported catalyst growth, the metal catalysts are prepared on a support medium like a silicon substrate and inserted into a quartz tube inside a temperature-controlled furnace. A carbon-rich gas is flushed into the tube at atmospheric pressure at high temperatures and the tube growth can be sustained for longer periods of time. In the gas phase growth, the catalyst and the carbon source are introduced into the tube simultaneously either in the gas form or in aerosol. The following decomposition and reaction can happen either suspended in the gas flow or by self-deposition on the surfaces of the reactor walls.

The supported catalyst method is the most commonly-used CVD technique to grow nanotubes. The most widely-used carbon-rich gas sources are acetylene (C_2H_2), methane

(CH_4), ethylene (C_2H_4), and propylene (C_3H_6), and some other aromatic compounds. The most common metal catalysts are Fe, Ni and Co. Si and SiO_2 wafers are the basic choices for the support medium. Since the catalysts can be made in advance, it offers more freedom compared to other production methods in positioning the nanotubes and controlling the direction of their growth [12, 13]. The specific patterns can be prepared on the substrate by the use of techniques such as lithography to incorporate the as-grown nanotubes with nanotube-based electronic circuits [14]. The diameter of the grown nanotubes can be adjusted by varying the size of the catalyst particles [15-17].

The laser ablation method, similar to arc-discharge, was used earlier to produce fullerenes [18]. In laser ablation a solid graphite target is placed inside a quartz tube at high temperature and the material is blasted with a pulsed Nd:YAG laser to evaporate the carbon target [19]. If the solid target does not contain any metal catalysts, the product will be multi-walled carbon nanotubes. SWNTs can be obtained by doping the solid graphite target with certain transition metals [20]. The best working catalyst system is a Ni/Co mixture to produce carbon nanotubes of uniform diameter [21, 22]. Rh/Pd as catalyst was shown to produce mostly metallic SWNTs with diameters as small as 0.85 nm [23]. It has been exclusively used to synthesize SWNTs due to the high quality of the tubes grown. It has been shown that the yield and the diameter of the grown tubes increase as the temperature of the furnace does and the yield reaches a maximum at about 1200 ^{o}C [24]. The quantity of the tubes grown (1g/day) and the costs of the laser systems has limited its application for industrial scale production. Promising new techniques are emerging for scaling-up the production like gas-phase catalytic growth of SWNTs from carbon monoxide (HiPco) [25]. Cleaner nanotubes are produced at rates up to 10 g/day

with diameters as low as 0.7 nm in high pressure (30-50 atm) and temperature (900-1100 ^{o}C).

3.2 Production of SWNTs by Laser Ablation

The oven-laser ablation apparatus used in this work is similar to the ones described elsewhere [19, 20]. It consists of a quartz tube 10 cm in diameter mounted inside an electric furnace with three different heating zones that operate at 1090 ^{o}C, 1150 ^{o}C and 1090 ^{o}C approximately. The argon gas was introduced as a carrier gas into the system at the front end of the quartz tube and the argon flow was kept at 400 sccm (standard cubic centimeters per minute) to maintain a pressure of 750 Torr inside the tube. A metal-graphite composite target rod (less than 1% atomic weight corresponds to metal catalysts) 0.5 inch (1.27 cm) in diameter was prepared following the recipe given by [26] and placed at the central stage of the electric furnace. The Nd/YAG laser beam (532 nm, 8ns pulse and 10 Hz repetition rate) with a power of 220 mJ/Pulse was focused to a 3 mm spot on the target. The laser beam scanned the target surface to vaporize the material uniformly during the growth. Most of carbon plume was carried to the downstream end of the tube by the flow of the Argon gas. The carbon soot was collected on the inner surface of the quartz tube which was cooled with water coils both upstream and downstream of the gas flow. The metal powders used as catalyst were Ni (5-15 μm particle size, 0.6 %), Ni (2.2-3 μm, 0.6%), Ni (0.08-0.15 μm, 0.6%), Fe (<10 μm, 0.6%), Co (1.6 μm, 0.6%), Ni/Co (0.3% each), Ni/Fe (0.3% each), Co/Fe (0.3% each), Co/Si (0.3% each) and Fe/Si (0.3% each). The silicon powders used were approximately 0.07-

0.1 μm in size. The ternary mixtures of Ni/Co/Si (0.3% each) and Ni/Fe/Si (0.3% each) were also used.

The carbon soot was dispersed in ethanol by sonication and placed on a lacey carbon coated TEM grid. The sample was studied in a JEOL JEM-2010F transmission electron microscope with a field emission gun at 80 kV to avoid knock-on damage to the single-walled carbon nanotubes (below the threshold energy of 86 keV) [27]. The nano-beam electron diffraction has been applied to study the structure of individual nanotubes. A parallel illumination beam of electrons 20-30 nm in diameter was formed in the nano-beam mode by using a 10 μm condenser aperture and maximizing the first condenser lens current. The TEM and HRTEM imaging were also used to study the morphology and structure of the grown nanotubes.

3.3 TEM and NBED Characterization

In this work, TEM and high resolution TEM images are used extensively to determine the yield, the quality, and the structure of carbon nanotubes. TEM images showed that single Fe and single Ni (5-15 and 2.2-3 μm particle size) alone produced SWNTs in insignificant quantities. Single Ni with the smallest particle (0.15 μm) size has produced some SWNTs with very small yield. Co as a single catalyst was the best to produce SWNTs with considerable quantities. The bimetallic catalysts which were the combinations of Ni/Co, Ni/Fe and Co/Fe were the best and had given a significant yield compared to single Co alone in catalyzing the tubes. The low magnification images of Ni with smallest particle size and Ni/Fe bimetallic catalyst system illustrate this point in Fig.3.3.1 and Fig.3.3.2. The Ni/Fe catalyst produced thicker bundles than others and it

had a larger catalyst particle size which can be seen in the images. The SWNTs grown from this catalyst were not as crystalline as those of other catalysts. It has been known that bimetallic catalyst systems like Ni/Co give the highest yield of SWNTs in laser ablation. Our results follow the precedent in the literature [20, 22, and 23]. In addition to these known catalyst systems, a new catalyst combination has been used and shown to be successful in growing tubes in large quantities. It is a mixture of Co and Si in equal parts and it will be discussed in detail in next section.

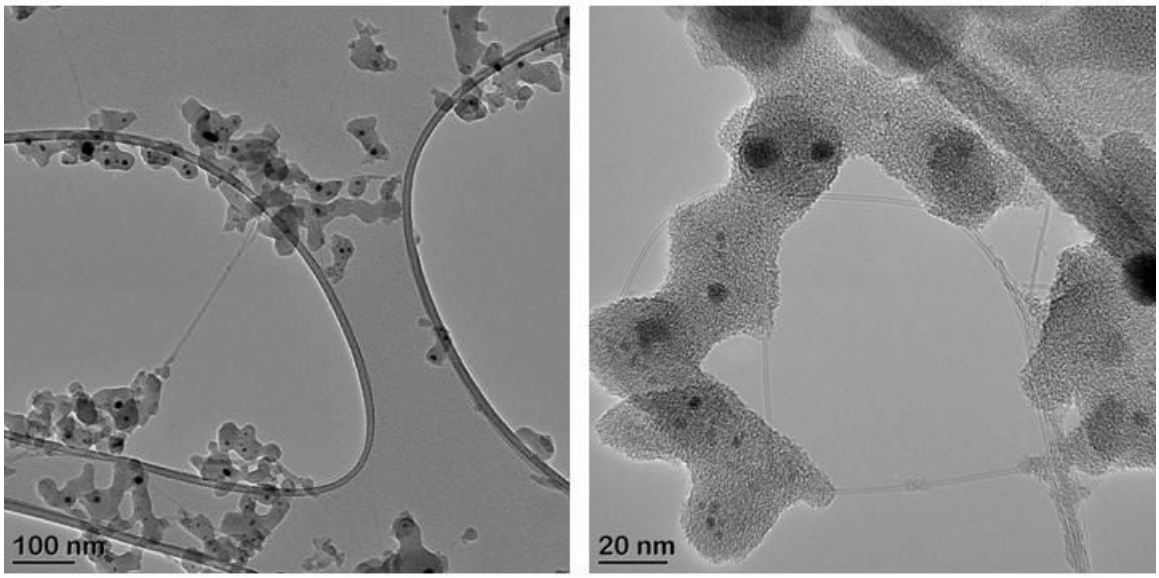

Fig. 3.3.1 (a) Low magnification TEM image of sample grown by single Ni (particle size of 0.15 μm) showing amorphous carbon, catalyst particles and a few SWNTs. (b) Higher magnification image of same sample showing a few SWNTs.

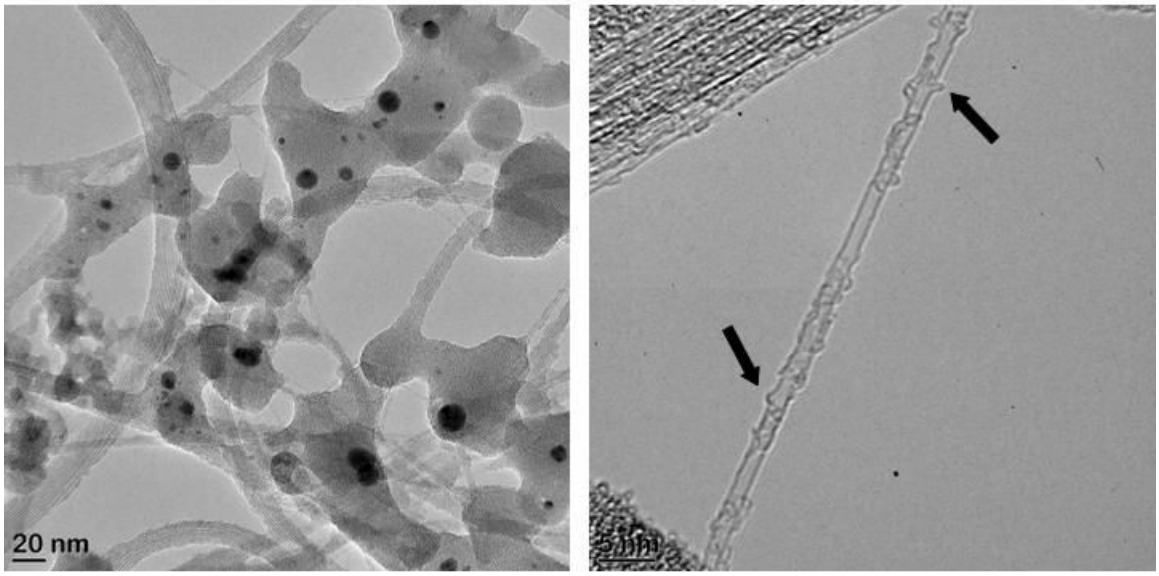

Fig. 3.3.2 (a) Low magnification TEM image of sample grown by Ni/Fe catalyst mixture showing amorphous carbon, catalyst particles and thick bundles of SWNTs. (b) High magnification TEM image of an isolated tube from the same sample. The black arrows point to the as-grown defects in the tube (image taken at 80 kV below the threshold of radiation damage).

Nano-beam electron diffraction was used to map the helicity and diameter of isolated individual SWNTs in order to determine their atomic structures [28]. Fig. 3.3.3 shows a high-resolution TEM image and electron diffraction pattern of one of the tubes studied. The *v/u* ratio for this tube was determined to be 0.697 ± 0.006 measured directly from the layer line spacings in its electron diffraction pattern. The diameter was estimated to be 2.3 nm using its HRTEM image. These values correspond well to the nanotube of chiral indices of (20, 14). Once the chiral indices are determined, the tube's diameter and

helicity are also calculated. The tube has a chiral angle of 28.18° and a diameter of 2.318 nm. It is a metallic tube since the difference of chiral indices is divisible by 3.

A magnified view of the diffraction pattern of this tube is given in Fig.3.3.4 showing the principal layer lines indicated by arrows. The line intensity profile on the first layer line from this diffraction pattern is given in Fig.3.3.5. This intensity distribution can be used to determine the chiral index v since it is proportional to the square of the Bessel function of order v (eq. 2.1.9). From the experimental curve, the ratio of the first two peak positions of Bessel function can be calculated and this is shown in the figure. This ratio is 1.316 ± 0.018 which corresponds to a Bessel function of order 14. The curve in purple is the fitted intensity using the Bessel function of order 14 and the agreement with the experimental intensity curve is quite good. Once one of the indices was determined, the other can be found immediately since their ratio is known (0.697). The second index would be 20. So, this is a complementary way to find the chiral indices in comparison to the method described in the previous paragraph. If the peak positions in intensities from other layer lines are discernible, this method can be used to determine both indices without even calculating the chiral index ratio [29]. These two methods can be used in tandem to identify the chiral indices or to make the identification more accurate. Table 3.3.1 shows the ratio of first two peak positions for Bessel functions of order up to 20. Figure 3.3.6 shows the simulated electron diffraction pattern of nanotube (20,14). This procedure was repeated for a large number of nanotubes (total 40 in numbers) to establish a helicity and diameter map.

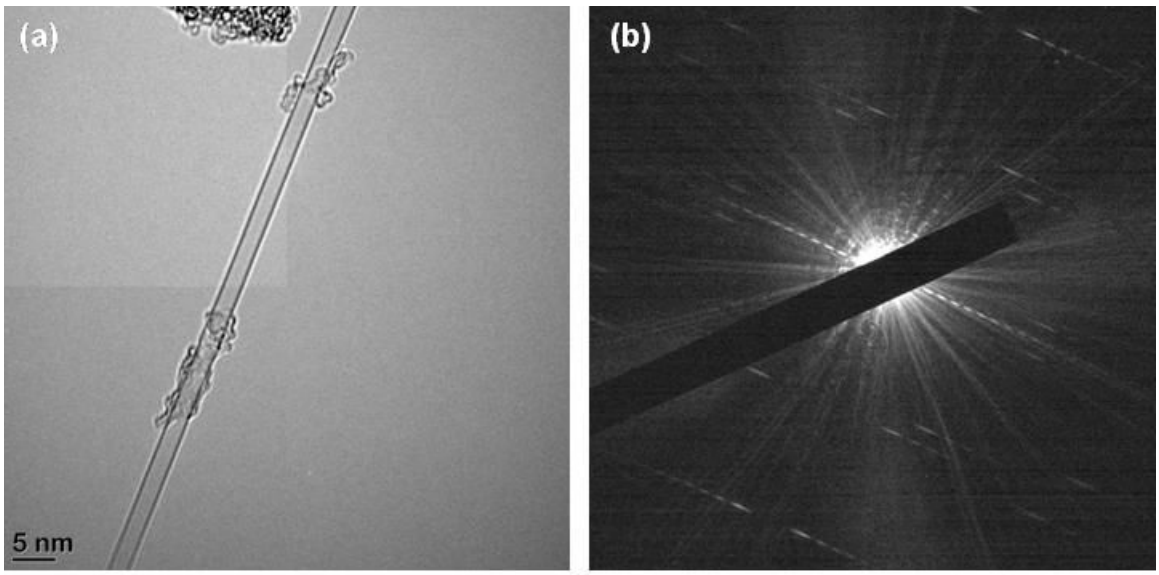

Fig. 3.3.3 (a) High resolution TEM image and (b) nano beam electron diffraction pattern of a single-walled carbon nanotube. The tube in the image has chiral indices of (20, 14) which give 2.319 nm for the tube diameter and 24.18^{o} for the tube helicity and it is a metallic tube.

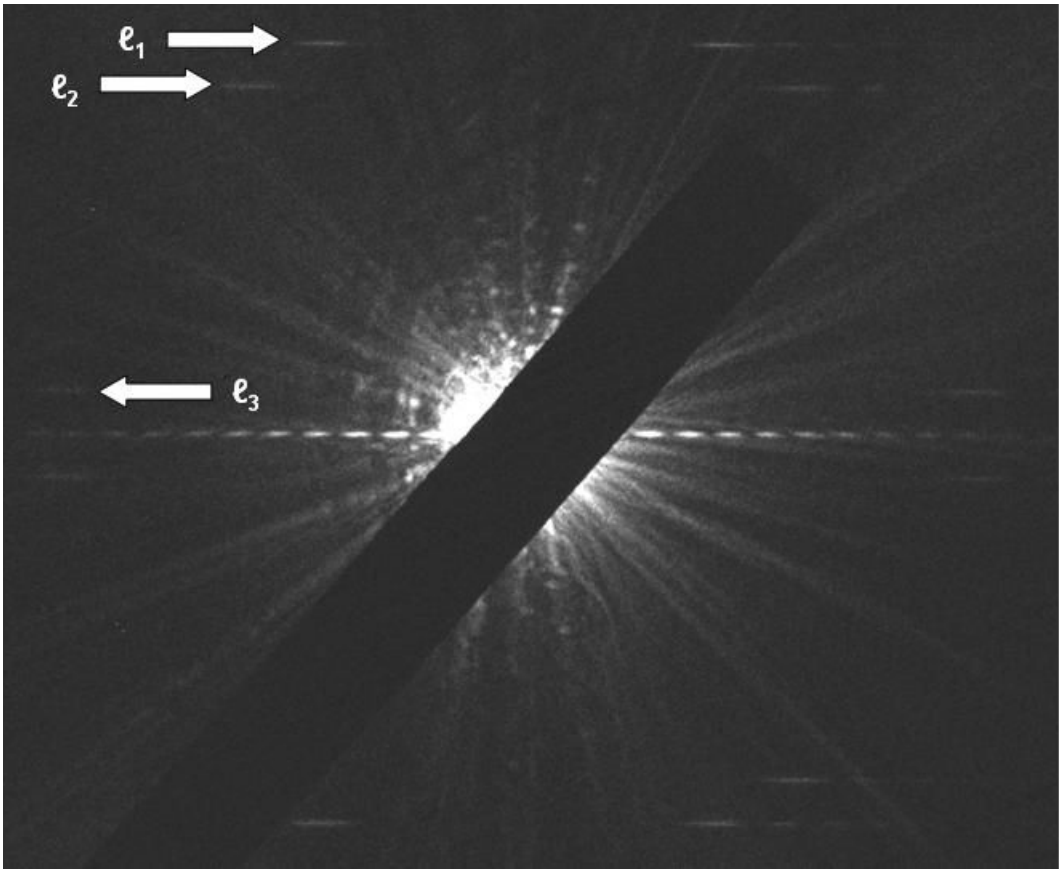

Fig. 3.3.4 Magnified view of electron diffraction pattern from Fig. 3.3.3 (b). The white arrows mark the principal layer lines.

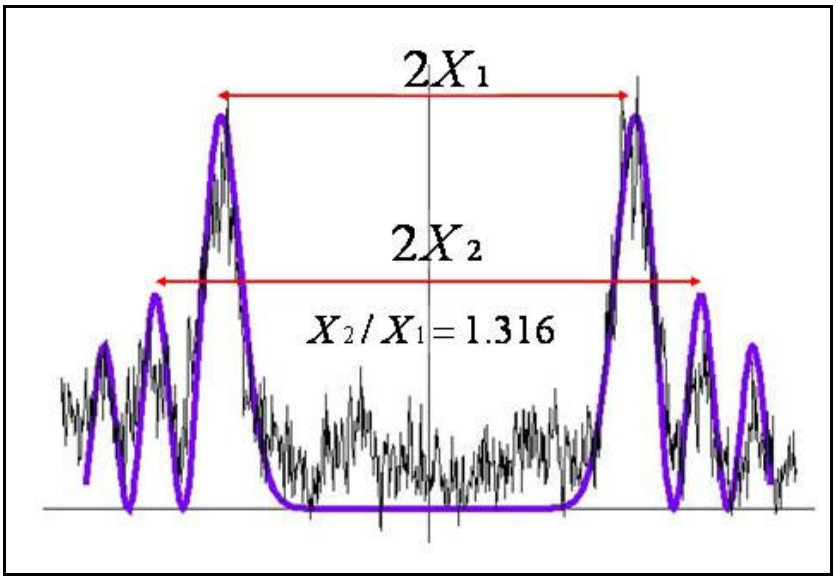

Fig. 3.3.5 Experimental intensity on the first layer line l_1 from the diffraction pattern. The ratio of the positions of the second peak (X_2) and the first peak (X_1) is 1.316 ± 0.018, which corresponds to $|J_{14}(X)|^2$ which is plotted in purple.

Table 3.3.1 The ratio of the peak positions for Bessel functions.

n	X_2 / X_1	N	X_2 / X_1
1	2.896	11	1.372
2	2.196	12	1.351
3	1.908	13	1.332
4	1.746	14	1.315
5	1.640	15	1.301
6	1.564	16	1.288
7	1.508	17	1.276
8	1.463	18	1.266
9	1.427	19	1.256
10	1.397	20	1.247

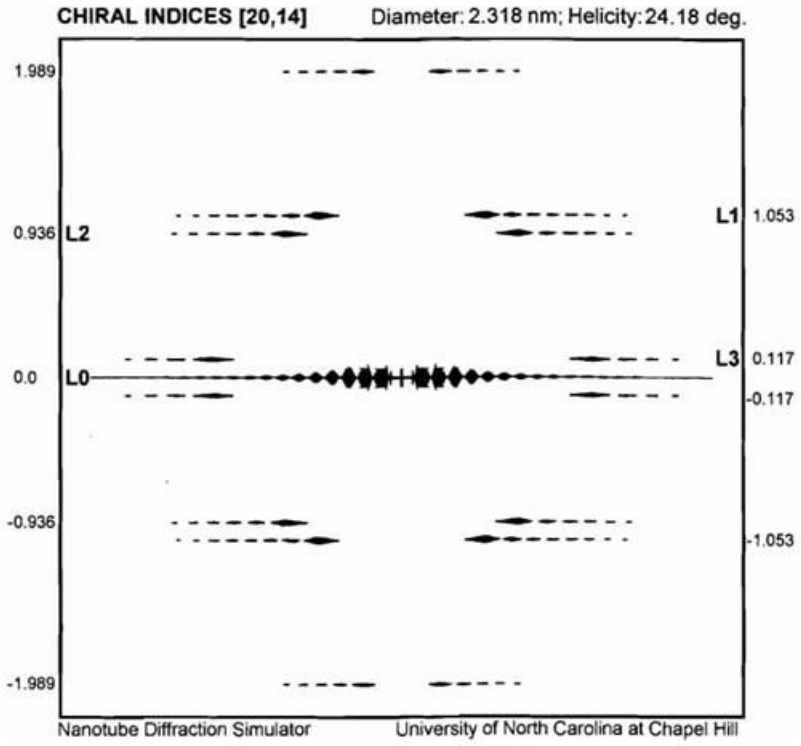

Fig. 3.3.6 Simulated electron diffraction pattern of carbon nanotube (20, 14).

3.4 Analysis of SWNTs Produced by Si Containing Catalysts

Co-Si is not a known catalyst system to catalyze carbon nanotubes in laser ablation. So far, only one paper in the literature reported the successful growth of carbon nanotube products on a $CoSi_2$/Si interface [30]. Fig. 3.4.1 shows the morphology and typical structure of carbon nanotubes catalyzed by a Co and Si mixture (each 0.3 % at.). In this product, what we see is the typical results from laser ablation: amorphous carbon, graphitic particles, and carbon-coated catalyst particles and of course SWNTs. The images showed that this composite produced the best quality nanotubes with the greatest yield among all single Co and Co composite catalysts. In the meantime, catalyst particle

size was found to be very uniform and was around 10 nm and less. The catalyst particle size in the Co-Si system was the smallest among Co or Co composite catalysts. Fig. 3.4.2 shows the experimental histograms for the diameter and helicity distributions of 40 isolated individual SWNTs (randomly selected) grown by the Co/Si system. The average diameter fitted by a Gaussian fit of the peak was 1.50 nm with a standard deviation of 0.16 nm. The chiral indices showed that the ratio of the number of metallic to semiconducting nanotubes was 17/23. Out of all the tube species observed (31 distinct helicities); the ratio of the number of metallic to semiconducting tubes was 13/18. This shows that this catalyst system favors the metallic nanotubes slightly. The helicity distribution shows that there are two peaks at around 12^{o}-14^{o} and 24^{o}-26^{o}. In these two bins, 42.5% of nanotubes are located (17 in number).

The effects of introducing Si into other bimetallic catalyst systems were also investigated. Two ternary catalyst systems (Ni/Co/Si and Ni/Fe/Si) were obtained and studied. The Ni/Co/Si system produced nanotubes with a smaller average diameter. The yield and quality of carbon nanotubes catalyzed by this catalyst are comparable with nanotubes catalyzed by Ni/Co; the catalyst particle size is uniform and smaller than that in the Ni/Co catalyst. The chirality of nanotubes has also been studied by nano-beam electron diffraction. A total of 26 tubes have been studied. The histograms of diameter and helicity angle are shown in Fig. 3.4.3. Among all nanotubes studied, carbon nanotubes catalyzed by Ni/Co/Si showed the smallest diameter range, which is from 0.872 to 1.543 nm. The average diameter was 1.29±0.07 nm and over 50% nanotubes were located at high helicity angles. Compared with nanotubes catalyzed by other catalysts, nanotubes catalyzed by Ni/Co/Si (0.3% each) showed more tubes with smaller

diameters and low helicity angles. Meanwhile, the ratio of the number of metallic nanotubes and semiconducting nanotubes was determined to be 7/19.

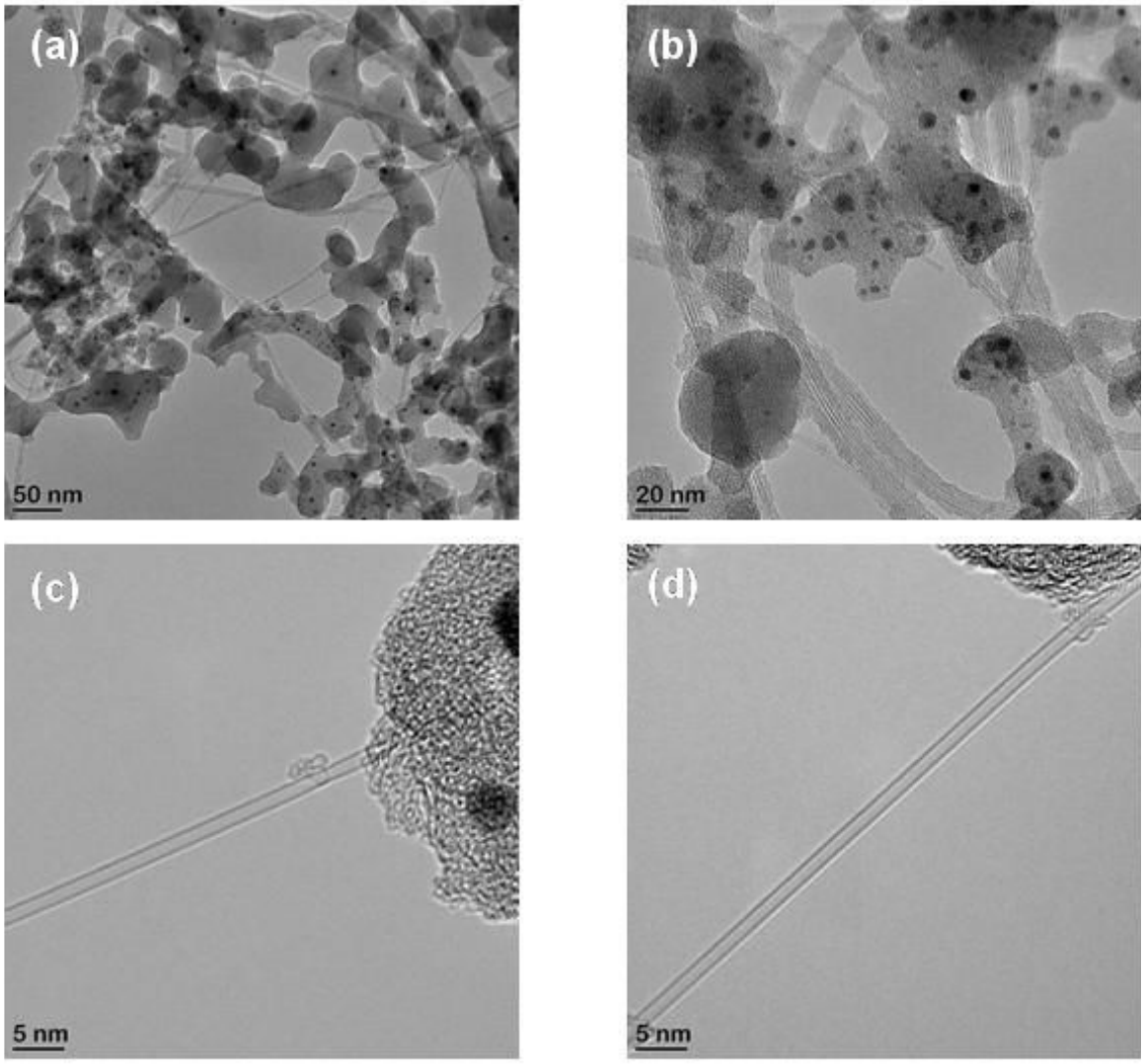

Fig. 3.4.1 (a) Low-magnification TEM image showing the morphology of nanotubes grown by Co/Si catalyst. (b) Another low-magnification image showing bundles of SWNTs, amorphous carbon regions and catalyst particles. (c) High-resolution image of an isolated SWNT showing the crystallinity. (d) Another high-resolution image for an isolated SWNT again showing the quality of the grown nanotubes.

Carbon nanotubes catalyzed by the Ni/Fe catalyst had a good yield, but the quality was not good. Si powder was added to the Ni/Fe composite to see its effects. The yield of carbon nanotubes catalyzed by Ni/Fe/Si catalyst is comparable with that of nanotubes catalyzed by Ni/Fe, but the quality is better than that of nanotubes catalyzed by Ni/Fe catalyst. The chirality of nanotubes has also been studied by NBD. A total of 25 nanotubes were studied. The histograms of diameter and helicity distributions are shown in Fig. 3.4.4. The average diameter was 1.17±0.15 nm and about 50% nanotubes were located at high helicity angles. Compared with nanotubes synthesized by other catalysts, nanotubes grown by Ni/Fe/Si had smallest average diameter and more nanotubes are located at high chiral angles than for the other two Si-containing catalyst composites. The ratio of the number of metallic nanotubes and semiconducting nanotubes was determined to be 9/16.

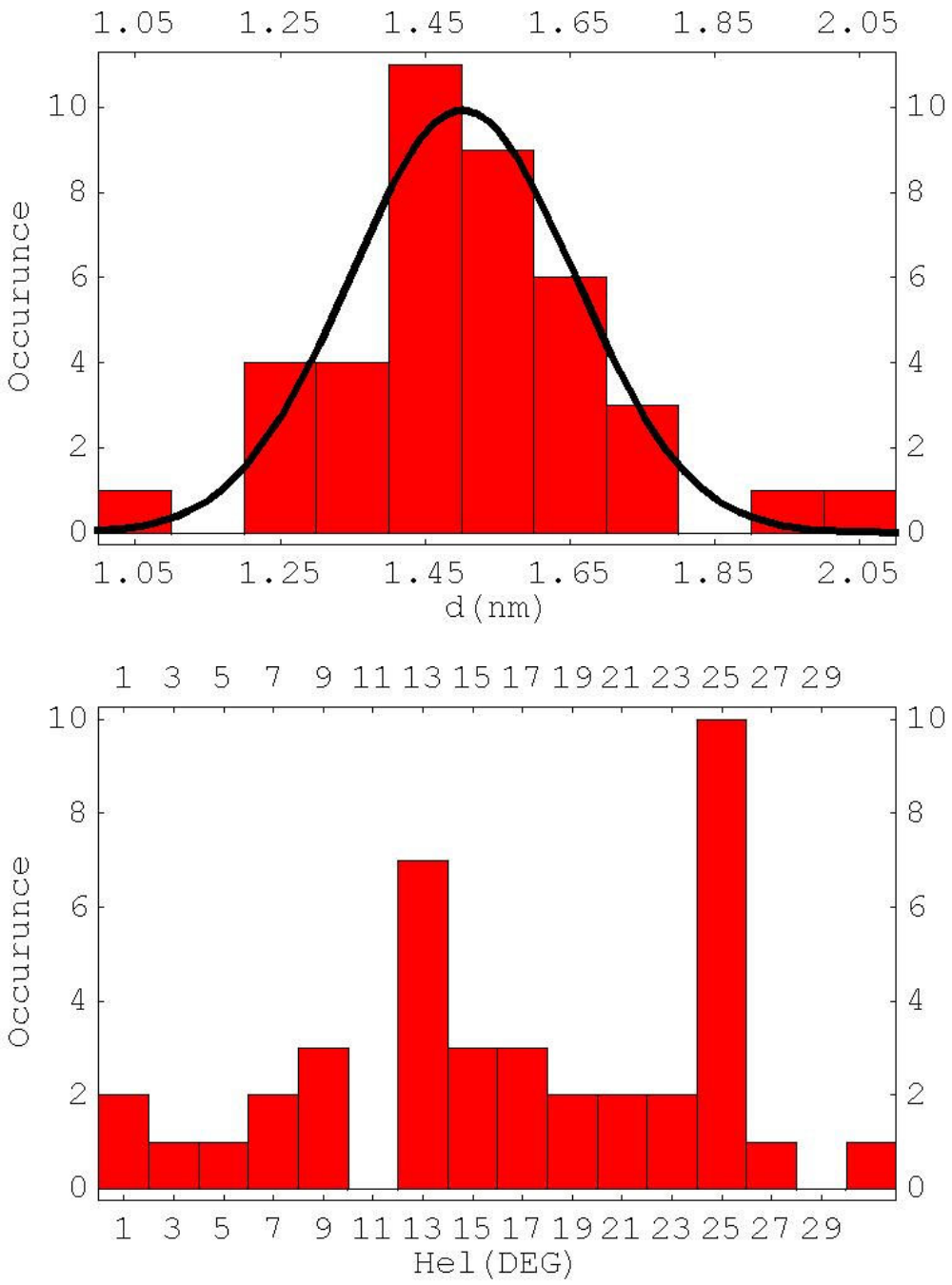

Fig. 3.4.2 Diameter (top) and helicity (bottom) distributions of nanotubes grown by the Co/Si bimetallic catalyst system obtained from 40 isolated nanotubes. The black solid line is a Gaussian fit for diameter distribution (0.2 nm bin size). The average diameter obtained is 1.50 ± 0.16 nm. The bin size is 2^{o} for helicity distribution. There is only one armchair nanotube observed among forty studied.

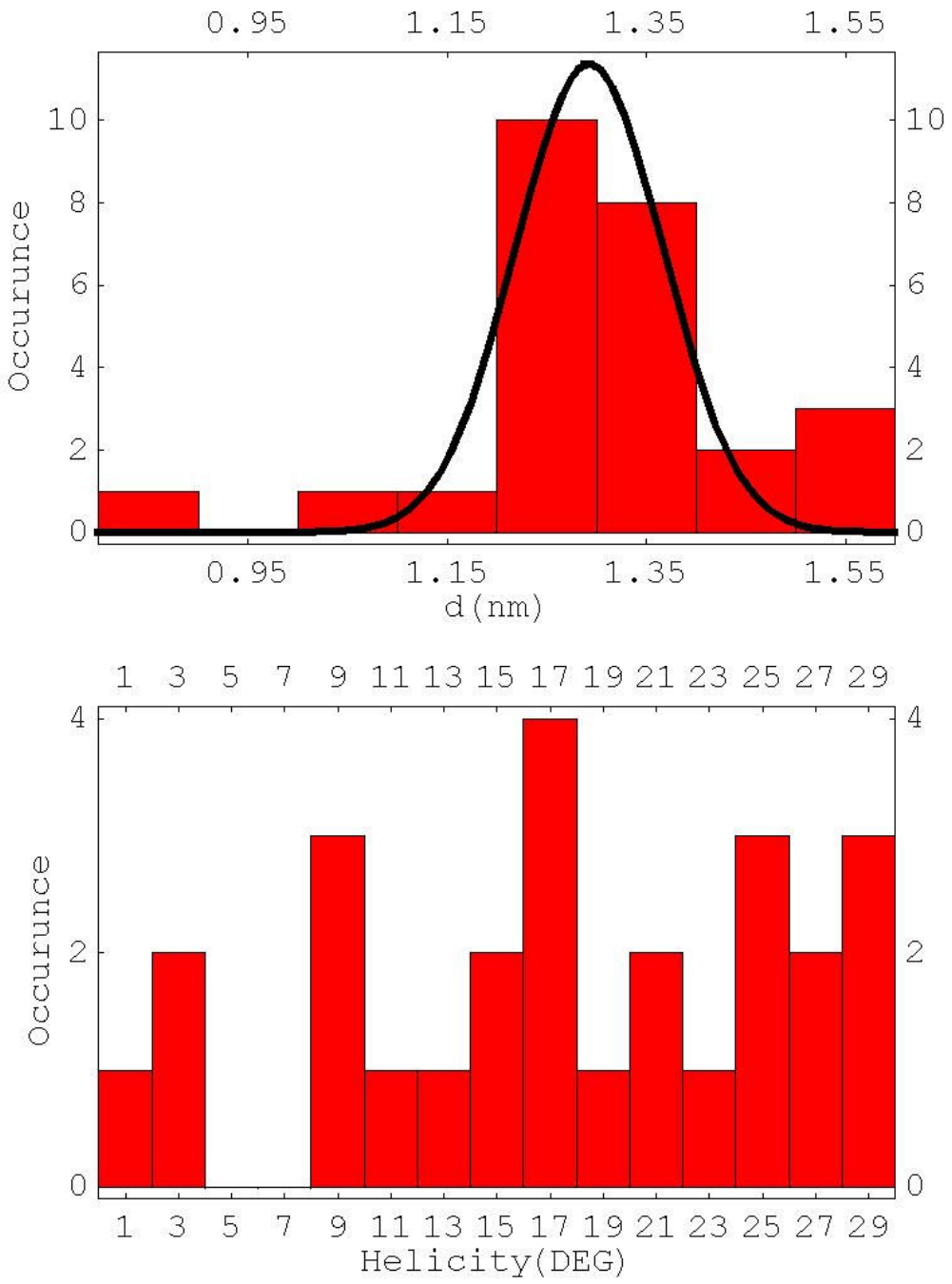

Fig. 3.4.3 Diameter and helicity distributions of nanotubes grown by the Ni/Co/Si ternary catalyst system obtained from 26 isolated nanotubes. The black solid line is a Gaussian fit for diameter distribution (0.2 nm bin size). The average diameter obtained is 1.29 ± 0.07 nm with narrowest distribution observed. The bin size is 2^{o} for the helicity distribution. Most of the nanotubes have helicities over the 10^{o} range.

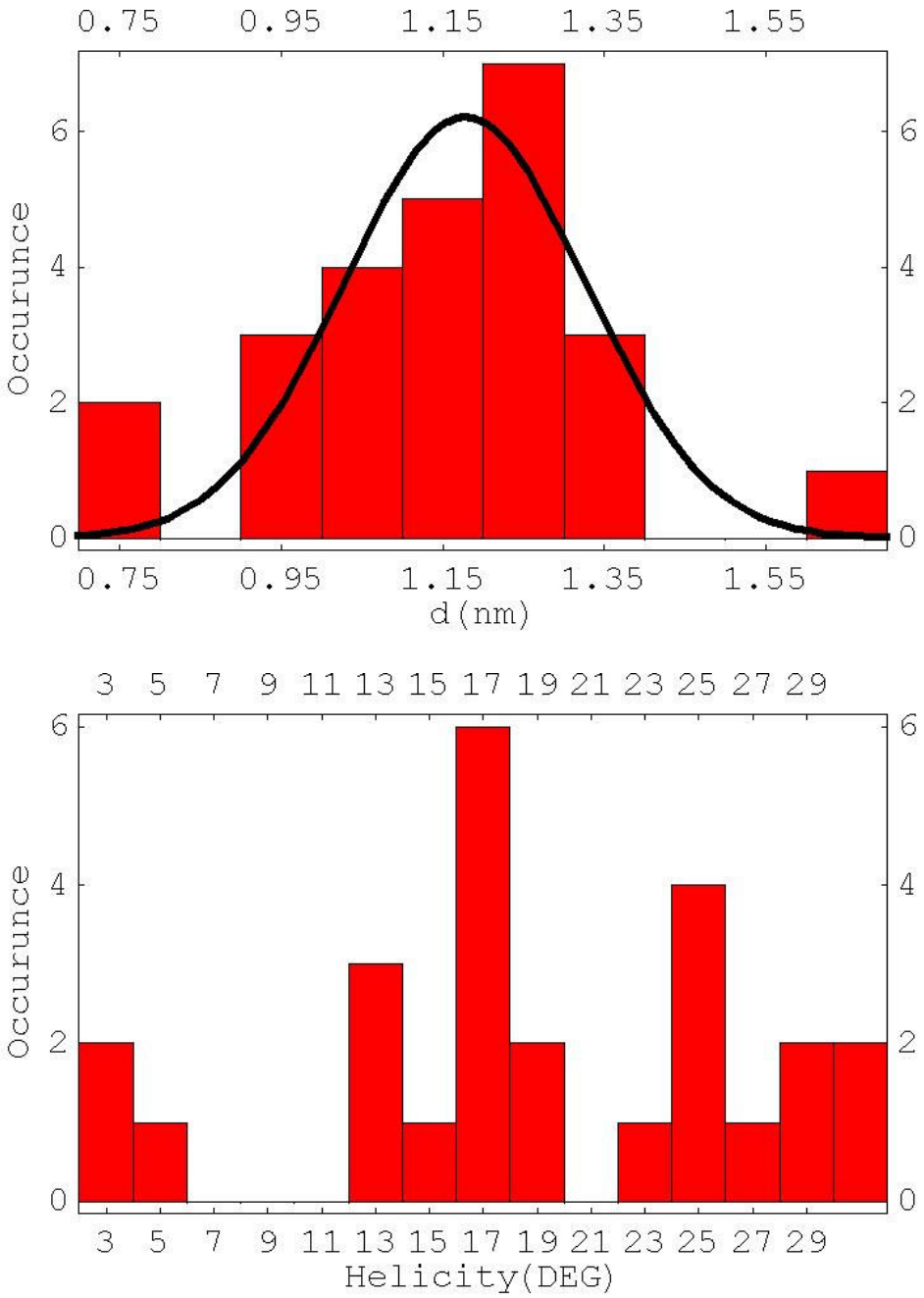

Fig. 3.4.4 Diameter and helicity distributions of nanotubes grown by the Ni/Fe/Si ternary catalyst system obtained from 25 isolated nanotubes. The black solid line is a Gaussian fit for diameter distribution (0.2 nm bin size). The average diameter obtained is 1.17 ± 0.15 nm being the smallest among three samples. The bin size is 2^{o} for helicity distribution. Most of the nanotubes have helicities over the 10^{o} range again.

3.5 Summary and Conclusions

Despite all efforts to elucidate the growth mechanism of single-walled carbon nanotubes, there is yet no consensus on how the nucleation and the subsequent growth happen or on the methods to control the structure of grown tubes. Earlier models, such as the "scooter mechanism" [21] have been abandoned in favor of new models involving different forms of the vapor-liquid-solid (VLS) model of 1960's [31]. Optical spectroscopy studies on the laser ablation plume suggest that the tube growth starts milliseconds after the ablation and may last up to a few seconds [32]. New growth mechanisms in their most basic forms include the conversion of a solid form of carbon in the plume to nanotubes by precipitation on the surface of the catalyst particles when they are in molten or in partially molten state [33-36]. It was also suggested that fullerenes formed at very early stages of the plume and their interactions with the catalyst particles might be responsible for the nucleation of carbon nanotubes [23, 34].

Normalized occurrence of helicities for the nanotubes grown by Co/Si was plotted to see if there is a strong preference for helicity. The distribution of helicities was calculated for all nanotubes of diameter from 1.053 to 2.048 nm (smallest and largest observed for Co/Si). There are 124 nanotubes with different chiral indices in this diameter range. For the Co/Si catalyzed nanotubes, we observed 31 different tube species out of 40 nanotubes studied. The normalized distribution shown in Fig.3.5.1 is calculated by dividing the number of observed nanotubes by the number of expected nanotube species at each helicity. A few prominent peaks are seen in the figure. The reason for these helicity preferences is not yet known. The total energy of nanotubes is weakly dependent on the structure. Energetically we expect to find every type of nanotube species in the sample. It

has been suggested that the growth kinetics favor chiral nanotube growth because of higher growth rate compared to the zigzag or the armchair tubules [28]. Considering our diameter range, the number of our sampling is only one third of the total nanotube species. Although we studied the nanotubes randomly to avoid selective sampling, only isolated tubes were selected and no tubes in any bundle were studied. Next step should be studying and be quantifying the nanotube species in the sample by Resonant Raman Spectroscopy [37]. In this way better statistics of the tube species in the sample can be gained and any strong preference for helicity distribution, if it exists, can be identified. If the tendency of helicities observed here is really the result of new catalyst used, the role that Si atoms play might be modifying the growth front and promoting the tube growth in certain ways, such as lowering the activation energy barrier for the diffusion of carbon atoms to the tube edge [38]. This needs to be investigated further.

For ternary Si catalyst systems, the average diameter of the nanotubes observed was slightly smaller than that of the tubes grown by binary Si catalyst. This can be explained by the increased solubility of carbon in the catalyst particles. Adding a third element to the binary catalyst mixture decreases the eutectic temperature of new alloy more since the furnace temperature was kept constant for all production runs. This causes more carbon to be dissolved in the particles at the early stages of ablation. Since the particles reach the supersaturated state faster, the nucleation and growth start earlier when the particle size is smaller. Further collisions in the plume lead particles to accrete more metal atoms and to increase in size. However, the nanotube diameter is determined by the size of the particle at the time of nucleation. This agrees with our observations from the TEM images since the isolated SWNTs were found to be attached to the particles larger in size.

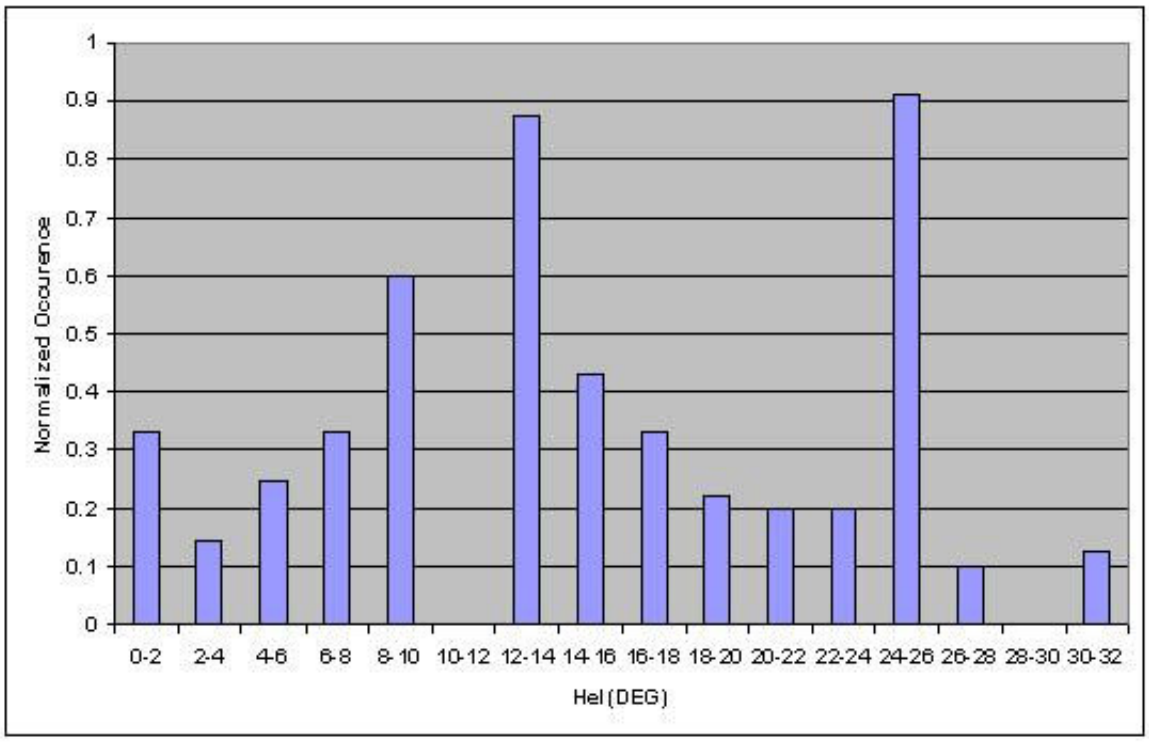

Fig. 3.5.1 Normalized occurrence calculated by dividing the number of observed nanotubes (40 total) by the number of nanotube species expected (124 total) at each helicity.

3.6 References

1. Iijima, S. (1991). Helical microtubules of graphitic carbon. *Nature* **354**, 56-58.

2. Krätschmer, W., Lamb, L. D., Fostiropoulos, F., Huffman, D. R. (1990) Solid C_{60}: a new form of carbon. *Nature* **347**, 354-358.

3. Iijima, S., Ichihashi, T. (1993). Single-shell carbon nanotubes of 1-nm diameter. *Nature* **363**, 603-605.

4. Bethune, D. S., Kiang, C. H., de Vries, M. S., Gorman, G., Savoy, R., Vazquez, J., Beyers, R. (1993). Cobalt-catalyzed growth of carbon nanotubes with single atomic layer walls. *Nature* **363**, 605-607.

5. Ebbesen, T.W., and Ajayan, P.M. (1992). Large-scale synthesis of carbon nanotubes. *Nature* **358**, 220-222.

6. Seraphin, S., Zhou, D. (1994). Single-walled carbon nanotubes produced at high yield by mixed catalysts. *Appl. Phys. Lett*. **64**, 2087-2089.

7. Kiang, C. H., Goddard, W. A., Beyers, R., Bethune, D. S. (1995). Carbon nanotubes with single-layer walls. *Carbon* **33**, 903-914.

8. Journet, C., Maser, W. K., Bernier, P., Loiseau, A., de la Chapelle, M. L., Lefrant, S., Deniard, P., Lee, R., Fischer, J. E. (1997). Large-scale production of single-walled carbon nanotubes by the electric arc technique. *Nature* **388**, 756-758.

9. Yacaman, M. J., Yoshida, M. M., Rendon, L., Santiesteban, J. G. (1993). Catalytic growth of carbon microtubules with fullerene structure. *Appl. Phys. Lett*. **62**, 202-204.

10. Lee, C.J., Kim, D.W., Lee, T.J., Choi, Y.C., Park, Y.S., Kim, W.S., Lee, Y.H., Choi, W.B., Lee, N.S., Kim, J.M., Choi, Y.G., Yu, S.C. (1999). Synthesis of uniformly distributed carbon nanotubes on a large area of Si substrates by thermal CVD. *Appl. Phys. Lett*. **75**, 1721-1723.

11. Andrews, R., Jacques, D., Rao, A.M., Derbyshire, F., Qian, D., Fan, X., Dickey, E.C., Chen, J. (1999). Continuous production of aligned carbon nanotubes: a step closer to commercial realization. *Chem. Phys. Lett.* **303**, 467-474.

12. Kong, J., Soh, H.T., Cassell, A.M., Quate, K.F., Dai, H. (1998). Synthesis of individual single-walled carbon nanotubes on patterned silicon wafers. *Nature*, **395**, 878-881.

13. Lee, K.H., Cho, J.M., Sigmund, W. (2003). Control of growth orientation for carbon nanotubes. *Appl. Phys. Lett.* **82**, 448-450.

14. Huang, S., Mau, A.H.W. (2003). Aligned carbon nanotubes patterned photo-lithographically by silver. *Appl. Phys. Lett.* **82**, 796-798.

15. Nerushev, O.A., Dittmar, S., Morjan, R.E., Rohmund, F., Campbell, E.E.B. (2003). Particle Size dependence and model for iron-catalyzed growth of carbon nanotubes by thermal CVD. *J Appl. Phys.* **93**, 4185-4190.

16. An, L., Owens, J. M., McNeil, L. E., Liu, J. (2002). Synthesis of nearly uniform SWNT using identical metal-containing molecular nano-clusters as catalysts. *J. Am. Chem. Soc.* **124**, 13688-13689.

17. Zhao, Y., Nakano, H., Murakami, H., Sugai, T., Shinohara, H., Saito, Y. (2006). Controllable growth and characterization of isolated single-walled carbon nanotubes catalyzed by Co particles. *Appl. Phys. A*. **85**, 103-107.

18. Kroto, H. W., Heath, J. R., O'Brien, S. C., Curl, R. F., Smalley, R. E. (1985). C_{60}: Buckminsterfullerene. *Nature* **318**, 162-163.

19. Guo, T., Nikolaev, P., Rinzler, A. G., Tomanek, D., Colbert, D. T., Smalley, R. E. (1995). Self-assembly of tubular fullerenes. *J. Phys. Chem*. **99**, 10694-10697.

20. Guo, T., Nikolaev, P., Thess, A., Colbert, D. T., Smalley, R. E. (1995). Catalytic growth of single-walled nanotubes by laser vaporization. *Chem. Phys. Lett*. **243**, 49-54.

21. Thess, A., Lee, R., Nikolaev, P., Dai, H., Petit, P., Robert, J., Xu, C., Lee, Y. H., Kim, S. G., Rinzler, A. G., Colbert, D. T., Scuseria, G. E., Tomanek, D., Fischer, J. E., Smalley, R. E. (1996). Crystalline ropes of metallic carbon nanotubes. *Science* **273**, 483-487.

22. Rinzler, A.G., Liu, J., Dai, H., Nikolaev, P., Huffman, C.B., Rodriguez-Macias, F.J., Boul, P.J., Lu, A.H., Heymann, D., Colbert, D.T., Lee, R.S., Fischer, J.E., Rao, A.M., Eklund, P.C., Smalley, R.E. (1998). Large-Scale purification of

single-wall carbon nanotubes: process, product and characterization. *Appl. Phys. A* **67**, 29-37.

23. Kataura, H., Kumazawa, Y., Maniwa, Y., Ohtsuka, Y., Sen, R., Suzuki, S., Achiba, Y. (1995). Diameter control of single-walled carbon nanotubes. *Carbon* **38**, 1691-1697.

24. Bandow, S., Asaka, S., Saito, Y., Rao, A. M., Grigorian, L., Richter, E., Eklund, P. C. (1998). Effect of the growth temperature on the diameter distribution and the chirality of single-walled carbon nanotubes. *Phys. Rev. Lett*. **80**, 3779-3782.

25. Bronikowski, M.J., Willis, P.A., Colbert, D.T., Smith, K.A., Smalley, R.E. (2001). Gas-phase production of carbon single-walled nanotubes from carbon monoxide via the HiPco process: A parametric study. *J. Vac. Sci. Technol. A* **19**, 1800-1805.

26. Fleming, L. B. (2003). *PhD Thesis* University of North Carolina at Chapel Hill.
27. Smith, B. W., Luzzi, D. E. (2001). Electron irradiation effects in single wall carbon nanotubes. *J. Appl. Phys*. **90**, 3509-3515.

28. Liu, Z., Zhang, Q., Qin, L. C. (2000). Determination and mapping of diameter and helicity for single-walled carbon nanotubes using nano-beam electron diffraction. *Phys. Rev. B* **71**, 245413.

29. Liu, Z. and Qin, L.C. (2005). A direct method to determine the chiral indices of carbon nanotubes. *Chem. Phys. Lett.* **408**, 75-79.

30. Biro, L. P., Molnar, G., Szabo, I., Vertesy, Z., Horvath, Z. E., Gyulai, J., Konya, Z., Piedigrosso, P., Fonseca, A., Nagy, J. B., Thiry, P. A. (2000). Selective nucleation and growth of carbon nanotubes at the $CoSi_2$/Si interface. *Appl. Phys. Lett*. **76**, 706-708.

31. Wagner, R.S., Ellis, W.C. (1964). Vapor-liquid-solid mechanism of single crystal growth. *Appl. Phys. Lett.* **4**, 89-90.

32. Puretzky, A.A., Geohegan, D.B., Fan, X., Pennycook, S.J. (2000). In situ imaging and spectroscopy of single-wall carbon nanotube synthesis by laser vaporization. *Appl. Phys. Lett.* **76**, 182-184.

33. Geohegan, D.B., Schittenhelm, H., Fan, X., Pennycook, S.J., Puretzky, A.A., Guillorn, M.A., Blom, D.A., Joy, D.C. (2001). Condensed phase growth of

single-wall carbon nanotubes from laser annealed nanoparticulates. *Appl. Phys. Lett*. **78**, 3307-3309.

34. Sen, R., Suzuki, S., Kataura, H., Achiba, Y. (2001). Growth of single-walled carbon nanotubes from the condensed phase. *Chem. Phys. Lett*. **349**, 383-388.

35. Gorbunov, A., Jost, O., Pompe, W., Graft, A. (2002). Solid-liquid-solid growth of single-wall carbon nanotubes. *Carbon* **40**, 113-118.

36. Gavillet, J., Loiseau, A., Ducastelle, F., Thair, S., Bernier, P., Stephan, O., Thibault, J., Charlier, J.C. (2002). Microscopic mechanisms for the catalyst assisted growth of single-wall carbon nanotubes. *Carbon* **40**, 1649-1663.

37. Jorio, A., Santos, A.P., Ribeiro, H.B., Fantini, C., Souza, M., Vieira, J.P.M., Furtado, C.A., Jiang, J., Saito, R., Balzano, L., Resasco, D.E., Pimenta, M.A. (2005). Quantifying carbon-nanotube species with resonance Raman scattering. *Phys. Rev. B* **72**, 075207.

38. Lee, Y.H., Kim, S.G., Tomanek, D. (1997). Catalytic growth of single-wall carbon nanotubes: An Ab Initio study. *Phys. Rev. Lett.* **78**, 2393-2396.

Chapter 4

Structure Characterization of MWNTs

After the formulation of the kinematical theory of diffraction from carbon nanotubes [1-3], it has been used to understand and calculate the electron diffraction patterns from a known structure specified by the chiral indices (u,v). The reverse problem is the assignment of the chiral indices from an electron diffraction pattern, which has been shown that it can be done with accurate and unambiguous results. There are two methods to obtain the helicity of carbon nanotubes. The first method uses a correction factor to obtain the chiral angle from the diffraction patterns [4]. The second one uses the ratio of the layer line spacings measured from the electron diffraction patterns [5]. In this study, we choose to adapt the second method to determine the helicities since it produces much better accuracy over the first one. Higher accuracy in helicity measurements coupled with the information of number of walls and diameters from TEM images can provide the assignment of chiral indices of many shells in a carbon nanotube. This was demonstrated for a quadruple-walled carbon nanotube and it was suggested that this technique can be extended to determination of chiral indices of up to 15 walls [6].

A one-step direct method involving Bessel functions and electron scattering intensity distribution in the diffraction patterns was developed recently to retrieve the chiral indices of carbon nanotubes [7] and it was applied to determine the atomic structure of a

large number of single-walled nanotubes [8]. This method even allows the determination of the chiral indices without measuring the helicity from the diffraction pattern but it is limited in the way that the electron beam must be perpendicular to the tube axis otherwise corrections are needed. Electron diffraction from carbon nanotubes was also discussed using mostly geometric illustrations in a review article [9]. Recent studies combined the TEM and diffraction analysis with optical spectroscopy to determine the physical structure, vibrational properties and optical transition energies of individual single-walled carbon nanotubes simultaneously [10, 11]. Torsional pendulums built on individual SWNT devices enabled to achieve large elastic deformations on the structure in order to determine the handedness of the nanotubes by diffraction analysis [12]. Many electron diffraction studies of carbon nanotubes as seen in the literature show that it is the most popular and powerful technique to study their atomic structure with a high accuracy. [13-27].

4.1 Characterization of DWNTs

DWNTs represent the next hierarchical structure after SWNTs in the family of carbon nanotubes. They consist of two single-walled carbon nanotubes nested within one another concentrically. The electron diffraction pattern of a DWNT can be explained in terms of a sum of the electron diffraction patterns due to the single-walled carbon nanotubes constituting the DWNT. The structure of each wall can be determined from an experimental electron diffraction pattern and the structural correlation between the adjacent walls can be studied in this way.

In this study, the chiral indices of isolated single DWNTs were determined using the nano-beam electron diffraction method. The DWNT sample was provided by J. Liu of Duke University produced by a CVD process. The tubes usually have lengths over 1 micron usually and tend to entangle and bundle with each other. To study an individual isolated double-walled nanotube, a straight section of tube over a length of 50 nm is needed to place an electron probe of nanometer size over it such that the electron diffraction pattern taken in this way will reveal the structure of each tube and will not deteriorate due to curved sections or other tubes or bundles of tubes. A dilute concentration of the purified DWNT sample was prepared in ethanol by ultra-sonication for hours. One or two drops of the solution was then placed down on a lacey-carbon-covered TEM grid. The electron microscope (JEOL JEM-2010F) was operated at an acceleration voltage of 120 kV, which is below the threshold of knock-on damage (140 kV) for graphite, to avoid radiation damage to the tubes [28]. The diffraction patterns were recorded on a Gatan high resolution (2k×2k) slow scan CCD camera.

Two sets of reflections (Fig. 4.1.1) are visible in the diffraction pattern of a double-walled carbon nanotube, as well as intense radial lines emanating from the central beam. These lines are due to electrons scattered into high angles at the condenser aperture and partially shadowed by the tube [27]. If both shells are chiral nanotubes with different helicities, we will observe 6 layer lines in total above and below the equatorial layer line. If both layers are chiral but have the same helicity, we will see 3 layer lines in total. The first step to determine the chiral indices of each nanotube is to accurately measure the layer line spacings from the diffraction pattern. Then the ratio of the indices for each shell

can be calculated using the measured layer line spacings. The whole procedure can be summarized in the following:

1. Measure accurately the layer line spacings for each layer line seen in a diffraction pattern.
2. Measure the diameter of each wall as accurately as possible from its high resolution TEM image using the line intensity profiles.
3. Identify the layer lines corresponding to each helicity. The total number of lines should be 3 for each helicity other than 0^o or 30^o. Use the complementary relations like $D_1 = D_2 + D_3$ if necessary.
4. Calculate the ratio of the chiral indices for each helicity observed from the diffraction pattern using the equation below [6]:

$$v/u = (2D_2 - D_1)/(2D_1 - D_2)\,. \qquad (4.1.1)$$

5. List all possible chiral indices that give the observed *v/u* ratio experimentally.
6. Select the chiral indices that give the diameters matching closely the ones measured from the high resolution images and the graphite c-axis spacing (*c/2* ≈0.335 nm).

Once the chiral index assignment for each layer is complete, the true diameter (eqn.1.2.3), the chiral angle (eqn.1.2.2) and the metallicity of each layer can be determined.

Another approach is to calculate the ratio of the layer line spacings of the first two layer lines (D_1 / D_2). This ratio is independent of the calibration of the diffraction pattern or the camera length used to acquire it or the tilt angle of the tube with respect to the electron beam. This ratio can also be expressed in terms of the chiral indices of (u, v):

$$D_1 / D_2 = \frac{(2u+v)}{(2v+u)}. \qquad (4.1.2)$$

This ratio can be calculated for all possible chiral indices spanning a range up to the chiral indices (u,u). Then a table can be constructed for this ratio and for corresponding chiral indices, diameters and chiral angles. We can measure the layer line spacings (D_1 and D_2) and calculate their ratio (D_1 / D_2) directly from the measured spacings. Then we can look up this measured ratio in the table and find the corresponding chiral indices matching the measured diameters. The highest diameter tube in our table is a (30, 30) armchair tube with a diameter of 4.07 nm.

In some cases, reflections are either too weak to be distinguished from the electron noise in the CCD camera or missing due to poor crystallinity of the nanotubes. This affects especially the third layer line (L3) in the diffraction patterns. The scattering intensity on this layer line is proportional to the square of Bessel function of order $(u+v)$. Since the peak heights of Bessel functions decrease with increasing order, the scattering intensity in the reciprocal space will diminish quickly for the layer line L3. This is combined with the fact that the farther away from the tubule axis in reciprocal space, the weaker the reflections will be due to the quickly falling electron scattering factors. The number of scatterers also has a contribution to the small scattering intensities observed. As the diameter of the tube decreases, the number of scatterers does as well and the scattering intensities are proportional to the square of the number of the atoms involved in the process. The combination of all these effects explains the weak intensities observed in some of the diffraction patterns of DWNTs and the missing third layer line L3. This might make the identification of the layer lines with the same helicity difficult

but fortunately there are only two possibilities to match the layer lines (L1 and L2) of same helicity seen in the diffraction patterns of DWNTs. This might prove to be problematic for multi-walled nanotubes of several walls. In any case, the higher order layer lines (L4 for example) observed might also be useful to determine the layer lines due to the same nanotube. The equation $D_1 = D_2 + D_3$ can be rewritten to include the layer line spacing of L4:

$$D_4 = D_1 + D_2$$

$$\text{or } 2D_1 = D_4 + D_3 . \tag{4.1.3}$$

Then the ratio of v/u can be expressed in terms of D_4 and D_1 as

$$v/u = \frac{(2D_4 - 3D_1)}{(3D_1 - D_4)} \text{ [29].} \tag{4.1.4}$$

The result would be more accurate if equation (4.1.4) were used since the error in the *v/u* ratio due to small errors in the measurement of spacings would be reduced greatly. Again, the ratio of the fourth layer line to first layer line (D_4 / D_1) can be calculated directly from the measurements and looked up in a table instead of calculating *v/u* ratio. This ratio, in terms of the chiral indices, is given as

$$D_4 / D_1 = \frac{3(u+v)}{(2u+v)} . \tag{4.1.5}$$

All these ratios (v/u, D_1 / D_2 and D_4 / D_1) have been calculated for the nanotubes with the possible indices of up to (30, 30) and are listed in the appendices.

Two examples are given below to illustrate how the procedure works for the assignment of the chiral indices of DWNTs. Again, looking back at Fig. 4.1.1, we see six layer lines and the measured spacings in descending order are 861.4, 786.4, 714.3, 477.2,

384.2 and 74.0 all in arbitrary units. The layer lines can be grouped in two ways corresponding to two distinct helicities observed in the experimental diffraction pattern using the equation $D_1 = D_2 + D_3$. The lines with the spacings 861.4, 477.2 and 384.2 are due to one shell in the DWNT labeled as group A and the lines with the spacings 786.4, 714.3 and 74 are due to the second shell labeled as group B. The ratio of the chiral indices *v/u* is calculated to be 0.075 (group A) and 0.748 (group B), respectively. The diameters of the shells of the DWNT measured from the high resolution image (inset in Fig. 4.1.1) are 1.94 nm and 1.23 nm. Thus, the final assignment for the chiral indices is (27, 2) and (12, 9) for the outer and the inner shell respectively. The chiral angles are 3.54^{o} and 25.28^{o} and diameters are 2.197 nm and 1.429 nm respectively, with an inter-shell distance of 0.384 nm which is about 15% larger than the c-axis spacing of graphite. The outer shell is semiconducting and the inner shell is metallic.

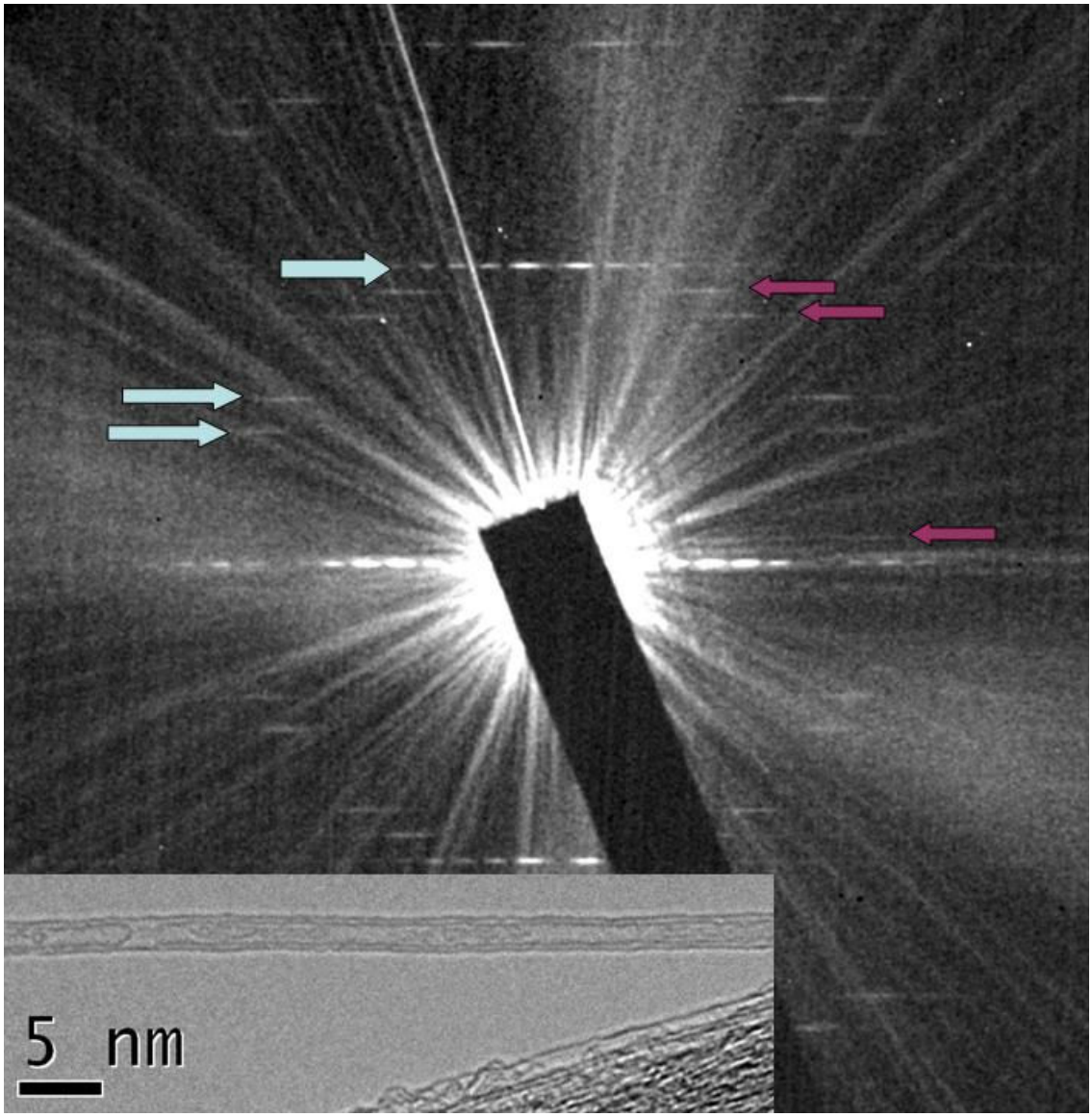

Fig. 4.1.1 Experimental electron diffraction pattern of a double-walled carbon nanotube taken at 120 kV accelerating voltage. The blue and purple arrows mark the layer lines due to each shell, respectively. The inset shows an HRTEM image of the DWNT.

In a second example, only four layer lines are seen clearly in the diffraction pattern (Fig. 4.1.2). The measured layer line spacings are 1183.3, 1043.2, 755.2 and 428.6. The number of observed layer lines suggests that one of the shells is an armchair tube and the other is a chiral tube. The reasoning behind this is if both shells are armchair, then there should be only one layer line; if both are zigzag, there should be only two layer lines. The three layer lines with the exception of the 1043.2 measurement form the reflections of one shell and the fourth one is due to the reflections of the second shell. For the chiral tube, the measured *v/u* ratio is calculated to be 0.203. The diameters measured from the TEM image were 1.69 nm and 0.91 nm (inset in Fig. 4.1.2). The possible indices for the chiral tube are (10, 2) and (20, 4). Since the scattering intensities on a given layer line are dominated by a single Bessel function of an integer order, the observed intensity can be fit with an appropriate Bessel function to determine its order. For the first layer line that belongs to the chiral tube, the scattering intensity is proportional to the square of the Bessel function of order *v*. This was determined to be $v = 4$ by fitting the intensity using Bessel functions. So, the outer shell of the DWNT is tube (20, 4). It has a chiral angle of 8.95^{o} and a diameter of 1.744 nm. The inner shell is an armchair tube and unfortunately only the first peak of the Bessel function is identifiable in the intensity distribution. So, the fitting is not an option. The (7, 7) and the (8, 8) nanotubes have diameters (0.949 nm and 1.085 nm, respectively) that are very close to the observed ones. This makes a unique assignment of the indices for inner shell ambiguous. However, the equatorial layer line can be used to identify which chiral index assignment fits the intensity of this line best with its diameter value. The intensity on the equatorial line is only governed by the Bessel function of order zero and the total intensity is a sum of contributions from each

shell of the nanotube. The structure factor on this line composed of N shells can be given as

$$F(R, l = 0) = f \sum_{i}^{N} d_i J_0(\pi R d_i), \tag{4.1.6}$$

where f is the atomic form factor of the carbon atom and d_i is the diameter of shell i [15]. The intensity is then proportional to the square modulus of the structure factor ($I = |F(R)|^2$). The atomic form factor of carbon for fast electrons can be obtained from the values tabulated in the *International Tables for Crystallography C* [30]. The values can be fitted to cast it into a continuous function by using the Doyle-Turner equation with exponentials [31]:

$$f(s) = \sum_{i=1}^{4} a_i \exp(-b_i s^2), \tag{4.1.7}$$

where s is the scattering vector in the reciprocal space and defined as $s = 2\sin(\theta)/\lambda$ with λ being the wavelength of the fast electrons and 2θ is the scattering angle. The intensity of the equatorial line in the diffraction pattern (Fig. 4.1.3.) was fitted using the two possible choices of chiral indices assignment for this nanotube. The assignment of (20, 4) and (8, 8) gives the best agreement between the simulated and the experimental intensity curves and this is shown in Fig. 4.1.3.

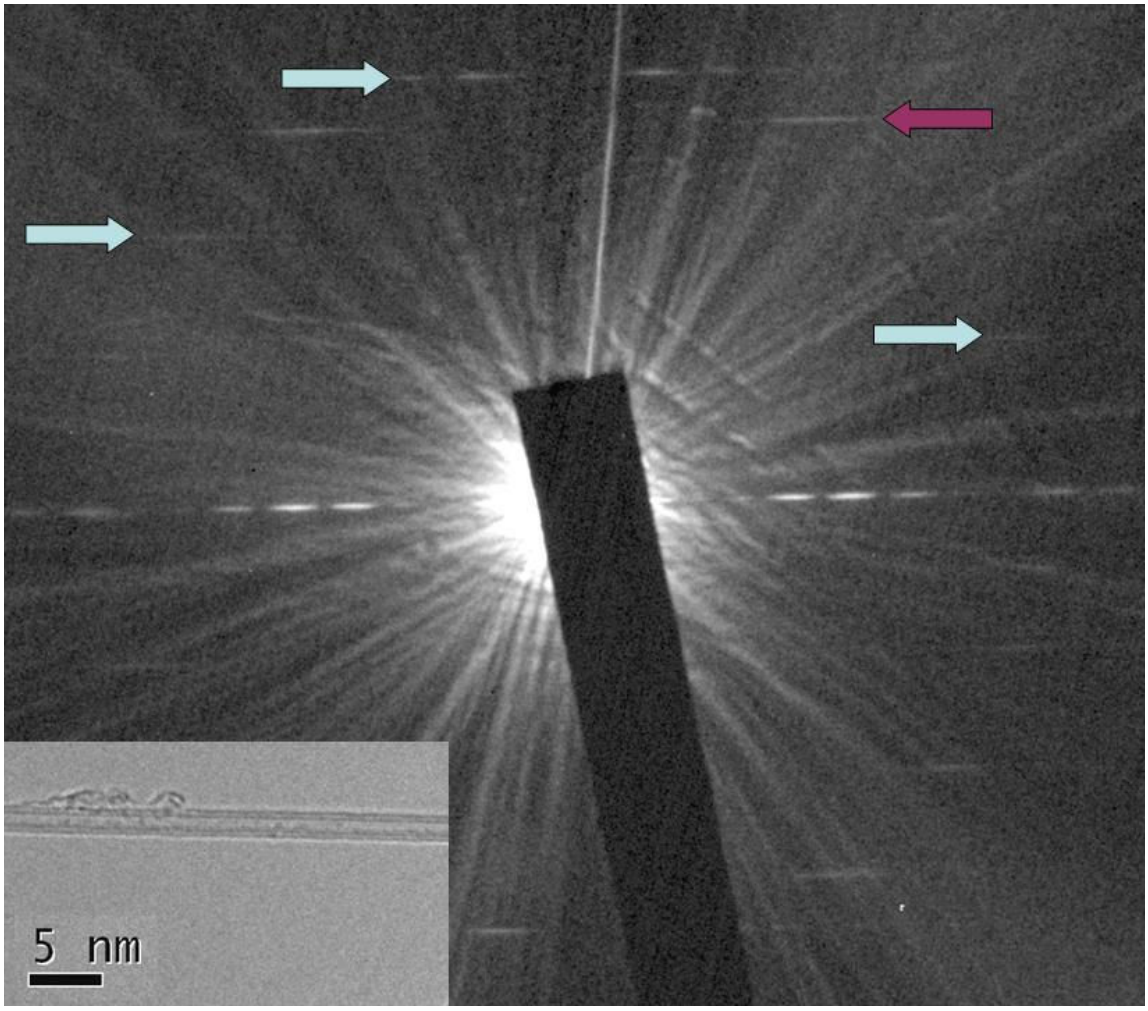

Fig. 4.1.2 Experimental electron diffraction pattern of a double-walled carbon nanotube taken at 120 kV accelerating voltage with a nano-beam diffraction. The blue and purple arrows mark the layer lines due to each shell. The inset shows an HRTEM image of the DWNT.

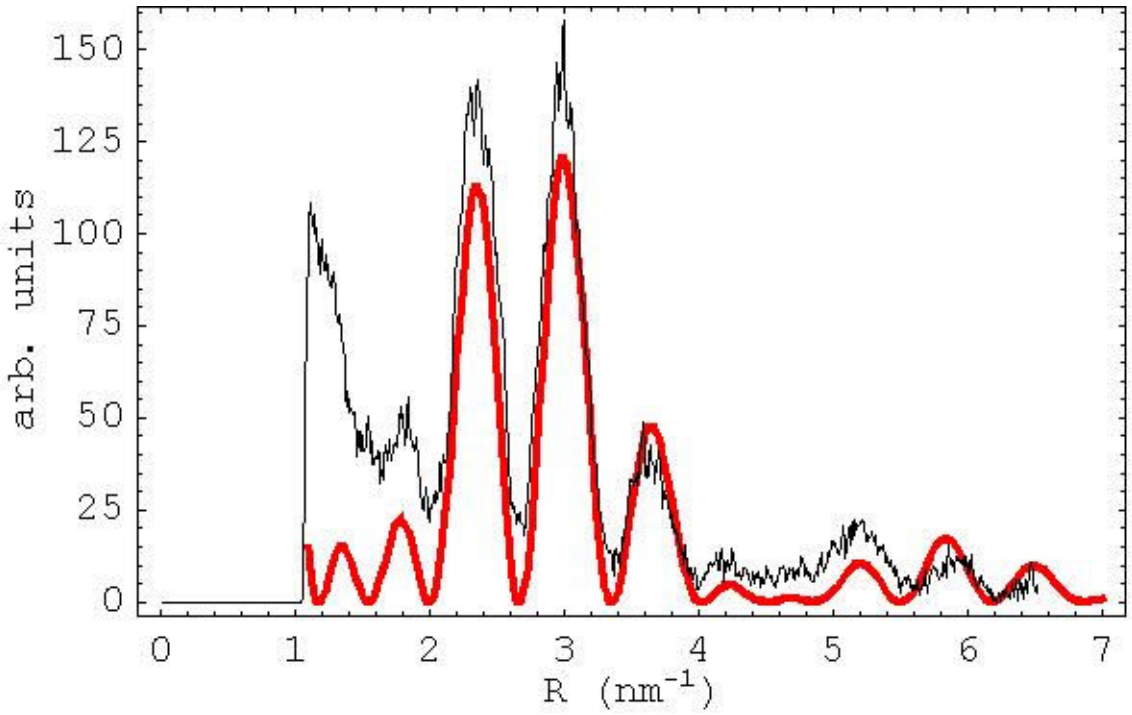

Fig. 4.1.3 The black curve is the experimental intensity of the equatorial line from the diffraction pattern of a DWNT and the red curve is the simulated intensity for a DWNT with chiral indices of (20, 4) and (8, 8) for outer and inner shells respectively.

A total of 22 DWNTs were analyzed using the techniques explained above and their chiral indices were determined. The chiral indices assigned, diameter, chiral angle, metallicity, and the inter-layer distance for all 22 double-walled nanotubes characterized are listed in the appendices. There were only three armchair and two zigzag shells. There were nineteen metallic walls out of 44 shells. Among the observed DWNTs, there were 7 M-S (inner-outer), 7 S-S, 4 S-M and 4 M-M nanotubes. For the inner shell, 11 were metallic and 11 were semiconducting. For the outer shells, 8 were metallic and 14 were semiconducting. These DWNTs were all expected to be metallic or at least their outer shell to be metallic [32]. However, our study shows that there is no strong tendency towards the metallicity of the constituent shells of the DWNTs studied here.

The distribution of chiral angles is rather random for the inner and outer shells (see Fig. 4.1.4). Half of the inner shell tubes have chiral angles in the range between 20^{o} and 30^{o}. Only three DWNTs were commensurate with one being a zigzag tube. However, our results indicate no strong correlation towards the chirality between the inner and outer shells (mostly being incommensurate with each other). Our results do not completely agree with previous studies by electron diffraction on DWNTs. Hirahara et al. [33] reported the chirality of DWNTs being distributed toward higher angles (more than half of the tubes) when the diameters of the DWNTs are less than 3 nm but observed a random distribution when they are larger than 3 nm. Gao et al. [34] saw that most of the tube walls have chiral angles higher than 18^{o}. The DWNTs characterized here have usually diameters less than 2.0 nm but do not show strong tendency for chiral angles distributed toward near armchair structures. However, Hirahara et al. used a sampling

much larger than ours in their study. They also saw no strong correlation between the orientation of the inner and outer shells.

The inter-layer distances varied from 0.307 nm to 0.434 nm. On average the inter-wall distance was 0.36 ± 0.40 nm. Although the distribution of wall spacings covers a wide range, the strong tendency for inter-wall spacings in the range of 0.30-0.32 nm can be noticed (see Fig. 4.1.5). Our average wall spacing agrees well within its uncertainty with the spacings reported before for DWNTs studied by electron diffraction [33, 34]. The wall spacing is 0.344 nm for turbostratic graphite with uncorrelated orientation of layers, which is consistent with the average interlayer spacing obtained from X-ray diffraction of MWNTs [35]. It is 0.335 nm for ideal graphite with ABAB Bernal stacking. Our wall spacing here is 5% larger than the former value and 7% larger than the latter value.

Theoretical work of Saito et al. showed that the stability of DWNTs is independent of the chirality but depends strongly on the interlayer spacing [36]. They reported an interlayer spacing of 0.34 nm on a potential well almost flat for spacings from 0.33 to 0.35 nm only considering weak van der Waals forces. One explanation for larger interlayer spacing in our study could be the size effects in carbon nanotubes. It was observed that the interlayer distance is function of the diameter of MWNTs and decreases with increasing nanotube diameter approaching the value of turbostratic graphite at a diameter of about 10 nm [37]. They are more pronounced for small diameter nanotubes and this could be one reason why we have seen an increased tendency for small interlayer spacing here. Of course one would expect larger spacings when we considered the size effects. Small diameter causes larger curvature which perturbs the geometric and electronic structure more compared to a flat graphene sheet. This might be the reason for

stronger interactions between the shells for small diameter nanotubes leading to smaller wall spacings although we might expect to see an increased repulsive force leading to increased wall spacing. The well-known ABAB stacking of graphite results from orbital interactions between the layers rather than van der Waals forces [38]. This results in a smaller spacing than that of turbostratic graphite. Since most of our tubes are incommensurate with each other, the smaller spacing observed must be due to something else. Since these tubes grown by CVD on catalyst particles, the interactions of nanotube seeds with electronic states of metal catalysts modify their electronic and geometric structure during the synthesis and the tubes will be frozen in their relative orientation to each other. Some charge transfer might take place between the substrate and the growing tubes and result in the modification of their electronic structure and consequent interaction between the shells. Some of DWNTs might also be defective since they have a smaller interlayer spacing than the usual.

It is known that the CVD can be used to produce nanotubes whose size depends roughly on the size of the catalysts particles. In the case of the DWNTs, the diameter of the outer shell will be proportional to the size of the catalysts. The diameter of the inner tube will be selected for an outer tube of a given diameter determined by the size of the catalyst particle within the constraint of the interlayer distance of the turbostratic graphite. For such a small tubes here, the diameter can not change continuously and is determined by the chiral indices (u,v). The diameter of the inner shell can not be adjusted according to the turbostratic spacing value exactly in general. The largest possible tube should be the inner tube usually and in some cases only stable tube pair might be obtained when the interlayer distance is slightly less than 0.344 nm. Same

interlayer spacing as ours was obtained from DWNTs grown from peapod structures [39]. In the conversion of SWNTs to DWNTs through C_{60} molecules, the diameter of the inner shell is determined by the outer SWNT similar to the role of the catalyst and the outer shell in our DWNTs and this support our conclusion above. This suggests the coupling of the inner and outer shell is loose. Therefore, interactions among the shells in a tube have a very small influence on the growth mechanism.

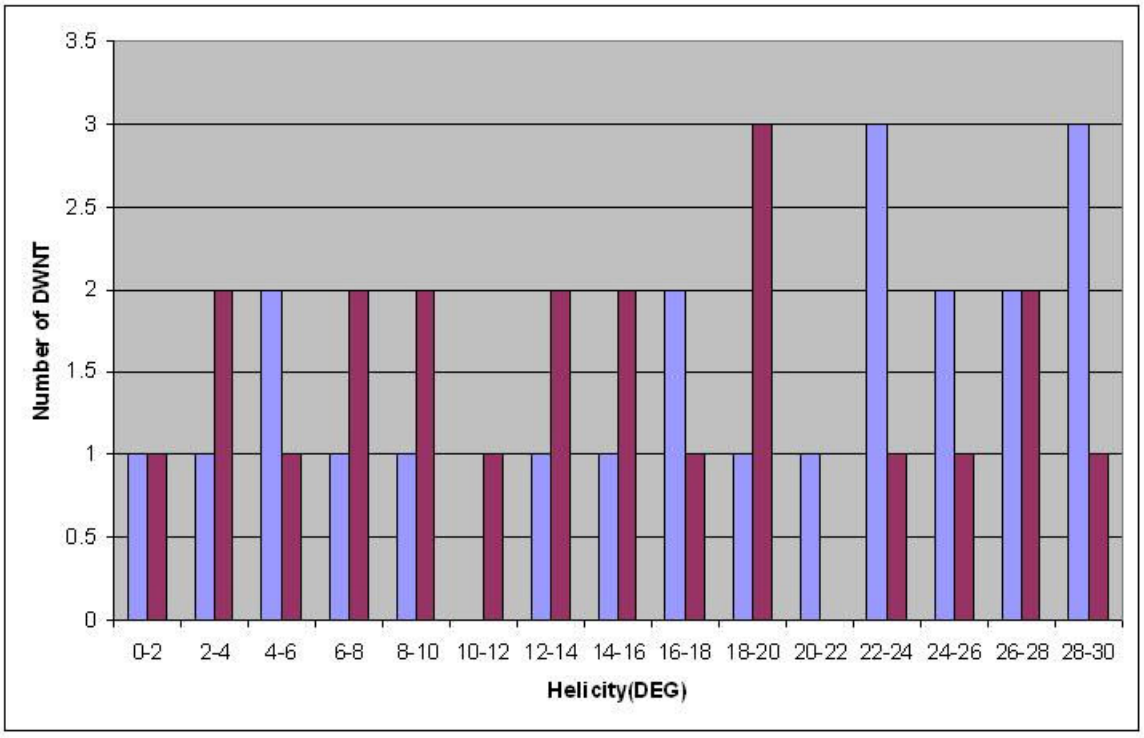

Fig. 4.1.4 Helicity distribution for the inner (lighter color) and outer shells (darker color) for all 22 DWNTs studied with 2^{o} binning size.

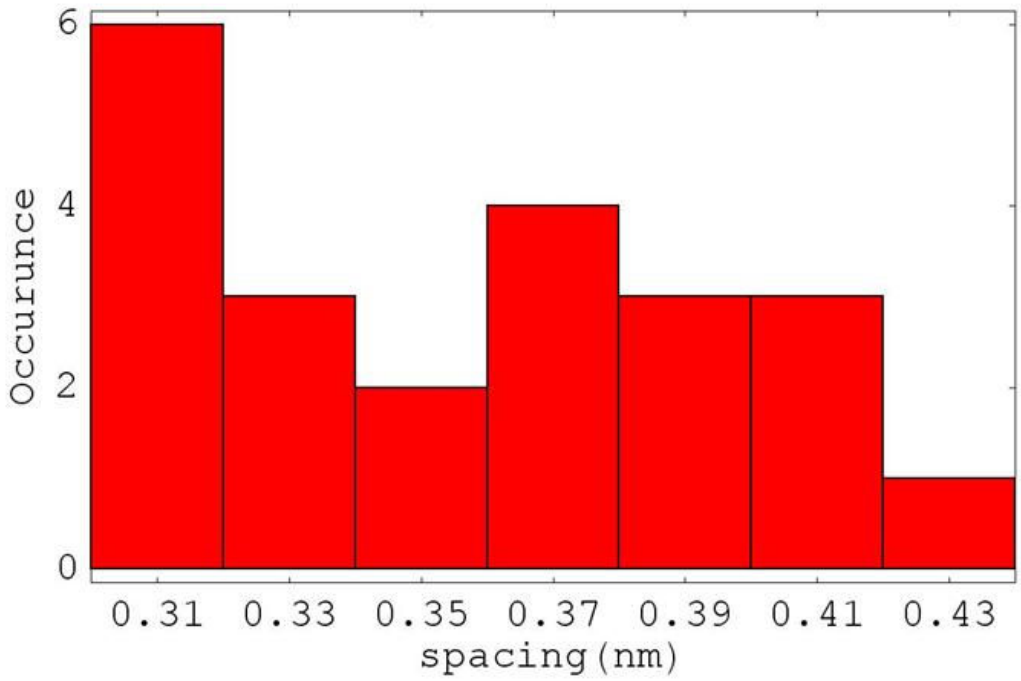

Fig. 4.1.5 Interlayer spacing distribution for all 22 DWNTs characterized in this work. The binning size is 2 nm.

4.2 Characterization of FWNTs

Few-walled carbon nanotubes (FWNT) are intermediate between SWNTs and MWNTs. They are composed of about 2 to 6 concentric shells generally. DWNTs are a special kind of FWNT with the lowest number of walls. They are smaller in diameter than MWNTs. Here, the FWNTs studied consist of 3 to 5 shells. The determination of the structure and the chiral indices is pretty straightforward for SWNTs and DWNTs. The layer line spacings can be measured accurately to calculate the ratio of chiral indices and the assignment of the chiral indices can be done uniquely with the aid of the measured diameters from the TEM images. As the number of shells in a nanotube increases, the number of possible choices of the chiral indices giving the same helicity increases as well with the increasing diameter and shell. Here, we are using the FWNTs as a stepping stone

before we attempt to determine the structure of MWNTs with the methods outlined in the previous section.

Seven FWNTs were studied and their chiral indices were assigned from the measured *v/u* ratios and diameters. The high order layer lines such as L4 were used whenever it is possible to simplify the assignment as well as to increase the accuracy. Among the seven few-walled nanotubes studied, three of them were five-walled, other three were quadruple-walled and one was a triple-walled carbon nanotube. We will discuss a few examples for the structure determination before we move onto that of MWNTs.

Example 1

Figure 4.2.1 shows an electron diffraction pattern of a triple-walled carbon nanotube. There are nine pairs of layer lines present in the pattern across the equatorial layer line. The *v/u* ratios were measured to be 0.5526, 0.7503 and 0.9373 ranking them from smallest to largest helicity. The chiral indices of three layers were determined to be (29, 16), (12, 9) and (17, 16) respectively. Their diameters and helicities are (1.429 nm, 25.29^{o}), (2.238 nm, 29.00^{o}) and (3.094 nm, 20.53^{o}), respectively, with inter-layer distances of 0.428 nm and 0.404 nm, respectively. These inter-layer distances are larger than the graphitic spacing. The innermost layer is metallic and other two layers are semiconducting.

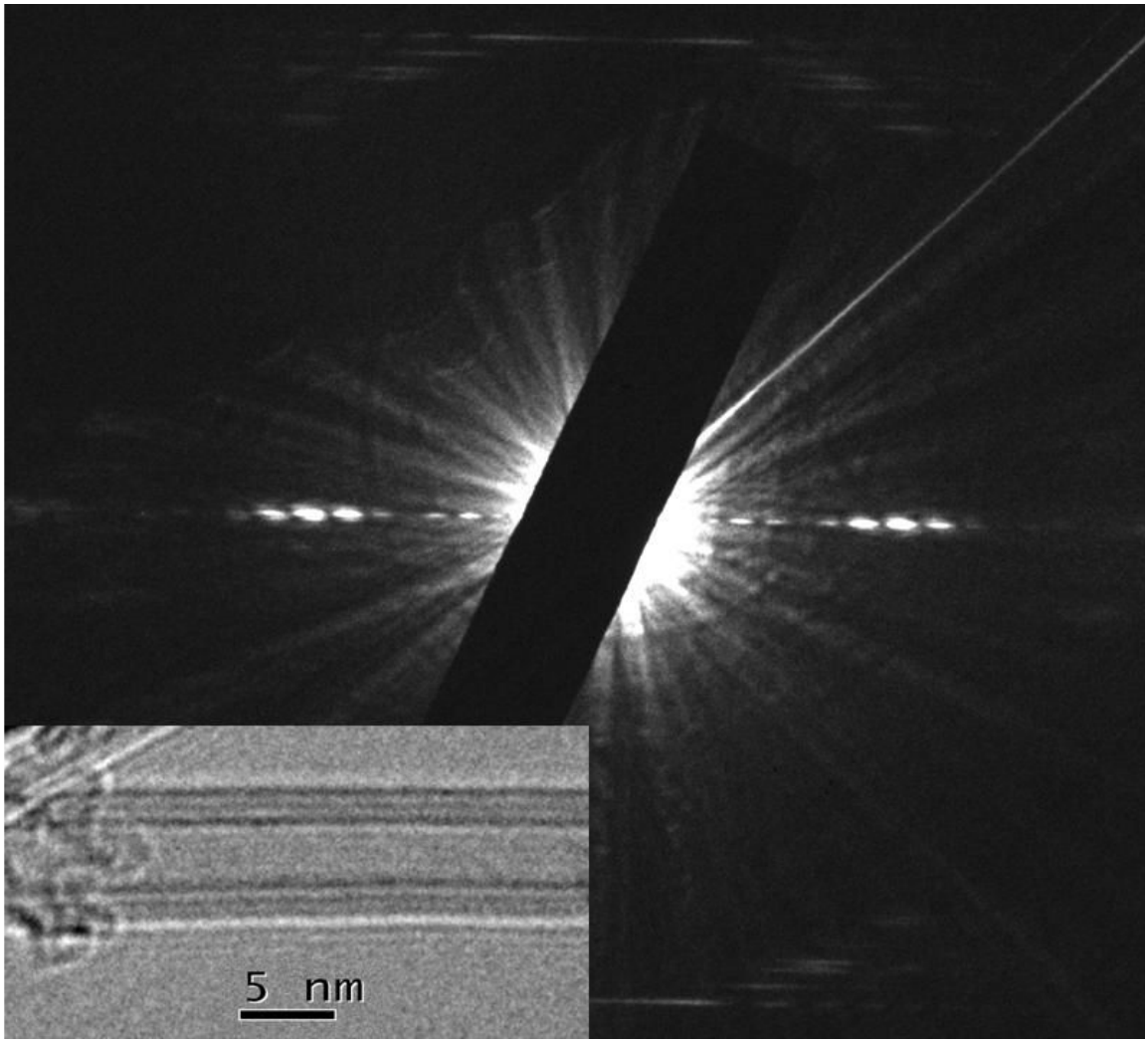

Fig. 4.2.1 Experimental electron diffraction pattern of a triple-walled carbon nanotube taken at 120 kV accelerating voltage with nano-beam diffraction. The inset shows an HRTEM image of the same nanotube. The chiral indices are (29, 16), (17, 16), and (12, 9), respectively.

Example 2

Figure 4.2.2 shows an electron diffraction pattern of a quadruple-wall carbon nanotube. There are ten pairs of layer lines in the diffraction pattern and four different helicities were identified. There are only two L1 layer lines meaning that each L1 layer line is composed of two overlapping lines of very close helicities. The measured *v/u* ratios were 0.0522, 0.0772, 0.2024 and 0.2304, respectively. Diameters of the innermost and the outermost layers were 2.6 nm and 4.7 nm respectively measured from the TEM image. The indices of the innermost layer were found to be (30, 6) giving (2.62 nm, 8.95^{o}) for its diameter and helicity. The rest were found by looking at the agreement between the experimental and simulated intensity of the equatorial layer line from the list of possible indices. They were determined to be (40, 3), (44, 10) and (58, 3), which give (3.26 nm, 3.58^{o}), (3.896 nm, 10.02^{o}), and (4.664 nm, 2.50^{o}), respectively. All layers except the innermost one in this nanotube are semiconducting. The inter-layer distances are 0.32 nm, 0.318 nm, and 0.384 nm.

Example 3

Figure 4.2.3 shows an electron diffraction pattern of a quintuple-walled carbon nanotube. There are fifteen pairs of layer lines observable in the diffraction pattern meaning that each layer has its own distinct helicity. The *v/u* ratios were calculated to be 0.054, 0.3226, 0.6579, 0.6986, and 0.9387, respectively. For the two layers with the smallest helicities, the intensity profile on the first principal layer line L1 was fitted by the appropriate order of Bessel function to determine their chiral indices (the order of Bessel functions were selected from the list containing possible choices of indices that satisfy the measured *v/u* ratios and diameters from the image). From the fitting of the

intensity, the chiral index v was determined to be $v = 2$ and $v = 8$ for first two smallest helicities. Thus, the chiral indices of these two layers were (37, 2) and (25, 8) by using the determined orders and the measured chiral index ratios. These indices give (2.335 nm, 13.44^o) and (2.979 nm, 2.61^o) for the diameters and helicities. The intensity fitting could not be done for the other layer lines due to very low signal-to-noise ratios. Instead, the graphitic inter-layer distance was used together with the measured *v/u* ratios to determine the indices of the three remaining layers. This was combined with fitting the intensity profile of the equatorial layer line to verify the final index assignment. Figure 4.2.4 shows the experimental intensity profile of the equatorial layer line and the simulated intensity obtained using the diameters from the chiral index assignment. The curves show that the agreement is quite good. So, the chiral indices of other three layer lines are (28, 26), (38, 26) and (44, 29), which give us (3.663, 28.78^o), (4.365, 23.82^o) and (4.985, 23.23^o) for diameters and helicities. The innermost three layers are semiconducting and the outermost two are metallic. The calculated inter-layer distances are 0.322 nm, 0.342 nm, 0.351 nm, and 0.31 nm.

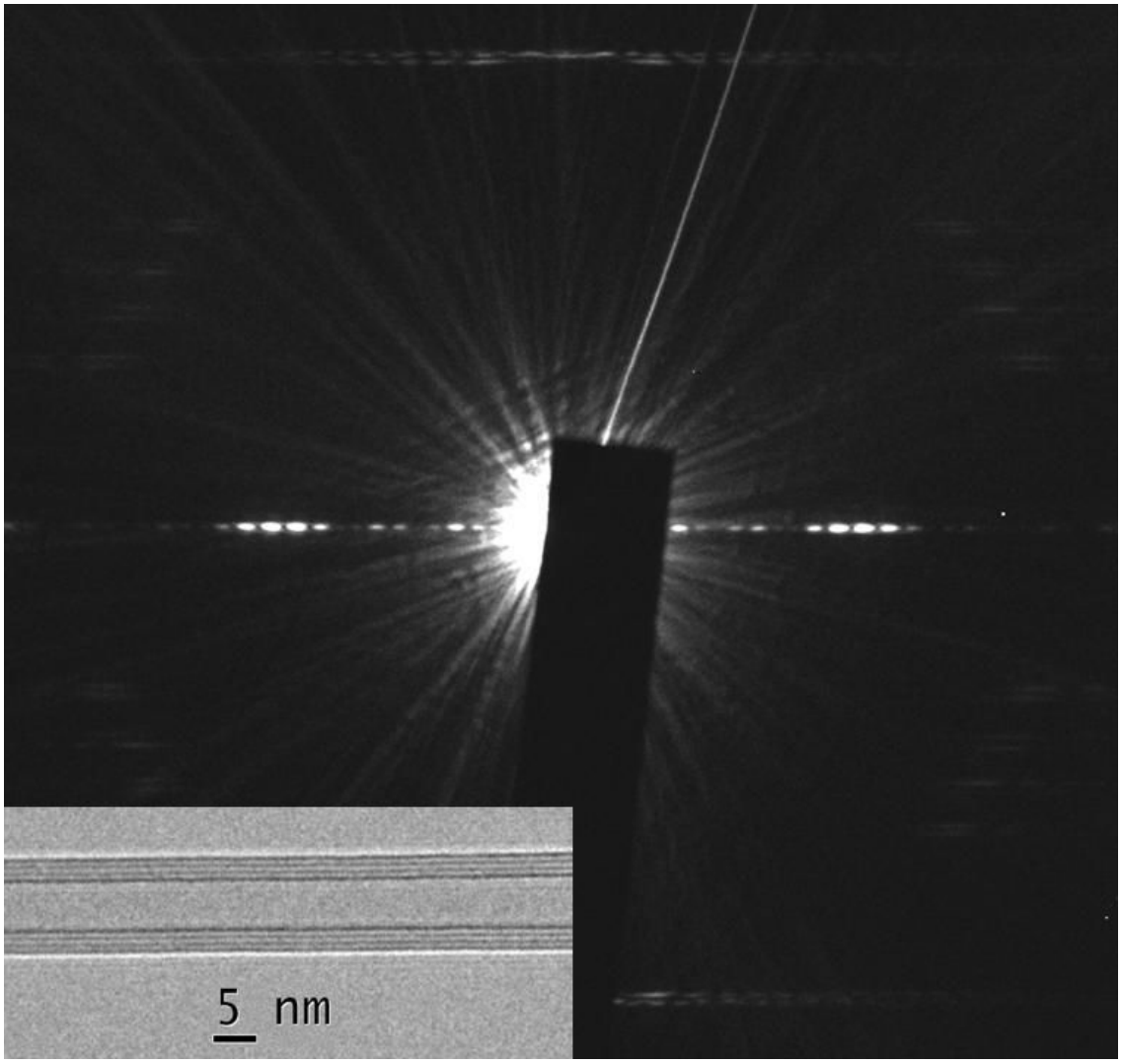

Fig. 4.2.2 Experimental electron diffraction pattern of a quadruple-walled carbon nanotube taken at 120 kV accelerating voltage with nano-beam diffraction. The inset shows the HRTEM image of the same nanotube.

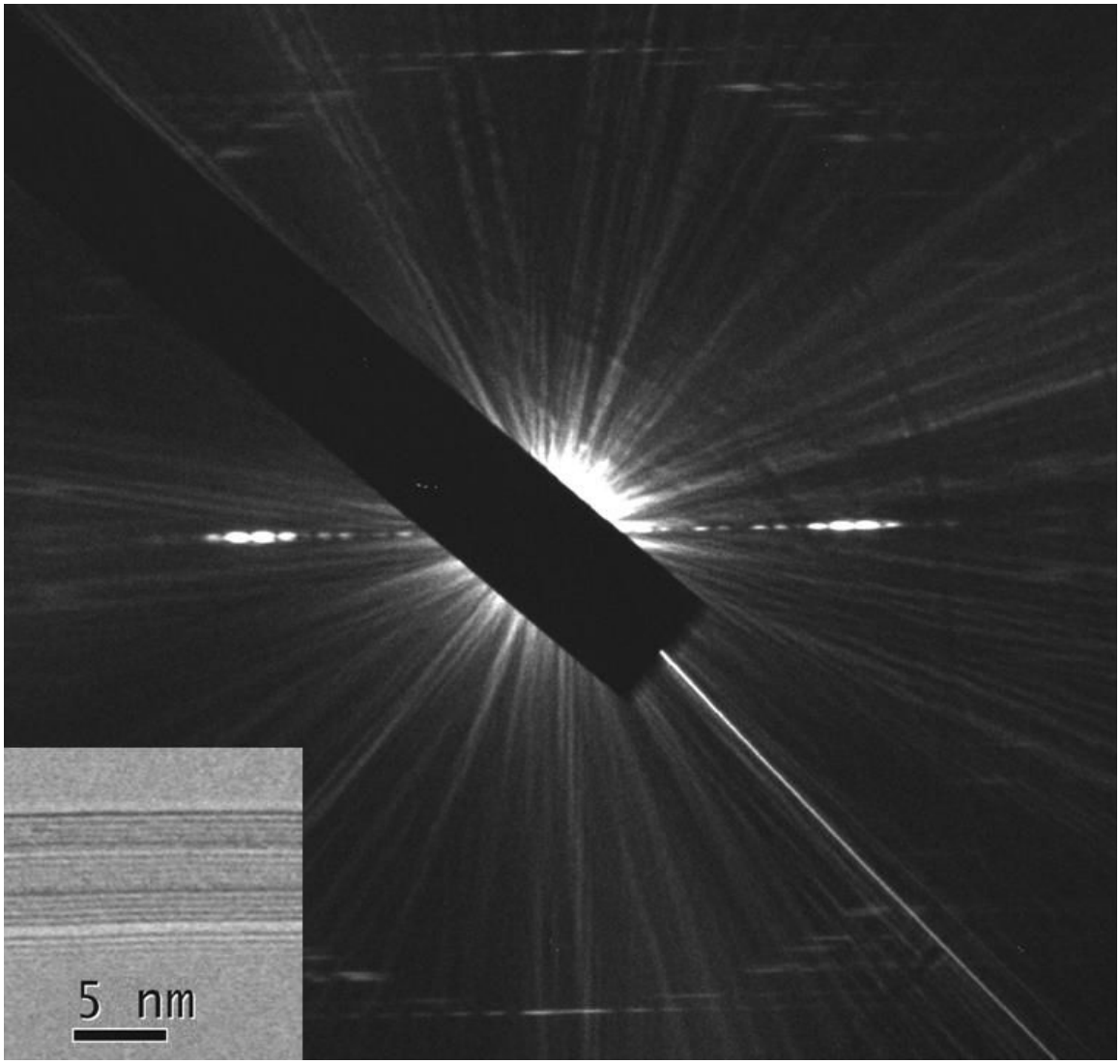

Fig. 4.2.3 Experimental electron diffraction pattern of a five-walled carbon nanotube taken at 120 kV accelerating voltage with nano-beam diffraction. The inset shows the HRTEM image of the same nanotube.

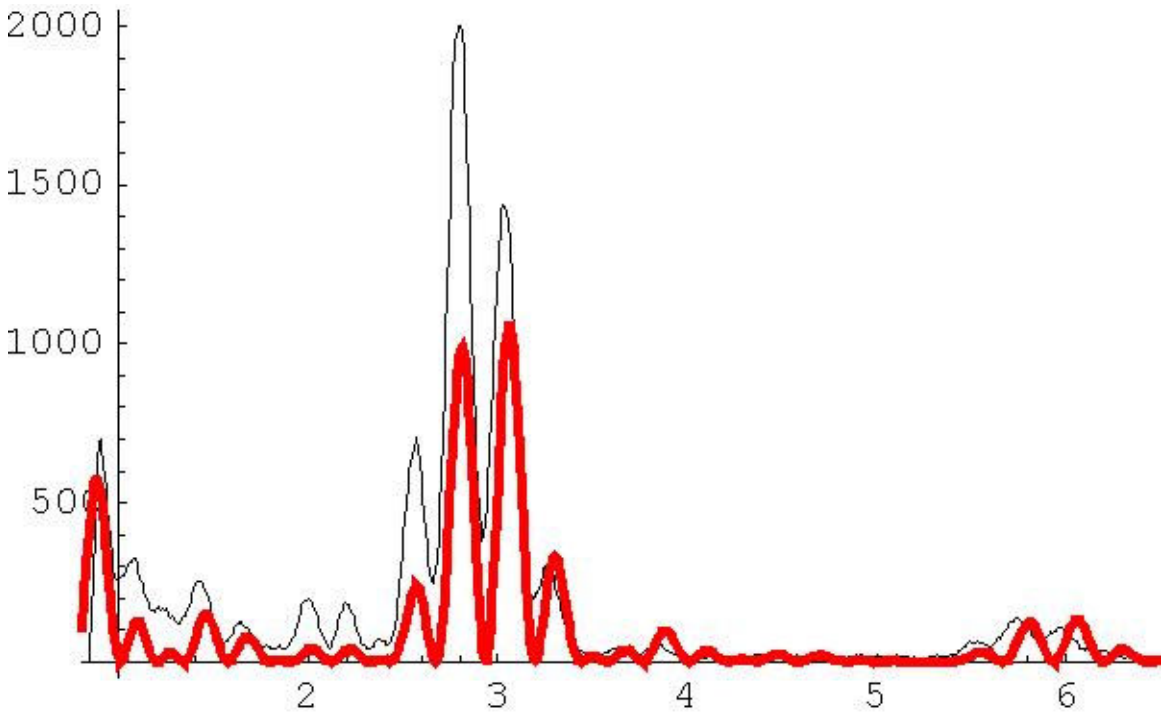

Fig. 4.2.4 The black curve is the experimental intensity of the equatorial line from the diffraction pattern of the five-walled carbon nanotube shown in inset of Fig. 4.2.3 and the colored curve is the simulated intensity for the same nanotube with the chiral index assignment listed in the text as an example 3. The horizontal axis is in the reciprocal of nm.

Example 4

Figure 4.2.5 shows an electron diffraction pattern of another quintuple-walled carbon nanotube. There were 10 layer lines measured from this experimental diffraction pattern. If all walls were chiral tubes with different helicities, there would have been 15 layer lines in the diffraction image. Having 10 layer lines means that either some layer lines overlap with one another or some helicities are repeated more than once. Table 4.2.1 shows the measured layer line spacings in arbitrary units. These layer lines are grouped into four categories for four different helicities that can be possibly constructed out of the observed layer lines. The L3 line is the same for group A and group C and the L1 line is the same for group A and group B. Here in the table, the listed errors result from the errors in the equation $D_1 = D_2 + D_3$ and can be propagated to calculate the errors in the ratio of chiral indices *v/u*. Usually the symmetry of the diffraction patterns of the nanotubes can be used to determine which helicity repeats itself, but unfortunately here the overlap of layer lines with different helicities makes the use of such a procedure harder [21]. Table 4.2.2 lists the measured diameter of each wall from the TEM images, the inter-wall spacings and the experimental *v/u* ratios. Note that the diameter on each row does not correspond to the measured *v/u* ratio on the same row. The inter-wall spacings found from the measured diameters are very uniform and this can also be seen in the HRTEM image of the tube. Once the diameters and the v/u ratios are known, the possible chiral indices satisfying the measured ratios within the experimental error can be selected and the ones that give the measured diameters within the constraints of the inter-wall distances can be tabulated. The error in *v/u* ratios was calculated by using the simple

error propagation and the errors in layer line spacings from Table 4.2.1. The equation for the error of *v/u* ratio that was found from the equation $(2D_2 - D_1)/(2D_1 - D_2)$ is

$$U_{v/u} = \frac{3\sqrt{D_1^{\,2} + D_2^{\,2}}\,U_D}{(2D_1 - D_2)^2} \tag{4.2.1}$$

In equation (4.2.1), D_1 and D_2 are the first two layer line spacings measured, and U_D is the error in the measured layer line spacings and defined as $D_1 - (D_2 + D_3)$. Table 4.2.3 represents such a selection of indices for each measured helicity. Table 4.2.4 shows for each measured shell diameter the possible chiral indices matching from Table 4.2.3 and each column is a possible assignment of indices for the whole nanotube. The diameters calculated for each set of possible indices are given next to them in Table 4.2.4. When all possible choices of indices were determined, it was considered that one helicity should repeat itself. Among all choices of chiral indices, only four assignments listed in Table 4.2.4 give the best matches for the diameters, inter-wall distances and the chiral angles within the estimated uncertainties. Again, the experimental intensity of the equatorial layer line was fitted using the four probable assignments. The chiral index assignment in column IV has the closest agreement out of all simulated curves with the experimental one (Fig. 4.2.6) in terms of the peak positions and the inter-wall distances. So, the chiral indices of each shell in this five-walled carbon nanotube are (55, 11), (46, 10), (41, 4), (21, 19) and (23, 5) ranked from larger to smaller diameter. The percent errors between the assigned helicities and experimental ones are 0.4%, 4.0%, 1.8%, 0.4% and 4.0% following the order of indices above, and these errors are in good agreement with the experimental errors listed in Table 4.2.1 within two standard deviations. Assignment III from Table 4.2.4 is simulated and plotted together with the experimental intensity (see

Fig. 4.2.7). The arrows in the figure point to the differences between the simulated and experimental curves. It shows that changing the index assignment of two shells leads to a few differences in the simulated intensity which are large enough to distinguish two curves apart from each other. Especially the (200) and (400) spots and intensity modulations within do not have a good agreement with the simulation in terms of peak positions and shapes.

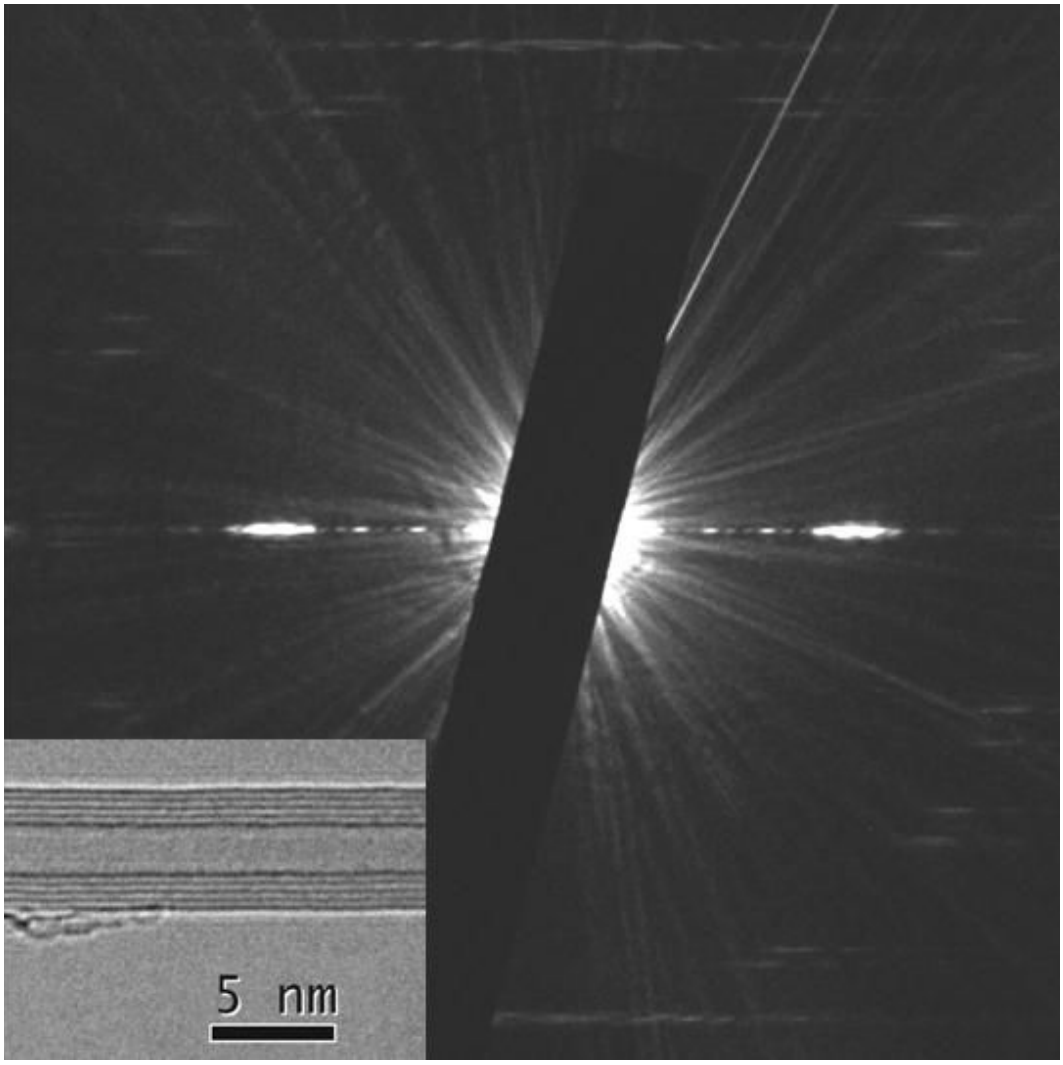

Fig. 4.2.5 Experimental electron diffraction pattern of a five-walled carbon nanotube taken at 120 kV accelerating voltage with nano-beam diffraction. The inset shows the HRTEM image of the same nanotube.

Table 4.2.1 Experimentally measured layer lines and *v/u* ratios.

Group	D1	D2	D3	U_D	*v/u*-exp	%error in *v/u*
A	1282.4	823.2	463.1	-3.9	0.2090	2.8
B	1282.4	729.2	554.2	-1	0.0959	1.4
C	1266.4	805.2	463.1	-1.9	0.1991	1.4
D	1131.8	1093.3	38	0.5	0.9013	0.2

Table 4.2.2 Diameter of each wall measured from HRTEM image.

d (nm)	inter-wall d (nm)	*v/u*-exp
4.82	0.340	0.2090
4.14	0.340	0.0959
3.46	0.356	0.1991
2.75	0.356	0.9013
2.04		

Table 4.2.3 Experimental *v/u* ratios and corresponding possible choices of chiral indices.

v/u-exp	list of possible indices						
0.2090	(24,5)	(48,10)	(47,10)	(23,5)	(44,9)	(46,10)	
0.0959	(21,2)	(42,4)	(31,3)	(41,4)			
0.1991	(55,11)	(35,7)	(50,10)	(30,6)	(40,8)	(25,5)	(56,11)
0.9013	(20,18)	(32,29)	(21,19)				

Table 4.2.4 Four possible chiral index assignments for the whole nanotube.

d (nm)	I	II	III	IV
	4.80	4.80	4.87	4.80
4.82	(55,11)	(55,11)	(56,11)	(55,11)
	4.14	4.20	4.21	4.05
4.14	(32,29)	(51,5)	(48,10)	(46,10)
	3.38	3.49	3.46	3.38
3.46	(41,4)	(40,8)	(42,4)	(41,4)
	2.62	2.71	2.71	2.71
2.75	(30,6)	(21,19)	(21,19)	(21,19)
	2.02	2.02	2.10	2.02
2.04	(23,5)	(23,5)	(24,5)	(23,5)

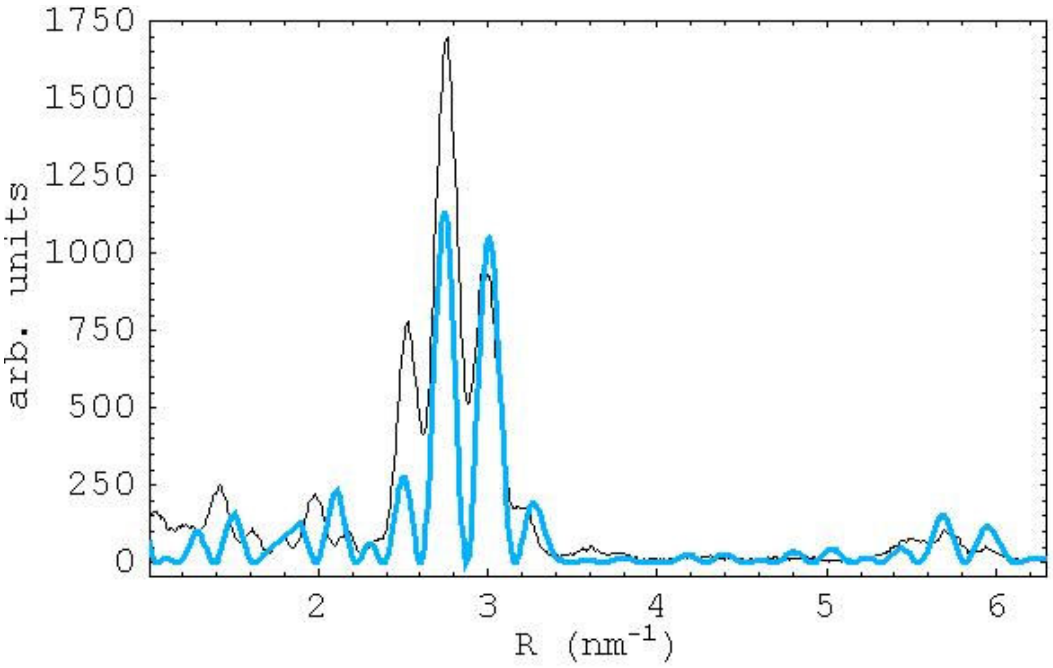

Fig. 4.2.6 The black curve is the experimental intensity of the equatorial line from the diffraction pattern of the five-walled carbon nanotube and the colored curve is the simulated intensity for a nanotube with the chiral index assignments listed as in column IV in the Table 4.2.4.

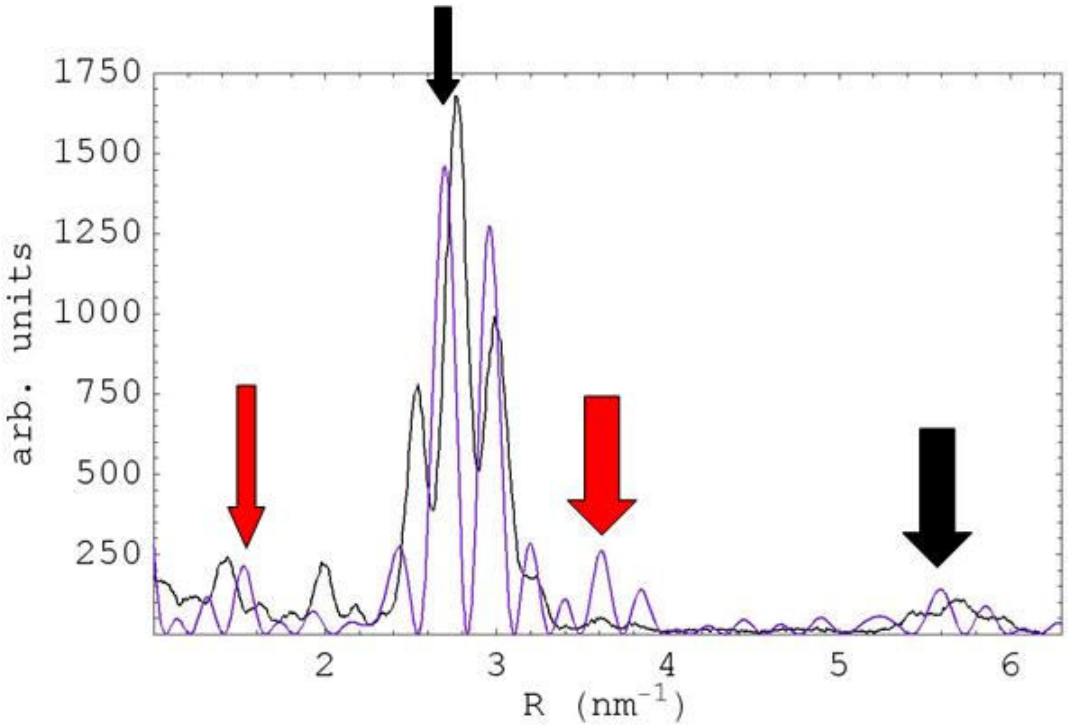

Fig. 4.2.7 The black curve is the experimental intensity of the equatorial line from the diffraction pattern of the five-walled carbon nanotube and the colored curve is the simulated intensity for a nanotube with the chiral index assignments listed as in column III in the Table 4.2.4. Arrows show the peaks that do not match well with each other in terms of intensity and position. Black arrows mark the (200) and (400) diffraction spots of graphite.

4.3 Characterization of MWNTs

4.3.1 Introduction

The techniques presented in the last two sections for the structure determination can be extended to multi-walled nanotubes by reiterating them with a few minor additional steps. Since the zigzag and the armchair nanotubes represent two extreme circumstances, it's worthy analyzing them more closely. Figures 4.3.1 (a) and (b) show the simulated diffraction patterns of (15, 0) zigzag and (9, 9) armchair single-walled carbon nanotubes. The square frame in the diffraction pattern has a length 4.4/a where a is the in-plane lattice parameter of graphite ($a = 0.246$ nm). In the diffraction pattern of a zigzag nanotube, the layer lines L2 and L3 coincide with each other whereas the layer lines L1 and L2 are coincident for an armchair nanotube and the layer line L3 falls on the equatorial line. The numbers given next to each layer line show the position of the line along the tubule axis in the reciprocal space in multiples of the lattice parameter with respect to the equatorial line. For a zigzag nanotube, the layer line L1 lies the farthest away from the equator which is consistent with the orientation of hexagons in the reciprocal space seen in the simulated pattern. For an armchair nanotube, the case is the exact opposite of the zigzag tube and the line L1 lies closest to the equator. For all other chiral tubes, the chiral angles lie between the zigzag (0^o) and the armchair (30^o) margins meaning that the layer line L1 will have a position in a range from $1/a$ to $2/(\sqrt{3}a)$ (we'll omit the factor of $1/a$ from now on since each line is scaled by the same number). Therefore, we can identify three zones in which all 3 principal layer lines will fall for nanotubes of all helicities. These zones can be called the L1, L2 and L3 zones. For a chiral nanotube, the L1 line might take the values from 1.0 to 1.154, the L2 be from 0.577

to 1.0 and from 0 to 0.577 for the L3 line. For a zigzag nanotube, the L1 is 1.154, L2 is 0.577, and the L1 is 1.0 for an armchair structure. For a (20, 14) chiral tube (Fig. 3.3.6), the L1, L2 and L3 are located at 1.053, 0.936 and 0.117, respectively and these values fall in their respective zones.

This can be understood if we consider the lattice structure of graphene and its diffraction pattern. Figure 4.3.2 shows the graphene lattice structure and its diffraction pattern in the reciprocal space. The primitive lattice vectors in the real space are $\vec{a}_1$ and $\vec{a}_2$ with an inter-angle of 60°, which start and terminate at carbon atoms. In the reciprocal space, the basis vectors that define the diffraction spots are

$$\vec{a}_1^{\,*} = \frac{2}{3a^2}(2\vec{a}_1 - \vec{a}_2)$$

$$\vec{a}_2^{\,*} = \frac{2}{3a^2}(-\vec{a}_1 + 2\vec{a}_2)\,. \qquad (4.3.1)$$

The strongest-intensity peaks of the single-walled carbon nanotubes are formed by the primary graphene reflections. The three principal layer lines labeled as L1, L2 and L3 result from the graphene reflections of (010), $(\bar{1}00)$ and (110) respectively, which are degenerate at 60 degrees. In the reciprocal space of graphene, the vertical projections of these reflections have a length of $2/(\sqrt{3}a)$, $1/a$, and $1/(\sqrt{3}a)$ with respect to the horizontal axis. So, the layer lines L1 and L2 of a zigzag tube are formed by the (010) and $(\bar{1}00)$ reflections and the layer line L1 of an armchair tube is formed by the (110) reflection. Any diffraction line of a nanotube is formed by these graphene reflections rotated at an angle corresponding to the helical angle of the tube and lies in the zones defined by the primary reflections of graphene.

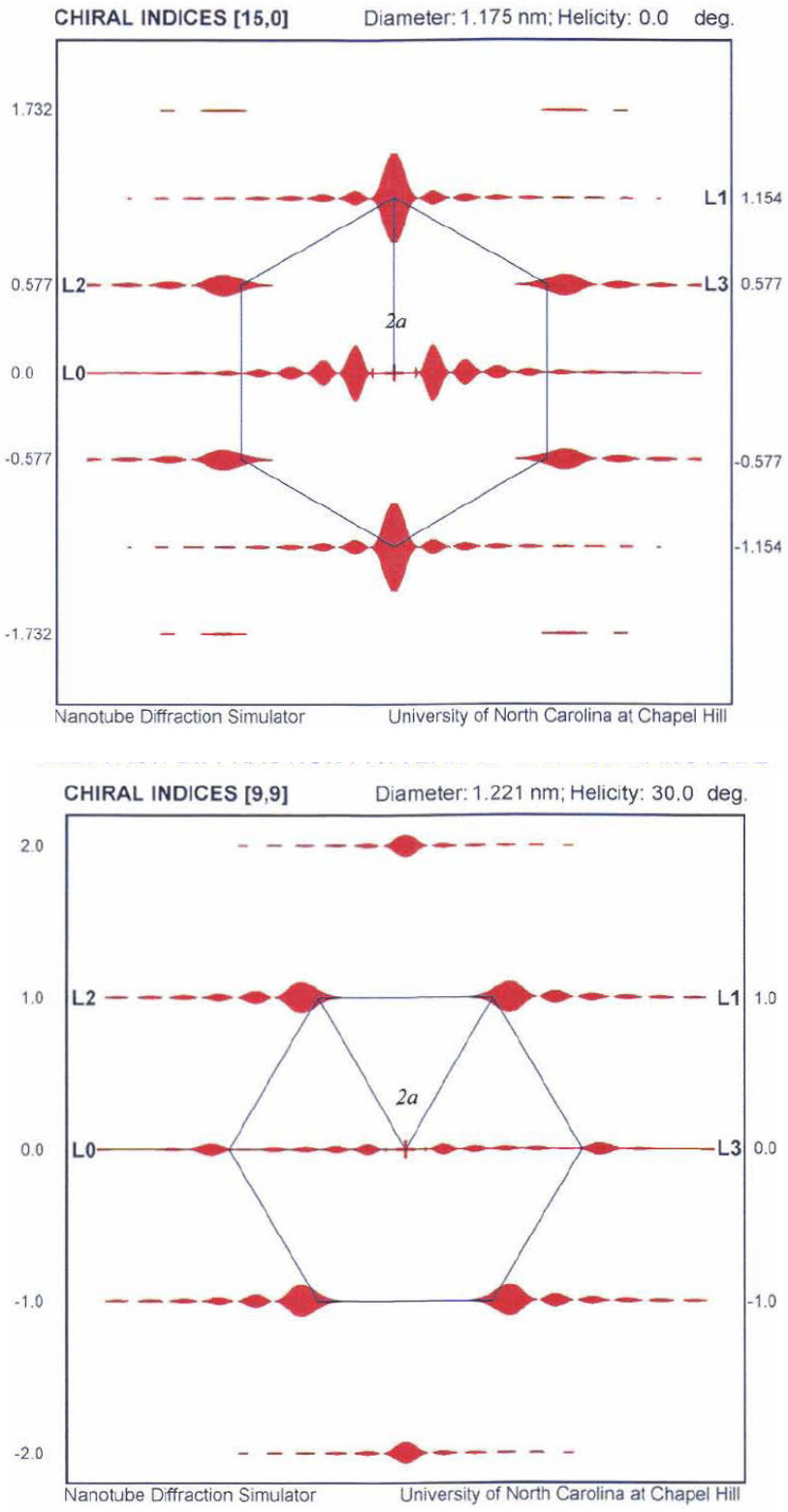

Fig. 4.3.1 (a) Simulated electron diffraction patterns of (15, 0) and (b) (9, 9) carbon nanotubes respectively.

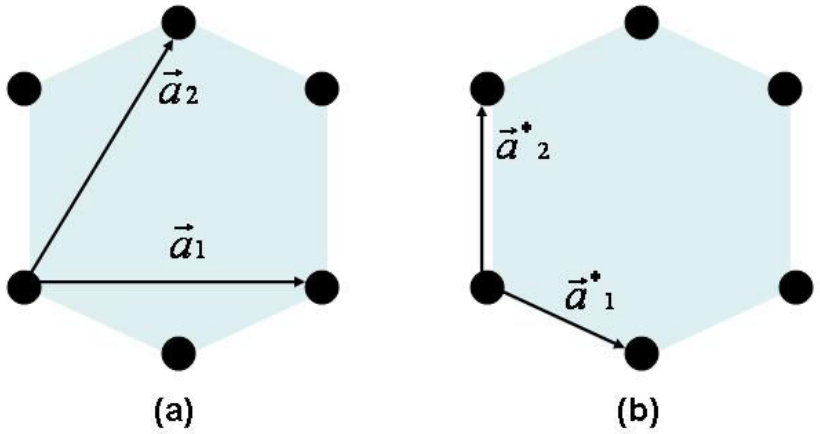

Fig. 4.3.2 (a) Graphene lattice points with basic lattice vectors in real space (b) Graphene structure in reciprocal space with reciprocal basic lattice vectors.

Then the simple ratio of layer line spacings for index determination can be understood in terms of the layer line positions. Since L1 varies between 1.0 and 1.154 and L2 varies between 0.577 and 1, the simple ratio of D1/D2 will vary between 1.0 and 2.0. This can be given in terms of the chiral indices by equation 4.1.2.

A more accurate measurement will be measuring the higher order reflections like the L4 layer line which is formed by the $(\bar{1}10)$ graphene reflections. This line varies between 1.732 to 2.0 from a zigzag to an armchair structure. Then the ratio of D_4 / D_1 will vary between 1.5 and 2.0. This might cause a problem since a better differential precision of numbers will be needed to differentiate between two chiral index ratios although the measurement error might be small with the use of longer distances in diffraction pattern (For example, the *v/u* ratios of 0.7692 and 0.7714 versus the D_4 / D_1

ratios of 1.9167 and 1.9175 to distinguish between (39, 30) and (35, 27), respectively). Instead, the ratio of D_4 / D_2 can be used since this will change between 2.0 and 3.0 and can be expressed as

$$\frac{D_4}{D_2} = \frac{3(u+v)}{(u+2v)}. \tag{4.3.2}$$

For a multi-walled carbon nanotube of N walls, we expect to see 3N layer lines if the helicity from each wall is unique. This means that there will be N layer lines in each zone containing L1, L2 and L3 reflections. If one helicity was repeated, there will be 3N-3 layer lines in total and N-1 layer lines in each zone. For shells with close helicities, some layer lines might appear overlapped in the electron diffraction patterns due to experimental limitations and this will make the number of layer lines uneven in each zone. In this case, $D_1 = D_2 + D_3$ can be used as a complementary to group the layer lines into their respective helicities.

The procedure for the structure determination of multi-walled carbon nanotubes from diffraction patterns is:

1. Measure three principal layer lines accurately from electron diffraction patterns and include the higher order layer lines in the measurement if they are clearly visible.
2. Acquire a high resolution TEM image of the nanotube to estimate the number of walls and their diameters.
3. If the number of layer lines is three times the number of the walls, each wall has a different helicity and each zone in the diffraction pattern has the same number of layer lines. This means that the first N layer line spacings are in the

first zone, the second N are in the second zone and so on starting from higher spacings to lower spacings.

4. In case one or more helicities are repeated, the number of layer lines won't be equal to three times the number of walls. Step 3 still holds and there is still same number of layer lines in each zone.
5. The last two rules are based on the assumption that there is no zigzag or armchair structure in the nanotubes forming the MWNT. These two structures can be identified out of the all layer lines because the intensity of the L1 layer line is governed by a Bessel function of order zero for a zigzag nanotube and this will be seen as a strong diffraction spot in the first line. The same is true and applicable for the intensity of the L4 layer line of an armchair tube.
6. When the zigzag or the armchair structures or the overlapping of the layer lines complicate the identification of the zones for each layer line, equation $D_1 = D_2 + D_3$ should be used as a complement to identify each helicity present in the diffraction pattern by keeping in mind that a layer line can not belong to two different zones. As the *v/u* ratio (helicity) increases, the L1 layer line approaches the L2 line and the L3 line moves toward the equatorial layer line. If any proposed helicity contradicts this, it should be discarded.
7. Once all helicities are classified, the ratio of chiral indices (v/u) are calculated using equation (4.1.1). The ratio of D_4 / D_1 or equation (4.1.4) can be used as a complement if possible to help assign the chiral indices.
8. Find all possible chiral indices satisfying the measured ratios within the experimental uncertainties and the measured diameters.

9. In some cases, it's possible to find that there are chiral indices for each measured diameter and helicity within experimental error. This means that for a seven-walled tube with seven distinct helicities, for example, there will be 49 possible chiral indices. If possible, use the intensity on the layer lines and Bessel functions to pinpoint the certain chiral index value. For example if $v/u = 0.3$ and $v = 12$ found from Bessel function fit of the intensity, it means that the chiral indices are (40, 12).
10. Use the inter-wall distance as a constraint and start with the assignment of the tubes of smaller diameters since there are fewer possibilities for the chiral indices of smaller nanotubes. If some helicities are repeated in the structure, this limits the choice of the chiral indices to the integer multiple of the smallest ones for the repeating helicity. Pick ones that match the measured diameters or use Bessel functions to fit the intensity on that particular layer line if there is a breaking of the symmetry in intensities with respect to the tubule axis [13].
11. Check the index assignment by comparing the simulated intensity of the equatorial layer line with the experimental intensity to improve accuracy. Repeat this until the simulated intensity matches the experimental one for each possible index assignment.

All this assignment procedure is solely based on the *v/u* ratios and the measured diameters. The layer line intensities other than the equatorial line can be fitted to aid the indexing. However, the tilt of the tube with respect to the incident electron beam, overlapping layer lines and the closer peak positions of high order Bessel functions need to be corrected or calibrated.

4.3.2 Application of Indexing Method

Example 1

Figure 4.3.3 is a high resolution image of a twelve-walled nanotube taken at 120 kV and Fig. 4.3.4 is the line intensity profile of the same nanotube used to determine the number of walls and the diameter of each wall. The minima in the line intensity profile coincide with the darker contrast lines seen in the high-resolution image and they correspond to the projected structure of the side-walls of the nanotube. Figure 4.3.5 shows an electron diffraction pattern taken from this tube. There are only 23 layer lines visible on the diffraction image for this 12-walled carbon nanotube. Figure 4.3.6 shows magnified views of the frames within which the layer lines were used to determine the total number of helicities present in the diffraction pattern. Table 4.3.1 shows all 23 layer line spacings measured in arbitrary units and their classifications to the groups of helicities in addition to the ratio of chiral indices and its percent error for each measured helicity. As we can see, the first layer line is composed of contributions from 5 layer lines that belong to 5 different helicities.

It's seen from the table that there are nine helicities experimentally observed for the 12 walls of the nanotube. The five helicities labeled from A to E are near-zigzag structures with chiral angles close to one another. The other remaining five, labeled from F to J, are near armchair structures. There was neither a zigzag nor armchair tube among the observed helicities. Table 4.3.2 lists all possible chiral indices that give diameters that are close to the measured ones from the image, within the experimental error of v/u ratio calculated in previous table.

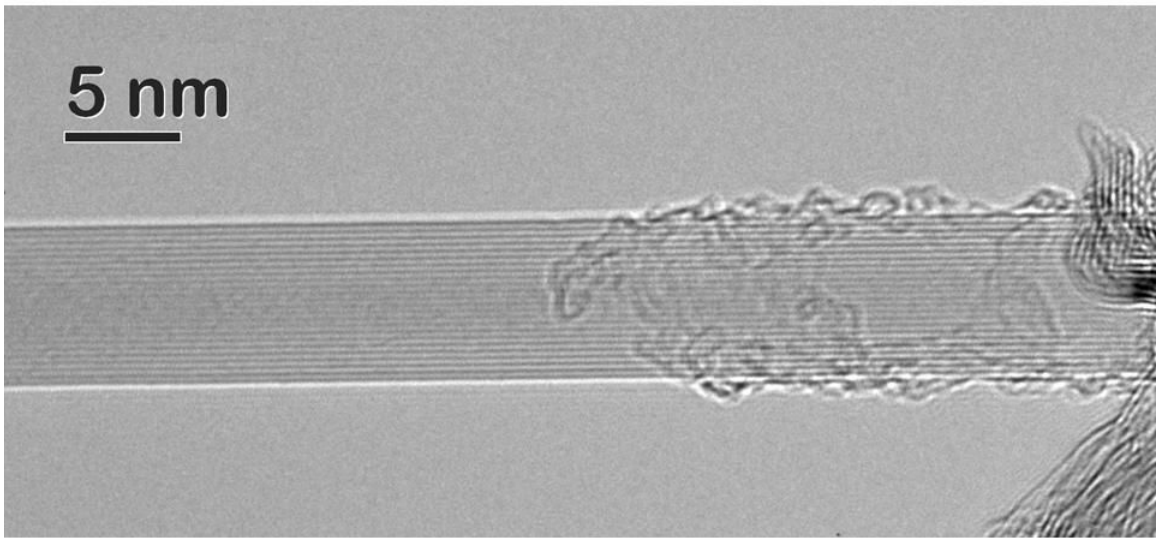

Fig. 4.3.3 High resolution TEM image of 12-walled carbon nanotube.

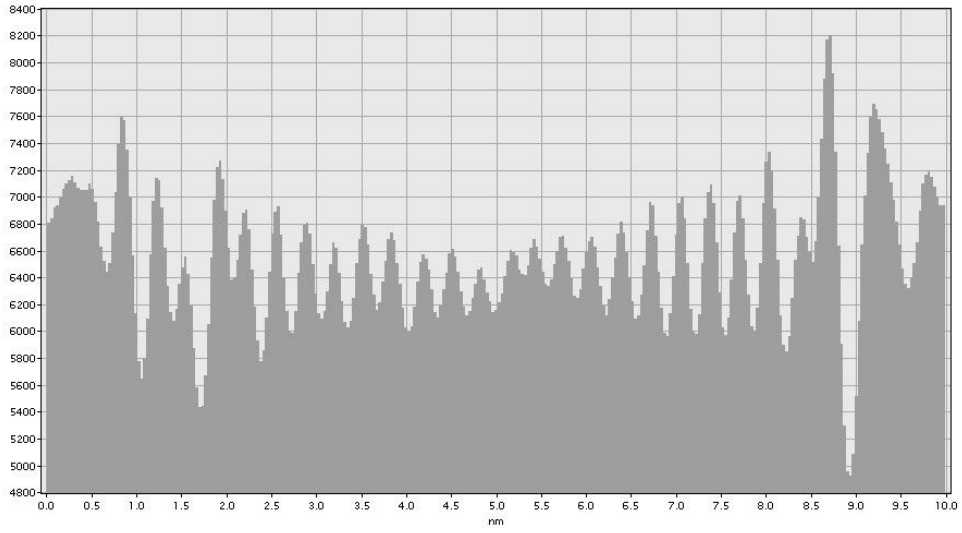

Fig. 4.3.4 Line intensity profile of the MWNT shown in the Fig. 4.3.4. The unit of the horizontal axis is nanometers.

The diameter of each wall was measured along the length of the tube over three different places and they are shown in Table 4.3.3. The table shows that the diameters of the walls are very close to each other for each measurement. The symmetry of the layer lines with respect to the tubule axis is a powerful tool to determine which helicities are repeated in the diffraction pattern [21]. It was determined that group E and group H helicities are repeated twice. This result gives the helicities of the total 11 walls. The last wall is the innermost walls seen in the TEM image of the nanotube. None of the experimentally observed helicities match the theoretical helicity of all possible tubules whose diameter varies from 0.3 nm to 0.8 nm. The helicity that comes being closest to one of the possible smallest nanotubes is group A with a *v/u* ratio of 0.1704 and the possible small tube is (6, 1) nanotube with a diameter of 0.513 nm and the *v/u* ratio of 0.1666. In this case the error between the measured and the calculated *v/u* ratios is bigger than the experimental error bounds. The intensity profile on the second layer line of group A shows that the intensity is governed by Bessel functions of high order and the diameter is rather large since the oscillations in Bessel functions have smaller widths. One of the possible chiral indices for group A from Table 4.3.2 was used to fit the intensity on this layer line. The structure factor on this layer line is given by

$$F(R,\Phi,l_2) = f\chi u J_u(\pi d\sqrt{R^2 + (l\tan\beta/c)^2}) \times \exp[in(\Phi + \pi/2)] \qquad (4.3.3)$$

where β is the tilt angle of the tube relative to the incident electron beam and χ is a constant [22]. The square modulus of equation 4.3.3 was used to fit the observed intensity and the best agreement is obtained for a (64, 11) tube. For a (64, 11) tubule, $l_2 = (u + 2v)/M$ =86 and c=29.89 nm^{-1}. The tilt angle β that gave the best fit was 9^o.

The intensities of the first layer line for group F and group G were also used to determine their chiral indices since there is no overlapping with any other layer line and the order of the Bessel function for the best choices is in the range of 20-30. The assignment of (37, 23) and of (30, 21) gives the best fits to the observed intensity curves for group F and group G, respectively, using the same tilt angle as in the previous fit of the (64, 11) tube.

The indices can be assigned starting with the tubes of smaller diameters. The best choice for the observed diameter of 0.9 nm is the (8, 7) nanotube that belongs to group H. Since this group's helicity is repeated, the next best choice is the (16, 14) nanotube for the observed diameter of 2.15 nm. For the breakdown of the symmetry, two walls of the same helicity should have chiral indices with opposite evenness and oddity [13]. Since the symmetry of the first layer line is broken for group H, the values of v should have opposite evenness/oddity. The same is true for group E and the best two choices for it are (19, 2) and (57, 6) nanotubes whose diameters are very close to the observed diameters of 1.5 nm and 4.8 nm. Once these choices are fixed, there are more possibilities for the tubes of larger diameters. The best possible index assignments are listed in table 4.3.4 with the calculated diameters given next to each set of possible indices.

For the innermost shell, there are few possibilities that can be listed if we use the graphitic c-axis spacing as a constraint together with the diameter of the second innermost wall which is 1.018 nm of the (8, 7) nanotube. The possible choices are (3, 3), (4, 3), (4, 2), (5, 2), (5, 1), (5, 0) and (6, 0): seven in total. Unfortunately, it's not possible to determine which one is correct since this is the tube with the smallest diameter also meaning that its contribution to the intensity of the equatorial line is almost negligible.

The variations in the diameter of this tube in the fit of the equatorial line have only a very small effect on the simulated intensity curve.

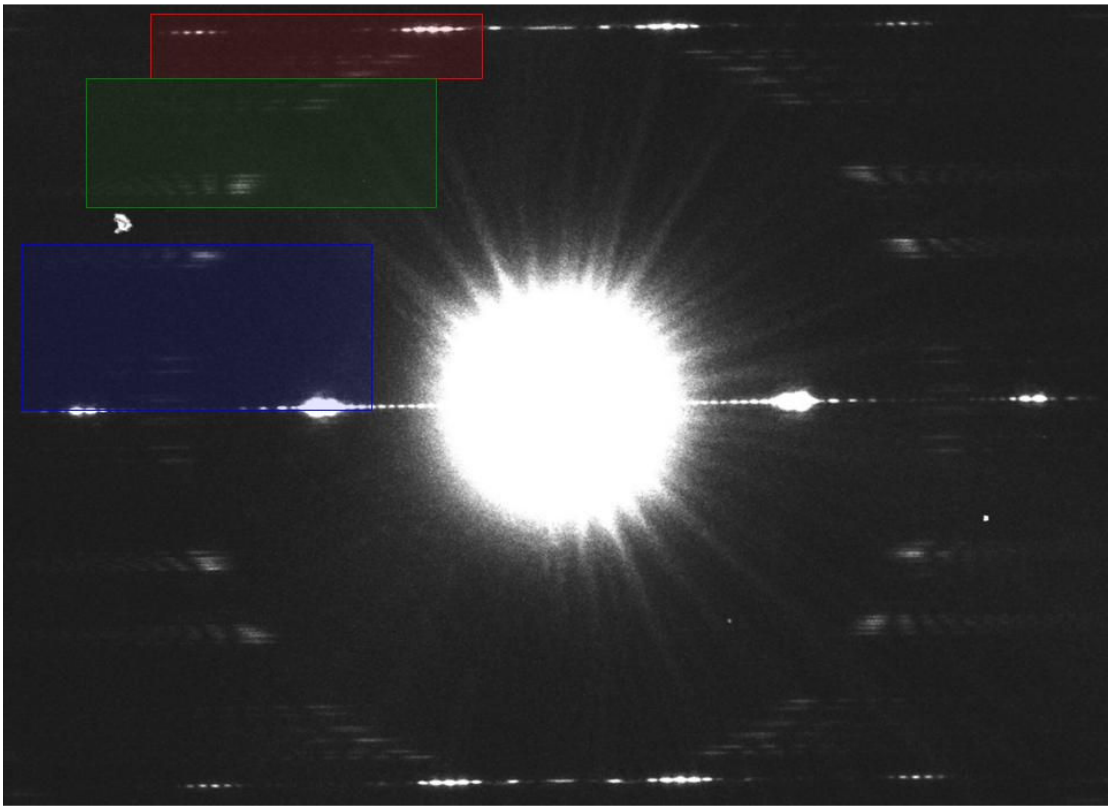

Fig. 4.3.5 Electron diffraction pattern of the 12-walled carbon nanotube shown in Fig. 4.3.4 taken with an electron nano probe at 120 kV. Red, green and blue colored regions correspond to the L1, L2 and L3 zones, respectively.

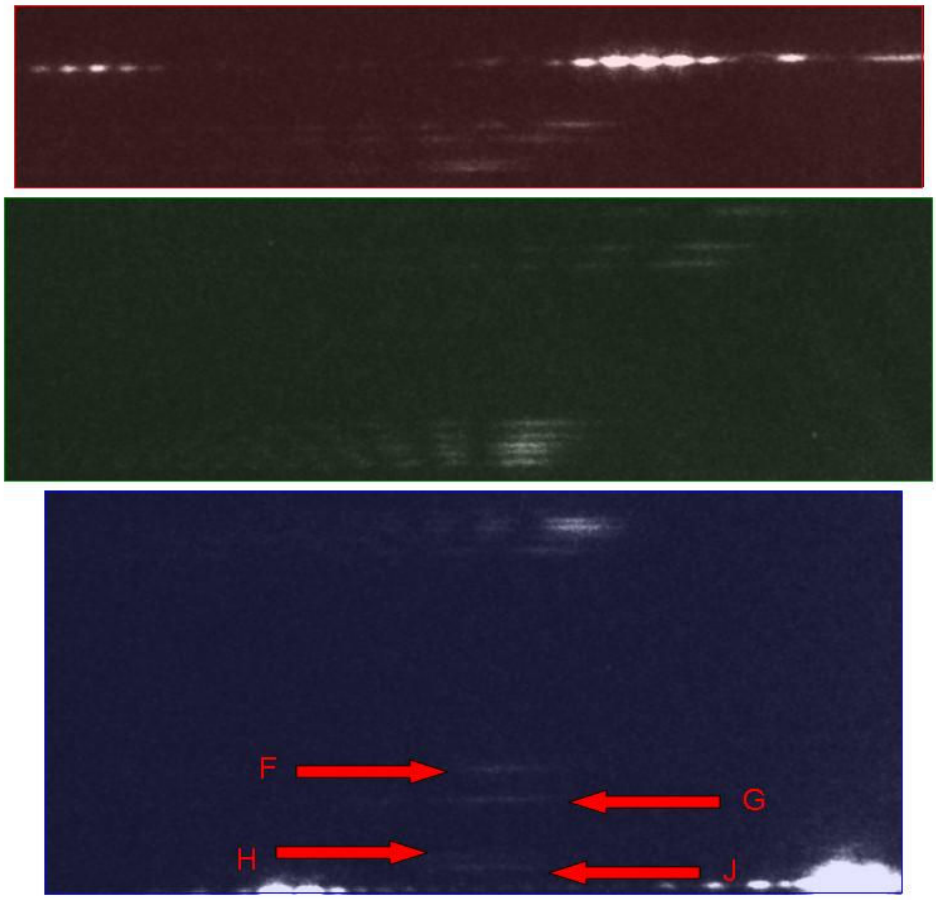

Fig. 4.3.6 Magnified view of layer lines seen in the electron diffraction pattern given in Fig. 4.3.5. The colored regions correspond to the L1, L2 and L3 zones, respectively. In the L3 zone, the arrows point to the third layer lines of group F, G, H and J reflections.

Table 4.3.1 Experimentally measured layer lines and *v/u* ratios for the 12-walled MWNT.

Group	D1	D2	D3	U_D	*v/u*-exp	%error in *v/u*
A	1403.9	867.3	534.7	-1.9	0.1704	-1.5
B	1403.9	846.3	555.7	-1.9	0.1472	-1.7
C	1403.9	833.3	567.7	-2.9	0.1330	-2.7
D	1403.9	821.3	581.7	-0.9	0.1202	-0.9
E	1403.9	806.8	595.7	-1.4	0.1048	-1.6
F	1303.9	1114.4	191.1	1.6	0.6193	0.6
G	1281.9	1141.9	141	1	0.7046	0.4
H	1241.9	1194.4	52	4.5	0.8895	1.6
J	1236.9	1200.4	33.5	-3	0.9140	-1.0

Table 4.3.2 Experimentally measured diameters and corresponding possible choices of chiral indices for each diameter from each helical arrangement.

d (nm)	Group	A	B	C	D	E	F	G	H	J
7.55		(87,15)	(89,13)	(90,12)	(91,11)		(68,42)		(60,53)	(58,53)
6.87			(81,12)	(81,11)	(83,10)		(63,39)	(58,41)	(54,48)	(54,49)
6.19		(71,12)	(74,11)	(74,10)	(75,9)	(76,8)	(55,34)	(54,38)	(47,42)	(47,43)
5.48		(64,11)		(66,9)	(66,8)	(67,7)	(50,31)	(47,33)	(43,38)	(43,39)
4.84		(58,10)		(59,8)	(58,7)	(57,6)	(45,28)	(41,29)	(37,33)	(37,34)
4.19		(47,8)	(48,7)		(50,6)	(48,5)	(37,23)	(37,26)	(33,29)	(32,29)
3.55		(41,7)	(41,6)					(31,22)	(27,24)	
2.90		(35,6)	(34,5)		(33,4)	(38,4)		(27,19)		(23,21)
2.26			(27,4)		(25,3)		(21,13)		(18,16)	
1.61						(19,2)				(12,11)
0.97								(10,7)	(9,8)	
0.36										

Table 4.3.3 Diameter of each wall measured from HRTEM image for the 12-walled MWNT.

d (nm)		
I	II	III
7.49	7.47	7.49
6.81	6.79	6.81
6.16	6.15	6.13
5.45	5.50	5.46
4.81	4.82	4.81
4.13	4.17	4.16
3.52	3.49	3.52
2.87	2.85	2.87
2.19	2.20	2.20
1.58	1.55	1.58
0.94	0.94	0.97
0.36	0.32	0.32

Table 4.3.4 Four possible chiral index assignments for the 12-walled MWNT.

d (nm)	I	II	III	IV
7.49	7.45 (88,13)	7.59 (91,11)	7.45 (88,13)	
6.81	6.81 (81,11)			
6.16	6.11 (48,42)	6.11 (48,42)	6.08 (71,12)	6.29 (76,8)
5.45	5.49 (64,11)	5.49 (64,11)	5.563 (43,39)	5.49 (64,11)
4.81	4.72 (57,6)			4.84 (58,7)
4.13	4.11 (37,23)			
3.52	3.48 (30,21)			
2.87	2.85 (22,20)	2.85 (22,20)	2.75 (33,4)	2.85 (22,20)
2.19	2.09 (25,3)	2.29 (27,4)	2.04 (16,14)	
1.58	1.57 (19,2)			
0.94	1.02 (8,7)			
0.36				

Example 2

Figure 4.3.7 shows an electron diffraction pattern of a six-walled carbon nanotube. There are twelve layer lines observed in the diffraction pattern. The first principal layer line for all six layers fall on top of one another and all other layer lines (second and third principal layer lines) are closely spaced with respect to each other. This suggests that helicities for all layers are very close to each other. The calculated *v/u* ratios from measured layer line spacings were 0.1369, 0.1437, 0.1574, 0.1772, 0.2057 and 0.2373 for all six walls. Table 4.3.5 lists all possible indices for each wall and helicity. The diameters in the first column are diameters measured from the TEM image. The inter-layer distances are very uniform for this nanotube based upon diameters measured from its image. So, the best index assignment for the whole nanotube is given in table 4.3.6, which gives the most uniform inter-layer distances. The same table also lists the calculated diameters, helicities and metallicities based upon the assigned chiral indices.

Example 3

Figure 4.3.8 shows an electron diffraction pattern of a seven-walled carbon nanotube. There are only twelve pairs of layer lines in the diffraction pattern from which four different helicities were identified. This means that there are repeating helicities in this tube. Either three helicities repeat themselves twice or possibly one helicity might appear more than twice. Keeping this in mind and using the inter-layer distance as a constraint to get uniform wall separation, the final index assignment can be determined from the list of all possible chiral indices constructed. The measured *v/u* ratios were 0.3097, 0.5539, 0.6831 and 0.9581, respectively. The assigned indices were (20, 6), (50, 15), (9, 5), (36, 20), (22, 15), (47, 32) and (24, 23). The assignments (20, 6) and (50, 15) are one

repeating helicity and the (9, 5) and (36, 20) the other. The indices (22, 15) and (47, 32) do not have the same exact helicity but they are very close to each other (23.77^{o} and 23.74^{o} respectively). The simulated electron diffraction patterns confirm that their layer lines are located at the same positions in the reciprocal space. All layers except one in this tube are semiconducting. Table 4.3.7 lists all calculated diameters, helicities, and metallicities for this carbon nanotube.

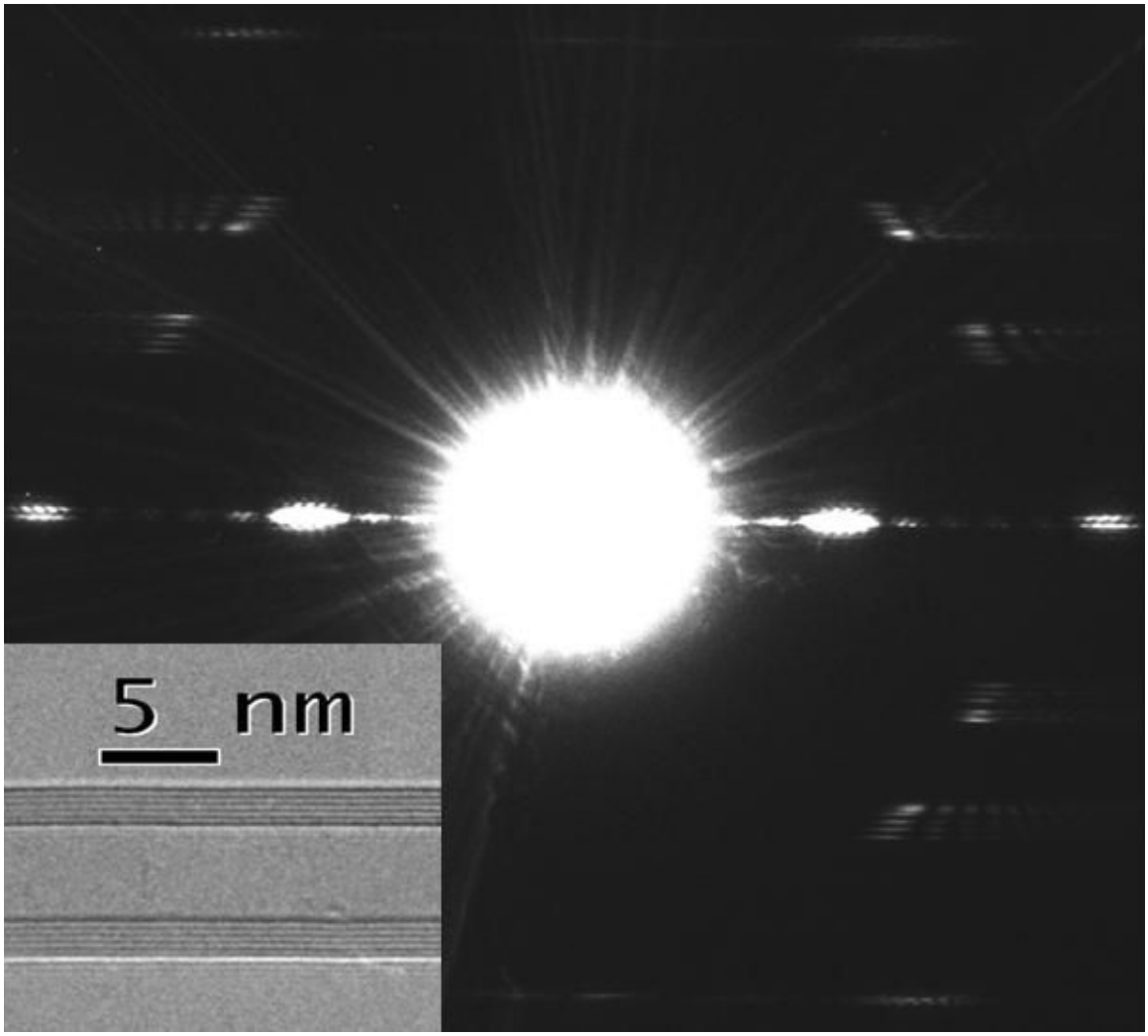

Fig. 4.3.7 Experimental electron diffraction pattern of a six-walled carbon nanotube taken at 120 kV accelerating voltage with nano-beam diffraction. The inset shows an HRTEM image of the same nanotube.

Table 4.3.5 Experimentally measured diameters and corresponding possible choices of chiral indices for each diameter from each helical arrangement.

d (nm)	v/u=0.241	v/u=0.212	v/u=0.187	v/u=0.155	v/u=0.141	v/u=0.131
8.45	(95,23)	(96,20)	(98,18)	(99,15)	(100,14)	(101,13)
7.74	(87,21)	(88,19)	(90,17)	(91,14)	(92,13)	(92,12)
7.03	(79,19)	(80,17)	(81,15)	(83,13)	(83,12)	(84,11)
6.32	(71,17)	(72,15)	(73,14)	(75,12)	(75,11)	(76,10)
5.61	(63,15)		(65,12)	(66,10)	(66,9)	(67,9)
4.90	(55,13)	(56,12)	(57,11)	(58,9)	(58,8)	(59,8)

Table 4.3.6 Final index assignment for the six-walled carbon nanotube.

u	*v*	d(nm)	α(DEG)	Type
71	17	6.331	10.49	M
56	12	4.923	9.52	S
81	15	7.004	8.35	M
66	10	5.601	6.95	S
92	13	7.763	6.52	S
101	13	8.464	5.98	S

Example 4

Figure 4.3.9 shows an electron diffraction pattern of an eight-walled carbon nanotube. There are twelve pairs of layer lines present in the diffraction pattern and four helicities identified from those layer lines. The experimentally-determined *v/u* ratios were 0.0339, 0.6066, 0.7643 and 0.8385. There are five choices for the helicities that repeat themselves in this nanotube. It was found that each helical group is repeated twice when the best chiral index assignment for the whole tube was determined. All chiral indices having same helicities next to each other are: (29, 1) and (58, 2); (15, 9) and (35, 21); (25, 19) and (50, 38); (6, 5) and (42, 35). Three walls are metallic and the rest are semiconducting. Table 4.3.8 lists all calculated parameters, such as diameter, helicity, based on the index assignment.

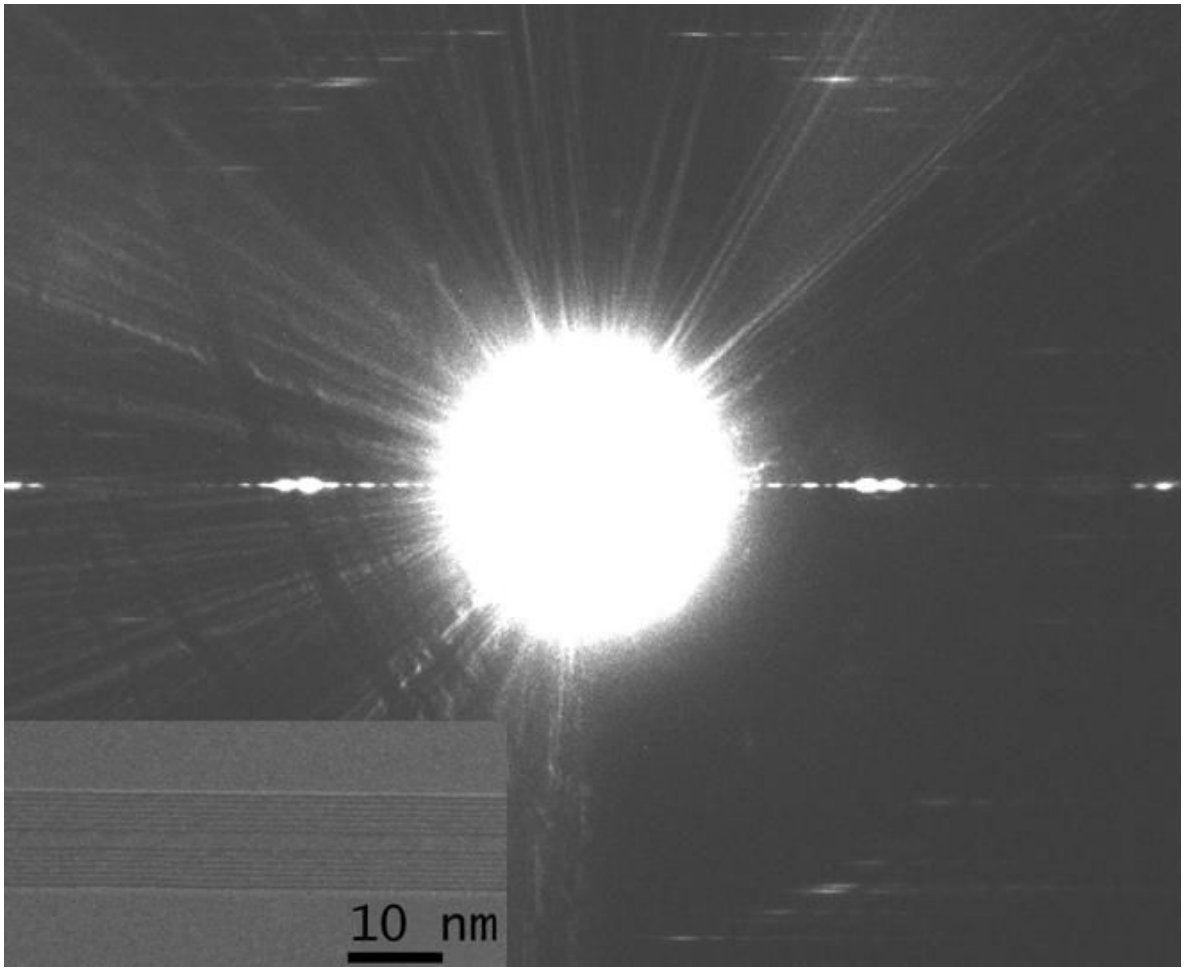

Fig. 4.3.8 Experimental electron diffraction pattern of a seven-walled carbon nanotube taken at 120 kV accelerating voltage with nano-beam diffraction. The inset shows the HRTEM image of the same nanotube.

Table 4.3.7 Final index assignment for the seven-walled carbon nanotube.

u	*v*	d(nm)	α(DEG)	Type
20	6	1.846	12.73	S
9	5	0.962	20.63	S
22	15	2.524	23.77	S
24	23	3.187	29.30	S
47	32	5.389	23.74	M
50	15	4.616	12.73	S
36	20	3.849	20.63	S

Example 5

Figure 4.3.10 shows an electron diffraction pattern of a nine-walled carbon nanotube. There are eighteen pairs of layer lines in the diffraction pattern from which nine distinct helicities were identified for this nanotube. The measured *v/u* ratios were 0.0311, 0.3455, 0.4980, 0.6271, 0.6832 and 0.7582 respectively. Again, some layers in this tube share the same helicities. The intensity profile of the second layer line, which is the first principal reflection of helicity of 0.3455, was fitted using Bessel functions to determine the chiral index *v*. It was found to be $v = 21$ which gives the chiral indices of (61, 21) for helicity corresponding to $v/u = 0.3455$. This was repeated using the intensity profile on the third layer line which is the first reflection for helicity $v/u = 0.4980$. This gives $v = 25$ for the order of Bessel function meaning that the chiral indices were (50, 25) for helicity $v/u = 0.4980$. These two helicities happen only once in this tube since their integer multiples do not match any other observed diameters from the TEM image. The assignment giving the most uniform inter-wall separation was chosen as the best index assignment for this nanotube and is given in Table 4.3.9 that lists diameters, chiral angles and metallicities.

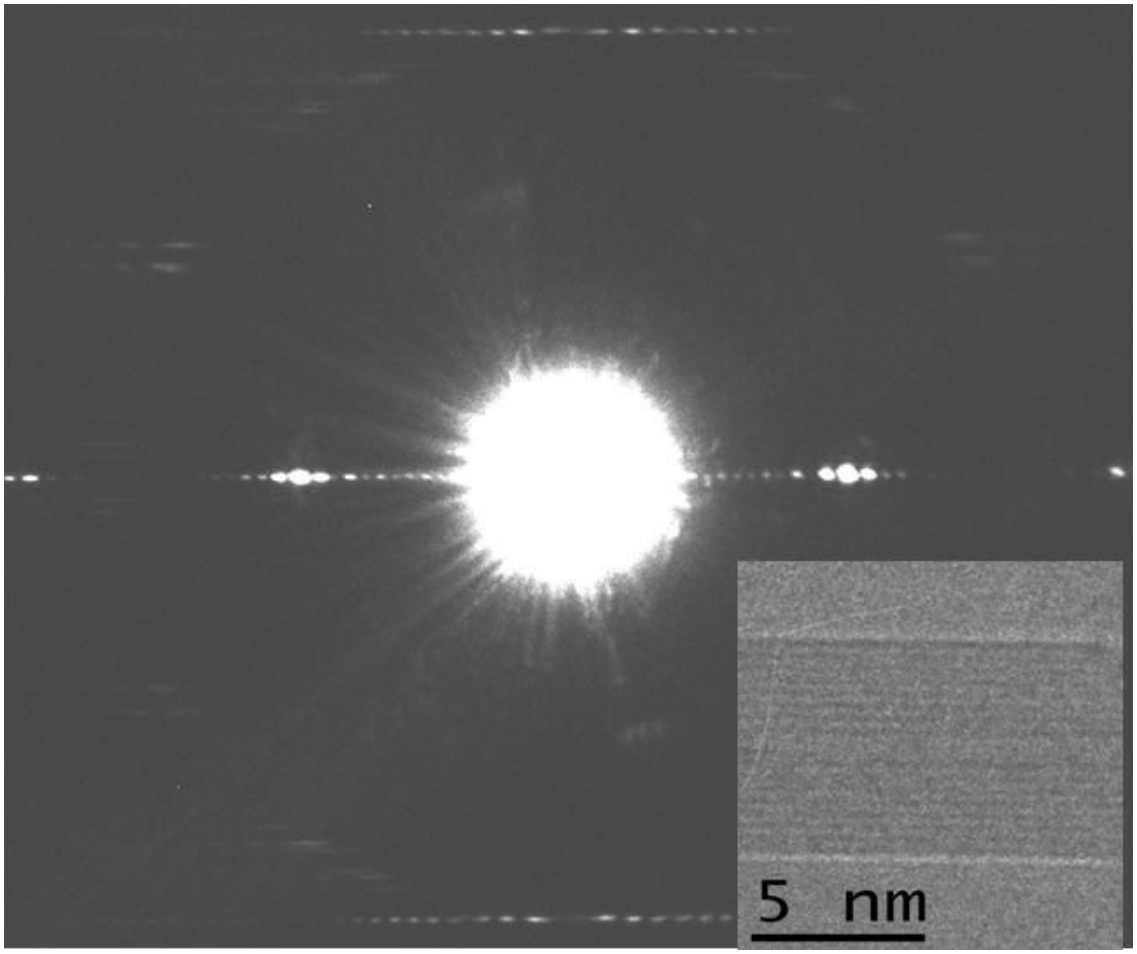

Fig. 4.3.9 Experimental electron diffraction pattern of an eight-walled carbon nanotube taken at 120 kV accelerating voltage with a nano-beam diffraction. The inset shows an HRTEM image of the same nanotube.

Table 4.3.8 Final index assignment for the eight-walled carbon nanotube.

u	*v*	d(nm)	α(DEG)	Type
29	1	2.311	1.68	S
15	9	1.644	21.79	M
25	19	2.993	25.50	M
6	5	0.747	27.00	S
58	2	4.622	1.68	S
42	35	5.229	27.00	S
50	38	5.986	25.50	M
35	21	3.837	21.79	S

Example 6

Figure 4.3.11 shows an electron diffraction pattern of a fourteen-walled carbon nanotube. This tube appears to be completely filled inside meaning that the innermost nanotube is one of the smallest nanotubes. There are twenty five pairs of layer lines in this tube's diffraction pattern from which eleven helicities were obtained. If we just rely on the equation $D_1 = D_2 + D_3$, then there would be 25 helicities which are many more than the number of walls present. In the diffraction pattern of carbon nanotubes, the zigzag tube represents the first principal layer line being farthest away from the equator and the armchair represents the one being closest to the equator. So, as the helicity of a tube increases, the L1 layer line gets closer to the equator (so does L3 line) while L2 moves away from the equator. This fact can be used to eliminate contradictory helicities. So, the remaining ones are the only possible ones and we have eleven of them in this case.

Table 4.3.10 lists the experimentally measured layer line spacings (in arbitrary units), *v/u* ratios obtained from them, errors in spacing readings ($D_1 - (D_2 + D_3)$) and the propagated percent errors in the *v/u* ratios. The chiral indices of group G, H, K and L were determined by fitting the intensity profile on their first principal layer lines. Their chiral index v was found to be $v = 13$, $v = 13$, $v = 31$ and $v = 31$, respectively, from the fitting with a common tilt angle of ~11.0°. Then, the chiral indices were calculated to be (79, 13), (71, 13), (84, 31) and (75, 31), respectively. This only leaves the choice of (29, 3) for group E out of all possible ones for it. This only gives us definite index assignments for five walls. The rest were determined by looking for close agreement with measured diameters and keeping the inter-layer distances as uniform as possible since as

indicated in the HRTEM image. Table 4.3.11 lists the final index assignment for this fourteen-walled nanotube with all calculated diameters, chiral angles. For this assignment, it was noticed that group J helicity (8.95^{o}) was repeated four times throughout the tube.

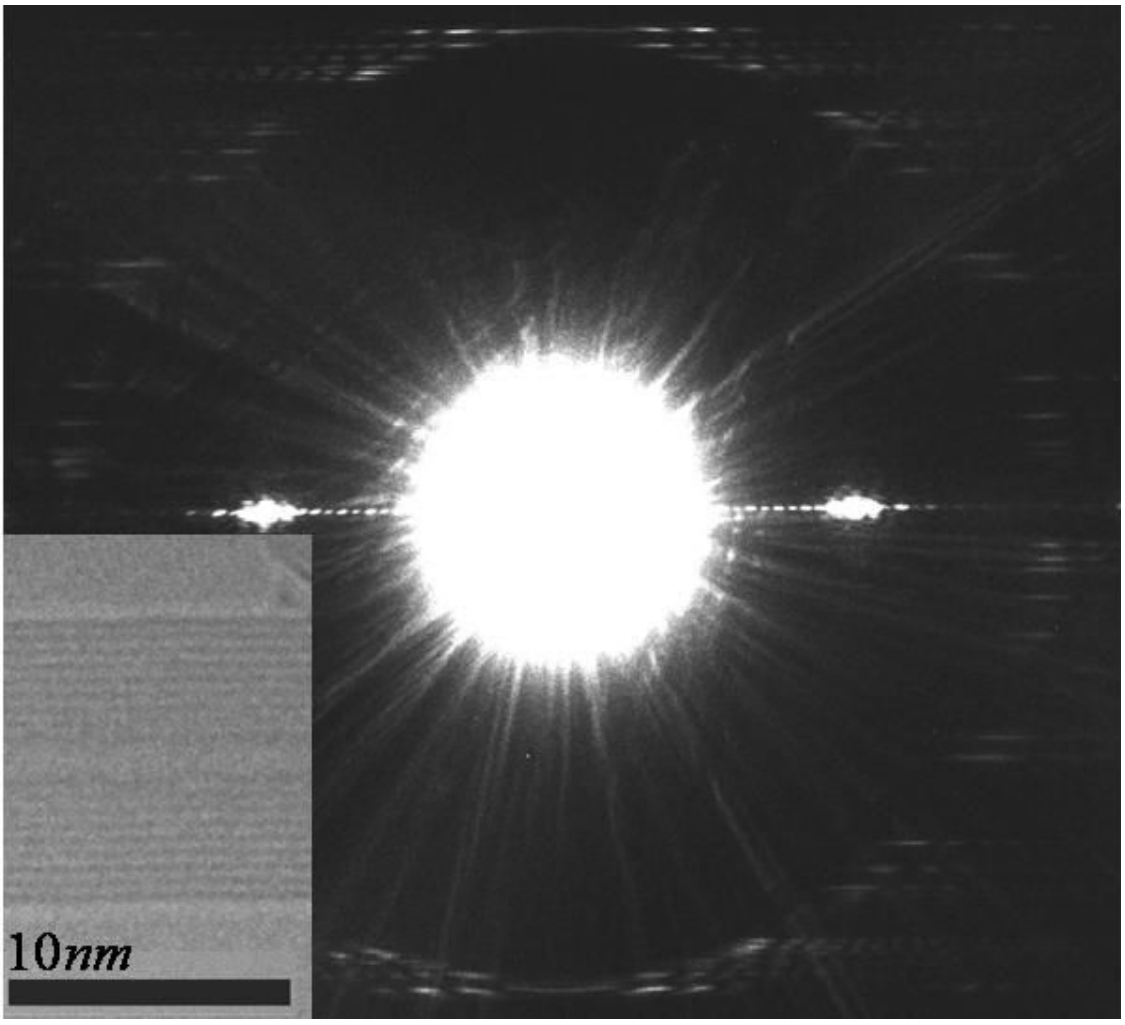

Fig. 4.3.10 Experimental electron diffraction pattern of a nine-walled carbon nanotube taken at 120 kV accelerating voltage with nano-beam diffraction. The inset shows an HRTEM image of the same nanotube.

Table 4.3.9 Final index assignment for the nine-walled carbon nanotube.

u	*v*	d (nm)	α(DEG)	Type
31	1	2.468	1.57	M
61	21	5.777	14.27	S
50	25	5.179	19.11	S
16	10	1.779	22.41	M
56	38	6.413	23.69	M
8	6	0.953	25.28	S
32	24	3.810	25.28	S
28	19	3.207	23.69	M
40	25	4.447	22.41	M

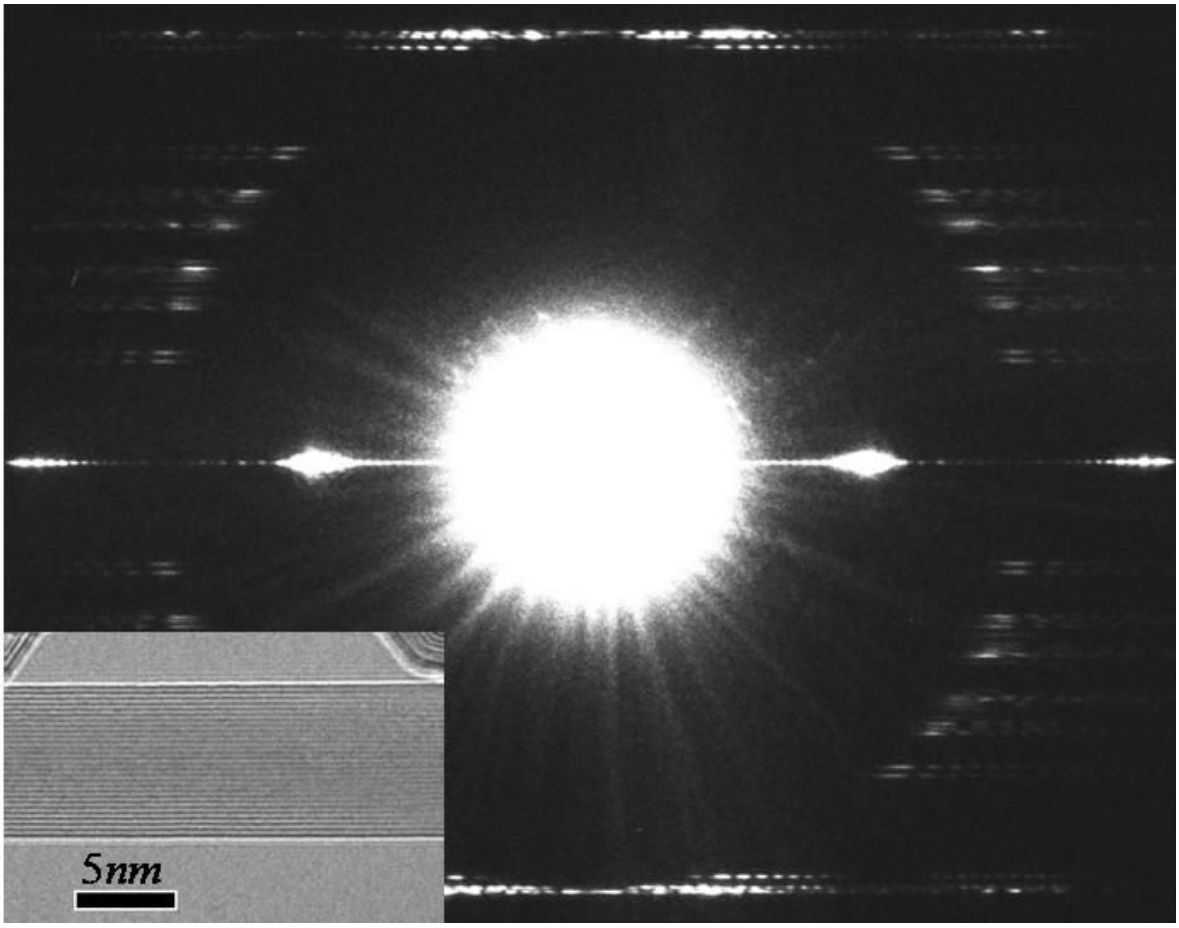

Fig. 4.3.11 Experimental electron diffraction pattern of a fourteen-walled carbon nanotube taken at 120 kV accelerating voltage with a nano-beam diffraction. The inset shows an HRTEM image of the same nanotube.

Table 4.3.10 Experimentally measured layer lines and *v/u* ratios for fourteen-walled MWNT seen above.

Group	D1	D2	D3	U_D	*v/u*	Error in *v/u*	%Error
A	1394.6	745	654	-4.4	0.0467	-0.0050	-10.70
B	1394.6	762.6667	629	2.9333	0.0645	0.0034	5.28
C	1394.6	773.3333	614	7.2667	0.0754	0.0086	11.34
D	1394.6	787.3333	603	4.2667	0.0899	0.0051	5.69
E	1394.6	802	591	1.6	0.1054	0.0020	1.86
F	1394.6	829	562.5	3.1	0.1344	0.0039	2.92
G	1380.6	848.5	532	0.1	0.1654	0.0001	0.08
H	1380.6	865.5	513.5	1.6	0.1848	0.0022	1.18
J	1380.6	878.5	500.5	1.6	0.1999	0.0022	1.11
K	1346.6	988.6	358	0	0.3699	0.0000	0.00
L	1346.6	1018.6	329.5	-1.5	0.4124	-0.0027	-0.66

Table 4.3.11 Final index assignment for the fourteen-walled carbon nanotube.

u	*v*	d (nm)	α(DEG)	Type
5	1	0.436	8.95	S
13	1	1.059	3.67	M
20	4	1.744	8.95	S
29	3	2.397	4.87	S
35	7	3.052	8.95	S
45	3	3.647	3.20	M
51	7	4.294	6.35	S
61	3	4.898	2.38	S
67	6	5.496	4.25	S
71	13	6.132	8.27	S
79	13	6.753	7.50	M
75	31	7.392	16.52	S
84	31	8.070	15.10	S
100	20	8.720	8.95	S

4.4 Summary and Conclusions

MWNTs characterized by electron diffraction here were grown by d.c arc-discharge in hydrogen gas [40]. Two important features that these nanotubes have are high-purity and a narrow channel in the center. The diameter of the innermost nanotubes is usually around 1.0 nm or less. Completely filled carbon nanotubes with the innermost core having the diameter roughly equal to the graphitic spacing was also observed before and in the present study. That was predicted to be (3, 3) armchair nanotube whose diameter was measured to be 0.4 nm from HRTEM images. From the example 6, we determined its chiral indices to be (5, 1) with a diameter of 0.436 nm in that case. The error in the diameter is due to low contrast seen in the central area of the nanotube in TEM images since smaller tubes have smaller number of carbon atoms. The nanotube (3, 3) is metallic whereas the nanotube (5, 1) is semiconducting. This shows the power of electron diffraction to determine the atomic structure of such small-scale molecules because one is going to be used as a nanowire while the other is as a nano-switch in future applications. That is why it is import to know the limitations in the current technique.

For each distinct helicity, we expect to see a different set of layer lines in reciprocal space. The overlapping of the layer lines belonging to two different sets can be used to estimate the maximum number of helicities that could be identified from the electron diffraction patterns. The accuracy for the identification of the helicities will be determined by L1 zone since this is the zone with shortest width (*0.154/a*) out of all three zones. As the chiral vector rotates away from the zigzag direction in real space, the L1 layer line moves away from the zigzag layer line at slower rate than the L2 and L3 lines move towards each other in reciprocal space. That is why we see the first layer lines

overlapping for group A and B helicity sets from example 7 (appendix C). The chiral angles of group A and B are 3.75^{o} and 4.50^{o}, respectively. Theoretical line positions obtained from diffraction simulations for these two helical sets are 1.152 and 1.151, respectively. If this difference (*0.001/a*) can be measured accurately from the diffraction patterns, total 154 different helicity can distinguished uniquely from L1 zone. Since we can not obtain this accuracy at the moment, this is a hypothetical upper limit. If we use three times this value as a measurable difference to be on the safe side, we can identify 50 different sets from a diffraction pattern which has to be shown experimentally yet.

The example 1 of the section 4.1.3 will be much better to estimate the error in measurements since there are five overlapping layer lines observed in L1 zone from the diffraction pattern. First five helical sets share a common layer line and this gives a maximum error of *0.006/a* from the simulated layer line positions using the chiral indices. Assuming a carbon nanotube whose all layers have a unique set of helicity, we should be able to characterize total 25 shells. Only L2 and L3 layer lines can be used in zoning scheme to identify each helical set and this will give a larger number for maximum number of shells that can be characterized. However, the accuracy in measuring the *v/u* ratio will be reduced due to the use of the smaller layer line spacings (D_2 and D_3) in calculation. In present study, the maximum number of shells whose chiral indices were determined was fourteen.

If a carbon nanotube is composed of shells of identical helicity, the number of walls whose chiral indices can be determined will be larger than our above estimate. In that case, all shells can be characterized in theory. There are tubes with peculiar chiral indices that can be nested within one another concentrically and satisfy the turbostratic spacing

constraint relative to each other. The (5, 5) armchair nanotube and the nanotubes meeting the equation (5n, 5n) can be used to construct a multi-wall carbon nanotube with any number of shells with a spacing of 0.339 nm (where n is integer). The (9, 0) nanotube is another example that will give a MWNT with a spacing of 0.352 nm. The list of other chiral indices, which can be used for the assembly of a MWNT of any number of shells within the acceptable limits of the turbostratic spacing, are (3n, 2n), (4n, n), (7n, 2n), and (8n, n) with spacings of 0.341, 0.359, 0.321, and 0.334 nm, respectively. The MWNT in the example 7 had four innermost tubes with chiral indices (3n, 2n).

This nanotube example might suggest that the interactions in small tubes are stronger due to pronounced curvature and might lead to the controlled growth of the first few shells in a carbon nanotube. Considering the role that interlayer spacing play in the stability of DWNTs [36], the stability of MWNTs is determined by the spacing constraint most likely. This stability condition governed by interlayer spacing might favor (3n, 2n) tube structures since the tubes with these indices have the closest interlayer spacing relative to the turbostratic value. Then the question is why do only first few shells have the same helicity? This might be due to statistical reasons. For small tubes, the chiral space is small and limited. For larger tubes, it is easier to find the tubes meeting the same spacing constraint but having the different helicities. One reason for regular stacking could be defective structure of MWNTs. It has been observed that not all MWNTs have a perfect Russian doll structure but some have scroll or polyhedral graphite structures [41, 42]. This is especially seen for larger MWNTs (> 10.0 nm). Some nanotubes can even include combination of all these types of structures inside one tube. Flat faces of polyhedral nanotubes will favor ABAB graphite stacking leading to short-range interlayer

correlations. This is most unlikely for the nanotubes studied here since they show electron diffraction patterns expected from circular nanotubes. Some nanotubes with defective interlayer spacing were seen during the course of this study. It will take further effort to investigate the reason behind such defects. Tilting and rotating nanotubes and acquiring several TEM images might reveal 3-D cross-section and tube structures other than Russian doll MWNTs. It will be interesting to study the nanotubes of larger diameters (> 10.0 nm) to test the validity of such claims and the limitations of electron diffraction procedure.

Repetitions of helical sets will increase the number of shells in a tube which can be identified unambiguously from the electron diffraction. However, it is difficult to give an estimate on an upper number since it will depend on the nature of MWNT under study. Although more than 30 shells structure could be determined, this will be very tedious task for hand-on-hand calculations. A powerful computer script (or scripts) can facilitate such a procedure great deal. Some steps can be outlined as a guideline to construct such script(s):

1. Script 1: Measuring the layer lines from the electron diffraction patterns and the number of shells and diameters from TEM images using computerized image analysis tools or tools aided with scripts. This will save a lot of time when we consider there are 60 layer lines for a nanotube of 20 shells with each having their own helicity.
2. Script 2: Zoning and grouping layer lines to identify each helical set (user intervention whenever needed, for overlapping layer lines for example).

3. Script 3: Calculating the *v/u* ratios and their experimental uncertainties for each helicity set.
4. Script 4: Find all possible chiral indices satisfying the measured ratios from a chiral space constructed from indices up to (100, 100). This will give 13.56 nm for a nanotube of largest diameter. This can be readjusted later for the study of larger diameter nanotubes.
5. Script 5: Calculate every possible index assignments using diameter values measured from TEM images. Exclude the ones that do not meet the turbostratic spacing constraint. The tolerance of ±0.4 nm obtained from DWNTs can be used for the spacing constraint in the assignment procedure.
6. Script 6: For every plausible index assignment, simulate the intensity of the equatorial layer line and compare it with the experimental one. Pick the matching one as a best index assignment.

Once the scripts are developed for each step, they can be reorganized into a single script in the future. Then indexing a carbon nanotube can be done with a single mouse click after acquiring an electron diffraction pattern. In-situ measurements like field emission or mechanical manipulations can be performed inside a TEM and the measured properties can be correlated with the known structure bridging the gap between the experiment and theory. For example, the number of layers participating in field emission can be investigated or the effect of inner layers on field emission current can be studied if only outer layer is emitting electrons. Or the electronic and optical properties on individual tubes can be measured to see how inner layers modify the local DOS and how it relates to theory after the structure determination.

4.5 References

1. Qin, L. C. (1994). Electron diffraction from cylindrical nanotubes. *J. Mater. Res*. **9**, 2450-2456.

2. Lucas, A. A., Bruyninckx, V., Lambin, Ph. (1996). Calculating the diffraction of electrons or X-rays by carbon nanotubes. *Europhysics Lett*. **35**, 355-360.

3. Lambin, Ph., Lucas, A. A. (1997). Quantitative theory of diffraction by carbon nanotubes. *Phys. Rev. B* **56**, 3571-3574.

4. Qin, L.C. (1998). Measuring the true helicity of carbon nanotubes. *Chem. Phys. Lett.* **297**, 23-28.

5. Gao, M., Zuo, J. M., Twesten, R. D., Petrov, I., Nagahara, L. A., Zhang, R. (2003). Structure determination of individual single-walled carbon nanotubes by nano-area electron diffraction. *Appl. Phys*. *Lett*. **82**, 2703-2705.

6. Liu, Z., Zhang, Q., Qin, L.C. (2005). Accurate determination of atomic structure of multiwalled carbon nanotubes by nondestructive nanobeam electron diffraction. *Appl. Phys. Lett*. **86**, 191003.

7. Liu, Z., Qin, L.C. (2005). A direct method to determine the chiral indices of carbon nanotubes. *Chem. Phys. Lett*. **408**, 75-79.

8. Liu, Z., Zhang, Q., Qin, L.C. (2005). Determination and mapping of diameter and helicity for single-walled carbon nanotubes using nano-beam electron diffraction. *Phys. Rev. B* **71**, 245413.

9. Amelinckx, S., Lucas, A.A., Lambin, Ph. (1999). Electron diffraction and microscopy of nanotubes. *Rep. Prog. Phys*. **62**, 1471-1524.

10. Meyer, J.C., Paillet, M., Michel, T., Moreac, A., Neumann, A., Duesberg, G.S., Roth, S., Sauvajol, J.L. (2005). Raman modes of index-identified freestanding single-walled carbon nanotubes. *Phys. Rev. Lett*. **95**, 217401.

11. Sfeir, M.Y., Beetz, T., Wang, F., Huang, L., Huang, X.M.H., Huang, M., Hone, J., O'Brien, S., Misewich, J.A., Heinz, T.F., Wu, L., Zhu, Y., Brus, L.E. (2006). Optical spectroscopy of individual single-walled carbon nanotubes of defined chiral structure. *Science* **312**, 554-556.

12. Meyer, J.C., Paillet, M., Roth, S. (2005). Single-molecule torsional pendulum. *Science* **309**, 1539-1541.

13. Cowley, J.M., Nikolaev, P., Thess, A., Smalley, R.E. (1997). Electron nano-diffraction study of carbon single-walled nanotube ropes. *Chem. Phys. Lett*. **265**, 379-384.

14. Qin, L.C., Ichihashi, T., Iijima, S. (1997). On the measurement of helicity of carbon nanotubes. *Ultramicroscopy* **67**, 181-189.

15. Henrard, L., Loiseau, A., Journet, C., Bernier, P. (2000). Study of the symmetry of single-wall nanotubes by electron diffraction. *Eur. Phys. J. B* **13**, 661-669.

16. Colomer, J.F., Henrard, L., Lambin, P., Van Tendeloo, G. (2002). Electron diffraction and microscopy study of single-wall carbon nanotube bundles produced by different methods. *Eur. Phys. J. B* **27**, 111-118.

17. Kociak, M., Hirahara, K., Suenaga, K., Iijima, S. (2003). How accurate can the determination of chiral indices of carbon nanotubes be? *Eur. Phys. J. B* **32**, 457-469.

18. Hirahara, K., Bandow, S., Kataura, H., Kociak, M., Iijima, S. (2004). Stretching of carbon-carbon bonds in a 0.7 nm diameter carbon nanotube studied by electron diffraction. *Phys. Rev. B* **70**, 205422.

19. Kociak, M. Suenaga, K., Hirahara, K., Saito, Y., Nakahira, T., Iijima, S. (2002). Linking chiral indices and transport properties of double-walled carbon nanotubes. *Phys. Rev. Lett*. **89**, 155501.

20. Colomer, J.F., Henrard, L., Launois, P., Van Tendeloo, G., Lucas, A.A., Lambin, Ph. (2004). Interpretation of electron diffraction from carbon nanotube bundles presenting precise helicity. *Phys. Rev. B* **70**, 075408.

21. Liu, Z., Qin, L.C. (2005). Breakdown of 2mm symmetry in electron diffraction from multiwalled carbon nanotubes. *Chem. Phys. Lett*. **402**, 202-205.

22. Liu, Z., Qin, L.C. (2004). Symmetry of electron diffraction from single-walled carbon nanotubes. *Chem. Phys. Lett*. **400**, 430-435.

23. Liu, Z., Qin, L.C. (2005). A practical approach to determine the handedness of chiral carbon nanotubes by electron diffraction. *Chem. Phys. Lett*. **405**, 265-269.

24. Liu, Z., Qin, L.C. (2005). Measurement of handedness in multiwalled carbon nanotubes by electron diffraction. *Chem. Phys. Lett*. **411**, 291-296.

25. Jiang, H., Brown, D.P., Nasibulin, A.G., Kauppinen, E.I. (2006). Robust Bessel-function-based method for determination of the (n, m) indices of single-walled carbon nanotubes by electron diffraction. *Phys. Rev. B* **74**, 035427.

26. Zhang, J., Zhu, J. (2006). Orientation dependence of diffraction intensities from helical structures. *Chem. Phys. Lett*. **420**, 171-176.

27. Meyer, J.C., Paillet, M., Duesberg, G.S., Roth, S. (2006). Electron diffraction analysis of individual single-walled carbon nanotubes. *Ultramicroscopy* **106**, 176-190.

28. Smith, B.W., Luzzi, D.E. (2001). Electron irradiation effects in single wall carbon nanotubes. *J. Appl. Phys*. **90**, 3509-3515.

29. Qin, L.C. (2007). Determination of the chiral indices (n, m) of carbon nanotubes by electron diffraction. *Phys. Chem. Chem. Phys*. **9**, 31-48.

30. Wilson, A.J.C., Prince, E. (1999). *International Tables for Crystallography C*. Kluwer Academic Publishers: Boston.

31. Doyle, P.A., Turner, P.S. (1968). Relativistic Hartree-Fock X-ray and electron scattering factors. *Acta Cryst. A* **24**, 390-397.

32. Hou, Ye, Lu, Jie private communication.

33. Hirahara, K., Kociak, M., Bandow, S., Nakahira, T., Itoh, K., Saito, Y., Iijima, S. (2006). Chirality correlation in double-walled carbon nanotubes as studied by electron diffraction. *Phys. Rev. B* **73**, 195420 1-11.

34. Gao, M., Zuo, J.M., Zhang, R., Nagahara, L.A. (2006). Structure determinations of double-walled carbon nanotubes grown by catalytic chemical vapor deposition. *J. Mater. Sci.* **41**, 4382-4388.

35. Saito, Y., Yoshikawa, T., Bandow, S., Tomita, M., Hayashi, T. (1993). Interlayer spacings in carbon nanotubes. *Phys. Rev. B* **48**, 1907-1909.

36. Saito, R., Matsuo, R., Kimura, T., Dresselhaus, G., Dresselhaus, M.S. (2001). Anomalous potential barrier of double-wall carbon nanotubes. *Chem. Phys. Lett.* **348**, 187-193.

37. Kiang, C.H., Endo, M., Ajayan, P.M., Dresselhaus, G., Dresselhaus, M.S. (1998). Size effects in carbon nanotubes. *Phys. Rev. Lett.* **81**, 1869-1872.

38. Yoshizawa, K., Kato, T., Yamabe, T. (1996). Interlayer interactions in two-dimensional systems: Second-order effects causing ABAB stacking of layers in graphite. *J. Chem. Phys.* **105**, 2099-2105.

39. Abe, M., Kataura, H., Kira, H., Kodama, T., Suzuki, S., Achiba, Y., Kato, K., Takata, M., Fujiwara, A., Matsuda, K., Maniwa, Y. (2003). Structural transformation from single-wall to double-wall carbon nanotube bundles. *Phys. Rev. B* **68**, 041405(R).

40. Zhao, X., Ohkohchi, M., Wang, M., Iijima, S., Ichihashi, T., Ando, Y. (1997). Preparation of high-grade carbon nanotubes by hydrogen arc discharge. *Carbon* **35**, 775-781.

41. Reznik, D., Olk, C.H., Neumann, D.A., Copley, J.R.D. (1995). X-ray powder diffraction from carbon nanotubes and nanoparticles. *Phys. Rev. B* **52**, 116-124.

42. Maniwa, Y., Fujiwara, R., Kira, H., Tou, H., Nishibori, E., Takata, M., Sakata, M., Fujiwara, A., Zhao, X., Iijima, S., Ando, Y. (2001). Multiwalled carbon nanotubes grown in hydrogen atmosphere: An X-ray diffraction study. *Phys. Rev. B* **64**, 073105.

Chapter 5

Tungsten Disulfide (WS_2) Nanotubes

5.1 Introduction

News of the first synthesis of WS_2 nanotubes by Tenne et al. [1] in 1992 and followed by that of MoS_2 [2] later opened new possibilities and challenges in the field of nanotube research with a wide range of potential applications. The research on inorganic nanotubes has been a field that has grown steadily ever since. There have been reports of successful synthesis of over 50 different kinds of inorganic nanotubes so far [3]. Some tubes are still at the stage of theoretical modeling and development without any sign of experimental evidence. The first WS_2 nanotubes were synthesized by combining two processes [1,2,4]: (1) needlelike WO_3 oxide particles were produced by heating a tungsten filament in the presence of water vapor in vacuum and (2) WS_2 nanotubes were grown from WO_3 particles by heating under the flow of H_2/N_2 (forming gas) and H_2S gas mixture. Since then, new synthesis methods, such as the fluidized bed reactor, have been developed for their large scale production [5-8]. It has also been shown that the intercalation of inorganic fullerene-like structures with alkali atoms and synthesis of photosensitive films in this way have become affordable with these new production techniques. The synthesis of first single-walled WS_2 nanotubes on template multi-walled carbon nanotubes, which

offer new possibilities in terms of nano-composite materials and applications, has been reported as well [9, 10].

The morphology, structure and defects of WS_2 nanotubes have been examined and characterized by HRTEM and ED extensively and the chirality of the tubes has been assessed by using TEM dark-field imaging techniques [11-13]. Like bulk WS_2, WS_2 nanotubes were predicted to be semiconducting [14]. Recently, a scanning tunneling microscopy (STM) study of WS_2 tubes confirmed the semiconducting behavior of these nanotubes [15]. The WS_2 and its cousin MoS_2 materials have been extensively used as a solid lubricant in industry. WS_2 inorganic fullerene-like nanoparticles have been shown to be much better solid lubricants than their bulk counterparts due to their ultra-low friction and wear properties [16]. The repeated tests over a period of two months showed that there is no deterioration in image quality obtained from the tubes used as tips in scanning probe microscopy [17]. A recent study on their elastic properties reported an experimental Young's modulus of 152 GPa and a tensile strength of 16 GPa [18].

Here, we apply the electron diffraction technique developed for the identification of the chiral indices of carbon nanotubes to the WS_2 nanotubes. Like for carbon nanotubes, determining the structure of WS_2 nanotubes unambiguously has vital importance for their applications in nano-electronics. Although WS_2 nanotubes are predicted to be semiconducting regardless of chirality, recent studies show that the energy gap of the tubes is a monotonically increasing function of the diameter [15,19]. Moreover, for a zigzag tube $(u,0)$ of diameter less than 1 nm, it was calculated that the tube has a very narrow band gap and exhibits quasimetallic behavior [14]. Synthesis, structure and self-assembly of sub-nanometer single-wall MoS_2 nanotubes of $(3,3)$ armchair structure have

been reported recently with predictions that these tubes might be metallic with a small but finite density of states at the Fermi level [20]. So, in light of all these findings, accurate determination of the atomic structure of WS_2 nanotubes becomes essential for their future potential applications, and TEM (using ED and HRTEM) is the instrument that is highly capable of probing and resolving the atomic structure of these tubules.

5.2 Structure

A single layer of WS_2 in its most stable form can be described by a metal layer sandwiched by two sulfur layers forming a hexagonal cell [1, 14]. The triple layers are stacked on top of each other similar to graphite. Strong covalent bonds exist inside the triple layers but the interactions between the adjacent sulfur layers are van der Waals-like. Within the sandwich layer, each W atom is bonded to six sulfur atoms forming a trigonal bi-prism. Figure 5.2.1 shows the structure of a single layer of WS_2 looking down the c-axis where the dark colored spheres are W atoms. Figure 5.2.2 shows the stacking of WS_2 layers similar to graphite stacking separated by the inter-layer distance of 0.62 nm (c/2) [14, 19].

The WS_2 layers can be rolled onto the surface of a cylinder similar to the graphene layers by choosing a specific direction in the two-dimensional crystal lattice. As for the case of carbon nanotubes, this direction can be described by a chiral vector written in terms of the primitive 2D lattice vectors and two integers: $\vec{C} = u\vec{a} + v\vec{b}$ ($|\vec{a}| = |\vec{b}|$). In this way, there are three classes of tubular structure similar to carbon nanotubes: $u = v$ "armchair" nanotubes, $u \neq 0$ and $v = 0$ "zigzag" nanotubes and $u \neq v \neq 0$ "chiral" nanotubes. The diameter of the tube obtained by rolling up a single WS_2 sheet is given by

$$D = a\sqrt{u^2 + v^2 + uv}/\pi \tag{5.2.1}$$

where a is the in-plane lattice constant of tungsten disulfide ($a = 0.315nm$) [21]. Similarly to carbon nanotubes, the chiral angle α can be calculated using the integers that define the chiral vector:

$$\tan\alpha = \sqrt{3}v/(2u + v). \tag{5.2.2}$$

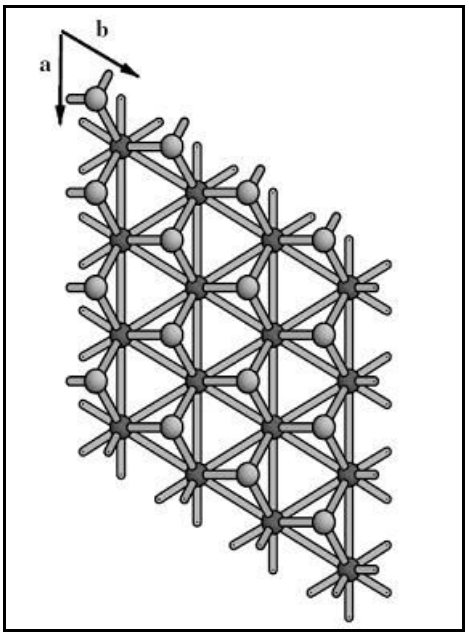

Figure 5.2.1 Top view of a WS_2 triple layer where the dark colored atoms are W. Adapted from reference [14].

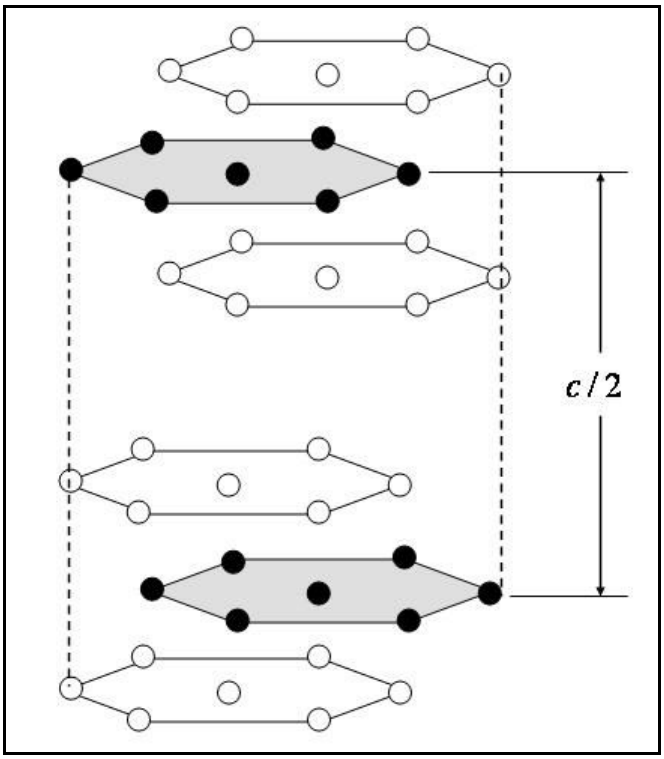

Figure 5.2.2 Graphic stacking of WS_2 triple layers where dark circles stand for tungsten atoms and open circles for sulfur atoms.

5.3 TEM and NBED Characterization of WS_2 Nanotubes

The WS_2 nanotubes were characterized by using high resolution electron microscopy and nano-beam electron diffraction. Samples were provided by Professor R. Tenne. These nanotubes consist of multiple concentric walls. The smallest number of walls observed was 3. No single-walled WS_2 nanotube was observed in this study. These tubes have very large diameters, unlike their carbon nanotube counterparts. The innermost diameter of the multi-walled WS_2 nanotubes is usually about 9-10 nm. Most tubes studied here were open ended and usually they appear to be coming out of polyhedral WS_2 or starting material WO_{3-x} nanoparticles [11]. The microscope (JEOL JEM-2010F) was operated at 200 kV for the imaging and diffraction experiments. The diffraction patterns were acquired on both the photographic films and the CCD camera.

Example 1

The techniques used for carbon nanotube characterization was also employed here to measure the chirality and to determine the chiral indices of the perimeter vector for the WS_2 nanotubes. Figure 5.3.1 shows a TEM image of a WS_2 tube that is composed of 5 walls. The next figure (Fig. 5.3.2) shows the electron diffraction pattern taken from this tube. The first-order and the higher-order reflections are easily visible in the diffraction pattern. In the first-order reflections, the three principal layer lines are clearly seen and the small separation of the layer lines between each set suggests that the helicities of all the walls are close to each other as well. There were 3 layer lines in the first zone, 5 in the second zone, and 5 in the third zone in total.

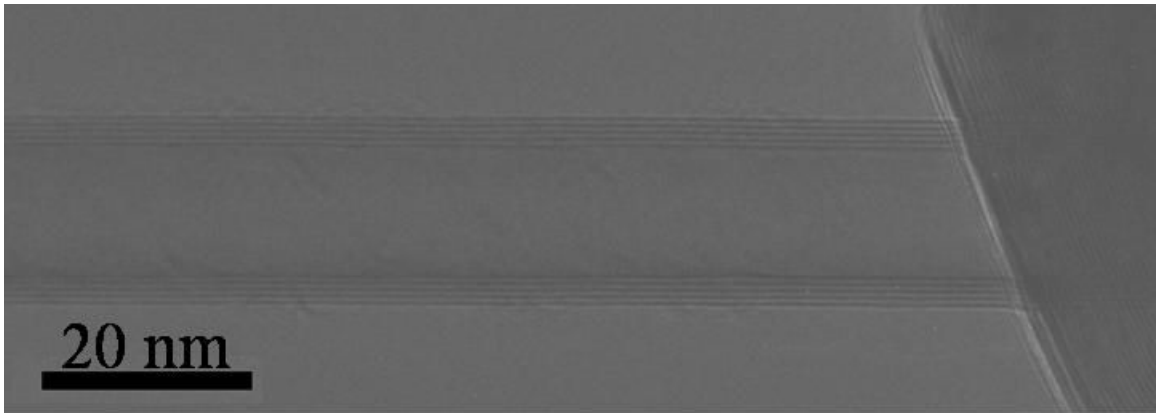

Fig. 5.3.1 High resolution TEM image of a 5-walled WS_2 nanotube.

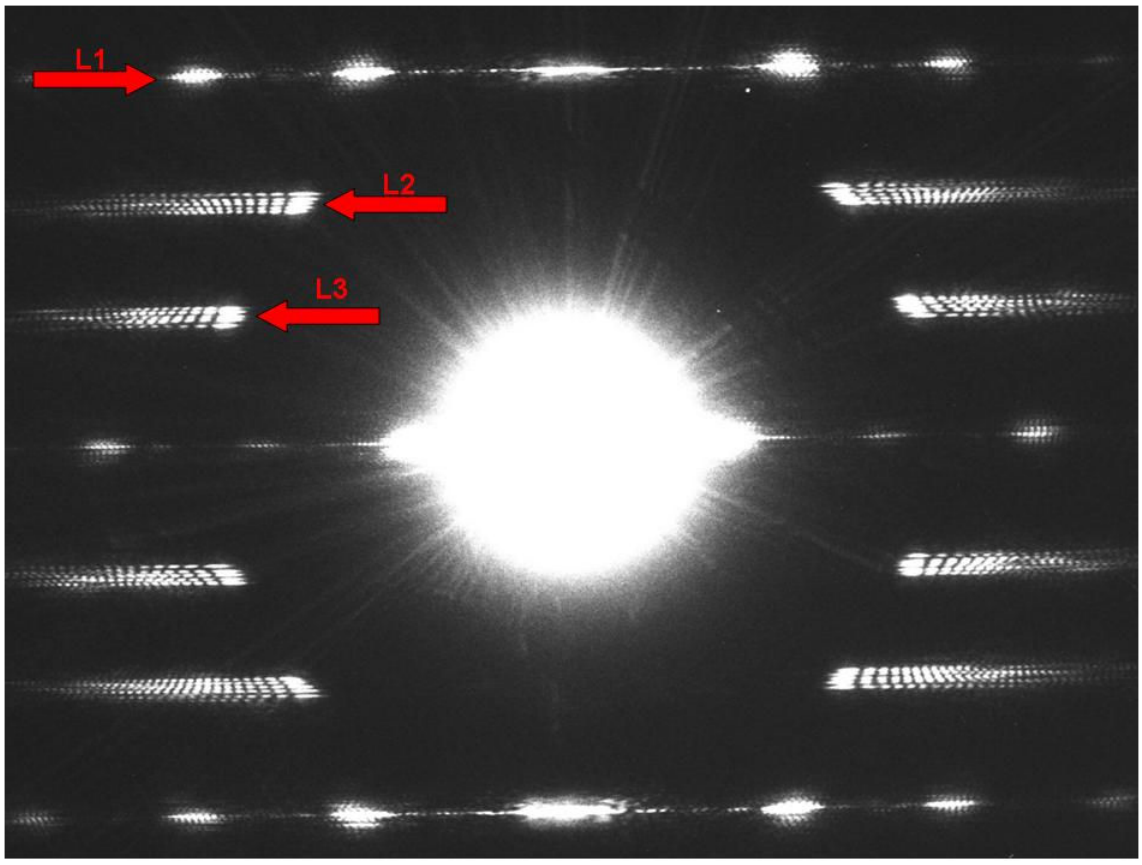

Fig. 5.3.2 Electron diffraction pattern taken from the 5-walled WS_2 nanotube shown in Fig. 5.3.1. Red arrows indicate principal layer lines.

The lines in the first zone are close to each other and this makes the determination of the ratio of chiral indices less accurate. Instead, the layer line spacings of the second and the third zone were used to find the v/u ratio with the use of the equation below:

$$\frac{v}{u} = \frac{D_2 - D_3}{D_2 + 2D_3}. \tag{5.3.1}$$

Table 5.3.1 shows the measured layer line spacings and the v/u ratios, and the chiral angles calculated from the spacings. The errors in the v/u ratios were also included in the table. The errors in the v/u ratios were calculated using error propagation through equation (5.3.1) and the new error equation is

$$U_{v/u} = \frac{3U_D\sqrt{D_2^{\,2} + D_3^{\,2}}}{(D_2 + 2D_3)^2}, \tag{5.3.2}$$

where U_D is the non-zero error stemming from the layer line spacings and given by $U_D = D_1 - (D_2 + D_3)$ (listed in Table 5.3.1 also). The last column of Table 5.3.1 shows the percent relative uncertainties calculated for each v/u ratio (not absolute uncertainties). Table 5.3.2 lists all possible chiral indices within the experimental uncertainties for each helicity group. The first column of the table shows the measured diameters from the TEM images in nanometers. The possible chiral indices were selected by looking at the difference between the true diameters from the indices and the measured diameters. The theoretical value of the inter-wall distance (0.62 nm) can be used as a constraint to eliminate some of the chiral indices. The other useful aid would be the use of the intensity modulations seen in each layer line. The intensity on each line is governed by Bessel functions of order n where n is directly related to the chiral indices of

the tube and the oscillations in the intensity have a period inversely proportional to the tube diameter.

Table 5.3.1 List of measured layer line spacings (in arbitrary units), experimental ratio of chiral indices and the percent error bars in *v/u* (last column) for the five distinct helicities identified from diffraction pattern.

Group	D1	D2	D3	U_D	*v/u*	%error in *v/u*
A	1476.4	1000.2	478.6	-2.4	0.2665	0.78
B	1496.4	980.7	514.1	1.6	0.2323	0.57
C	1466.4	962.7	500.6	3.1	0.2353	1.11
D	1476.4	944.7	533.6	-1.9	0.2043	0.75
E	1476.4	929.2	547.1	0.1	0.1888	0.04

Table 5.3.2 Possible choices of chiral indices for each helicity and measured diameter.

d (nm)	A	B	C	D	E
15.74	(136,36)	(138,32)	(139,33)	(141,29)	(143,27)
14.58		(129,30)	(128,30)	(132,27)	(132,25)
13.43	(116,31)		(119,28)		(122,23)
12.28		(108,25)			(111,21)
11.07			(97,23)	(98,20)	

Table 5.3.3 Final chiral index assignment for the 5-walled WS_2 nanotube with calculated chiral angles and diameters. The seventh column shows the percent deviation between the experimental and theoretical *v/u* ratios.

Group	*u*	*v*	d (nm)	*v/u*	*v/u*-exp	%error	α (DEG)
A	116	31	13.457	0.2672	0.2665	0.29	11.54
B	108	25	12.276	0.2315	0.2323	-0.34	10.19
C	97	23	11.061	0.2371	0.2353	0.77	10.40
D	141	29	15.794	0.2057	0.2043	0.66	9.17
E	132	25	14.650	0.1894	0.1888	0.29	8.52

The higher the tube diameter is, the smaller the width of oscillations will be or vice versa. It has been determined from the oscillations in the intensity that tubes of helicities in group D and E have the largest diameters. The only possible choice for the largest tube is the chiral indices of (141,29) from group D. The group E comes from the second largest tube and its chiral indices are assigned to be (132, 25). The only choice for the smallest tube is group C with the chiral indices of (98, 23). Once the structure of these two walls is determined, the rest can be assigned easily. Table 5.3.3 shows the final assignment of chiral indices, diameters, and helicity for this five-walled WS_2 nanotube.

Example 2

The second example is another five-walled WS_2 nanotube. Again, the TEM image (Fig. 5.3.3) and the diffraction pattern (Fig. 5.3.4) were acquired on the photographic films. The layer line spacings were recorded from the diffraction pattern and listed in Table 5.3.4. The first layer lines from the principal reflections of each wall almost coincide with each other. The second layer line spacings for each wall are close to each other as well as those of the third layer line and this fact suggests that the helicity of each wall is in close proximity to each other and they also have near-zigzag structures. Table 5.3.5 lists the experimentally-measured diameters from the TEM image and the possible chiral indices for each helicity group within experimental uncertainty for the diameter of each wall. There are only two possible choices of chiral indices for group A and group D's helicities. It is determined from the oscillations and the periodicity of the intensity on the layer lines that group A has the smallest diameter among all the walls. This is one of two choices for the smallest-diameter nanotube and for group A as well. So, group A has been assigned with the chiral indices of (80, 19).

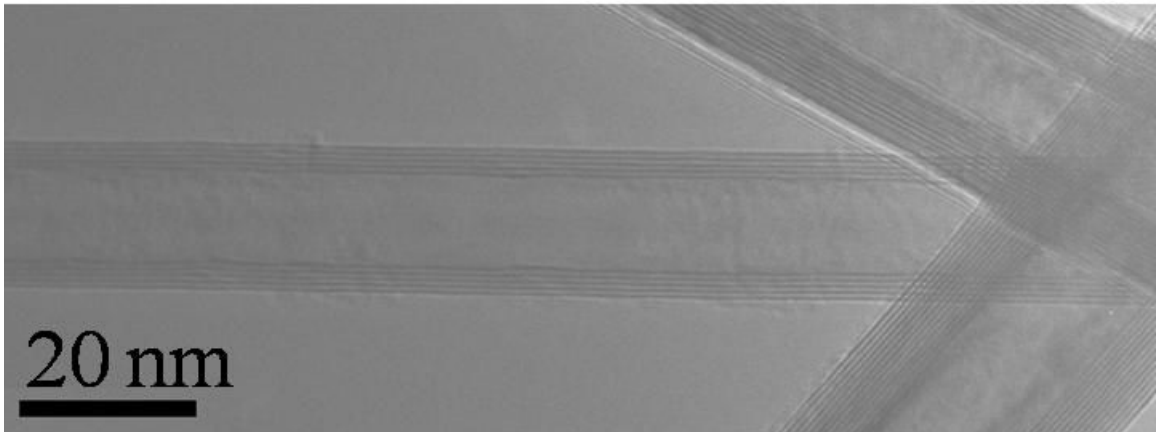

Fig. 5.3.3 High resolution TEM image of another 5-walled WS_2 nanotube.

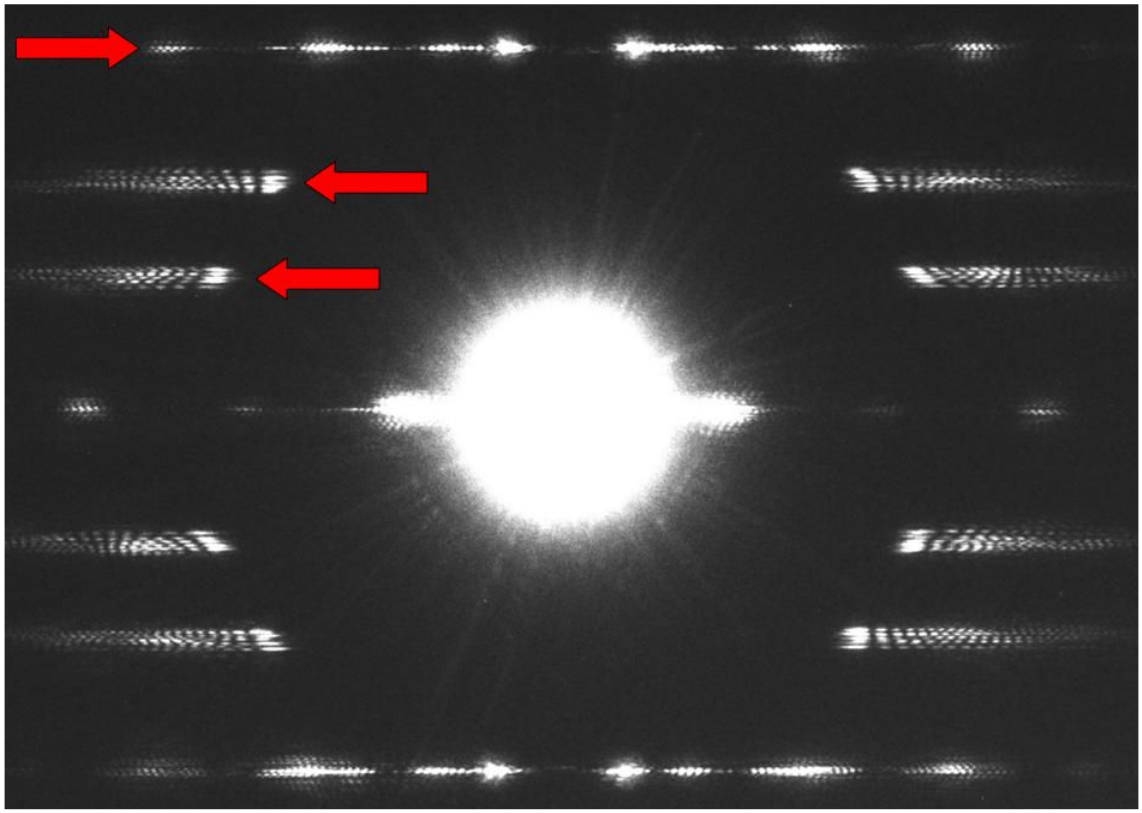

Fig. 5.3.4 Electron diffraction pattern of nanotube shown in Fig. 5.3.3 with red arrows marking principal layer lines.

Table 5.3.4 List of measured layer line spacings (in arbitrary units), experimental ratio of chiral indices and its percent error in *v/u* for the five distinct chiralities identified from diffraction pattern.

Group	D1	D2	D3	U_D	*v/u*	%error in *v/u*
A	1438.3	946.7	490.6	1	0.2366	0.36
B	1438.3	925.7	510.1	2.5	0.2136	0.98
C	1438.3	910.2	526.1	2	0.1957	0.84
D	1438.3	891.7	542.1	4.5	0.1769	2.04
E	1438.3	877.2	556.1	5	0.1614	2.44

Table 5.3.5 List of possible choices of the chiral indices. First column is diameters measured from TEM image.

d (nm)	A	B	C	D	E
13.79		(122,26)		(125,22)	(126,20)
12.58	(110,26)	(112,24)	(113,22)	(114,20)	(115,19)
11.48		(102,22)	(103,20)		(105,17)
10.38		(93,20)			(95,15)
9.12	(80,19)		(82,16)		

Table 5.3.6 Final index assignment for the 5-walled WS_2 nanotube with calculated helicity and diameters. The seventh column shows the percent deviation between the experimental and theoretical *v/u* ratios.

Group	*u*	*v*	d (nm)	*v/u*	*v/u*-exp	% error	α (DEG)
A	80	19	9.124	0.2375	0.2366	0.39	10.42
B	102	22	11.490	0.2157	0.2136	0.99	9.57
C	113	22	12.579	0.1947	0.1957	-0.53	8.74
D	125	22	13.770	0.1760	0.1769	-0.53	7.97
E	95	15	10.360	0.1579	0.1614	-2.18	7.22

This also agrees with the fact that it has the smallest intensity on its second layer line compared to all other's and the intensity is proportional to the diameter of the tube. The best choice for the second smallest tube comes from group E and it is a (95, 15) nanotube. The only choices left for the largest-diameter tube come from group B and D. Group D has larger intensity and smaller peak widths than group B. This means group D is the largest tube and its indices should be (125, 22). There are two groups and two possibilities left. The best index assignment is showed in table 5.3.6 with calculated diameters, chiral angles and inter-wall distances.

Example 3

The third example is a tube with the smallest number of walls (3 walls) observed in this study (Fig. 5.3.5). In the diffraction pattern (Fig. 5.3.6), there are only two lines seen in the first and the second zone and the third line is hardly visible in the third zone. The walls in this tube have larger helicities compared to the two previous cases. The experimentally-measured *v/u* ratios are very close again. All the measured quantities are listed in Table 5.3.7. Table 5.3.8 lists all experimentally possible chiral indices and measured diameters from the TEM images. Since there are only 3 walls, there are six possible index assignments and they are all listed in Table 5.3.9. The last column gives the best agreement between the experimental inter-wall distances and the calculated ones. So, the chiral indices from the inner to the outer shell are (90, 39), (98, 47), and (112, 46), respectively. The shells in this tube have diameters of 11.49, 12.848, and 14.113 nm and have chiral angles of 17.14^{o}, 18.52^{o}, and 16.44^{o}, respectively.

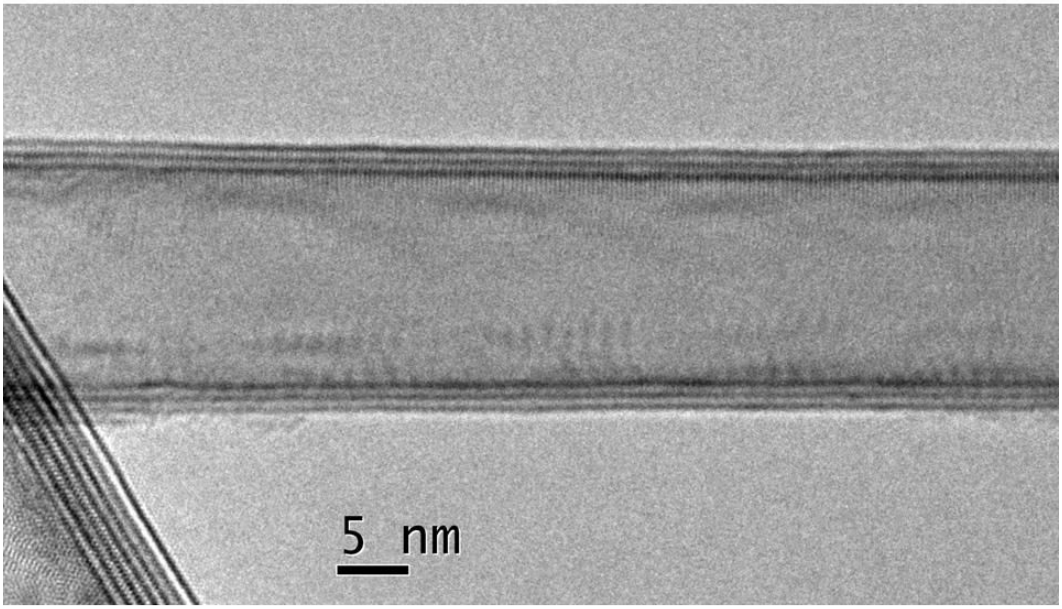

Fig. 5.3.5 A 3-walled WS_2 nanotube and its high resolution TEM image. It was acquired on the CCD camera (example 3).

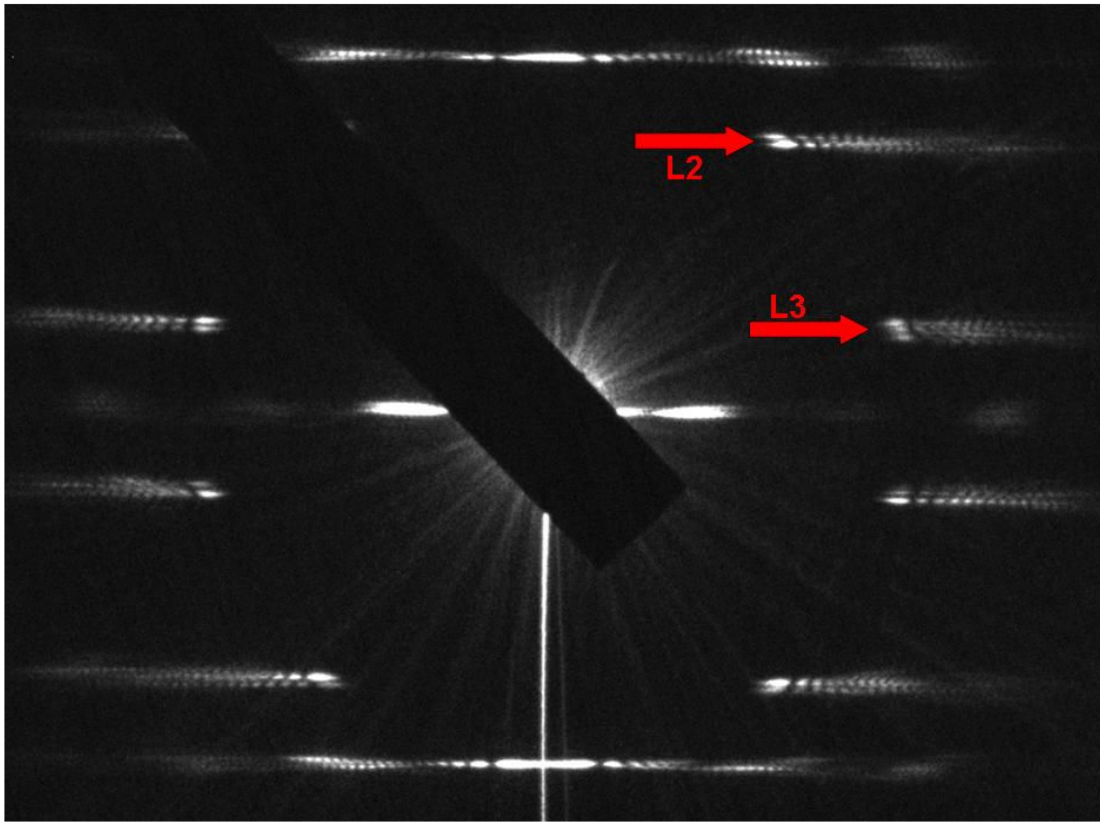

Fig. 5.3.6 Electron diffraction pattern of the 3-walled WS_2 nanotube shown in Fig. 5.3.5.

Table 5.3.7 List of measured layer line spacings (in arbitrary units), experimental ratio of chiral indices and the percent error bars in *v/u* for the three distinct chiralities identified from diffraction pattern.

Group	D1	D2	D3	U_D	*v/u*	%error in *v/u*
A	911.8	700.6	212.8	-1.6	0.4331	-0.64
B	926.8	700.6	228.2	-2	0.4083	-0.81
C	911.8	718.7	191.2	1.9	0.4791	0.73

Table 5.3.8 Possible chiral indices for each chirality and measured diameter.

d (nm)	A	B	C
14.13	(111,48)	(112,46)	(108,52)
12.86	(101,44)	(103,42)	(98,47)
11.56	(90,39)	(91,37)	(88,42)

Table 5.3.9 Final index assignment for the 3-walled WS_2 nanotube shown in fig.5.3.6.

d (nm)	I	II	III	IV	V	VI
14.127	(108,52)		(111,48)		(112,46)	
12.858	(103,42)	(101,44)	(98,47)	(103,42)	(101,44)	(98,47)
11.555	(90,39)	(91,37)		(88,42)		(90,39)

Example 4

The last example is another five-walled WS_2 nanotube with a defect at one end. The outermost layer is not continuous and does not extend to the end of the tube. Thus, the nanotube has five walls up to the defect and only four walls after the defect. The first high-resolution TEM image shows the nanotube having the five walls near the large inorganic fullerene-like particle (Fig. 5.3.7). The second image shows where the defect starts and the disappearance of the outermost wall (Fig. 5.3.8). Two separate diffraction patterns taken from the five-walled segment and the four-walled segment of the tube were obtained using a nano-beam electron probe. Figures 5.3.9 and 5.3.10 show the diffraction patterns of the five-walled and four-walled nanotubes, respectively, together with insets that display a magnified view of the layer lines in the second and the third zone. There is only one layer line in the first zone again for all helicities present. Even if a unique index assignment can not be determined for this tube, the indices of the outer layer can be found accurately. The diameters measured from the high resolution image, ranking from the largest to the smallest, are 16.04 nm, 14.74 nm, 13.51 nm, 12.27 nm and 10.90 nm (± 0.03 nm of uncertainty in each diameter). Tables 5.3.10 and 5.3.11 show the measured layer line spacings and the grouping of layer lines for each diffraction pattern. Group E helicity is for the outermost wall with a measured v/u ratio of 0.1451. The best assignment for the chiral indices of this wall is (148, 21) using the measured diameter and the *v/u* ratio.

The arrows in the diffraction pattern of the four-walled part of the tube indicate that group A has the lowest intensity of all, meaning that it might have the smallest diameter. Then, the best assignment for group A becomes (97, 20). The intensity of the reflections

in the second layer line for group C and D have the highest brightness among all. So, these tubes should have larger diameters than those of group A and group B. The best indexing for the second largest-diameter tube is a (135, 22) nanotube of group D helicity. The remaining two can be assigned easily since the only choice left for group B is a (110,21) nanotube. Table 5.3.12 shows the final indexing assignment for this nanotube. The inter-wall distances measured from TEM image and calculated from the true diameters match one another well.

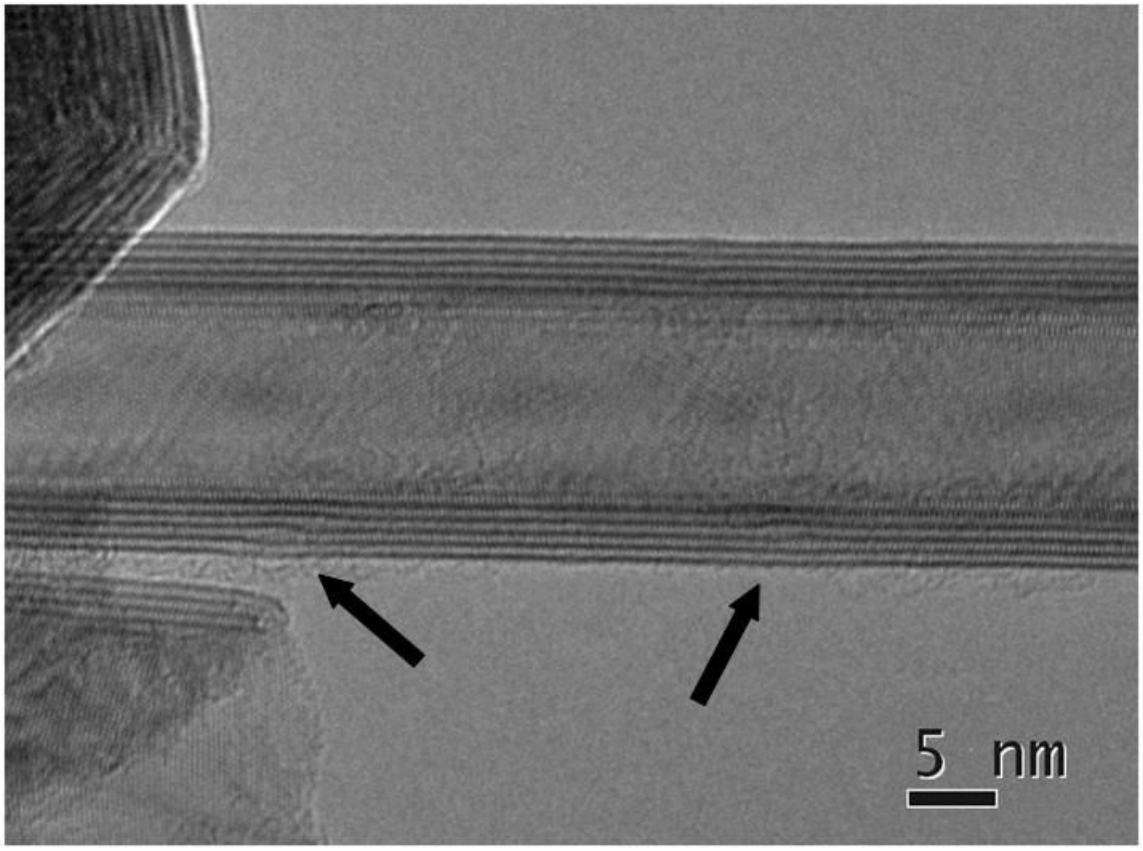

Fig. 5.3.7 High resolution image of a 5-walled WS_2 nanotube. Black arrows point to the layer defects.

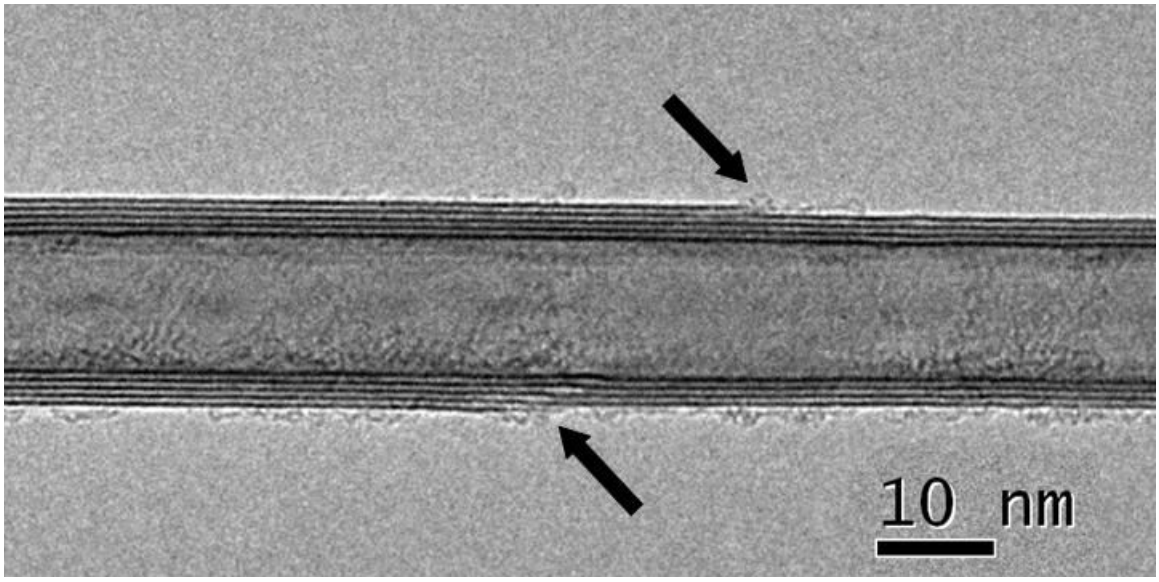

Fig. 5.3.8 Another high resolution image of the WS_2 tube given in Fig. 5.3.7 showing a defect where the outer layer of the tube disappears. The black arrows point to where the outer layer terminates.

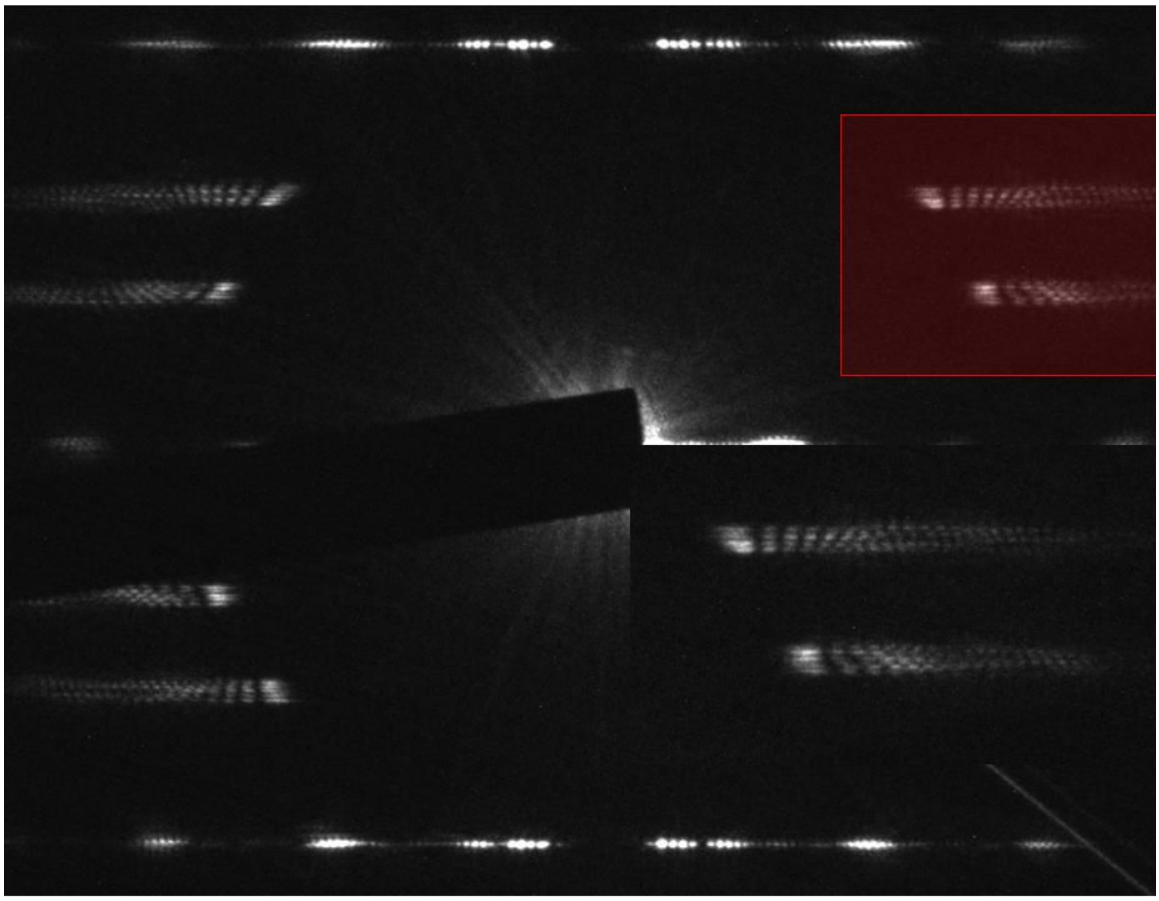

Fig. 5.3.9 Electron diffraction pattern of the WS_2 nanotube shown in Fig.5.3.7 acquired from a defect-free portion of the tube. The inset shows a magnified view of the layer lines highlighted in red frame.

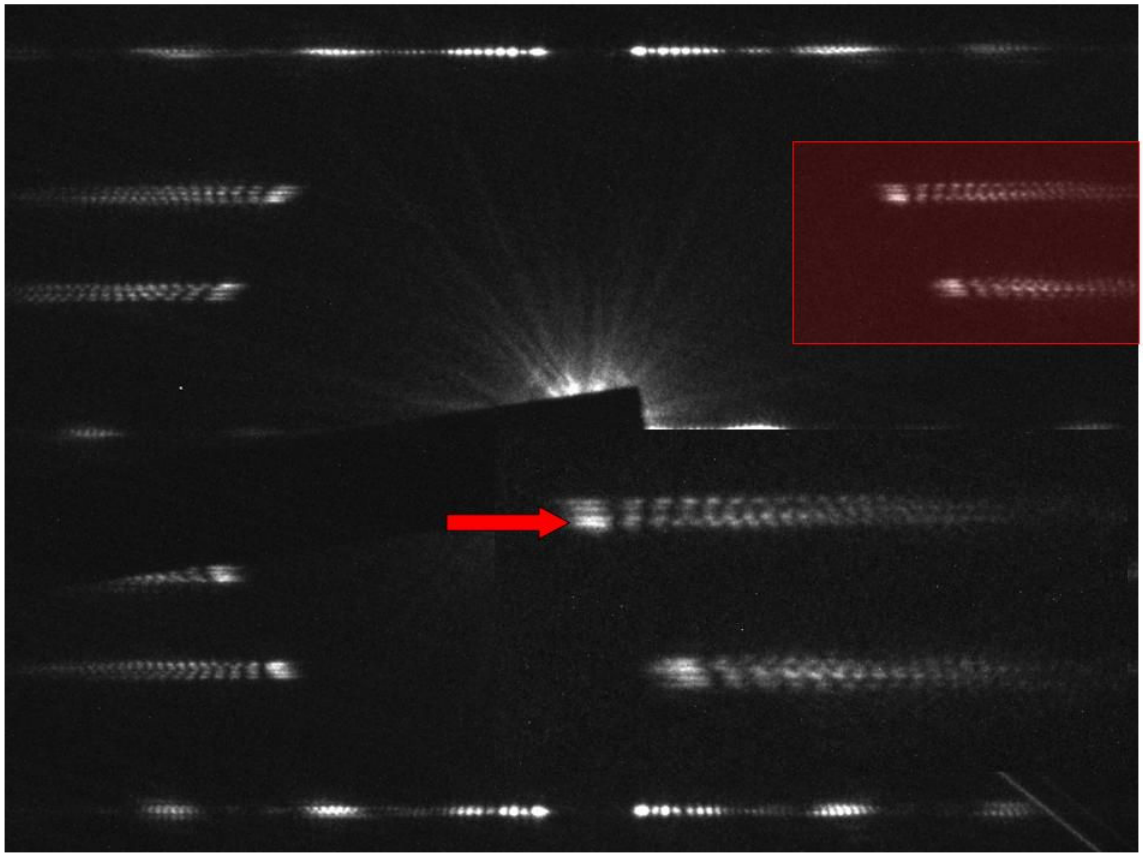

Fig. 5.3.10 Electron diffraction pattern of the WS_2 nanotube shown in Fig.5.3.8 acquired from a portion of the tube with 4-walls. The inset shows a magnified view of layer lines highlighted in red frame. The red arrow points to layer lines with higher intensity.

Table 5.3.10 List of measured layer line spacings (in arbitrary units), experimental ratio of chiral indices and the percent error for the five distinct chiralities identified from diffraction pattern of fig.5.3.10.

Group	D1	D2	D3	U_D	*v/u*	%error
A	1062.3	680.2	380.1	2	0.2083	1.08
B		670.2	390.1	2	0.1931	1.15
C		659.2	401.1	2	0.1766	1.23
D		647.7	411.1	3.5	0.1610	2.32
E		636.2	421.6	4.5	0.1451	3.25

Table 5.3.11 List of measured layer line spacings (in arbitrary units), experimental ratio of chiral indices and the percent error bars in *v/u* for the four distinct chiralities identified from diffraction pattern of fig.5.3.11.

Group	D1	D2	D3	U_D	*v/u*	%error
A	1059.85	680.9	376.2	2.75	0.2126	1.47
B		669.9	387.7	2.25	0.1953	1.28
C		657.4	401.2	1.25	0.1755	0.77
D		647.9	410.7	1.25	0.1614	0.83

Table 5.3.12 Final index assignment for the 5-walled WS nanotube with an incomplete outer shell. The seventh column shows the percent deviation between the experimental and theoretical *v/u* ratios.

Group	*u*	*v*	d (nm)	*v/u*	*v/u*-exp	error	α (DEG)
A	97	20	10.868	0.2062	0.2083	-1.04	9.19
B	110	21	12.219	0.1909	0.1931	-1.14	8.58
C	123	22	13.571	0.1789	0.1766	1.27	8.09
D	135	22	14.763	0.1630	0.1610	1.24	7.43
E	148	21	15.997	0.1419	0.1451	-2.18	6.55

5.4 Summary and Conclusions

Chiral indices of five tungsten disulfide (WS_2) nanotubes have been determined unambiguously. The results on the structure showed that the helicity of these tubes varies monotonically although there is no clear mathematical correlation between the helicity and diameter of each shell in these tubes. The tube of example 4 is the only example where a linear relation exists between diameter and helicity of adjacent walls. The differences in not only the chiral angles of adjacent walls but also in the chiral angles that are ranked in descending order exhibit no strong relationship. Most tubes in this study have a near zigzag structure although the number studied is rather low. The general morphology of these tubes indicates that they are straight and long with a few layer defects and they have open ends.

The average interlayer distance calculated from all tubes structurally characterized here is 0.60 nm, which is 3% lower than the known interlayer distance of bulk WS_2 (0.62 nm). It varied from as low as 0.52 nm up to as high as 0.68 nm. A recent work on infrared vibrational properties of WS_2 nanoparticles showed that the total and local charge environment of inorganic fullerene-like nanoparticles of WS_2 change compared to the bulk material due to nanoparticle curvature [22]. While the intra-layer total and local effective charges decrease, the inter-layer total effective charge increases slightly. They also showed that the curvature within a nanoparticle is not uniform for each layer. WS_2 nanotubes with non-circular cross-sections have also been observed before [23]. Considering the similarity of the structure between WS_2 nanoparticles and nanotubes, we can assume that the strong interactions between the layers and the non-uniform curvature might explain the observed large variations in the interlayer distances (almost 13%). It

might also be affected by the layer defects, stresses in the bent layers (the inner walls are subject to more strain than the outer ones), or contaminants (like starting ingredients or oxide phases) in the gap between the layers, or the mismatch of sulfide growth front against the lattice structure of oxide core and related memory effects. The inner-most inter-layer distances observed in this study is usually smaller than the known value and this might support the last assumption (previous sentence) that the innermost layers did not have enough relaxation time since they were formed at very late stages of the reaction. A recent high pressure x-ray diffraction study on bulk WS_2 revealed that the material is more compressible along the c-direction and 10% contraction can be obtained with an applied pressure of 25 GPa [24]. If we apply this value to estimate the force needed for 10% change for a nanotube of 10 nm in diameter and 1.0 μm in length, we obtain a force of a few mili-Newton, which is easily applicable to the material by rubbing it between two hands.

Two main synthesis routes exist for the synthesis of WS_2 nanotubes with similar growth mechanisms [7]. The first one is a solid-gas phase reaction that takes place in two separate steps and involves the synthesis of sub-oxide WO_{3-x} whiskers followed by reduction and sulfidization with H_2/N_2 and H_2S gases at 800-900 ^oC. The second one is a gas phase reaction in a vertical chamber where oxide precursors (with N_2 gas) in powder form are fed in from top and forming and sulfidizing agents are fed in from bottom maintaining the powder aloft. It allows large scale production of WS_2 nanotubes (100 grams per 10 hour shift) [7]. The general growth mechanism involves a substitution reaction where oxygen atoms reduced by H_2 gas are replaced by sulfur atoms from the H_2S gas. Hydrogen reduces the oxide fast and the reaction with H_2S forms a

monomolecular layer of WS_2 or two on the surface of the whiskers. The encapsulation of the whiskers by a few layers prevents the coalescing with neighboring ones since the sulfide layers are chemically unreactive. Further growth proceeds inward via the reduction of inner core and slow diffusion controlled sulfidization process [5]. In the gas phase reaction, the nanotube growth starts on the nanoparticles via an oxide protrusion. It is an open ended growth where all layers grow at the same time or with a small time lag (it has been observed that all the layers end at about the same length). Two reactions are very vital for the growth of the nanotube: slowing down the reduction and sulfidization and promoting the tip growth by higher vapor pressure of the oxide [7].

In the solid-gas phase reaction, the tubes have close ends since the growth starts with the encapsulation of the oxide template by a few WS_2 layers and proceeds radially inward. Tubes grown by this method also have higher number of layers with smaller hollow cores since the density of the WO_3 and WS_2 differs by 5% only. Tubes grown by a gas phase reaction have hollow cores occupying almost 70% of total volume with 5-8 shells on average [7]. They are open ended and usually one end is connected to other polyhedral WS_2 nanoparticles and this is consistent with our observation of the abundance of polyhedral WS_2 nanoparticles and open ended tubes with large hollow cores meaning that tubes in this study were grown by a gas phase reaction. This fact combined with the observed close helicities of adjacent layers in these nanotubes suggests that there are strong interactions among the shells as the tube grows. This assumption is reasonable considering that the effective charge is different for the curved WS_2 layers causing stronger interactions among them [22]. The observation of only helical nanotubes in this study agrees with the previous findings of WS_2 nanotubes from

gas-phase reaction. This kind of growth structure is energetically and kinetically favorable since it provides a continuous growth front for the layers [7]. The observation of only near zigzag nanotube structures here also suggests that the growth of the tubes with small chiral angles is more favorable in terms of energetics and kinetics of the synthesis reaction than the armchair growth mode. In the solid-gas phase reaction, the growth has a quasi-epitaxial fashion due to the single growth front and progresses inwards [4]. The first one or two layers serve as a template for further growth inward. In the tubes studied here, the outer layers mostly have smaller chiral angles than the inner ones further supporting that near the zigzag growth mode is promoted and more favorable energetically.

The small variations in observed chiral angles might results from the growth mode via defects since large sulfur atoms can only move towards the inner oxide core through the defects in the shells. High temperature synthesis reaction anneals and eliminates some defects and the further growth proceeds via other ones (new ones or kinetically less favorable ones) and this might change the growth front, thus, the helicity. One might expect that the helicity will approach to that of the bulk material as the nanotube diameter increases. Thus it might be possible to obtain nanotubes with pure zigzag structure by tuning the diameter. In this way, the diameter, hence the band gap can be adjusted for specific applications in nano-electronics, photoluminescence, etc. From example 4, we estimate that a nanotube with an innermost diameter of 10 nm and an outermost diameter of 30 nm will be approximately composed of 33-35 shells and its outermost shell will be a zigzag tube. However, nanotubes of smaller diameter with non-helical structures have

already been observed [8, 13]. For open-ended growth, small variations in the growth rate at the tip are most likely the cause of observed small variations in helicities.

5.5 References

1. Tenne, R., Margulis, L., Genut, M., Hodes, G. (1992). Polyhedral and cylindrical structures of tungsten disulfide. *Nature* **360**, 444-446.

2. Feldman, Y., Wasserman, E., Srolovitz, D.J., Tenne, R. (1995). High-rate, gas-phase growth of MoS_2 nested inorganic fullerenes and nanotubes. *Science* **267**, 222-225.

3. Remskar, M. (2004). Inorganic nanotubes. *Adv. Mater.* **16**, 1497-1504.

4. Rothschild, A., Sloan, J., Tenne, R. (2000). Growth of WS_2 nanotubes phases. *J. Am. Chem. Soc.* **122**, 5169-5179.

5. Feldman, Y., Frey, G.L., Homyonfer, M., Lyakhovitskaya, V., Margulis, L., Cohen, H., Hodes, G., Hutchison, J.L., Tenne, R. (1996). Bulk synthesis of inorganic fullerene-like MS_2 (M=Mo, W) from the respective trioxides and the reaction mechanism. *J. Am. Chem. Soc*. **118**, 5362-5367.

6. Homyonfer, M., Alperson, B., Rosenberg, Y., Sapir, L., Cohen, S.R., Hodes, G., Tenne, R. (1998). Intercalation of inorganic fullerene-like structures yields photosensitive films and new tips for scanning probe microscopy. *J. Am. Chem. Soc.* **117**, 2693-2698.

7. Margolin, A., Rosentsveig, R., Albu-Yaron, A., Popovitz-Biro, R., Tenne, R. (2004). Study of the growth mechanism of WS_2 nanotubes produced by fluidized bed reactor. *J. Mat. Chem.* **14**, 617-624.

8. Li, Y.D., Li, X.L., He, R.R., Zhu, J., Deng, Z.X. (2002). Artificial lamellar meso-structures to WS_2 nanotubes. *J. Am. Chem. Soc.* **124**, 1411-1416.

9. Whitby, R.L.D., Hsu, W.K., Fearon, P.K., Billingham, N.C., Maurin, I., Kroto, H.W., Walton, D.R.M., Boothroyd, C.B., Firth, S., Clark, R.J.H., Collison, D. (2002). Multi-walled carbon nanotubes coated with tungsten disulfide. *Chem. Mat.* **14**, 2209-2217.

10. Whitby, R.L.D., Hsu, W.K., Boothroyd, C.B., Kroto, H.W., Walton, D.R.M. (2002). Tungsten disulfide coated multi-walled carbon nanotubes. *Chem. Phys. Lett.* **359**, 121-126.

11. Rothschild, A., Popovitz-Biro, R., Lourie, O., Tenne, R. (2000). Morphology of multi-wall WS_2 nanotubes. *J. Phys. Chem. B* **104**, 8976-8981.

12. Zhu, Y.Q., Hsu, W.K., Terrones, H., Grobert, N., Chang, B.H., Terrones, M., Wei, B.Q., Kroto, H.W., Walton, D.R.M., Boothroyd, C.B., Kinloch, I., Chen, G.Z., Windle, A.H., Fray, D.J. (2000). Morphology, structure and growth of WS_2 nanotubes. *J. Mat. Chem.* **10**, 2570-2577.

13. Margulis, L., Dluzewski, P., Feldman, Y., Tenne, R. (1996). TEM study of chirality in MoS_2 nanotubes. *Journal of Microscopy* **181**, 68-71.

14. Seifert, G., Terrones, H., Terrones, M., Jungnickel, G., Frauenheim, T. (2000). On the electronic structure of WS_2 nanotubes. *Solid Sate Comm.* **114**, 245-248.

15. Scheffer, L., Rosentsveig, R., Margolin, A., Popovitz-Biro, R., Seifert, G., Cohen, S.R., Tenne, R. (2002). Scanning tunneling microscopy study of WS_2 nanotubes. *Phys. Chem. Chem. Phys.* **4**, 2095-2098.

16. Rapoport, L., Bilik, Y., Feldman, Y., Homyonfer, M., Cohen, S.R., Tenne, R. (1997). Hollow nanoparticles of WS_2 as potential solid state lubricants. *Nature* **387**, 791-793.

17. Rothschild, A., Cohen, S.R., Tenne, R. (1999). WS_2 nanotubes as tips in scanning probe microscopy. *Appl. Phys. Lett.* **75**, 4025-4027.

18. Kaplan-Ashiri, I., Cohen, S.R., Gartsman, K., Ivanovskaya, V., Heine, T., Seifert, G., Wiesel, I., Wagner, H.D., Tenne, R. (2006). On the mechanical behavior of WS nanotubes under axial tension and compression. *Proc. Nat. Acad. Science* **103**, 523-528.

19. Seifert, G., Terrones, H., Terrones, M., Jungnickel, G., Frauenheim, T. (2000). Structure and electronic properties of MoS_2 nanotubes. *Phys. Rev. Lett.* **85**, 146-149.

20. Remskar, M., Mrzel, A., Skraba, Z., Jesih, A., Ceh, M., Demsar, J., Stadelmann, P., Levy, F., Mihailovic, D. (2001). Self-assembly of sub-nanometer diameter single-wall MoS_2 nanotubes. Science 292, 479-481.

21. Albe, K., Klein, A. (2002). Density functional theory calculations of electronic band structure of single-crystal and single-layer WS_2. *Phys. Rev. B* **66**, 073413 1-3.

22. Luttrell, R.D., Brown, S., Cao, J., Musfeldt, J.L., Rosentsveig, R., Tenne, R. (2006). Dynamics of bulk versus nanoscale WS_2: Local strain and charging effects. *Phys. Rev. B* **73**, 035410.

23. Rosentsveig, R., Margolin, A., Feldman, Y., Popovitz-Biro, R., Tenne, R. (2002). WS_2 nanotube bundles and foils. *Chem. Mat*. **14**, 471-473.

24. Selvi, E., Yanzhang, M., Aksoy, R., Ertas, A., White, A. (2006). High pressure X-ray diffraction study of tungsten disulfide. *J. Phys. Chem. Sol*. **67**, 2183-2186.

Chapter 6

Short-Range Order (SRO) in Carbon Soot and Boron Nanowires

6.1 Introduction and Motivation

The recent work on the growth of SWNTs suggests that they can be grown by post-annealing a soot sample containing the seeds or precursors needed for their synthesis [1, 2]. This means that a condensed phase of carbon can be converted to nanotubes by metal catalysts during the annealing. What the catalyst particles are doing is to dissolve amorphous carbon on one side and to precipitate it in the form of nanotube on the other side as long as precursors exist in the sample. An understanding of these precursors is important for understanding the nucleation of carbon nanotubes. The precursors, which are nano-crystallite graphitic particles, are embedded in the surrounding amorphous carbon. If we want to learn about the structure of these precursors, we need to study the structure of amorphous carbon in greater detail using analytical methods, such as radial distribution function (RDF) analysis, and fluctuation electron microscopy (FEM). The RDF analysis has also been applied to amorphous boron nanowires to reveal their atomic structure.

6.2 Amorphous Carbon Soot

A total of five samples of carbon soot were synthesized by laser ablation. Two samples were obtained by laser ablation of a pure solid carbon target. The other three were produced from the ablation of a solid carbon target containing a new catalyst (0.3% at. each of Si and Co) for SWNT production. All samples were studied in TEM with imaging and nano-beam diffraction. Two soot samples produced without any catalyst were also studied by a new technique known as fluctuation electron microscopy (FEM) to probe their medium-range structure [3]. They were produced at 300 ^{o}C and 600 ^{o}C (labeled as sample A and sample B respectively). The samples grown from the catalyst-containing target were produced at 650, 600, and 550 ^{o}C where the yield of SWNTs is minimal (sample C, sample D and sample E, respectively). The samples grown without any catalyst particles did not contain any SWNTs. All samples contained graphitic particles and some MWNTs also.

TEM images of the soot samples are given in Fig. 6.2.1. These images were taken from the sample grown at 600 ^{o}C without any catalyst and show that it consists only of amorphous carbon, large graphitic particles and multi-walled nanotubes. The TEM images given in Fig. 6.2.2 are from the sample grown at 650 ^{o}C with the bimetallic Co/Si catalyst. This sample has a few SWNTs, MWNTs, graphitic particles, and catalyst particles of a few nanometers in diameter. Before diffraction experiments were performed, the samples produced with the catalysts were treated in acid to remove the catalyst particles. Otherwise, the strong scattering intensity from these nanocrystalline metal particles would interfere with the signals from amorphous carbon whose structural information was desired. The acid treatment was a simple purification process which

included ultra-sonication of the soot in a mixture of HNO_3 and H_2SO_4 for a few hours, followed by filtration of the solution. The TEM images of the acid-treated samples show that they still contain some metal catalyst particles. So, the acid treatment did not completely remove the particles but just reduced their size and concentration in the samples.

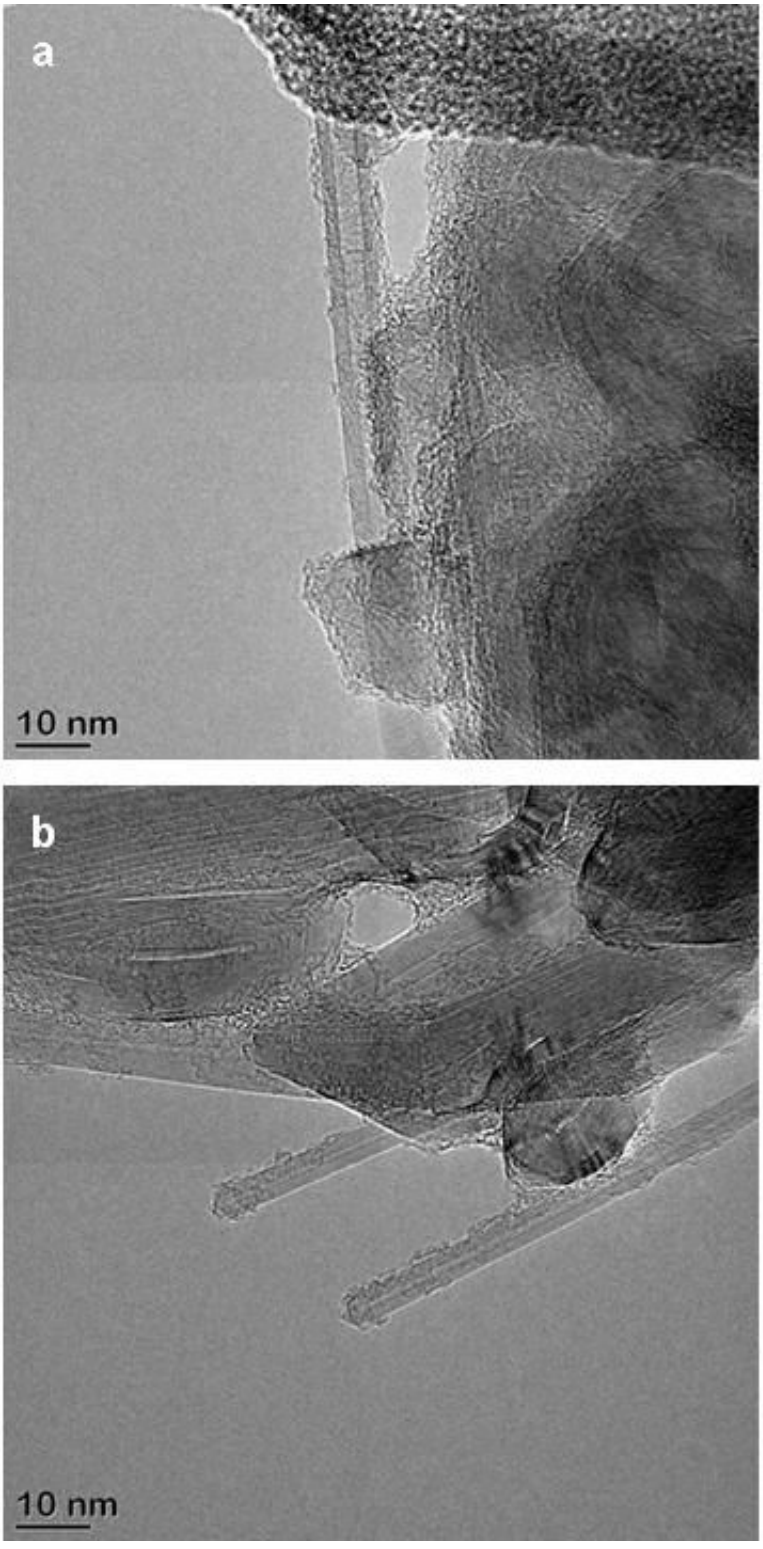

Fig. 6.2.1 (a) and (b) Morphology of carbon soot sample grown at 600 ^{o}C without any catalyst showing graphitic particles and multi-walled carbon nanotubes.

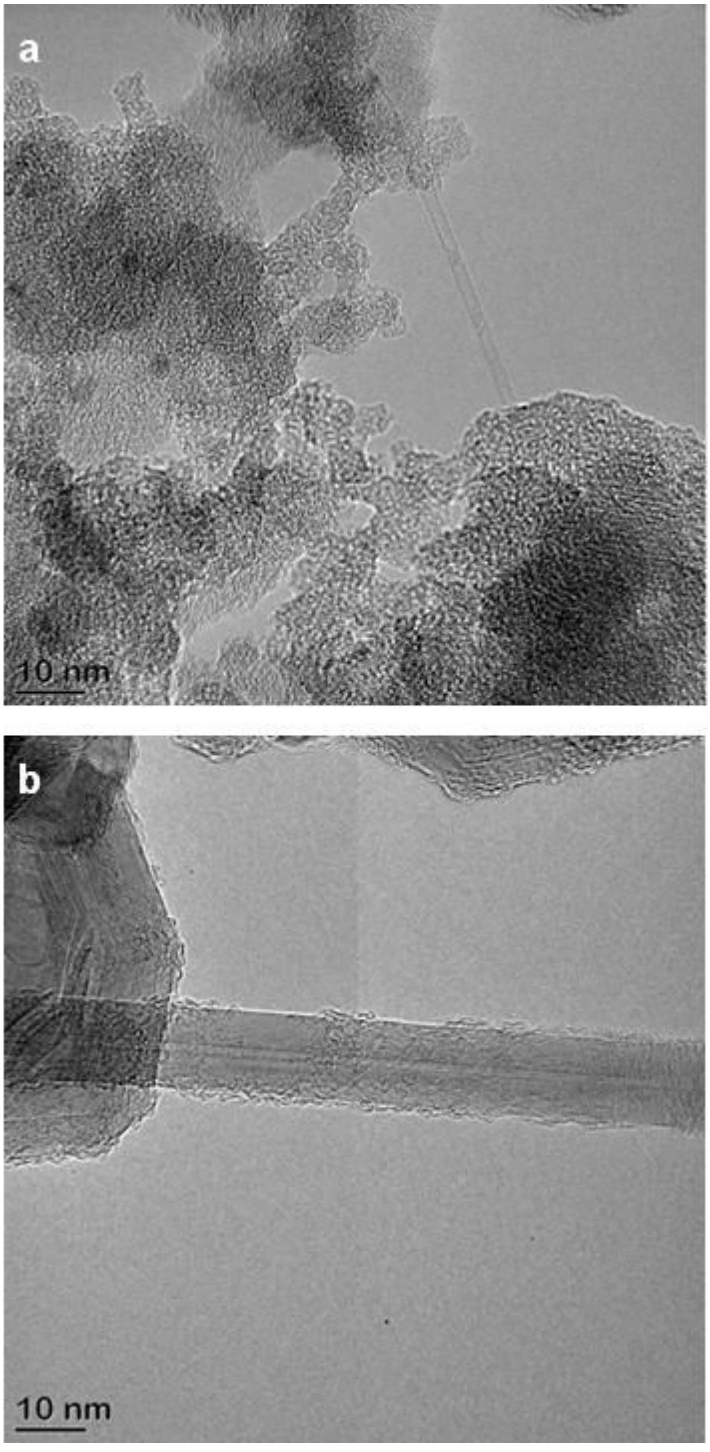

Fig. 6.2.2 (a) Morphology of soot sample grown at 650 ^{o}C with Co/Si catalyst is showing a single-walled carbon nanotube, amorphous carbon, and catalyst particles. (b) Another image showing a multi-walled carbon nanotube from the same sample.

6.3 Electron Diffraction and RDF Analysis of Soot

6.3.1 Theoretical Background

For any form of matter, such as gases, liquids or amorphous solids, the structure factor can be written as a sum of the scattering amplitude from each atom and expressed as

$$F(\vec{q}) = \sum_{j=1}^{N} f_j \exp(-2\pi\vec{q} \cdot \vec{r}_j) \tag{6.3.1}$$

for a total number of N atoms. In equation (6.3.1), $\vec{q}$ is the scattering vector with the amplitude $q = 2\sin\theta/\lambda$ where λ is the wavelength of the radiation and 2θ is the scattering angle, f_j is the atomic scattering amplitude (also known as the atomic form factor) and $\vec{r}$ is the position vector of the atoms. The total scattering intensity from the collection of these N atoms is then

$$I(\vec{q}) = \left|F(\vec{q})\right|^2 = \sum_j \sum_k f_j f_k \exp(-2\pi i\vec{q} \cdot \vec{r}_j) \exp(2\pi i\vec{q} \cdot \vec{r}_k), \tag{6.3.2}$$

or $$I(\vec{q}) = \sum_j \sum_k f_j f_k \exp(-2\pi i\vec{q} \cdot \vec{r}_{jk}), \tag{6.3.3}$$

where $\vec{r}_{jk} = \vec{r}_j - \vec{r}_k$ is a difference vector. If the system is spherically symmetric, each $\vec{r}_{jk}$ vector will take all orientations in space with equal probability and then the average intensity is given by

$$\left\langle I(q)\right\rangle = \frac{1}{4\pi r^2{}_{jk}} \sum_j \sum_k f_j f_k \int\int \exp(-2\pi i q r_{jk} \cos\theta) r_{jk}{}^2 \sin\theta d\theta d\phi$$

$$= \sum_j \sum_k f_j f_k \frac{\sin(2\pi q r_{jk})}{2\pi q r_{jk}}. \tag{6.3.4}$$

Equation (6.3.4) is called the Debye formula or Debye scattering equation [4]. It only involves the distances of each atom from every other atom and not the vector positions. For a given model where the atomic positions are known, this intensity can be calculated

as well as obtained experimentally. Unfortunately, the opposite is not true. The atomic positions can not be obtained from a known experimental intensity.

The intensity equation (6.4.4) can be written in two separate terms as

$$I(q) = \sum_j f^2 + \sum_j f^2 \sum_k \frac{\sin(2\pi q r_{jk})}{2\pi q r_{jk}}, \tag{6.3.5}$$

where $j = k$ is the first term in the sum. This first term is called the independent scattering since it has no dependence on inter-atomic distances. The second term is called the interference scattering and carries the required structural information on the material. This second term can be represented by a density function $\rho(r)$ and the scattering intensity for a collection of N atoms of the same kind becomes

$$I(q) = Nf^2 + Nf^2 \int 4\pi r^2 [\rho(r) - \overline{\rho}] \frac{\sin(2\pi q r)}{2\pi q r} dr\,. \tag{6.3.6}$$

In terms of the experimentally measured quantity $I(q)$, the observable intensity in normalized units is

$$S(q) = \frac{I(q) - Nf^2}{Nf^2}. \tag{6.3.7}$$

This is also called the static structure factor [5]. With a little algebra, the intensity equation (6.3.6) can be rewritten as

$$qS(q) = 2\int r[\rho(r) - \overline{\rho}]\sin(2\pi q r) dr\,. \tag{6.3.8}$$

Using the Fourier transform relations, this equation can be converted to obtain the density function $\rho(r)$ from the static structure factor:

$$4\pi r^2[\rho(r) - \overline{\rho}] = 8\pi r \int qS(q)\sin(2\pi q r) dq\,, \tag{6.3.9}$$

where $\bar{\rho}$ is the average density of the material and $4\pi r^2[\rho(r)-\bar{\rho}]$ is called the reduced radial distribution function (RDF). So, the RDF of a material can be deduced from an experimental diffraction intensity using equation (6.3.9). Since this only gives the average inter-atomic distances, it's worthy noting that it represents the minimum structure in the material.

6.3.2 RDF of Carbon Soot

Electron diffraction patterns were taken from all samples at the accelerating voltage of 120 kV. All patterns were collected on the CCD camera and later calibrated using the {111} lattice spacing of a polycrystalline Au sample. A nano-beam electron probe was employed in the collection of all diffraction intensities. It was generated with the use of the smallest condenser aperture (10 μm) available, exciting the first condenser lens to maximum to create the smallest virtual source size, and by using the smallest α setting (α-1) to get a small convergence angle for the beam. Then, the diffraction images were focused by adjusting the brightness to obtain the sharpest possible spots in the diffraction patterns.

Since the metal catalyst particles still existed in the sample, the areas containing them in the soot sample were avoided in the collection of diffraction patterns. Moreover, the patterns were only collected at the edge of the soot areas where the thickness is minimal so that the inelastic scattering effects can be minimized. The low- and high-magnification TEM images are given in Fig. 6.3.1 displaying the metal particles. The dark contrast seen in the soot areas is due to the thickness effects whereas the edge areas look as if they were transparent. The circle in the high-magnification image shows the location where a

nano-beam probe of 30-40 nm in diameter was placed. The sample area inside the circle looks disordered with no observable nano-crystals or any other structural order.

Fig. 6.3.2 shows a diffraction pattern taken from the area marked by the circle in Fig. 6.3.1. The lines in the diffraction pattern define the angular sector used to obtain the radial intensity distribution by azimuthal averaging. This uncorrected intensity is given in the inset in Fig. 6.3.2 with the horizontal axis in calibrated unit.

Fig. 6.3.3 shows a q-weighted structure factor from one of the samples, from which the reduced RDF curve can be constructed. The part before the first peak was not available experimentally due to the beam stopper but it was extended back to the origin by a smooth interpolation. The details of the RDF analysis can be found in the section on boron nanowires (Ch. 6.1.5 and subsequent sections). The RDF curves calculated for all 5 samples are given in figure 6.3.4. The peak positions from each curve agree with one another well, suggesting that the short-range order structure of all samples is identical. Table 6.3.1 shows the positions of the first two peaks found from each RDF curve with their experimental uncertainties. Also included in the table are the peak positions of graphite, amorphous carbon and amorphous diamond given in the literature [6-8]. The first peak position from our RDF curves agrees well with the experimental value reported before for amorphous carbon.

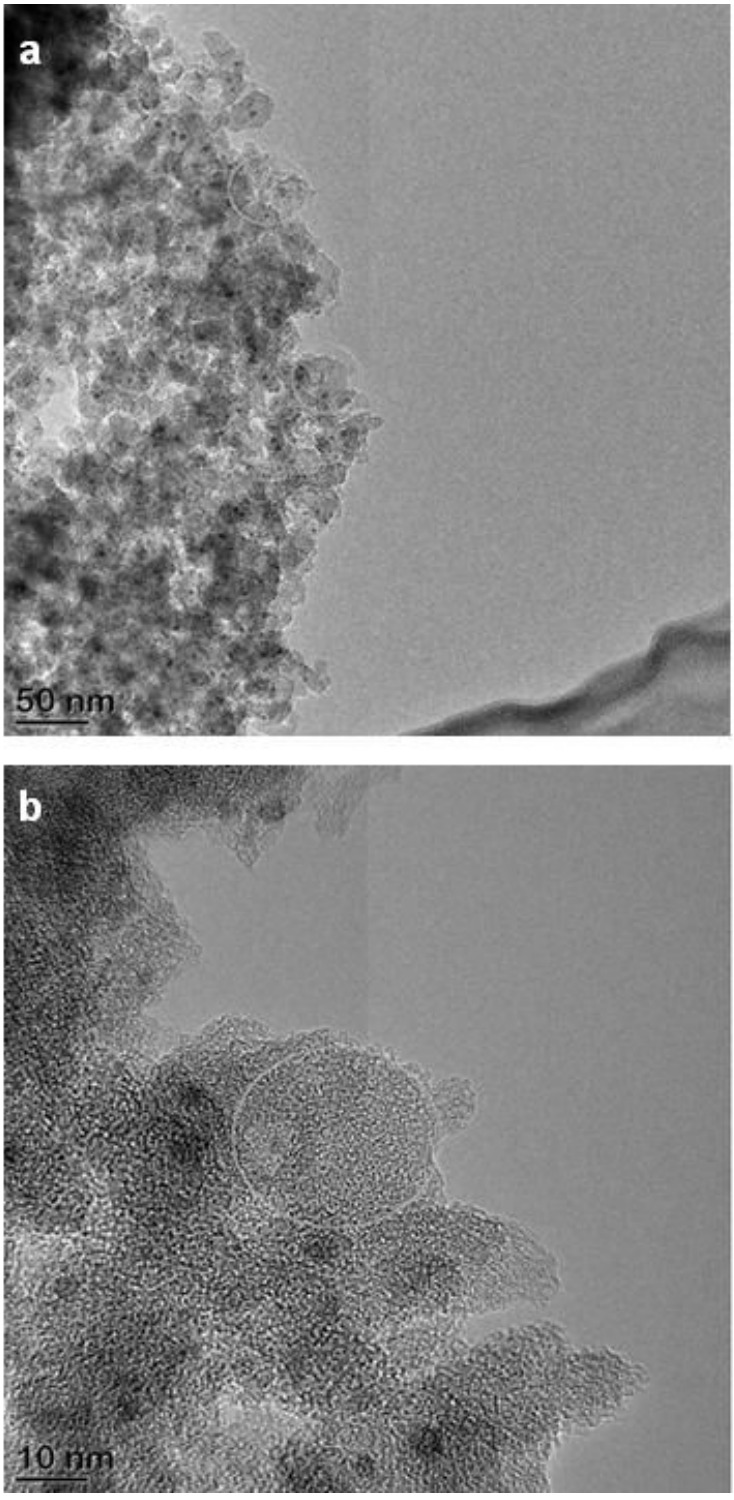

Fig. 6.3.1 (a-b) High magnification TEM images of soot sample showing amorphous carbon and catalyst particles. The circle in (b) indicates where a NBED pattern was acquired.

Table 6.3.1 List of first two peak positions from experimental reduced RDF curves and those of graphite, a-carbon and a-diamond reported in literature [6-8].

	r_1 (Å)	r_2 (Å)
Sample A	1.46 ± 0.20	2.58 ± 0.20
Sample B	1.44 ± 0.20	2.57 ± 0.20
Sample C	1.44 ± 0.20	2.57 ± 0.20
Sample D	1.45 ± 0.20	2.53 ± 0.20
Sample E	1.43 ± 0.20	2.56 ± 0.20
Graphite	1.42	2.46
a-Carbon expt. [6]	1.46 ± 0.04	2.49 ± 0.04
a-Carbon thr. [7]	1.44	2.56
a-Diamond expt. [8]	1.52	2.53

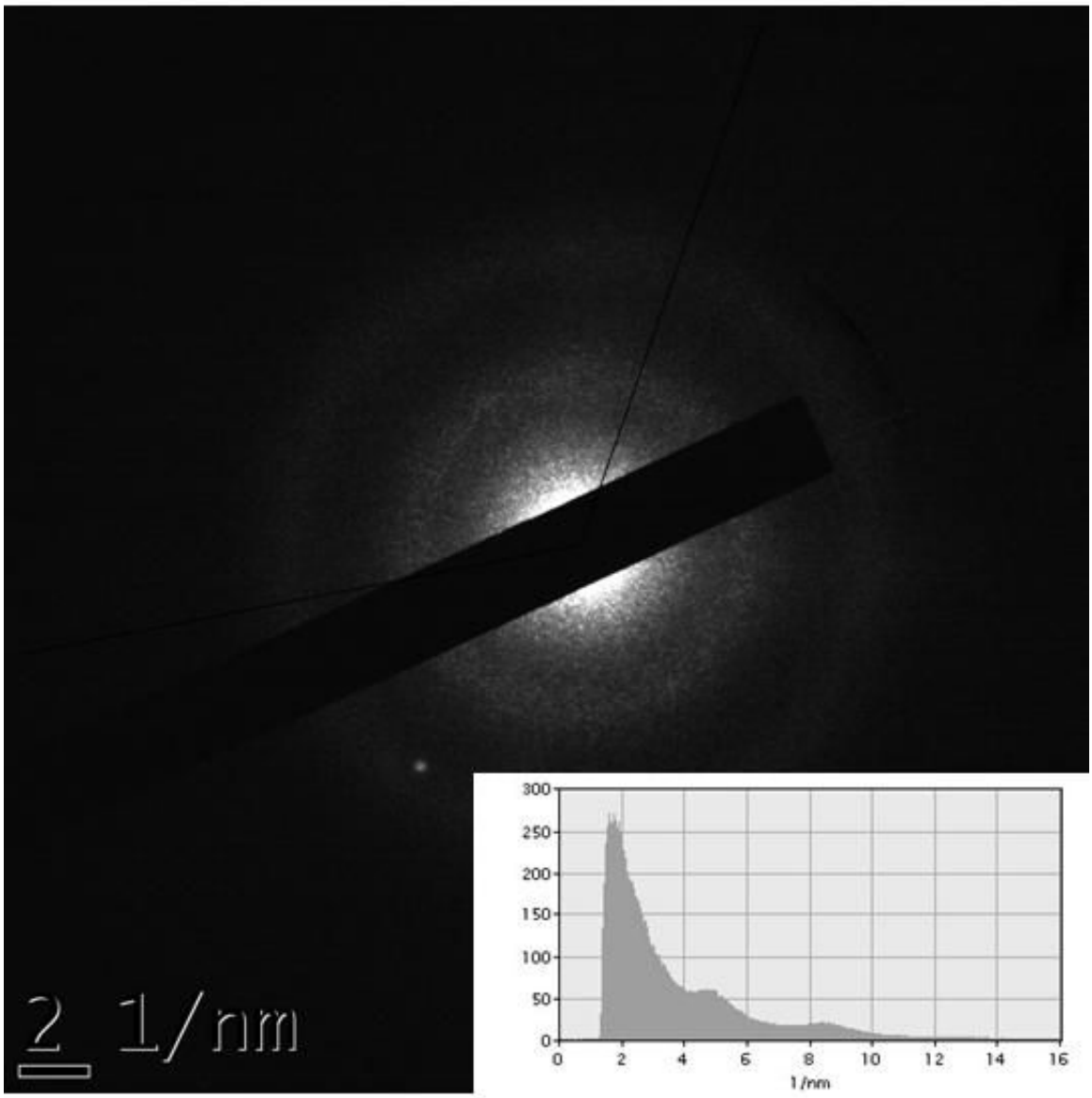

Fig. 6.3.2 Electron diffraction pattern obtained from the circled area in Fig. 6.3.1. The lines indicate the angular sector within which the intensity was averaged azimuthally. The inset shows the azimuthally-averaged radial intensity distribution obtained with the horizontal axis in calibrated unit and with the vertical axis in arbitrary unit.

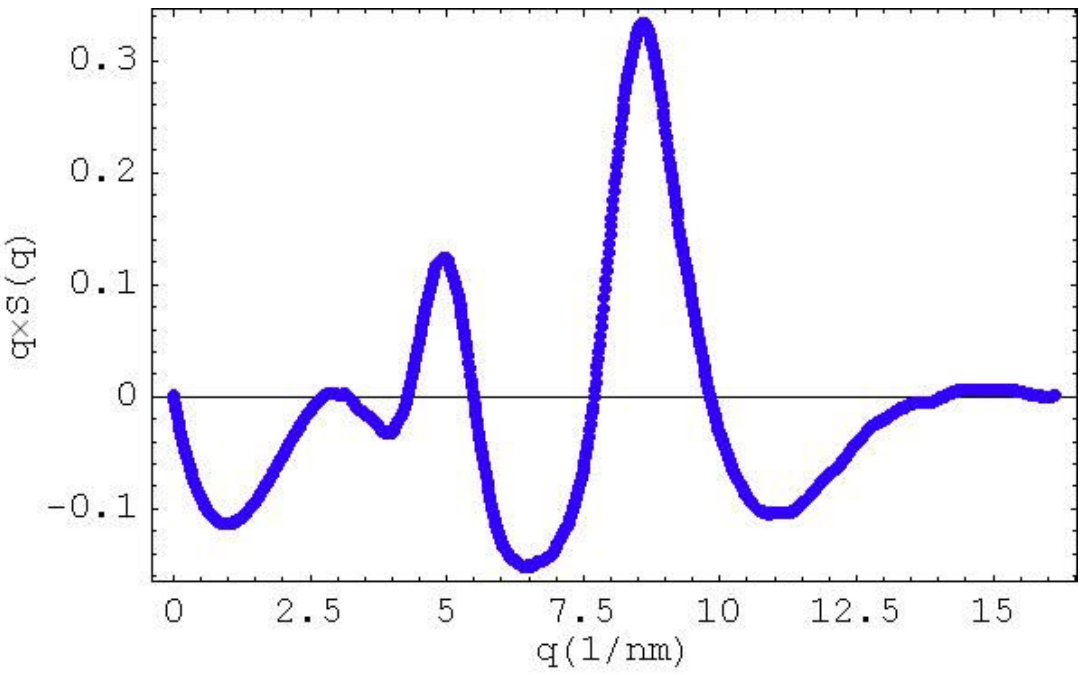

Fig. 6.3.3 *q*-weighted static structure factor curve obtained from sample B.

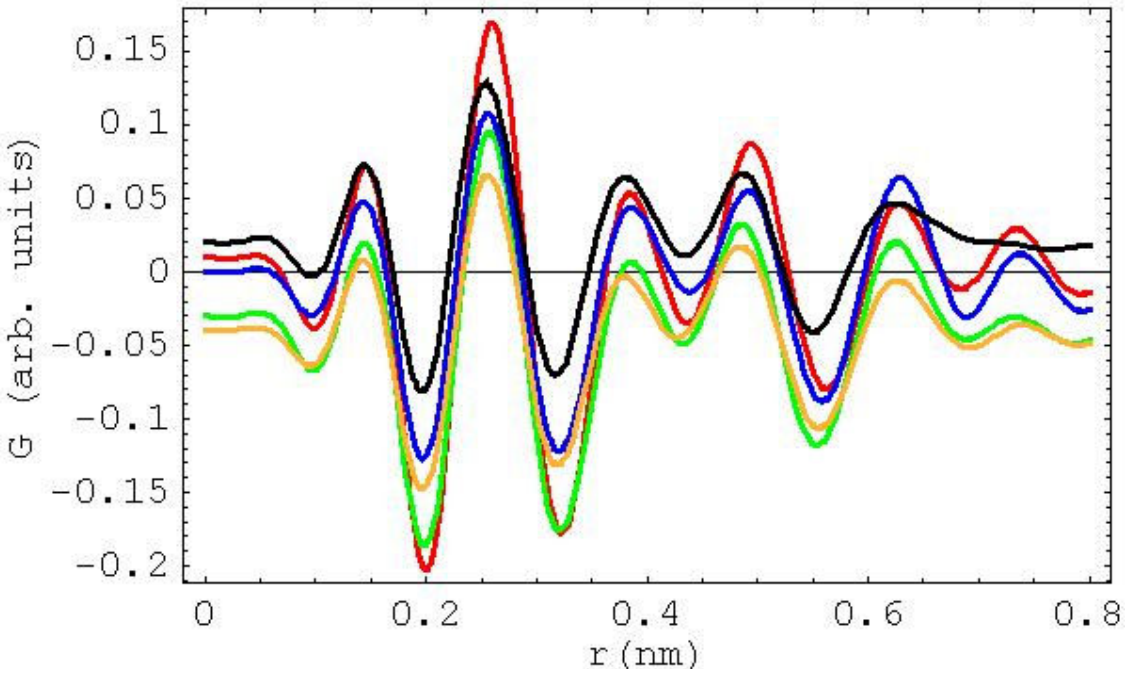

Fig. 6.3.4 Experimental reduced RDF curves obtained for all 5 carbon soot samples (red: sample A, green: sample B, blue: sample C, black: sample D, and orange: sample E). All curves are displaced in vertical direction relative to each other for clarity.

6.4 Fluctuation Electron Microscopy (FEM) on Soot

6.4.1 Theory and Overview

Fluctuation electron microscopy was first implemented by Treacy and Gibson (1996) [3] by using the partial spatial coherence of an electron illumination as a variable parameter to study the statistics of dark field images in a TEM, and named variable coherence microscopy. Here, the coherence parameter is the tilt angle of the electron beam with respect to the optical axis which can be varied easily to study its effects on the statistics of the image speckles. In the treatment, the aberrations of the microscope were ignored since moderate image resolution was used in the experiments, and the kinematical scattering theory was employed by applying this new technique only to thin foils of amorphous materials. The sample is treated as a collection of identical atoms at positions $\vec{r}_j$ and the illumination is a tilted plane wave with a wave vector $\vec{q}$ ($|\vec{q}| = 2\pi \sin\alpha / \lambda$ where α is the tilt angle of the cone and λ is the electron wavelength). The scattered waves are collected by an objective aperture centered on the optic axis. The beam is scattered by the object to an outgoing plane wave that is angled to the optic axis by an amount $\vec{k}$. The amplitude of the scattered wave far from the sample is

$$\phi_j(\vec{r},\vec{r}_j,\vec{q},\vec{k}) = i\lambda f_j(|\vec{k}-\vec{q}|)\exp(-i(\vec{k}-\vec{q})\cdot\vec{r}_j)\exp(i\vec{k}\cdot\vec{r}), \tag{6.4.1}$$

where $f_j(|\vec{k}-\vec{q}|)$ is the atomic form factor of the object and $\vec{r}$ is a spatial coordinate in the far field. The condition $\vec{k} = \vec{q}$ corresponds to a zero deflection of the beam. For the image formation, the scattering waves are collected by an objective aperture and focused on a plane in the far field that is conjugate with the sample plane. The image wave

function u_j of scatterer j is the coherent sum of the scattered plane waves that fall into the objective aperture:

$$u_j(\vec{r},\vec{r}_j,\vec{q},Q) = \iint_{obj} \phi_j(\vec{r},\vec{r}_j,\vec{q},\vec{k})d^2\vec{k}\,, \tag{6.4.2}$$

or

$$u_j(\vec{r},\vec{r}_j,\vec{q},Q) = i\lambda \exp(i\vec{q}\cdot\vec{r}_j)\iint_{obj} f_j(\left|\vec{k}-\vec{q}\right|)\exp(i\vec{k}\cdot(\vec{r}-\vec{r}_j))d^2\vec{k}\,. \tag{6.4.3}$$

For dark field imaging, we have $\left|\vec{q}\right| > Q$, since the undiffracted beam does not enter the objective aperture. For moderate-resolution imaging, where the individual scatterers are not resolved, the following approximation can be introduced:

$$u_j(\vec{r},\vec{r}_j,\vec{q},Q) = f_j(q)a_j(\vec{r}-\vec{r}_j,Q)\exp(i\vec{q}\cdot\vec{r}_j)\,, \tag{6.4.4}$$

where

$$a_j(\vec{r}-\vec{r}_j,Q) = i\lambda\iint_{obj}\exp(i\vec{k}\cdot(\vec{r}-\vec{r}_j))d^2\vec{k}\,. \tag{6.4.5}$$

The function $a_j(\vec{r}-\vec{r}_j,Q)$ represents the amplitude of the point-spread function of the optical system at position $\vec{r}$ when it is centered on the atom j. There are two equivalent methods to obtain images in a microscope [9]. In TEM, the sample is illuminated by a fixed, well-defined source and the scattered beam is collected and magnified by an objective lens and projected onto an image plane by projector lenses in the imaging system. The image differs from the sample in the sense that it's filtered and magnified by the imaging lenses in the microscope, whose most important part is the objective lens and aperture. In STEM, the sample is irradiated by a finely-focused electron probe that is formed by the objective lens and the images are built up by rastering the probe over the sample. The scattered wave is collected by the detectors and displayed as a two-

dimensional intensity array. Since these two methods can produce identical images, the function a_j can be interpreted in two different ways. For fixed illumination, $a_j{}^2$ is the point-spread function of the microscope that defines the resolution of the image. For a scanned probe, $a_j{}^2$ is the probe intensity profile defining the probed sample width and the resolution of the scanned image. The fluctuation microscopy relies on the variations in the scattered intensity between the sample sub-volumes. This shows up as a speckle in the dark field images of the amorphous materials and the speckle can be quantified by studying the mean and the variance of the image intensity. The normalized variance of the image is defined by

$$V(\vec{q},Q) = \left\langle I^2(\vec{q},Q)\right\rangle / \left\langle I(\vec{q},Q)\right\rangle^2 - 1. \tag{6.4.6}$$

The normalization of the second moment of the image intensity by the average image intensity eliminates the dependence of the normalized variance on the atomic form factor $f(q)$. For TEM imaging, the kinematical dark field image wave function is the sum of the individual scattered wave functions:

$$U_j(\vec{r},\vec{q},Q) = \sum_j u_j(\vec{r},\vec{r}_j,\vec{q},Q). \tag{6.4.7}$$

Then, the kinematical dark field image intensity at a specimen position $\vec{r}$ is given by

$$\begin{aligned} I(\vec{r},\vec{q},Q) &= \sum_{j,l} u_j(\vec{r},\vec{r}_j,q) \times u_j{}^*(\vec{r},\vec{r}_l,Q) \\ &= f^2(q)\sum_{jl} a_j(\vec{r},\vec{r}_j,Q) a_l{}^*(\vec{r},\vec{r}_l,Q)\exp(-i\vec{q}\cdot\vec{r}_{jl}). \end{aligned} \tag{6.4.8}$$

The quantity $\vec{r}_{jl}$ represents the position vector of atom *l* with respect to atom *j* and $f(k)$ is the atomic form factor (mono-atomic system). The mean image intensity is the average intensity over the sample area A:

$$\left\langle I(\vec{q},Q)\right\rangle = [f^2(q)/A]\sum_{j,l}\iint a_j a_l^{\,*} \times \exp(-i\vec{q}\cdot\vec{r}_{jl})d^2\vec{r}\ . \tag{6.4.9}$$

It's very straightforward to show that $\iint\limits_{sample} a_j a_l^{\,*} d^2\vec{r} = \lambda^2 \iint\limits_{obj} \exp(i\vec{k}\cdot\vec{r}_{jl})d^2\vec{k}$. With the help of this relation, the mean image intensity $\left\langle I(\vec{q},Q)\right\rangle$ becomes

$$\left\langle I(\vec{q},Q)\right\rangle = [\lambda^2 f^2(q)/A]\sum_{j,l}\iint_{obj} \exp[i(\vec{k}-\vec{q})\cdot\vec{r}]d^2\vec{k}\ . \tag{6.4.10}$$

In the expression (6.4.10), $\vec{k}-\vec{q}$ is the total scattering vector experienced by the beam at $\vec{q}$ in the objective aperture. Thus, the mean image intensity is nothing but the total diffracted intensity collected by the objective aperture and averaged over the image area A. We learn nothing more from the average image intensity than we do from the diffraction. The second moment of the image intensity might be a more useful quantity than the average image intensity:

$$\left\langle I^2(\vec{q},Q)\right\rangle = [f^4(k)/A]\sum_{jlmn}\exp[-i\vec{q}\cdot(\vec{r}_{jl}+\vec{r}_{mn})]\times\iint_{sample} a_j a_l^{\,*} a_m a_n^{\,*} d^2\vec{r}\ . \tag{6.4.11}$$

The integral over the sample in (6.4.11) can be simplified to [7]

$$\iint\limits_{sample} a_j a_l^{\,*} a_m a_n^{\,*} d^2\vec{r} = \lambda^4 \iint\limits_{obj} \exp[i\vec{k}\cdot(\vec{r}_{jl}+\vec{r}_{nl}+\vec{r}_{mn})]d^2\vec{k}_1 d^2\vec{k}_2 d^2\vec{k}_3\ . \tag{6.4.12}$$

With equation (6.4.12) placed in (6.4.11), the second moment of the image intensity is

$$\left\langle I^2(\vec{q},Q)\right\rangle = [\lambda^4 f^4(k)/A]\sum_{jlmn}\exp[-i\vec{q}\cdot(\vec{r}_{jl}+\vec{r}_{mn})]\times\iint_{obj}\exp(i\vec{k}\cdot\vec{r}_{jn})d^2\vec{k}_1\times\iint_{obj}\exp(i\vec{k}\cdot\vec{r}_{nl})d^2\vec{k}_2$$

$$\times\iint_{obj}\exp(i\vec{k}\cdot\vec{r}_{mn})d^2\vec{k}_3\ . \tag{6.4.13}$$

Two types of interference terms that appear in the mean image intensity and in the second moment of the image intensity is

$$F_{jl} = \exp(-i\vec{q} \cdot \vec{r}_{jl}) \ , \tag{6.4.14}$$

and

$$A_{jl} = \iint_{obj} \exp(i\vec{k} \cdot \vec{r}_{jl}) d^2\vec{k} = 2J_1(Qr_{jl}) / Qr_{jl} \, , \tag{6.4.15}$$

where J_1 is the first-order Bessel function. The F_{jl} term corresponds to the coherence strength for interference between scatterer *j* and *l*. It has been considered as a plane wave illumination so far. For a hollow-cone illumination, it can be replaced by a modified coherence strength term. The A_{jl} (Airy disks) terms are proportional to the point-spread function of the microscope. The F_{jl} interferences are controlled by the illumination optics and the A_{jl} interferences are controlled by the imaging optics of the microscope. With these two definitions, the normalized variance can be written as

$$V(\vec{q}, Q) = N_0 \frac{\sum_{jlmn} A_{jn} A_{nl} A_{mn} F_{jl} F_{mn}}{\sum_{pqrs} A_{pq} A_{rs} F_{jl} F_{mn}} - 1 \, , \tag{6.4.16}$$

where $N_0 = \pi A Q^2$ is the number of pixels in the image. The standard deviation is equal to the square root of V. The speckle is maximized when similar atom pairs are localized within the same column, which is determined by the width of the Airy discs. Therefore, the speckle reveals a higher-order pair-pair correlation and contains information beyond the first order pair correlation obtained from diffraction [9].

This new technique has been extensively applied to study the MRO structure of amorphous semiconductors, such as vacuum evaporated silicon Si and germanium Ge [10]. The dark field TEM images of amorphous materials show the speckles of white and dark spots against a smooth background. This variance observed in the images is sensitive to the imaging conditions of the microscope (like focusing). How FEM was used in these studies is that the low-resolution hollow-cone dark field images were acquired as a function of the tilt angle of the incident electron beam by maintaining the objective lens at optimum. For each image, the statistics of image intensity were studied by calculating the normalized variance and plotted as a function of the tilt angle. The variance plot shows two broad maxima in general. It has also been observed that the variance is reduced when the sample is annealed. These two facts were interpreted as a presence of significant medium-range order in the samples because the variance has a prominent functional dependence on the tilt angle and varies when the sample is annealed, unlike the diffraction intensities which remain same [9]. It was also shown recently that FEM measurements can be done by nano-diffraction mode in a scanning TEM (STEM) [11]. In this mode, a nanometer size probe can explore small volumes of the sample and the diffraction patterns can be collected at different sample points. This mode of FEM is called variable resolution microscopy and can be used to extract the length scale of medium-range order since the coherence length of the probe sets the length scale of the measurement [11]. The evolution of the peaks in the variance as a function of probe size can reveal the length scale of the ordering.

6.4.2 Experimentation and Results

Two pure carbon soot samples were studied by FEM using nano-diffraction patterns. The samples were produced by laser ablation of a solid graphite target (without any metal catalyst) at temperatures of 300 ^{o}C and 600 ^{o}C. The soot samples were dispersed in ethanol by ultra-sonication. The droplets of the suspensions were deposited on TEM grids to be studied. The convergent beam electron diffraction patterns were collected on both samples with a probe size of 1.3 nm at the accelerating voltage of 120 kV. The diffraction patterns were acquired on the CCD camera with an exposure time of two seconds. A single crystal Si with a [110] zone axis was used to calibrate the diffraction patterns. The number of the diffraction patterns acquired was approximately 200 for both samples.

For each sample, an average of all diffraction patterns and an average of their squares were calculated to obtain the variance in 2D. The radial intensity distribution was obtained by azimuthally averaging the diffraction intensity over a sector and avoiding the beam stopper. This average intensity as a function of the scattering vector gives the information on the short range order in the samples. This is given for both samples in Fig. 6.4.1. The curves are nearly identical. The Fourier inversion of this average scattering can be used to construct the RDF, which will give the information on the nearest bond distances in the samples. The scattering curves indicate that the short-range order in these samples is indistinguishable. This is also supported by the fact that the reduced RDF curves of these two samples from Fig.6.3.5 are nearly identical, with the first two peak positions in agreement with each other. This is also consistent with the recent findings on amorphous carbon films grown by pulsed laser ablation [12]. The only difference is that their results were obtained on as-grown and post-annealed samples.

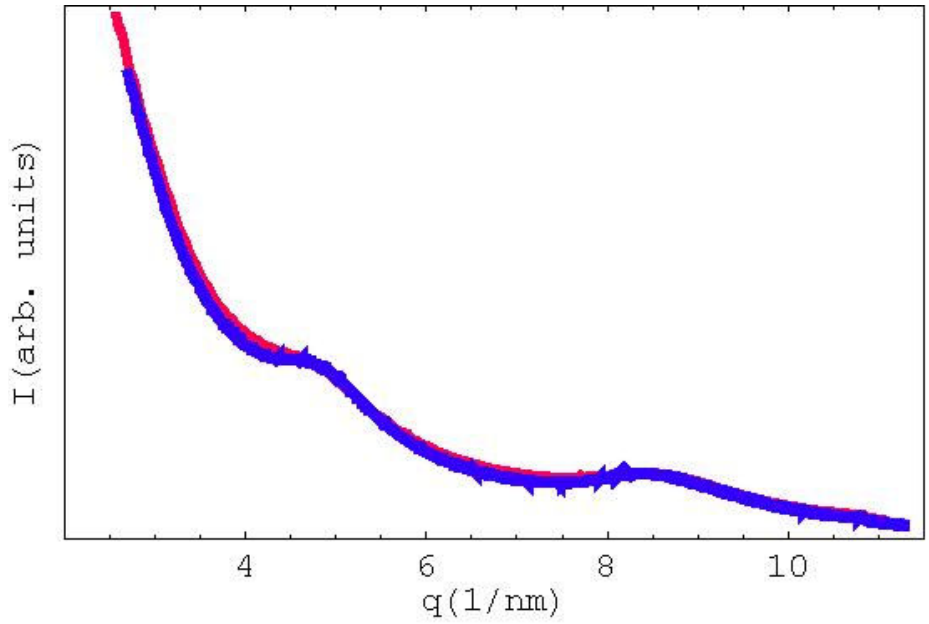

Fig. 6.4.1 Uncorrected average intensity curves for sample A (red curve) and sample B (blue curve).

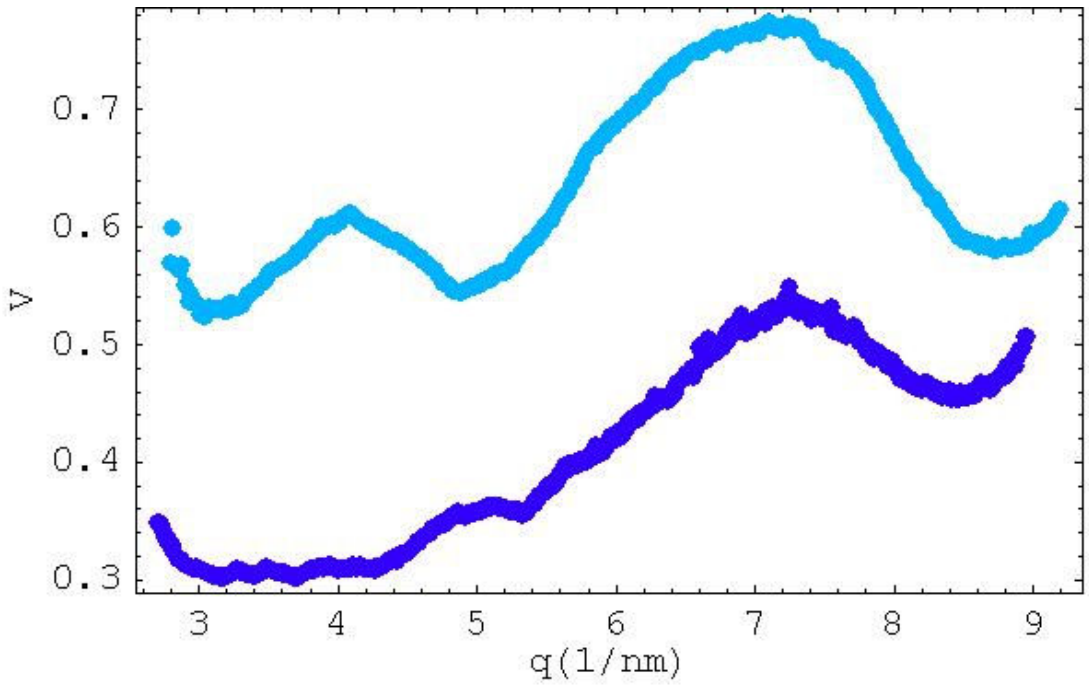

Fig. 6.4.2 Experimental variance curves of carbon soot samples. The curve in lighter blue is for sample A and the curve in darker blue is for sample B.

The variance curves calculated for both samples are given in Fig. 6.4.2. It's seen from the curves that the height of the first peak is reduced with increasing ablation temperature. The peak height in the variance curve is proportional to the number of corresponding structure units in the sample [12]. This change indicates that the sample produced at lower temperature has more medium range order than the other sample. Moreover, the peak position of the high temperature sample shifts to a higher q value. This indicates that the structural units associated with medium-range order in this sample are changing and resembling those of short-range order more. This is in contrast to the low temperature sample (remembering that the lower scattering vectors in reciprocal space are associated with greater distances in real space). The finding of the length scale in this sample necessitates further FEM experiments on the sample with different probe sizes. The height of this peak can be mapped until it reaches the maximum where the probe size is also the characteristic length scale of the MRO in the sample [11].

6.5 Boron and Its Structure

Boron has one of the most complex structural chemistry among all elements [13]. The complexity of boron structures results from its electron deficient nature due to one vacant p-orbital. More than 16 crystalline allotropes of boron have been reported in the literature but only three of them have been confirmed as crystalline states of boron so far [13-16]. The building blocks for boron structures are icosahedra. Icosahedron is one of the five platonic solids with 12 vertices, 30 edges and 20 equilateral triangle faces. The unit cell of the most common allotrope, the tetragonal boron, consists of four icosahedra (a boron atom sits at each vertex) and two boron atoms connecting the icosahedra to complete the

framework of the structure with a total number of 50 atoms in the unit cell (hence called T-50). The structure of T-50 boron is best described by the space group $P4_2/nnm$ with lattice constants of $a = 8.756$ Å and $c = 5.078$ Å [11]. Each atom in the icosahedron makes five intra-icosahedral bonds and one inter-icosahedral bond and for two additional boron atoms each makes four bonds to connect four icosahedra to each other [13]. Fig. 6.5.1 shows the model structure of tetragonal boron. Other two allotropes are α-rhombohedral (R-12) and β-rhombohedral (R-105) boron.

Research on boron has drawn a new attention in the last decade with its successful synthesis in the form of nanowires [17]. First nanowires grown by magnetron sputtering, which were amorphous in structure, were followed by the news of ones in the crystalline state synthesized by CVD [18]. It has also been predicted that nanotubes synthesized out of boron will have a metallic-like density of states with even higher conductivity than that of carbon nanotubes [19], and they should exhibit metallic behavior regardless of their chirality and diameter unlike carbon nanotubes [20]. This was realized a few years ago by the first synthesis of pure single-walled boron nanotubes [21].

This recent attention to boron is well understood considering that boron has been used in many technological applications ranging from nuclear engineering to semiconductor devices to a lightweight armor for space shuttles. Boron is a light material with a high melting point (2300 ^{o}C) and has hardness as high as diamond.

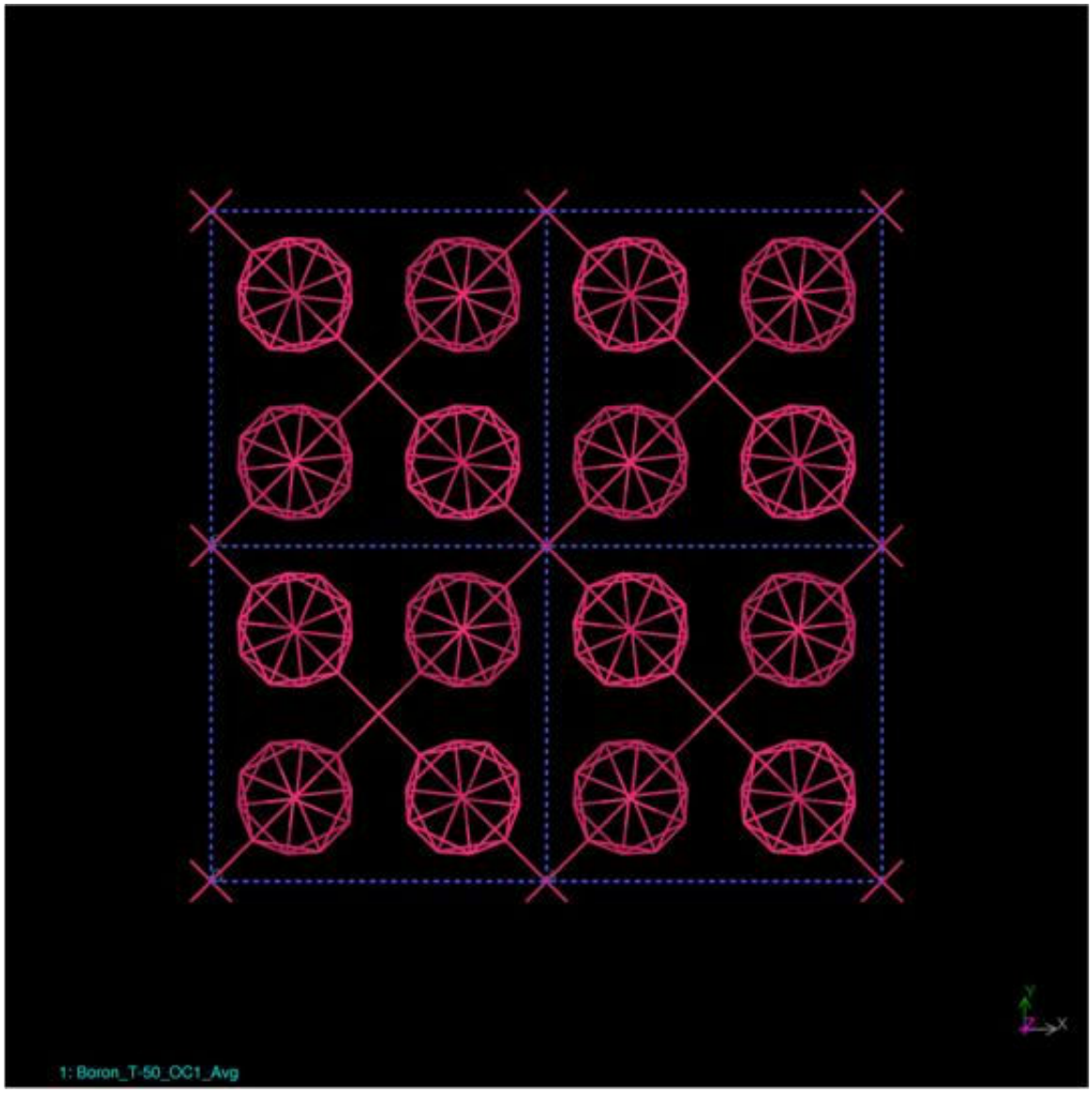

Fig. 6.5.1 Model structure of the crystalline tetragonal boron (T-50) with four unit cells drawn looking down at the c-axis.

6.6 Amorphous Boron Nanowires

The amorphous boron nanowires used in this study were fabricated by chemical vapor deposition. They have been studied by JEM-100CXII and JEM-2010F electron microscopes for imaging and diffraction experiments. A typical amorphous boron nanowire has diameter of a few tens to a few hundred nanometers with length up to a few μm, as shown in the TEM image given in Fig. 6.6.1. The disordered structure is well revealed in the high resolution electron micrograph given in Fig. 6.6.2. The selected area electron diffraction (SAED) patterns were acquired in the JEM-2010F microscope with a parallel illumination of electron beam. The diffraction patterns were recorded on both photographic film and the CCD camera. The data obtained on the CCD camera was chosen to be analyzed since the CCD camera has much better dynamical range for data recording with a linear response compared to the films. The patterns from the CCD camera were later calibrated using crystalline standard samples like polycrystalline gold or aluminum. Since the nanowires in this study might have diameters up to a few hundred nanometers, there is strong inelastic electron scattering in the diffraction data, being especially strongest in the forward direction. Lacking an energy filtering spectrometer available to eliminate inelastic electron scattering, theoretical and numerical approaches have been adopted to correct the data for it.

The SAED pattern taken on one of nanowires is given in Fig. 6.6.3. The diffused intensity rings seen on the image are characteristic of diffraction patterns from amorphous materials. The image is a 2D representation of the 3D structure of amorphous boron. The symmetry and homogeneity of the pattern suggest that the 3D structure of boron is isotropic and homogenous meaning that there is no preferred direction in the

material. With this observation, the radial intensity distribution can be obtained by averaging the intensity over an angular sector. The inelastic electron scattering manifests itself as a continuous background noise that decreases with scattering angle and overlaps with the elastic scattering intensities recorded in diffraction pattern. It results from the energy fluctuations of the electrons incident on the detector, and today it can be eliminated from the diffraction intensities obtained in microscopes equipped with an electron energy-loss spectrometer or can be reduced significantly by using the thinnest specimens available. The desired signal from a scattering experiment of an amorphous sample is the elastically scattered electrons which carry the information on the short-range order of the atomic arrangements in the material. The inelastic electron scattering can be due to many scattering mechanisms, such as fast secondary electron excitations, plasmon scattering, thermal diffuse scattering, etc., with each having different cross-sections and different contributions to the observed inelastic background in the final electron diffraction pattern. All the processes responsible for inelastic scattering are not as well understood as the elastic scattering and there are no theories available to correlate the inelastic scattering with the sample structure or to formulate it in a well-quantified way.

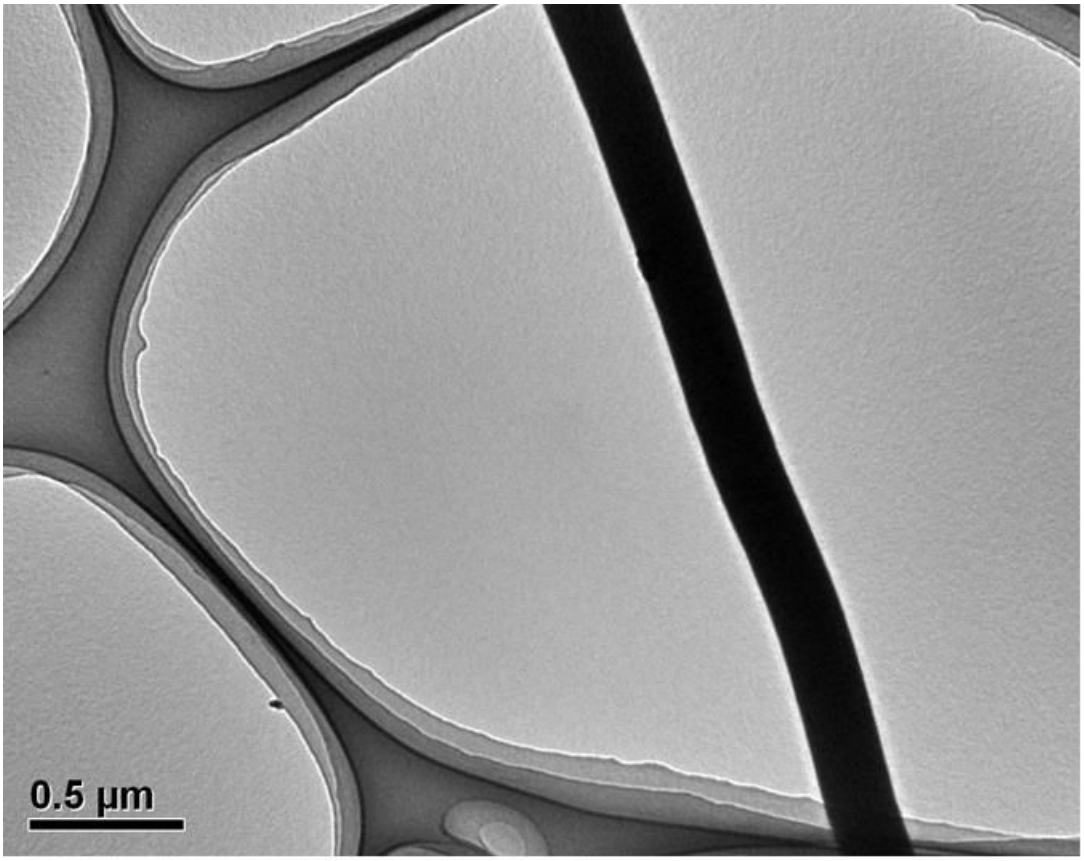

Fig. 6.6.1 Low magnification TEM image of a typical amorphous boron nanowire whose typical length is a few µm.

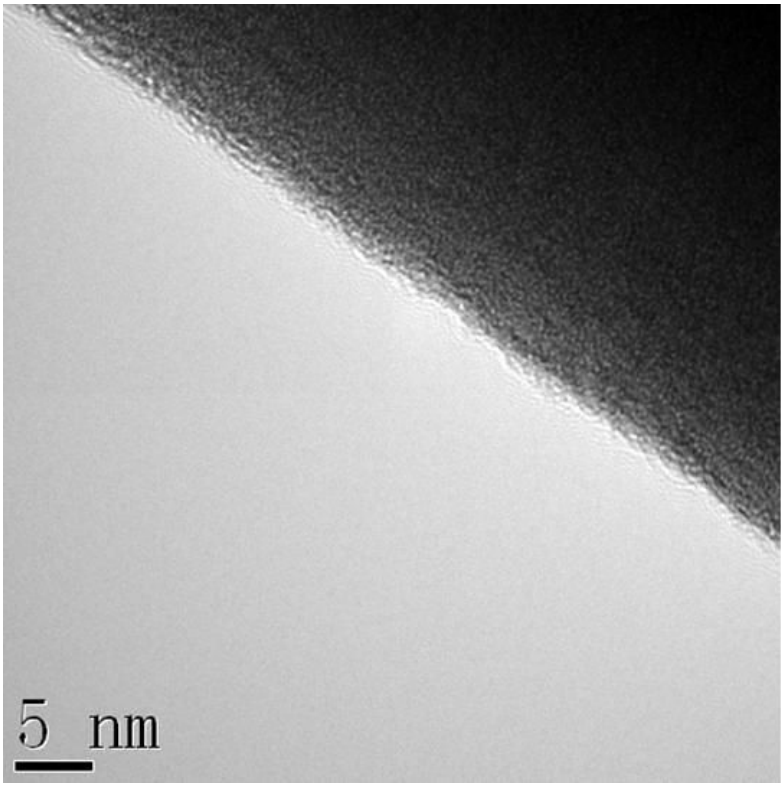

Fig. 6.6.2 High resolution TEM image of a boron nanowire showing a disordered structure.

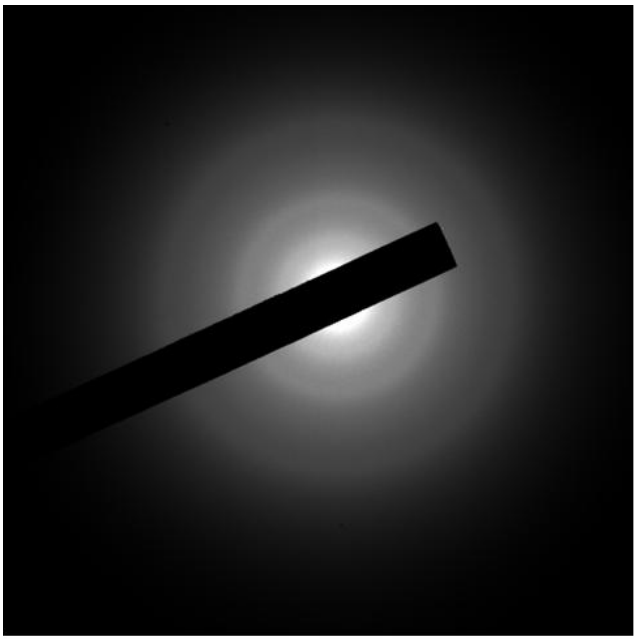

Fig. 6.6.3 Electron diffraction pattern of a boron nanowire.

6.7 RDF Analysis of Amorphous Boron Nanowires

The measured scattering intensity of an amorphous sample is averaged over the whole volume probed by the electron beam if there is no preferred orientation in the structure. The electron diffraction patterns show three concentric diffuse rings (in this case) that rise over a noisy background. After the inelastic scattering was accounted for, the remaining is the elastic scattering whose Fourier sine transform gives the reduced RDF which shows the nearest neighbor distances of the atoms in the structure. The RDF only gives the information about the few bond length distances from any given atom and quickly becomes zero after that. The measured elastic scattering intensity $I(q)$ needs to be converted to the intensity in absolute units to obtain the static structure factor $i(q) = \frac{I(q)}{Nf(q)^2} - 1$ where $f(q)$ is the atomic scattering factor for electrons and N is a normalization constant. The Fourier transform of the q-weighted static structure factor $q \times i(q)$ produces the reduced RDF $G(r) = 4\pi \times r(\rho - \overline{\rho})$. Here, ρ is the density at a distance r from any given atom, and $\overline{\rho}$ is the average atomic density of the sample over the whole volume. $G(r)$ is mathematically formulated in terms of the measured intensity as

$$G(r) = 8\pi \int_0^\infty q \times i(q) \sin(2\pi qr) dq \qquad (6.7.1)$$

where the scattering vector q is defined to be $2\sin\theta/\lambda$. Here, the integration is performed from zero to infinity. In practice, the data can only be collected up to a finite value of q. The termination of the data at a finite q value introduces false peaks called the truncation satellites in the reduced radial distribution function [22]. This can be

accounted for by multiplying $q \times i(q)$ with a modification function. There have been several modification functions used in the literature and the most common one is the Lorch modification function

$$M(q) = \frac{Sin[\pi q / q_m]}{\pi q / q_m}, \tag{6.7.2}$$

where q_m is the upper limit of the scattering vector [23]. The noise at high q values is intensified when the intensity is divided by $f(q)^2$ and later multiplied by q. To reduce this effect, the q-weighted static structure factor was multiplied with an exponential damping factor $\exp(-bq^2)$ where b was chosen to make the exponential 0.1 at the upper limit of the scattering vector q_m [24].

To obtain the structure of the amorphous nanowires, we need to estimate and to eliminate the inelastic scattering from our data so that the Fourier sine transform of the corrected part of scattering data gives us the reduced radial distribution function (RDF). The inelastic x-ray scattering is given by the relationship

$$S(q) = Z - f_x(q)^2, \tag{6.7.3}$$

where Z is the atomic number and $f_x(q)$ is the x-ray atomic scattering factor [4]. The inelastic electron scattering cross-section is related to the x-ray inelastic scattering cross-section by the Morse approximation and is given by the formula

$$\sigma_{inl} = 4S(q) / a^2 q^4, \tag{6.7.4}$$

where a is a constant [25]. The Morse approximation just represents the scattering from infinitely heavy particles by fast incident electrons by neglecting the dependence of energy loss on the scattering vector, recoil of bound electrons in the target and reaching

highly excited energy levels of the target by collision. The Morse approximation fails to describe the inelastic scattering at scattering vector values higher than 1.0 $Å^{-1}$ [25]. It falls off very quickly as a function of the scattering vector q due to inverse fourth power dependence. The scattering described by the Morse approximation and $f(q)^2$ is negligible at the high scattering vectors. Thus, another curve is needed to add to the $Nf^2 + C'\sigma_{inl}$ to estimate the inelastic scattering at high q values so that the measured intensity oscillates above and below the total intensity and the intensity measured matches it at higher values of scattering vectors. Then, the total scattering intensity taking into account this new curve can be formulated by

$$I_{Total} = Nf^2 + C'\sigma_{inl} + C''m(q). \tag{6.7.5}$$

Here, the second and third terms are the contributions due to the inelastic scattering. It has been made sure that $C'\sigma_{inl} + C''m(q)$ is a smoothly varying function and does not introduce any false peaks to the measured intensity.

Our experimental q-weighted static structure factor $q \times i(q)$ curve for amorphous boron nanowires is shown in Fig. 6.7.1. The first sharp diffraction peak is located at 2.5 nm^{-1}. The curve shows that the peaks get broader at high scattering angles and this is the one of the characteristics of the scattering from amorphous materials. Fig. 6.7.2 shows the experimental reduced RDF curve where the horizontal axis is the radial distance in nanometers from any given atom on average. The first peak in the reduced RDF, which is usually seen lower than 0.1 nm, results from numerical errors due to the truncation of the data, inaccuracy of normalization constant and errors in the scattering factors at high q values.

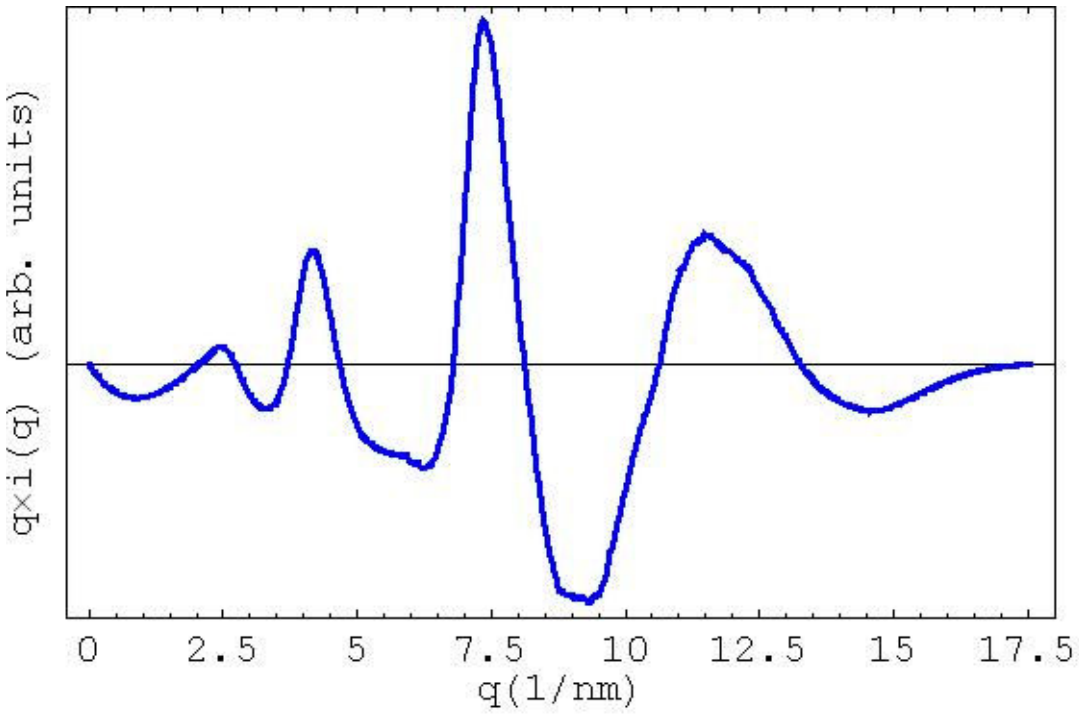

Fig. 6.7.1 Experimental *q*-weighted static structure factor of a boron nanowire.

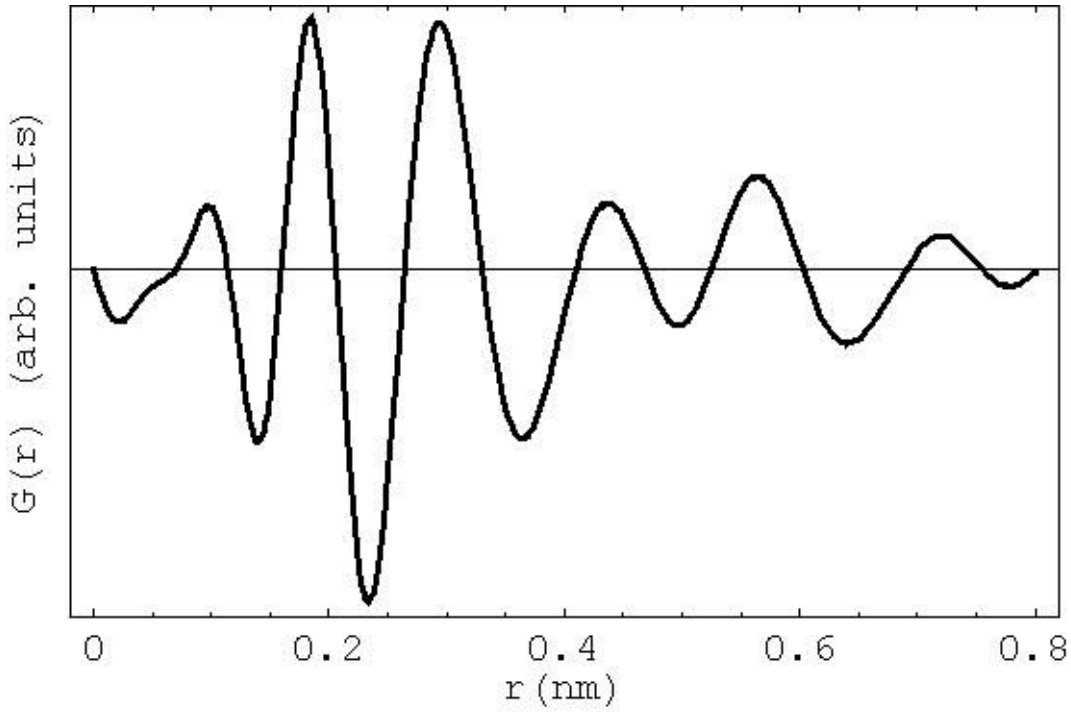

Fig. 6.7.2 Experimental reduced RDF curve of a boron nanowire.

The part of G(r) before the first real peak should be a straight line with a slope of -4πρ where ρ is the atomic density of the material under investigation [26]. The part before the real first peak, which is the first nearest neighbor distance of the atoms in the material, was replaced by a straight line. Then, we obtain a new $q \times i(q)$ curve by a reverse Fourier transformation of the reduced RDF. One more Fourier transformation of the new q-weighted static structure factor gives us the new corrected reduced RDF function. Fig. 6.7.3 and 6.7.4 show both the new q-weighted static structure factor and the corrected reduced RDF, respectively.

The positions of the first three peaks from the reduced RDF curve are 1.82±0.3 Å, 2.94±0.3 Å, and 4.36±0.3 Å, respectively. The positions reported for first three peaks of amorphous boron in the literature are 1.80 Å, 2.93 Å, and 4.38 Å, respectively [13]. Our peak positions are in agreement with the literature values. The resolution Δ in real space is limited by the maximum value of the scattering vector q_m in the Fourier space ($\Delta = 1/q_m$). The scattering vector q in our experiment was sampled out to $q_m = 18$ nm^{-1}. The first two peak positions of the tetragonal form of boron are 1.802 Å and 2.92 Å, respectively, and they correspond well with our experimental results of the first two peak positions [15].

The another important parameter for amorphous structure determination is the coordination number (CN), which is the average number of atoms surrounding any given atom at the first nearest neighbor and defined as

$$CN = \int_{r1}^{r2} J(r)dr \qquad (6.7.6)$$

where $J(r) = 4\pi r^2 \rho = rG(r) + 4\pi r^2 \overline{\rho}$ and, r_1 and r_2 define the upper and lower bounds of the distances associated with the first peak in the total RDF $J(r)$. The CN reported for amorphous boron in the literature is 6.3 [15] and the CN we calculated from our experimental RDF was approximately 6.0.

6.8 Summary and Conclusions

All carbon soot samples investigated in this work had nearly identical short-range orders. The first peak distance agreed closely with the expected and measured value reported before [6, 7]. Our second peak distance agreed especially well with the expected value by Parrinello et al. whom their simulated sample consisted of 85% sp^2 bonded and 15% sp^3 bonded carbon. In contrast, Li et al. reported a fraction of sp^3 bonded carbon to be 10% in their work [6]. This shows the sensitivity of the bond lengths to the composition of the bonding type in a sample. The bond angles were calculated by the relation $\theta = 2\sin^{-1}(r_2 / 2r_1)$ to asses the nature of the bonding (sp^2 vs. sp^3) [27]. The bond angles calculated here are 124.2°, 126.3°, 126.3°, 121.5°, and 127.0° from sample A to E respectively. The limited resolution in our RDF curves gives errors of 20-30% in our estimated bond angles. The bond angles are 120.0° for graphite, 109.5° for diamond and 110.0° for a-diamond respectively. Our bond angle values are much closer to that of graphite in absolute value although we can not rule out the possibility of some fraction of sp^3 bonded carbon in our samples. Our peak positions suggest that amorphous carbon in our soot samples is mostly sp^2 bonded carbon with a fraction of roughly 15% sp^3 type making the rest [7].

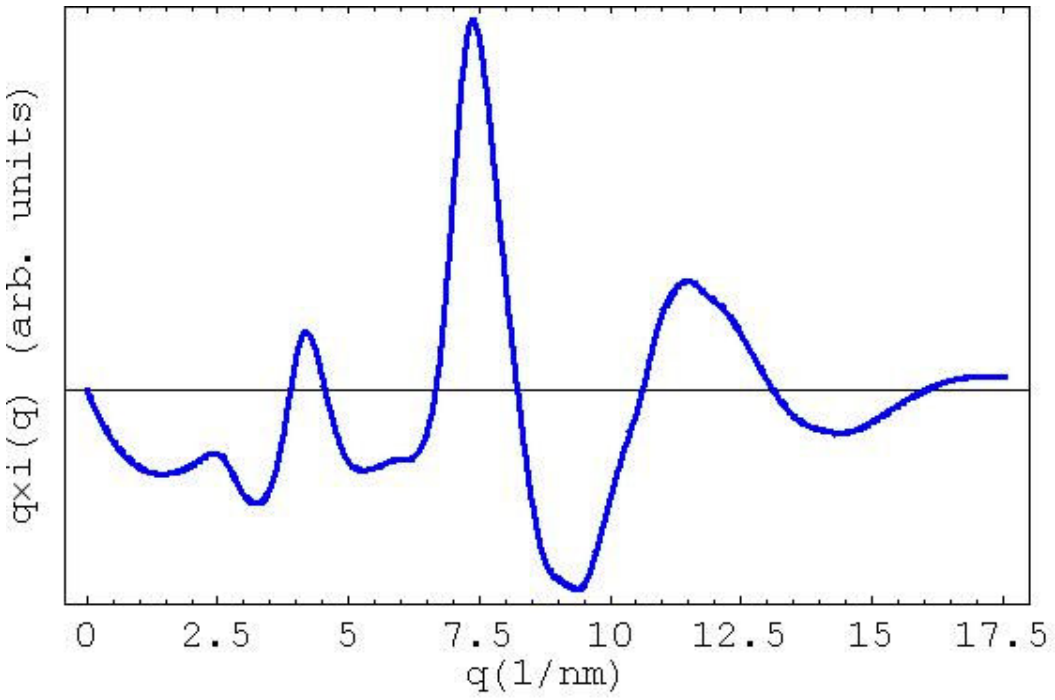

Fig. 6.7.3 Corrected experimental *q*-weighted static structure factor curve for a boron nanowire from which a new RDF was obtained by the Fourier transform.

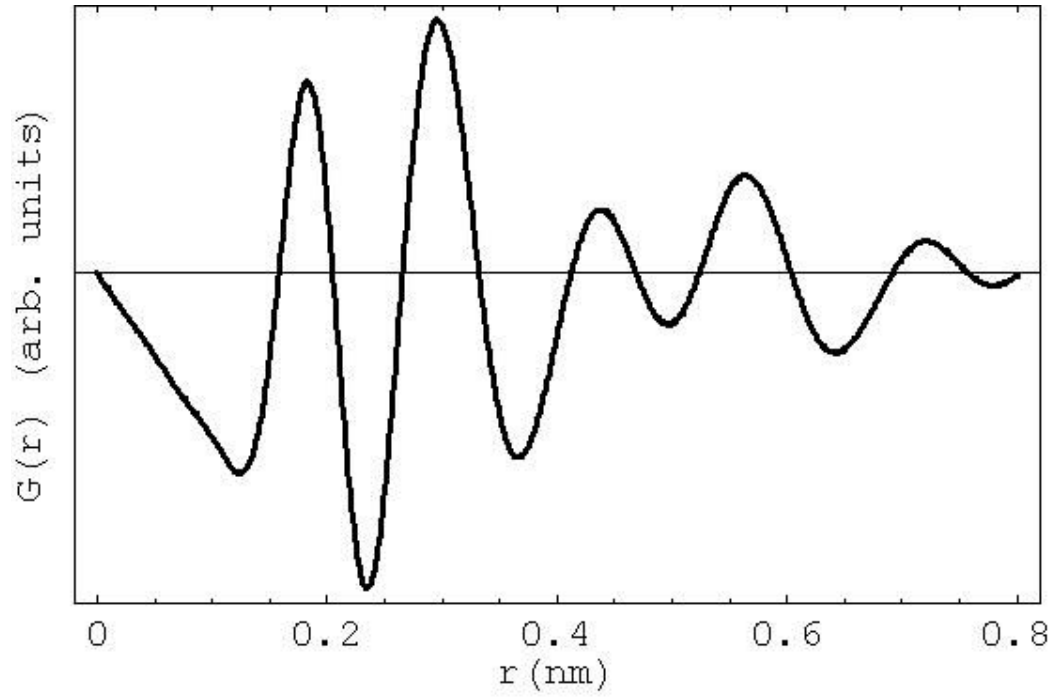

Fig. 6.7.4 Corrected experimental reduced RDF curve for a boron nanowire from which the coordination number of 6.0 was calculated.

In addition to the RDF analysis to study SRO, the FEM was also employed in order to study MRO in carbon soot samples. Unfortunately, only two soot samples were investigated by FEM since it is very time consuming. FEM showed that in the samples obtained by laser ablation of pure carbon target, MRO decreased with increasing furnace temperature. We know that SRO in these two samples are almost identical and resembles that of a-Carbon having sp^2 type bonding mostly. However, the RDF gives information on average structure by probing a volume much larger than the FEM does. The main reason of using FEM is to obtain information on local structure in the sample. The electron coherence length in our experiments determined by the probe size was on the order of 1.0-1.3 nm. Our results indicate that the concentration and size of the structural units on this length scale is decreasing in the sample as the furnace temperature increases although one would expect to see the opposite since the yield of fullerenes increases with temperature in laser ablation. One explanation for this could be that the fullerenes and graphitic cage-like particles are getting larger in size as observed from TEM images and these types of structures were avoided in our FEM experiments. What remaining is mostly amorphous carbon lacking small size fullerenes or nanoparticles.

The SRO order in boron nanowires was examined and we determined that it resembles that of bulk amorphous boron. It is well known that icosahedral B12 structural units exist even in amorphous boron. This suggests that icosahedral B12 is the most stable form of boron and the growth kinetics and energetics have a little effect on the structure of amorphous boron. The coordination number we calculated is little less than what is reported previously. This might indicate that nanowires might have a structure with more voids than an average one or the structure might be under large amount of strain. The

latter one is highly unlikely since the obtained peak positions and the bond angle (107.7^{o} estimated versus 108^{o} expected for intra-icosahedral bonding) agrees well with the known values [28]. Unfortunately, it is not possible to see the structure in more detail in HRTEM due to large thickness of wires.

We applied electron diffraction and RDF analysis successfully to determine SRO in soot samples and boron nanowires. Although the RDF analysis is well-know technique to study SRO in disordered materials, the analysis of the scattering intensities from electron diffraction requires the elimination of the contribution from inelastically scattered electrons, which could be done easily with energy loss spectrometers. In this work, we developed numerical means to eliminate the inelastic scattering in the absence of a spectrometer which costs about 0.5 million dollars for a modern day TEM. A new technique known as fluctuation electron microscopy was also applied in the study of MRO in carbon soot samples and we showed its sensitivity in studying MRO while regular electron diffraction can only reveal SRO.

6.9 References

1. Sen, R., Suzuki, S., Kataura, H., Achiba, Y. (2001). Growth of single-walled carbon nanotubes from the condensed phase. *Chem. Phys. Lett.* **349**, 383-388.

2. Geohegan, D.B., Schittenhelm, H., Fan, X., Pennycook, S.J., Puretzky, A.A., Guillorn, M.A., Blom, D.A., Joy, D.C. (2001). Condensed phase growth of single-wall carbon nanotubes from laser annealed nanoparticulates. *Appl. Phys. Lett.* **78**, 3307-3309.

3. Treacy, M.M.J. and Gibson, J.M. (1996). Variable coherence microscopy: a rich source of structural information from disordered materials. *Acta Cryst. A* **52**, 212-220.

4. Warren, B.E. (1990). X-Ray Diffraction. Dover Publishing Inc.: New York.

5. Qin, L.C., "Electron Amorphography" in *Progress in Transmission Electron Microscopy 1*, Eds. Zhang, X.F., Zhang, Z. (2001, Springer: New York).

6. Li, F. and Lannin, J.S. (1990). Radial distribution function of amorphous carbon. *Phys. Rev. Lett.* **65**, 1905-1908.

7. Galli, G., Martin, R.M., Car, R., Parrinello, M. (1989). Structural and electronic properties of amorphous carbon. *Phys. Rev. Lett*. **62**, 555-558.

8. Hirai, H., Tabira, Y., Kondo, K., Oikawa, T., Ishizawa, N. (1995). Radial distribution function of a new form of amorphous diamond shock induced from C60 fullerene. *Phys. Rev. B* **52**, 6162-6165.

9. Treacy, M.M.J., Gibson, J.M., Fan, L., Paterson, D.J., McNulty, I. (2005). Fluctuation microscopy: a probe of medium range order. *Rep. Prog. Phys.* **68**, 2899-2944.

10. Gibson, J.M. and Treacy, M.M.J. (1997). Diminished medium-range order observed in annealed amorphous germanium. *Phys. Rev. Lett.* **78**, 1074-1077.

11. Voyles, P.M. and Muller, D.A. (2002). Fluctuation microscopy in the STEM. *Ultramicroscopy* **93**, 147-159.

12. Chen, X., Sullivan, J.P., Friedmann, T.A., Gibson, J.M. (2004). Fluctuation microscopy studies of medium-range ordering in amorphous diamond-like carbon films. *Appl. Phys. Lett.* **84**, 2823-2825.

13. Donohue, J. (1982). *The Structures of the Elements*. Robert E. Krieger Publish: Malabar, Florida.

14. Hoard, J.L., Newkirk, A.E. (1960). An analysis of polymorphism in boron based upon x-ray diffraction results. *J. Am. Chem. Soc.* **82**, 70-76.

15. Krishnan, S., Ansell, S., Felten, J.J., Volin, K.J., Price, D.L. (1998). Structure of liquid boron. *Phys. Rev. Lett*. **81**, 586-589.

16. Kobayashi, M., Higashi, I., Takami, M. (1997). Fundamental structure of amorphous boron. *J. Sol. Stat. Chem*. **133**, 211-214.

17. Cao, L., Zhang, Z., Sun, L., Gao, C., He, M., Wang, Y., Li, Y., Zhang, X., Li, G., Zhang, J., Wang, W. (2001). Well-aligned boron nanowire arrays. *Adv. Mat*. **13**, 1701-1704.

18. Otten, C.J., Louire, O.R., Yu, M.F., Cowley, J.M., Dyer, M.J., Ruoff, R.S., Buhro, W.E. (2002). Crystalline boron nanowires. J. Am. Chem. Soc. **124**, 4564-4565.

19. Boustani, I., Quandt, A., Hernandez, E., Rubio, A. (1999). New boron based nanostructured materials. *J. Chem. Phys*. **110**, 3176-3185.

20. Hamada, N., Sawada, S., Oshiyama, A. (1992). New one-dimensional conductors: graphitic microtubules. *Phys. Rev. Lett.* **68**, 1579-1581.

21. Ciuparu, D., Klie, R.F., Zhu, Y., Pfefferle, L. (2004). Synthesis of pure boron single-wall nanotubes. J. Phys. Chem. B **108**, 3967-3969.

22. Kaplow, R., Strong, S.L., Averbach, B.L. (1965). Radial density functions for liquid mercury and lead. *Phys. Rev*. **138**, 1336-1345.

23. Waser, J., Schomaker, V. (1953). The Fourier inversion of diffraction data. *Rev. Mod. Phys.* **25**, 671-690.

24. Laaziri, K., Kycia, S., Roorda, S., Chicoine, M., Robertson, J.L., Wang, J, Moss, S.C. (1999). High-energy x-ray diffraction study of pure amorphous silicon. *Phys. Rev. B* **60**, 13 520- 13 533.

25. Wilson, A.J. and Prince, E. (1999). *International Tables for Crystallography C*. Kluwer Academic Publishing: Boston.

26. Galaup, S., Kihn, Y. (1998). Improvements in the treatment of elastic electron diffraction profiles for local order determination in polycrystalline samples. *Eur. Phys. J*. **4**, 281-290.

27. McKenzie, D.R., Muller, D., Pailthorpe, B.A. (1991). Compressive-stress-induced formation of thin-film tetrahedral amorphous carbon. *Phys. Rev. Lett*. **67**, 773-776.

28. Vast, N., Bernard, S., Zerah, G. (1995). Structural and electronic properties of liquid boron from a molecular-dynamics simulation. *Phys. Rev. B* **52**, 4123-4130.

Chapter 7

Summary and Conclusions

On the road to widespread technological applications of carbon nanotubes, the determination of their atomic structure accurately is an important step. Diffraction methods, especially electron diffraction have proven that it can achieve this better than any other available characterization tools today. In this study, we applied electron microscopy and diffraction extensively to a wide range of materials for structure determination.

Production of SWNT

A new catalyst mixture (Co/Si) was discovered to synthesize high quality single-walled carbon nanotubes with yield as good as previous contender Ni/Co mixture in laser ablation. We used TEM, high resolution TEM, and nanobeam electron diffraction (NBED) to determine the structure of as-grown nanotubes. These SWNTs have an average diameter of 1.50±0.16 nm which is similar to that of nanotubes synthesized by the Ni/Co catalyst. We showed that these tubes tend to have larger chiral angles with slight preference of metallicity in contrary to nanotubes of Ni/Co system. The histogram of normalized occurrence showed two prominent peaks at about 12^{o}-14^{o} and 24^{o}-26^{o} range. It is unknown yet if this is due to the fact that Si is also present in the catalyst. Observed preferences of helicities and metallicities might be due to a low number of

sampling and only one third of nanotube species seen out of the expected ones. Resonant Raman spectroscopy can help reveal the dominant nanotube species in this SWNT sample and shed some light on the role of Si on the distribution of helicities if it does have one. If the effect seen here was due to Si alone, this would open new possibilities in terms of controlling the structure of as-grown nanotubes.

Structure Determination of Carbon Nanotubes

A total of 22 DWNTs have been studied to determine their chiral indices. The use of higher order reflections for structure determination was also demonstrated. We found that the helicity distribution for the inner and outer shells in the examined DWNTs was rather uniform and only 3 out of 22 DWNTs analyzed here have a commensurate structure. This suggests that there is no strong correlation between the orientation of the inner and outer shells. The average inter-wall spacing was 0.36 ± 0.40 nm and this value is 5% bigger than that of turbostratic graphite with random stacking of layers. However, it agrees with previous reports on inter-wall spacing of DWNTs. Our spacing value can be explained by the size effects seen in carbon nanotubes before. The pronounced curvature in small nanotubes like DWNTs studied here leads to the modification of geometry and electronic structure which in turn modifies the wall spacing due to repulsive forces. This does not explain the strong preference towards the wall spacing in the range of 0.30-0.32 nm. This might be due to the fact that the diameter of the inner shell is determined by that of the outer shell whose diameter is roughly proportional to the size of the catalyst particle. Since the stability of DWNTs strongly depend upon inter-wall spacing, the most stable

tube pair is some times obtained when the spacing is less than that of turbostratic value due to the discrete nature of chiral space.

An electron diffraction procedure was established to obtain the chirality of each and every shell in MWNTs. Zone scheme developed here can be used to identify the layer line groups and every helicity can be determined accurately from the diffraction patterns. When this is combined with the diameters from the TEM images, we can determine the chiral indices of each shell in a carbon nanotube. We have identified the chirality of 13 MWNTs: one triple-walled, three quadruple-walled, two quintuple-walled, one six-walled, one seven-walled, one eight-walled, one nine-walled, one eleven-walled, and one fourteen-walled carbon nanotube. The procedure developed can be applied to nanotube with larger number of walls. Currently, the maximum number of walls studied was fourteen. We estimated using the error in layer line spacings that the structure of up-to 25 walls can be determined if each one has its own helicity. Future works will include testing this hypothesis by studying larger nanotubes. Improving the accuracy of diffraction patterns will also facilitate the index assignment. Several diffraction patterns over different sections of a tube can be acquired to obtain the multiple measurements for the v/u ratios. Diffraction patterns can be taken on both the CCD camera and the photographic films. The layer lines are much more clearly distinguished from the films whereas the equatorial layer line can be obtained from the patterns taken on the CCD camera to resolve it better since the films saturate quickly because of strong intensity of the equatorial line. Measurement of the layer line spacings and the assignment of the chiral indices are very time consuming at the moment (several days). Automation of the layer line spacing measurements and the use of computer scripts to try and to exhaust all

possible chiral index assignments (including the simulation of the equatorial line) will speed this procedure up greatly. The guidelines are given for such steps and scripts at the end of Chapter 4. The selection of the possible chiral indices using the *v/u* ratios and the experimental uncertainties is already automated.

The results from all DWNTs and MWNTs analyzed suggest that the structural orientation between the adjacent shells of a carbon nanotube is weak. When this is coupled with the weak dependence of formation energy of nanotubes on helicity, we can say that the interactions among the shells in a nanotube have a little effect on the growth mechanism. However, the inter-wall spacing plays a bigger role in the stability of a nanotube. We have seen that some nanotubes might favor (3n, 2n) nanotube structure whose inter-wall spacing comes closest to that of turbostratic graphite. It might be possible to adjust the structure of small nanotubes by finding and tuning the growth conditions that influence the spacing constraint.

WS_2 Nanotubes

These nanotubes are from the family of inorganic fullerene-like nanotubes with structures similar to carbon nanotubes. These were the first synthesized inorganic nanotubes showing that the layered structures of other compounds can be rolled up to form tubular structures, and they opened the door for the synthesis of new forms of nanotubes with widely-ranging properties. The tubes studied here for structure determination consist of a few walls, but usually they can have a few tens of walls. The innermost diameter of these tubes is about 9.0 nm, much larger than their carbon counterparts. We showed that the structure of up to five walls can be determined

unambiguously despite their large diameters and possibly this can be extended for extra few walls. The tubes characterized here have smaller chiral angles (less than 20^o) and tend to have a near zigzag structure. Observation of smaller chiral angles suggests that this kind of growth is more favorable energetically and kinetically. The closeness of helicities of adjacent layers in a tube can be explained by quasi-epitaxial growth of layers (layer-by-layer growth) since it proceeds inward from the template oxide whiskers in solid-gas phase reaction. This might make it possible to tune the structure of each layer precisely by controlling the synthesis conditions. Since these nanotubes are semiconducting, it is of utmost importance to know and engineer the structure precisely for their future applications in nano-photonics.

Order and Disorder

We employed the RDF analysis and electron diffraction to investigate the atomic structure of carbon soot prepared by laser ablation. Despite all the efforts to understand the nucleation of carbon nanotubes in laser ablation, there is yet no clear picture emerging to offer any insights into the real mechanism. We examined the effects of the temperature and the catalysts on the structure to see whether or not the crystallinity of carbon soot contributes to the nucleation of nanotubes. The SRO structure was identical for all samples regardless and closely similar to the amorphous carbon structure reported before which has mostly sp^2 bonded carbon with 15% sp^3 bonded making the rest. This suggests that the presence of catalyst or temperature has little effect on the SRO structure in carbon. The investigation of the MRO by FEM revealed that the temperature has an effect on the structure of soot. The existence of MRO in low temperature pure carbon

soot on the length scale of ~1.0-1.3 nm can be speculated by considering the coherence length of the electron probe. However, it is too early to say anything definite about the nature of the structural units or the nucleation of carbon nanotubes. Structural models are needed for future studies and for establishing correlations with experimental results.

Amorphous boron nanowires were also studied by the same techniques. The first two peak positions obtained were 1.82 and 2.94 Å with a coordination number of 6.0. These values correspond well with the structure of bulk amorphous boron reported previously and conforming once again that the icosahedral B_{12} unit survives in the amorphous phase of boron. This suggests that the growth kinetics and energetics have a little effect on the structure.

Our new technique makes the study of electron diffraction patterns of carbon nanotubes more easy and accessible for a general user. Normally, it will take expert microscopists to determine the structure. Simple guidelines outlined here should make the structure identification of any nanotubes with a few layers possible for a novice in the field. For more intricate structure problems, the automated procedures in the future will be employed and this will enable anyone with basic knowledge of carbon nanotube structure to obtain entire atomic structure in a matter of minutes. In this way, a large ensemble of carbon nanotubes can be studied and analyzed in order to understand their morphology, nucleation and growth better.

Although TEM is powerful in structural characterization of carbon nanotubes as an analytical instrument, it lags behind other methods when it comes to measuring their properties. Optical absorption spectroscopy or Raman spectroscopy or STM can study the geometry and electronic structure simultaneously. Recent works reported a combination

of TEM and spectroscopy measurements to reveal the structure and to measure the vibrational properties. The future of nanotube characterization will include both TEM and spectroscopic methods since the former can give high level of accuracy with identification of large number of shells while the latter one can have access to the properties. Moreover, the results of TEM and spectroscopic techniques can be checked against one another and necessary corrections and calibrations can be made in both methods to improve their accuracies.

Torsional springs based on individual carbon nanotubes offers interesting future applications in nano-electromechanical systems. For such devices to be used as nano-bearings or oscillators in DWNTs for example, it is vital to fully know the structure. Although the stability of a DWNT is not affected by the helicity of each shell, their relative motions to each other like mechanical rotations strongly depend on it. Then it becomes necessary in the design and engineering of these devices to consider the fine structure to realize its full potential. TEM can also reveal the handedness of carbon nanotubes which has not been studied well so far. The effect of torsion on the diffraction patterns of nanotubes were explained in recent theoretical works and the procedures were outlined to obtain the handedness from them. Torsional nano-electromechanical systems have the capability to achieve this when combined with TEM. DWNTs will be the simplest to perform such experiments and this can be expanded to MWNTs later. This is important since the handedness has great influence on optical properties of nanotubes.

Appendix A. Chiral Indices of Total 22 DWNTs.

	u1	v1	u2	v2	α1	α2	d1(nm)	d2(nm)	c/2(nm)	Type1	Type2
#1	8	8	20	4	30.00	8.95	1.085	1.744	0.329	M	S
#2	23	0	31	0	0.00	0.00	1.801	2.427	0.313	S	S
#3	12	9	27	2	25.28	3.54	1.429	2.197	0.384	M	S
#4	11	9	22	9	26.70	16.39	1.359	2.163	0.402	S	S
#5	20	1	18	15	2.42	27.00	1.607	2.241	0.317	S	M
#6	6	5	11	10	27.00	28.43	0.747	1.425	0.339	S	S
#7	9	3	18	5	13.90	11.93	0.847	1.641	0.397	M	S
#8	7	3	17	5	17.00	12.52	0.696	1.564	0.434	S	M
#9	11	1	16	8	4.31	19.11	0.903	1.657	0.377	S	S
#10	10	4	17	8	16.10	18.26	0.978	1.732	0.377	M	M
#11	7	7	14	11	30.00	26.04	0.949	1.699	0.375	M	M
#12	10	1	20	2	4.72	4.72	0.825	1.650	0.412	M	M
#13	12	2	19	7	7.59	15.08	1.027	1.825	0.399	S	M
#14	14	7	20	10	19.11	19.11	1.450	2.072	0.311	S	S
#15	11	7	18	11	22.69	22.07	1.231	1.986	0.377	S	S
#16	11	7	22	3	22.69	6.31	1.231	1.851	0.310	S	S
#17	10	7	23	4	24.18	7.89	1.159	1.976	0.409	M	S
#18	14	5	21	8	14.70	15.49	1.336	2.031	0.348	M	S
#19	16	3	23	5	8.44	9.64	1.385	2.025	0.320	S	M
#20	9	6	14	10	23.41	24.50	1.024	1.635	0.306	M	S
#21	7	7	17	5	30.00	12.52	0.949	1.564	0.307	M	M
#22	7	4	18	1	21.05	2.68	0.755	1.450	0.348	M	S

Appendix B. Chiral Indices of FWNTs.

Table1. Chiral Indices of A Four-Wall Carbon Nanotube (Example5).

u	v	d (nm)	Hel	Type
32	1	2.546	1.53	S
40	5	3.345	5.82	S
33	27	4.076	26.70	M
37	34	4.816	28.60	M

Table2. Chiral Indices of A Four-Wall Carbon Nanotube (Example6).

u	v	d (nm)	Hel	Type
30	28	3.934	28.86	S
57	4	4.628	3.36	S
44	34	5.304	25.77	S
59	28	6.023	18.38	S

Appendix C. Chiral Indices of an 11-walled MWNT.

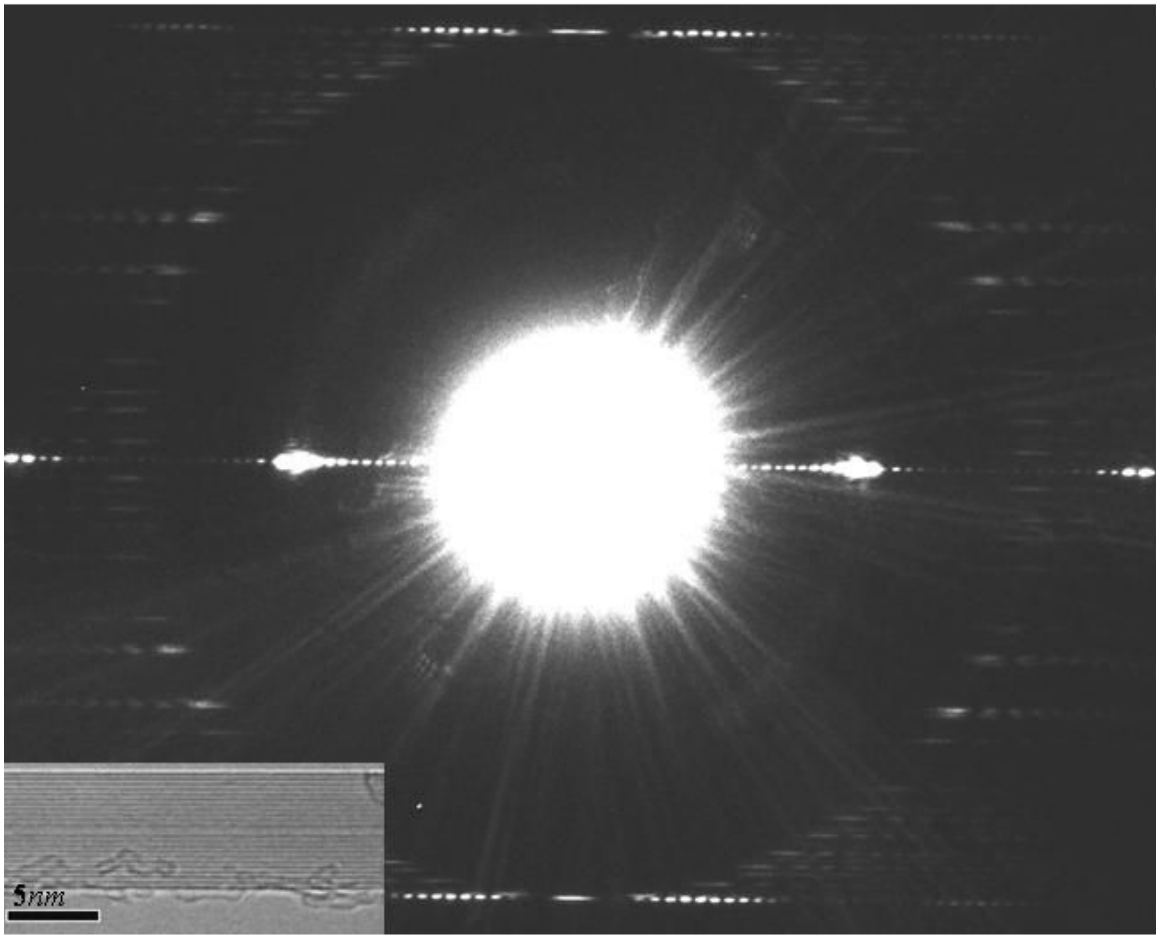

Fig. 1. Experimental electron diffraction pattern of an eleven-walled carbon nanotube taken at 120 kV accelerating voltage with a nano-beam diffraction. The inset shows an HRTEM image of the same nanotube.

Table 1. Experimentally measured layer lines and *v/u* ratios for the eleven-walled MWNT seen above.

Group	D1	D2	D3	Error	*v/u*	error in *v/u*	%error
A	1916.633	1067.7	849.1	-0.167	0.0791	-0.0001	-0.18
B	1916.633	1088.7	827.6	0.333	0.0950	0.0003	0.31
C	1904.3	1200.2	701.1	3	0.1902	0.0030	1.57
D	1847.8	1416.2	434.1	-2.5	0.4320	-0.0034	-0.78
E	1799.3	1505.2	296	-1.9	0.5785	-0.0031	-0.53
F	1768.8	1548.3	218.5	2	0.6675	0.0036	0.53
G	1735.8	1595.3	143	-2.5	0.7754	-0.0050	-0.65
H	1706.8	1626.3	80	0.5	0.8649	0.0011	0.13

Table 2. Final index assignment for the eleven-walled carbon nanotube.

u	*v*	d (nm)	α(DEG)	Type
6	4	0.683	23.41	S
12	8	1.365	23.41	S
18	12	2.048	23.41	M
24	16	2.731	23.41	S
42	4	3.456	4.50	S
47	9	4.079	8.61	S
43	25	4.665	21.31	M
44	34	5.304	25.77	S
60	26	5.982	17.14	S
52	45	6.584	27.61	S
89	7	7.259	3.75	S